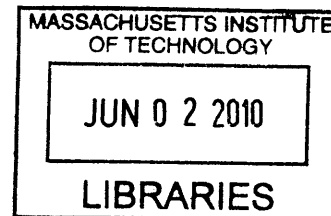


# Ultrafast Photo-Acoustic Spectroscopy of Super-Cooled Liquids

by

Christoph Klieber



B.A. Philosophie, College of Philosophy S.J., Munich, 2004  
Diplom Physik, Ludwig-Maximilian-Universität, Munich, 2006

Submitted to the Department of Chemistry  
in partial fulfillment of the requirements for the degree of

Doctor of Philosophy

at the

MASSACHUSETTS INSTITUTE OF TECHNOLOGY

June 2010

**ARCHIVES**

© Massachusetts Institute of Technology 2010. All rights reserved.

Author .....  
Department of Chemistry  
May 18, 2010

Certified by .....  
Keith A. Nelson  
Professor of Chemistry  
Thesis Supervisor

Accepted by .....  
Robert W. Field  
Chairman, Department Committee on Graduate Students





This doctoral thesis has been examined by a committee  
of the Department of Chemistry as follows:

Professor Mounji G. Bawendi .....  
Committee Chair

Professor Keith A. Nelson .....  
Thesis Supervisor

Professor Jianshu Cao .....  
Committee Member



# Ultrafast Photo-Acoustic Spectroscopy of Super-Cooled Liquids

by  
Christoph Klieber

Submitted to the Department of Chemistry on May 18, 2010,  
in partial fulfillment of the requirements for the degree of Doctor of Philosophy

## Abstract

Picosecond laser ultrasonic techniques for acoustic wave generation and detection were adapted to probe longitudinal and transverse acoustic waves in liquids at gigahertz frequencies. The experimental effort was designed for the study of supercooled liquids whose slower relaxation dynamics extend to gigahertz frequencies at high temperatures and whose faster dynamics are centered uniquely in the gigahertz frequency range.

The experimental approach used a unique laser pulse shaping technique and, in the case of shear acoustic waves, a crystallographically canted metal transducer layer, to generate frequency-tunable compressional and shear acoustic waves. Either time-domain coherent Brillouin scattering or interferometry was used to detect the waves in or after propagation through a liquid layer. The study of liquid-state gigahertz acoustic behavior required advances in both the experimental methodology and in the theoretical modeling of the results. A particular challenge was posed by the extraordinarily strong damping of gigahertz-frequency acoustic waves in liquids at some temperature ranges. This demanded the design and construction of a liquid sample cell allowing access to a wide range of liquid thicknesses, from less than a nanometer up to several microns. This was achieved by squeezing the liquid between two specially prepared high quality optical substrates held in a non-parallel configuration by a custom-designed sample holder jig. Several metallic layer materials were used for conversion of optical pulse energy into acoustic waves that were launched into the liquid samples, and different probe geometries were developed to enable access to a wide frequency range.

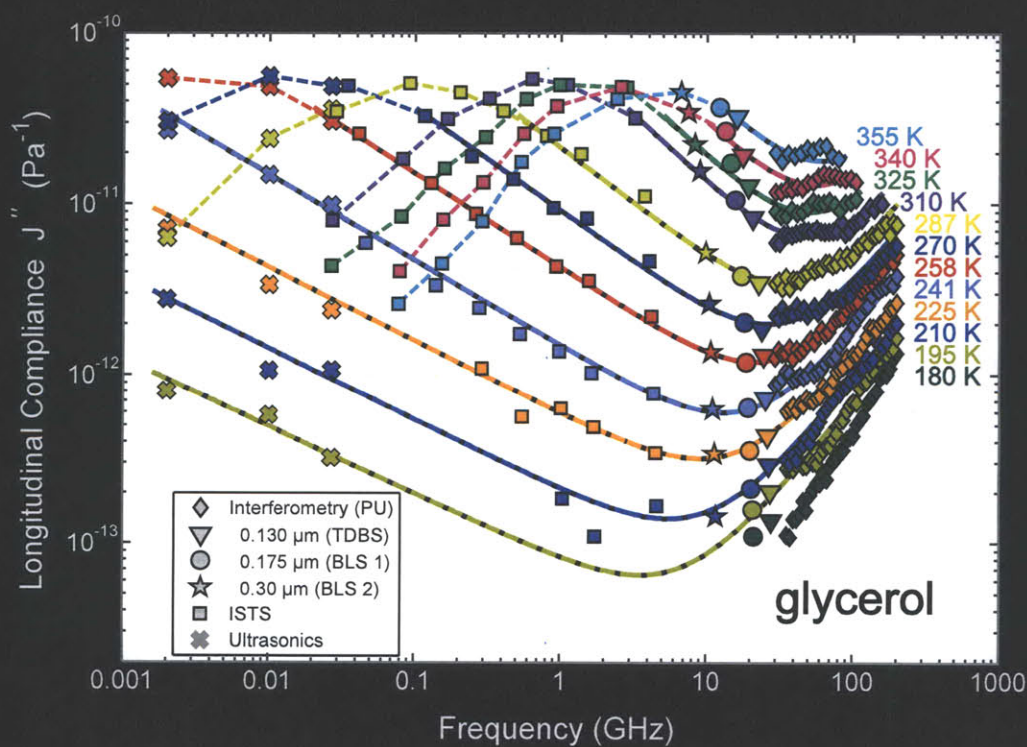
The developed spectroscopic strategies were then applied to the study of two liquids, glycerol and tetramethyl tetraphenyl trisiloxane (DC704). Measurements of the density responses of both liquids from 400 K to below their respective glass transition temperatures were carried out. Longitudinal acoustic waves were either monitored via time-domain Brillouin scattering in the liquid or via interferometry after transmission through variably thick liquid layers, granting access to longitudinal acoustic frequencies from 10 GHz up to about 200 GHz. The information obtained on gigahertz frequency liquid relaxation was pieced together with data from several other techniques to create broadband relaxation spectra (from millihertz up to gigahertz), allowing characterization of the complex structural relaxation dynamics over many orders of magnitude and enabling both empirical modeling and testing of the predictions of the mode-coupling theory of supercooled liquids.

The requirements for gigahertz shear wave generation and detection, including the properties of the photo-acoustic transducer materials, the sample and experimental geometry, and the detection material choices, are discussed. Results on shear wave propagation in glycerol and DC704 are presented. The technique for shear wave generation and detection is not limited to the study of viscous liquids but can also be applied to liquids like water, from which initial results are presented.

Thesis Supervisor: Keith A. Nelson  
Title: Professor of Chemistry



# ULTRAFAST PHOTO-ACOUSTIC SPECTROSCOPY OF SUPERCOOLED LIQUIDS



CHRISTOPH KLIEBER



ULTRAFAST  
PHOTO-ACOUSTIC SPECTROSCOPY  
OF SUPERCOOLED LIQUIDS

Doctoral Thesis

Christoph Klieber

Front cover: High frequency longitudinal compliance spectrum of glycerol  
Back cover: Deathstar Compact pulse shaper

---

Ultrafast Photo-Acoustic Spectroscopy of Supercooled Liquids

Christoph Klieber

PhD Thesis, Massachusetts Institute of Technology, Cambridge, MA—June 2010

© 2010 Massachusetts Institute of Technology. All rights reserved.

An electronic (full-color) version of this thesis can be found at:

<http://www.klieber.net>



---

# Preface

---

On my first trip to MIT and the Nelson group, I would never have foreseen that our relationship will go on for so long. I first met my future ‘Doktorvater’ (adviser) Keith Nelson in the summer of 2001 during his stay at the University of Würzburg — a meeting initiated by my undergraduate adviser Professor Ernst Rössler to whom I will always be indebted for arranging this meeting. I recall that Keith introduced me to ultrafast laser spectroscopy by showing me movie clips of coherent control of ‘phonon-polaritons’, an admixture of electromagnetic waves and lattice vibrations that move at light-like speeds. I, being in my second year of undergrad, had no real clue what was going on and was totally fascinated. Thereafter, he invited me for a research visit to his group which I happily accepted. I arrived at MIT in the spring of 2002 and spent ten wonderful weeks conducting research in his group. After this brief stint at MIT, which coincided with the completion of the first part of my degree at the University of Bayreuth with a ‘Vordiplom’, I moved to Munich to continue my physics degree at the Ludwig-Maximilian-University. At that time, I specialized in particle and astrophysics and also pursued a bakkalaureat in philosophy at the Jesuit College of Philosophy in Munich. I presented a thesis on the ‘Process philosophy of Alfred North Whitehead’ in early 2004. The all-round scientist Whitehead is most well-known for his *Principia Mathematica*, an epochal piece in logic which he coauthored with his student Bertrand Russell. Later in Whitehead’s life he turned his attention to philosophy and metaphysics, a progression which I think produces the greatest philosophers — a well worked out scientific world view together with the wisdom of age. I continued philosophical studies on this topic throughout 2004 under my supervisor Professor Godehard Brüntrup with the goal to pursue a PhD in philosophy. When I moved to MIT one year later, I interrupted those studies indefinitely but I am receptive to becoming a ‘real’ Doctor of Philosophy one day.

In retrospect, the spring of 2004 was quite decisive for my future scientific career. During an internship in a risk management consulting firm, I was fortunate to work with many PhD physicists who cautioned me against pursuing my interest in particle physics for my ‘Diplomarbeit’ and doctorate. Due to the nature of the experiments performed in particle and high energy physics, conducting doctoral work in these fields might be a rather boring and disappointing experience for a junior graduate student. Instead, they advised me to work in a field where I could have autonomy over all parts of my doctoral research: from deciding what to investigate, designing, building and running the experiments to the analysis and interpretation of the measured data. Acting on their advice, I contacted Keith and he happily agreed to take me under his wing and arranged for me to conduct my ‘Diplomarbeit’ work in his group. I enjoyed

the work so much that late one night in the summer of 2005 when Keith stopped by the lab, I asked him about the prospects of extending my ‘Diplomarbeit’ work into a PhD. The rest, or so they say, is history.

On hindsight, the predictions of the physicists in the consulting firm appear to be quite accurate — working in a huge project like LHC at CERN (where I would have most likely ended up) may have been exciting, but LHC is still not fully operational to date. It seems likely that I would have finished my doctoral studies without the chance to collect tangible results or see the actual project come to fruition.

After such a long time — a total of five-and-a-half years at the Nelson group in MIT for my ‘Diplomarbeit’ and PhD work, and even longer since my first visit — it is with great pleasure to reflect on these years and attempt to express my gratitude to all the people who have made the work and struggles not only possible, but also enjoyable. Keith has been a fantastic research adviser and I could not have asked for a better experience in his group. I am continually impressed by his enthusiasm and dedication to science. His busy schedules have never prevented him from generously offering his time whenever I needed his advice. I am extremely thankful for his mentorship and for giving me so much freedom and support to pursue interesting questions both in and outside the lab at whatever time of day (or night). His incredible optimism that everything will work out eventually, his unlimited trust in humans and his boundless enthusiasm and energy for science are attributes we should all aspire to.

Over the years, I have been privileged to work with a wide variety of talented individuals. It was Dr. Kenji Katayama a former postdoctoral associate in the Nelson group who introduced me to the field of ultrasonic studies and to laser physics in general in the winter of 2004/05. I am thankful to Dr. Emmanuel Peronne, a former postdoctoral fellow at the Nelson group during my ‘Diplomarbeit’ year, who not only generously shared his physics know-how with me but also taught me many helpful experimental methods and tricks, and helped me build the first Sagnac interferometer. Many thanks also go to my labmates during that time, Tina Hecksher and Ben Paxton for their fantastic company. Ben was always there when I had to face the frequent laser or computer problems and often advised me when I was at a loss with my experiments. With Tina not only I enjoyed the many, many exhausting weeks in lab together in order to get the stubborn new setup to run but also enjoyed many coffee breaks and chats. It was both an honor and a pleasure to have worked together with them. I am very grateful to Dr. Jaime Choi who trustfully left me the original Deathstar setup.

Dr. Darius Torchinsky — a former fellow fighter on the glass-formation front, so to say — was a partner in crime since the first time I visited MIT in 2002. He consistently supported me when facing challenging problems and provided good conversations in stressful times. Dr. Ka-Lo Yeh and Dr. Matthias Hoffmann are not only the cutest couple I know but also became great friends to me. Living with Matthias and having Ka-Lo over frequently ensured that life was never boring and we had many exciting

adventures together — from hiking trips with a broken car, to frequently fighting the jungles at IKEA and Market Basket, or chasing mice in the apartment, to name just a few.

I overlapped with many other graduate students and postdocs in the Nelson group. Josh Vaughan, Eric Statz, Kathy Stone, Taeho Shin, Gagan Saini, Daniel Turner and Dr. Thomas Hornung were in the group the year I did the research for my ‘Diplomarbeit’. In the subsequent year, in which I officially joined MIT as a graduate student, the Nelson group expanded significantly — with Johanna Wendlandt (now Wolfson), Harold Hwang, Christopher (Kit) Werley and Jeremy Johnson. Five of us almost doubled the size of the group at that time. Even though some students graduated and postdocs left, the group kept growing with new students: Kara Manke, Dylan Arias, Patrick Wen, Zhao Chen, Raoul Correa, Nate Brandt and Cassandra Newell, and postdocs: Maria Kandyla, Kung-Hsuan Lin, Kenan Gundogdu, Thomas Pezeril, Matthias Hoffmann, Janos Hebling, Vasily Temnov, Alexander Maznev, Brad Perkins and Sharly Fleischer. Zhao Chen, Taeho Shin and Vasily Temnov deserve particular mention for sharing with me an office and putting up with my occasional outbursts of insanity.

In 2007, Dr. Thomas Pezeril came to the group and brought with him the technique of shear wave generation. He is an extremely skilled experimentalist and only through our collaborative work were the exciting studies of shear wave propagation in liquids made possible. Shear waves in water are just around the corner. After a not so smooth start, we got to know each other better and better, and became very close friends. He and his lovely wife, Melanie Pezeril (and not to forget his son Quentin), hosted me at their place during two past trips to Le Mans and come July, he will become my *boss* once again when I join his research efforts in Le Mans where he offered me a postdoc position. I am very grateful for his unreserved support and friendship and am looking forward to working and spending more time with him together.

Kara Manke joined the group in 2008 and became an indispensable part of the high frequency photo-acoustics project. I am glad that she has already taken over the lead in the ‘RegA’ lab and is up to full speed with all the experiments. I am confident that she will advance the project well and will surely achieve great things in her remaining graduate student time. Who else can anybody possibly wish for in his or her thesis project? I wish her the best of luck and joy with everything inside and outside the lab.

Special thanks go to Gloria Pless and Li Miao for their administrative contributions. Gloria, in particular, became very special to me and it was a very sad moment when she informed me about her plans to retire.

My thanks also go to Professor Stéfan Andrieu for providing us with MBE canted iron samples, and Professor Cheng-Beom Eom and his student Seung-Hyub Baek for carrying out strontium ruthenate and titanate depositions which are essential for shear wave generation.

In addition to what was said above, I am indebted to Darius Torchinsky, Jeremy Johnson and Tina Hecksher scientifically for the work presented in this thesis, and especially for providing their longitudinal acoustic data on DC704 to me. Their results allowed us to compile the amazing broadband spectra over thirteen orders in frequency. I am very pleased with our progress on this piece of great collaborative work.

I want to express my greatest debt of appreciation to my best friends — several of which accompanied and shaped my life for already more than 20 years — for all they did for me. Home is wherever, whenever and however we connect or meet. As hard as it is, I have to restrict myself to only put down their names as I could fill volumes with the stories I experienced with each of them. As this is a scientific work, I list them in chronological order in which they irreversibly entered my life: Britta Schmidt, Jens Wolpert, Michael Veit, Andre Jung, Martin Kügemann, Anna Schreiber, Xaver Pasceo, Philipp Schleiffer, Frank Markert, Ka-Lo Yeh, Shane Smith, and Matthias Hoffmann. You all are awesome!

Last, but definitely not least, I would like to express my greatest debt of appreciation to my family for their everlasting love and support. In particular, it is impossible to express my gratitude to my awesome parents for their unreserved support and unshakable belief in me not only during the past years of my graduate studies, but throughout my whole life.

Finally, I am looking forward to my new work place at ENSIM in Le Mans, France (the city with the world-famous 24 hour race) and getting to know all my future coworkers! I am also excited to come back to Cambridge, and in particular the Nelson group, frequently over the next year.

A reminder to everybody who is or will become part of my life — always keep up a high spirit and everything will just work out magically as it always has!

Cambridge, MA  
May 2010

*Christoph Klieber*

*To my loving parents  
Who made everything possible,  
And my grandfather Victor  
Who will always be my inspiration.*



---

# Contents

---

<b>Abstract</b>	<b>5</b>
<b>Preface</b>	<b>11</b>
<b>List of Abbreviations and Notation</b>	<b>21</b>
<b>1 Introduction</b>	<b>21</b>
<b>2 Phenomenology and Theory of the Liquid-Glass Transition</b>	<b>27</b>
2.1 Phenomenology of Supercooling and Glass Formation . . . . .	28
2.2 General Features of Liquid Relaxation . . . . .	31
2.2.1 Correlation Functions and their Measurement . . . . .	31
2.2.2 The Susceptibility Spectrum . . . . .	32
2.2.3 Models for Liquid Relaxation . . . . .	36
2.3 The Landscape Paradigm . . . . .	38
2.3.1 Potential Energy Function . . . . .	38
2.3.2 Decoupling and Bifurcation between $\alpha$ and $\beta_{\text{slow}}$ relaxation . .	40
2.3.3 Strong and fragile glass-formers . . . . .	41
2.3.4 Breakdown of Stokes-Einstein relation for self-diffusion . . . .	42
2.3.5 Conclusion . . . . .	42
2.4 Mode-Coupling Theory of the glass transition . . . . .	43
2.4.1 Introduction . . . . .	43
2.4.2 Mode-Coupling Equations . . . . .	44
2.4.3 Predictions of the Mode-Coupling Theory . . . . .	47
2.5 Conclusions . . . . .	54
<b>3 Experimental Methods</b>	<b>55</b>
3.1 The Picosecond Ultrasonics Pump-Probe Setup . . . . .	56
3.1.1 The Femtosecond Laser System . . . . .	58
3.1.2 The Pump-Probe Setup . . . . .	60
3.1.3 Data Acquisition . . . . .	61
3.2 Generation of Gigahertz Frequency Acoustic Waves . . . . .	62
3.2.1 Acoustic Generation (Opto-Acoustic Conversion) . . . . .	62
3.2.2 Narrowband Acoustic Generation . . . . .	67
3.2.3 Notes on Amplified Laser System . . . . .	71

3.3	Concepts of Acoustic Strain Detection . . . . .	72
3.3.1	Reflectivity Change and Brillouin Scattering . . . . .	72
3.3.2	Interferometry . . . . .	75
3.4	Setup Characterization . . . . .	82
3.4.1	Brillouin Scattering . . . . .	82
3.4.2	Interferometric Detection . . . . .	83
3.5	Temperature Dependent Measurements . . . . .	86
<b>4</b>	<b>Liquid Sample Cell . . . . .</b>	<b>91</b>
4.1	Liquid Cell Design . . . . .	91
4.2	Substrates and Transducer Films . . . . .	94
4.3	Sample Design and Sample Construction . . . . .	97
4.3.1	Sample Holder Design . . . . .	97
4.3.2	Access to Wide Range of Liquid Thicknesses . . . . .	97
4.4	Sample Preparation and Handling . . . . .	101
4.5	Sample Heating . . . . .	103
4.5.1	Steady State Heating . . . . .	103
4.5.2	Simulation of Accumulative Heating . . . . .	108
4.5.3	Single-Shot Heating . . . . .	112
4.6	Conclusions . . . . .	112
	<b>Acoustic Spectroscopy of Glycerol and DC704 . . . . .</b>	<b>115</b>
<b>5</b>	<b>Longitudinal Waves Study of Glycerol and DC704 . . . . .</b>	<b>119</b>
5.1	Experimental Methods and Data Analysis . . . . .	119
5.1.1	Time-Domain Brillouin Scattering in Liquid . . . . .	120
5.1.2	Interferometry: Displacement Detection at Receiver . . . . .	123
5.2	Results . . . . .	127
5.2.1	Results: Glycerol . . . . .	127
5.2.2	Results: DC704 . . . . .	130
5.2.3	Non-Linear Interaction of Acoustic Wave with the Liquid . . . . .	133
5.3	Broadband Acoustic Spectra and Analysis . . . . .	141
5.3.1	Composition of Broadband Acoustic Spectra . . . . .	141
5.3.2	Broadband Spectrum Analysis of Glycerol . . . . .	146
5.3.3	Broadband Spectrum Analysis of DC704 . . . . .	153
5.4	Conclusions . . . . .	162
<b>6</b>	<b>Shear Acoustic Waves Study of Glycerol and DC704 . . . . .</b>	<b>165</b>
6.1	Theoretical Background on Shear Waves . . . . .	167
6.1.1	Optical Generation of Plane Coherent Shear Acoustic Waves . . . . .	167
6.1.2	Shear Strain Detection with Laser Picosecond Acoustics . . . . .	174
6.1.3	Optical and Acoustic Cavity Effect . . . . .	177
6.2	Experimental Methods . . . . .	184
6.2.1	Shear Brillouin Scattering Detection Setup . . . . .	186
6.2.2	Shear Brillouin Scattering Data . . . . .	188



6.2.3	Data Analysis . . . . .	192
6.3	Results and Discussion . . . . .	198
6.3.1	Glycerol . . . . .	198
6.3.2	DC704 . . . . .	207
6.3.3	Water . . . . .	207
6.4	Conclusions and Outlook . . . . .	210
<b>A</b>	<b>Physical Properties of Various Materials</b>	<b>213</b>
A.1	Optical Absorption and Skin Depth . . . . .	213
A.2	Temperature Dependent Parameters of Glycerol and DC704 . . . . .	217
A.2.1	Glycerol . . . . .	217
A.2.2	DC704 . . . . .	218
	<b>BIBLIOGRAPHY</b>	<b>219</b>
	<i>Curriculum Vitae</i>	<b>233</b>

# List of Abbreviations and Notation

PSG, PBG		Piezo-Electric Shear/Bulk Modulus Gauge
US		Ultrasonics
ISS, ISTS		Impulsive Stimulated (Thermal) Scattering
BS		Brillouin Scattering
BLS		Brillouin Light Scattering (Frequency Domain)
TDBS		Time-Domain Brillouin Scattering
PU		Picosecond Ultrasonics
DS, DSC		Deathstar/Deathstar Compact pulse shaper
MCT		Mode Coupling Theory of Supercooled Liquids
KWW		Kohlrausch-Williams-Watts
VTF		Vogel-Tamman-Fulcher
SRO		Strontium Ruthenate ( $\text{SrRuO}_3$ )
STO		Strontium Titanate ( $\text{SrTiO}_3$ )
$T_g$	[K]	Glass transition temperature
$T_0$	[K]	VFT characteristic temperature
$T_c$	[K]	Mode coupling theory crossover temperature
$P$	[mW]	Laser power
$F$	[mJ cm <sup>-2</sup> ]	Laser fluence
$\eta_s$	[Poise]	Static shear viscosity [1 P (Poise) = 0.1 Pa·s]
$\sigma$	[Pa]	Compressive, tensile, or shear stress
$\eta$	[%]	Acoustic strain (dimensionless quantity)
$q, k$	[m <sup>-1</sup> ]	Optical or acoustic wavevector
$\lambda$	[m]	Optical or acoustic wavelength $\lambda = 2\pi/q = c/\nu$
$\nu, \omega$	[Hz]	Optical or acoustic frequency $\nu = \omega/(2\pi)$
$C$	[GHz ns <sup>-1</sup> ]	Linear chirp constant
$\tau(\omega, T)$	[s]	Decay time constant
$\Gamma(\omega, T)$	[s <sup>-1</sup> ]	Acoustic attenuation rate $\Gamma = 1/\tau$
$\alpha(\omega, T)$	[m <sup>-1</sup> ]	Acoustic attenuation coefficient $\alpha = 1/(\tau c) = \Gamma/c$
$\ell(\omega, T)$	[m]	Mean free path $\ell = 1/\alpha$
$(\Gamma \cdot \lambda)(\omega, T)$	[m s <sup>-1</sup> ]	Scaled acoustic attenuation rate
$c_l, c_s$	[m s <sup>-1</sup> ]	Longitudinal and shear speeds of sound
$\hat{c}(\omega, T)$	[m s <sup>-1</sup> ]	Complex speed of sound $\hat{c}(\omega) = \left(\frac{1}{c(\omega)} - i\frac{\alpha(\omega)}{\omega}\right)^{-1}$
$\hat{M}(\omega, T)$	[Pa]	Complex longitudinal modulus $\hat{M}(\omega) = M' + iM'' = \rho \hat{c}_l(\omega)^2$
$\hat{G}(\omega, T)$	[Pa]	Complex shear modulus $\hat{G}(\omega) = G' + iG'' = \rho \hat{c}_s(\omega)^2$
$\hat{K}(\omega, T)$	[Pa]	Complex bulk modulus $\hat{K}(\omega) = K' + iK'' = \hat{M}(\omega) - \frac{4}{3}\hat{G}(\omega)$
$\hat{J}(\omega, T)$	[Pa <sup>-1</sup> ]	Complex longitudinal compliance $\hat{J}(\omega) = 1/\hat{M}(\omega)$
$\hat{\chi}(\omega)$	[-]	Mathematical susceptibility or response function
$c_0^l, M_0, K_0 (=M_0)$		Low frequency (quasi-static) speed of sound and moduli
$c_\infty^l, c_\infty^s, M_\infty, G_\infty, K_\infty$		Instantaneous or frozen speeds of sound and moduli

# CHAPTER 1

---

## Introduction

---

Disordered systems present condensed matter physics with one of its longest standing, most difficult and “grand challenge” problems of our time [BK05]. The physical properties of disordered materials and the transition from a supercooled liquid to the amorphous solid state are far from well understood. Despite an enormous amount of scientific activity surrounding the subject, both experimentally and theoretically, a generally accepted and conclusive view of this problem has not yet emerged.

A supercooled liquid is a substance that has been cooled below its freezing point without crystallization. As the material is cooled further, the viscosity dramatically increases, accompanied by a corresponding increase in the characteristic time for relaxation processes. At a certain temperature, the glass transition occurs, where changes in thermodynamic properties like the thermal expansion coefficient and the heat capacity are observed. In spite of these changes in thermodynamic properties, however, the glass transition is not a first or second order phase transition in the traditional sense, but an experimentally defined kinetic transition. So far, no conventional order parameter has been defined to describe behavior near the glass transition. The characteristic time scale for structural relaxation at the glass transition  $T_g$  is on the order of 100 seconds, corresponding to a viscosity of  $10^{13}$  poise ( $= 10^{12}$  Pa·s).

All liquids are believed to undergo this glass transition if cooled quickly enough [Kau48, DS01]. In view of this universality, the glassy state may be regarded as the fourth state of conventional matter [Dyr06]: glass is solid like the crystalline state, but is also isotropic and without long-range order like the liquid state. This unique combination of properties explains the immense importance of glasses for a variety of applications. The optical and physical properties of glass make it suitable for many engineering applications such as window glass, container glass, laboratory equipment, thermal insulation, fibers and optics, and optoelectronic materials. The glassy state

is crucial for food processing, and for the preservation of insect life under extremes of cold or dehydration. Additionally, most engineering plastics are amorphous solids.

There have been various attempts to describe the transition from a liquid into a glass in terms of a conventional phase transition like the entropy theory by Adams, Gibbs and DiMarzio [GD58, AG65], “free” volume models like those introduced by Cohen and Turnbull [CT59] or by Kovacs [Kov63], or the mode-coupling theory by Götze and Sjögren [GS88, Göt99]. The approach by which these theories explain the slowing down of the supercooled liquid with decreasing temperature differs substantially from case to case. In the entropy theory, it is assumed that the slowing down can be understood essentially from the thermodynamics of the system, whereas mode-coupling theory puts forward the idea that at low temperatures, nonlinear feedback mechanisms in the microscopic dynamics of the particles become so strong that they lead to the structural arrest of the system. One of the appealing features of mode-coupling theory over other theories of the glass transition is the fact that it is the only first principles theory and offers a wealth of predictions, some of which are tested in this thesis.

It is now broadly recognized that the glass transition must be viewed from a kinetic and dynamical perspective. The key to understanding these dynamics lies in the broad relaxation spectra measured by various techniques, such as NMR [BDHR01], mechanical [CO94, YN87, Mar98] and dielectric spectroscopy [LL02]. Each technique couples to its own particular degree of freedom of the system, such as rotational-rotational correlations (dielectric spectroscopy) or density-density correlations (mechanical spectroscopy), and each has its specific assets and drawbacks. Different quantities exhibit similar dynamical features, but there are variations as well, including typical time scales, widths, and relative intensities of relaxation features. For a direct comparison of different techniques in the high frequency regime, see Figure 1-1. Dielectric results on glycerol have been taken as evidence against the applicability of the mode-coupling theory [SKH<sup>+</sup>93], but the results from neutron and light-scattering experiments were stated to qualitatively [WHL<sup>+</sup>94, BR05] and quantitatively [FGMS97] agree with the mode-coupling theory predictions.

Generally, dielectric properties are relatively easy to measure and, as Lunkenheimer and Loidl have demonstrated impressively for glycerol [LL02], can cover a spectral range of over 18 orders of magnitude, allowing observation of follow viscous slowdown from over  $10^{13}$  Hz to below  $10^{-5}$  Hz. Mechanical techniques, be they longitudinal, shear or bulk, measure liquid properties that are more fundamental with respect to liquid structural relaxation dynamics. They can be applied to any type of material including those with low (or no) dipole moments. The strongest argument for mechanical spectroscopy is the fact that the probed variables include the

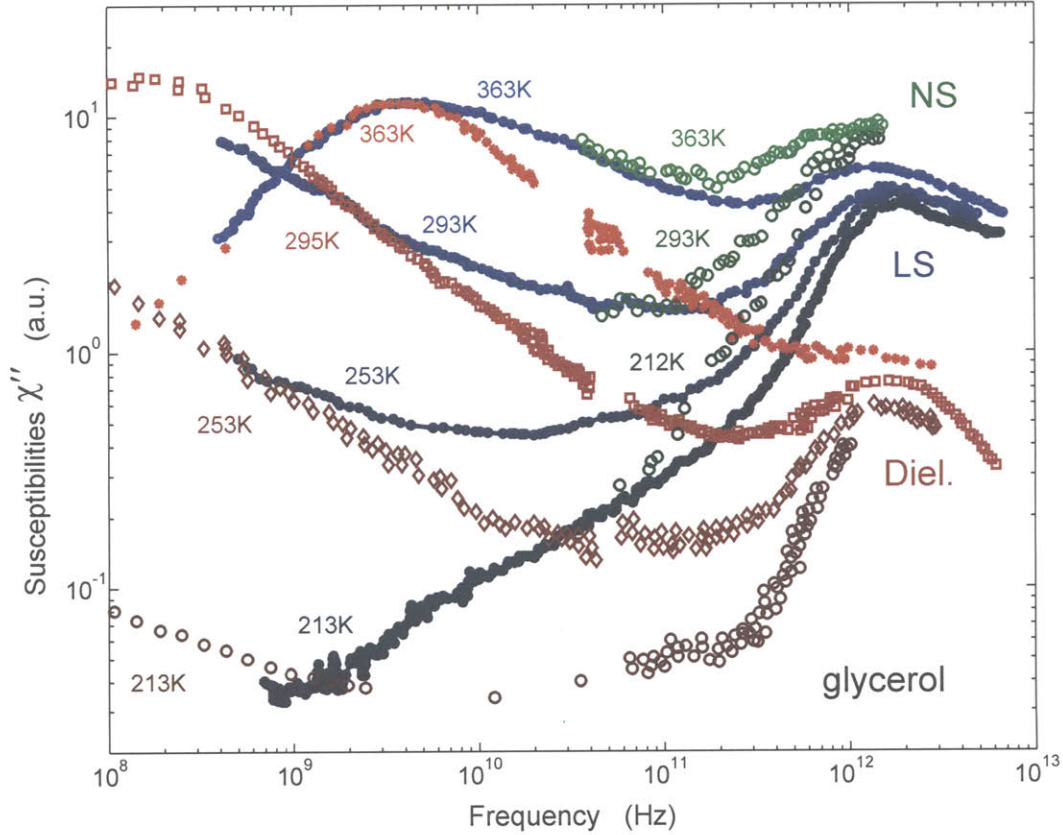


Figure 1-1: Comparison of susceptibilities [Lun99] from dynamic light scattering (LS) [WHL<sup>+</sup>94], neutron scattering (NS) [WHL<sup>+</sup>94] and dielectric susceptibilities (Diel.) [LPD<sup>+</sup>96] in the high frequency regime at different temperatures for glycerol. The susceptibility spectra were shifted vertically to adjust the intensities of the  $\alpha$ -peaks (to the low frequency side of the spectrum) of the different techniques for better comparison. Note the different positions of the minima and the different  $\alpha$ -peak/Boson-peak ( $\sim 1$  THz) intensity ratios. Analysis of dielectric spectroscopy results disagrees with mode-coupling theory predictions - contrary to NS and LS results which both, qualitatively and quantitatively, support its predictions. As described in the text, different techniques couple to different variables of glassy systems.

density, which is the variable treated in many of the models of glass forming liquids and in the mode-coupling theory, therefore permitting the most direct and reliable testing of its predictions. Figure 1-2 shows an overview of methods that probe mechanical properties (longitudinal, bulk and/or shear relaxation) in different frequency windows.

The work for this thesis adapts various picosecond ultrasonic approaches [Mar98, HW99, CFY<sup>+</sup>05, PRG<sup>+</sup>07] to extend the high frequency end of the mechanical spec-

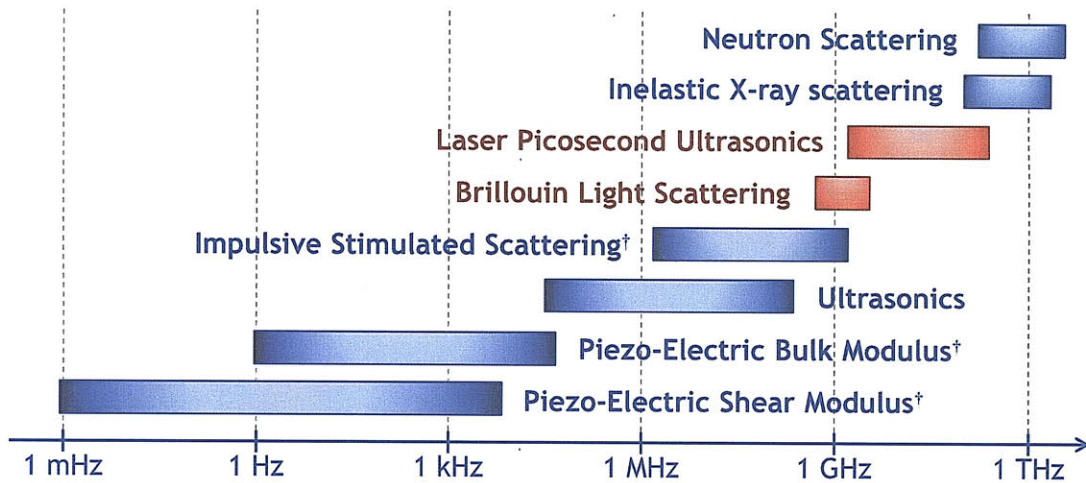


Figure 1-2: Survey of mechanical spectroscopic techniques. At low frequencies (from millihertz up to several kilohertz) the Piezo-Electric Shear Modulus Gauge (PSG) [CO95] and the Piezo-Electric Bulk Modulus Gauge (PBG) [CO94] can measure the shear and bulk moduli. At higher frequencies, ultrasonic approaches (US) [KBL01] provide both longitudinal and shear sound speeds and attenuation rates. In the megahertz frequency range, Impulsive Stimulated Scattering techniques [YN87] measure both longitudinal and shear sound velocities and damping, depending upon the experimental geometry. Brillouin light scattering (BLS) [CFSM03] (in both the frequency and time domains) and Laser Picosecond Ultrasonics (PU) [Mar98] grant access to most of the gigahertz frequency range. Finally, the highest frequencies are accessible through Inelastic X-ray scattering (IXS) [CFMR02] and Neutron Scattering (NS) [WHL<sup>+</sup>94]. The techniques developed and applied for the studies of this thesis are time domain BLS and PU with the goal of extending access of mechanical spectroscopy of liquids to the full gigahertz range.

trum — both longitudinal and shear — by over one order of magnitude to 200 GHz, and thereby represents the first direct acoustic measurements of liquids in this frequency range. In these measurements described in detail subsequently, laser illumination of a thin metal transducer film allows the generation of coherent longitudinal and shear acoustic wave packets that are transmitted into and through an adjacent liquid layer. The wave packets either propagate into an opaque metallic film, at the backside of which they are detected interferometrically, or into a transparent substrate in which they are detected through coherent time-domain Brillouin scattering. The

<sup>†</sup>The work of this thesis on the liquid DC704 was done in close collaboration with Darius Torchinsky (ISS) [Tor] and Tina Hecksher (PSG/PBG) [Hec] with the goal to compile a broad relaxation spectrum of this material over 13 decades in frequency.

density and shear relaxation dynamics of the liquid are revealed through the measured acoustic frequency-dependent damping and dispersion. This laser pump-probe technique has been applied in a number of different situations as described below.

In Chapter 2, we present an introduction to relaxation in glass-forming liquids, starting with basic phenomenology. While some useful thermodynamic approaches to understanding the liquid-glass transition are briefly sketched, and the potential energy landscape approach is introduced, this chapter focuses heavily on a dynamical approach and on the aforementioned first-principles-based mode-coupling theory. The mode coupling formalism is introduced, along with the theory's predictions most relevant to relaxation measurements. Some experimental tests and shortcomings of these predictions are also summarized.

Chapter 3 introduces the general concepts and the details of the experimental methods which have been developed and deployed to perform measurements of longitudinal and shear waves in supercooled liquids. We start by describing different laser-based generation mechanisms for longitudinal and shear acoustic waves at broadband and narrowband gigahertz frequencies. The "Deathstar" approach for generation of optical pulse sequences used for excitation of multiple-cycle acoustic waves, and a new and compact Deathstar apparatus are discussed. We proceed with the detection methods of time-domain Brillouin scattering and interferometry. The chapter concludes with notes on temperature-dependent measurements in two different cryostats.

A particular challenge was posed by the design and construction of a liquid sample cell that allowed incorporation of the above described generation and detection approaches of gigahertz acoustic waves to thin liquid layers. A wide range of liquid thicknesses proved to be necessary, starting from less than a nanometer up to several microns. This was achieved by squeezing the liquid between two specially prepared high quality optical substrates held by a custom-designed sample holder jig. Specifics of this design are described in Chapter 4 along with notes on sample preparation. A detailed study of the implications of sample heating and other effects caused by the excitation laser pump pulses is also presented.

The following two chapters, 5 and 6, apply the developed spectroscopic strategies to the study of two liquids, glycerol and tetramethyl tetraphenyl trisiloxane (DC704), the latter a silicone oil commonly used as a diffusion pump fluid. An analysis and interpretation of their results within the framework of mode-coupling theory is also presented. Glycerol is an associated liquid which forms a hydrogen-bonding network, making it intermediate between fragile and strong systems (see Chapter 2 for details about this classification). DC704 is likely to be entirely van-der-Waals bonded due to the presence of phenyl groups and classifies as a fragile liquid.



Chapter 5 discusses measurements of the density responses of both liquids from below their respective glass transition temperatures up to 400 K. First, optically generated longitudinal acoustic waves were monitored via time-domain Brillouin scattering while propagating through a very thick liquid layer. This allowed direct extraction of acoustic speeds and attenuation rates at a fix wave-vector. Subsequently, the experiment was repeated with multiple-cycle acoustic waves and, instead of monitoring the propagating pulse train in the liquid, its arrival at a receiver metal film was observed by an interferometric detection setup. This approach is analogous to conventional ultrasonic measurements and has permitted determination of the liquid response at specified frequencies from  $\sim 10$  GHz up to about 200 GHz. We describe the analysis we have performed, which compares the arrival times and amplitudes of strain pulses transmitted through different liquid thicknesses in order to extract the liquid response. The obtained information is pieced together with data from several other mechanical techniques to create a broadband relaxation spectrum, allowing characterization of the viscous slowdown over many orders of magnitude and enabling analysis in terms of mode-coupling theory. In particular, the predicted power-law behavior of the fast dynamics and its connection to the slow dynamics is tested.

Chapter 6 has a similar structure to the previous chapter, but concerns measurements of transverse, or shear, acoustic modes. We start by motivating the interest in shear wave propagation in liquid — a medium that at low frequencies supports only longitudinal sound waves. At higher frequencies, the dynamical properties of liquids move from the hydrodynamic regime (liquid-like or viscous behavior) to the elastic regime (solid-like or elastic behavior) and allow shear waves to propagate. Thereafter, we elaborate on the particular requirements that gigahertz shear wave generation poses to the properties of the photo-acoustic transducer materials, the sample and experimental geometry required to detect shear waves in various substrate materials, which allow access to a range of frequencies. After the theory of detection in an acoustic-optical cavity is developed, we present results on shear wave propagation in glycerol and DC704. The technique for shear wave generation and detection is not limited to the study of viscous liquids but can also be applied to liquids like water. Measurements in this direction are under way and will be presented.



## CHAPTER 2

---

# Phenomenology and Theory of the Liquid-Glass Transition

---

Glasses are disordered materials that lack the periodicity of crystals but behave mechanically like solids [DS01]. Natural glasses can form as a result of natural forces, for example, when lightning strikes a sandy region, when hot lava quickly cools, or as the result from meteors crashing into Earth. Some living organisms also exploit the glass transition (the transformation of a glass-forming liquid into a glass, e.g. through rapid cooling), for example, by forming a solid barrier between the delicate interior of the organisms and the extreme external environmental conditions [CCC98]. Glasses are among the oldest materials used by humans. They were known in prehistoric times, where volcanic glass was used to manufacture knives and arrow tips. The first glass containers were manufactured in Egypt around 1500 B.C., and glass blowing was probably discovered in Phoenicia in the first century B.C. Today, glasses are materials of utmost importance for technological applications and ubiquitous in our every day life, e.g. in architecture (windows) and packaging (containers and glass wool) or more recent applications, e.g. in medicine (bioactive implants and amorphous drugs) or in communication (optical fibers made of very pure amorphous silica) [Lun99] to just name a few. And it is now believed that most water in the Universe is glassy [JB94].

Despite its significance in many aspects of modern life, the glassy state of matter is poorly understood from a fundamental physical point of view [And95]. For example, even though the liquid-glass transition resembles a second-order phase transition in which a liquid is transformed continuously into an amorphous solid with no latent heat, the glass-liquid system exhibits no diverging correlation length, symmetry change, or obvious order parameter during the transition as is expected in a thermodynamic phase transition. The glass transition is therefore generally better understood as a dynamical phenomenon. The ongoing challenge is to find a theoretical frame-

work that is capable of providing a detailed description of the relaxation dynamics of liquids and their evolution with decreasing temperature towards and including the liquid-glass transition.

In the discussion below, we will outline a few useful thermodynamic and kinetic approaches to understanding the relaxation processes in glass forming liquids. We begin by introducing basic phenomenological aspects of the liquid-glass transition and its description using relaxation theories. In the second part, we introduce a useful approach that allows one to relate the complex phenomenology of supercooling and vitrification to molecular-scale events by focusing our attention on the liquid's energy landscape, which is a multidimensional surface that describes the potential energy of the liquid as a function of its molecular coordinates. Finally, we introduce the dynamical approach of first-principles-based mode-coupling theory, with special emphasis toward the analysis of mechanical relaxation measurements presented in this thesis.

## 2.1 Phenomenology of Supercooling and Glass Formation

Supercooling is the cooling of a liquid well below its melting temperature  $T_m$  without crystallization. See Figure 2-1 (a). The common feature of glass forming liquids is their ability to supercool. We may distinguish between at least two different supercooled regions. In the moderately supercooled region, the system behaves more or less like a liquid; it relaxes structurally, i.e. responds to stress by molecular reorientation and intermolecular rearrangements. However, on further cooling, the liquid becomes glassy and begins to behave like a solid; it can no longer flow, or relax, on accessible time scales, and the liquid's structure seems to be frozen in. Over a narrow temperature range, the liquid's characteristic molecular relaxation time changes dramatically, by many orders of magnitude. The glass transition temperature  $T_g$  is defined as the temperature at which the relaxation time of the liquid reaches an arbitrarily chosen value of 100 seconds [EAN96]. This dynamic transition usually occurs at around  $T_g \approx 2 T_m/3$  and is accompanied by a sudden jump in heat capacity (a calorimetric transition), as measured on an experimentally accessible time scale. See Figure 2-1 (b).

When the liquid is cooled at a slower rate, the time available for configurational sampling at each temperature becomes longer, and therefore, the liquid can become colder before it falls out of the liquid-state equilibrium. As a consequence, the glass transition temperature  $T_g$  increases with the cooling rate, the properties of the glass

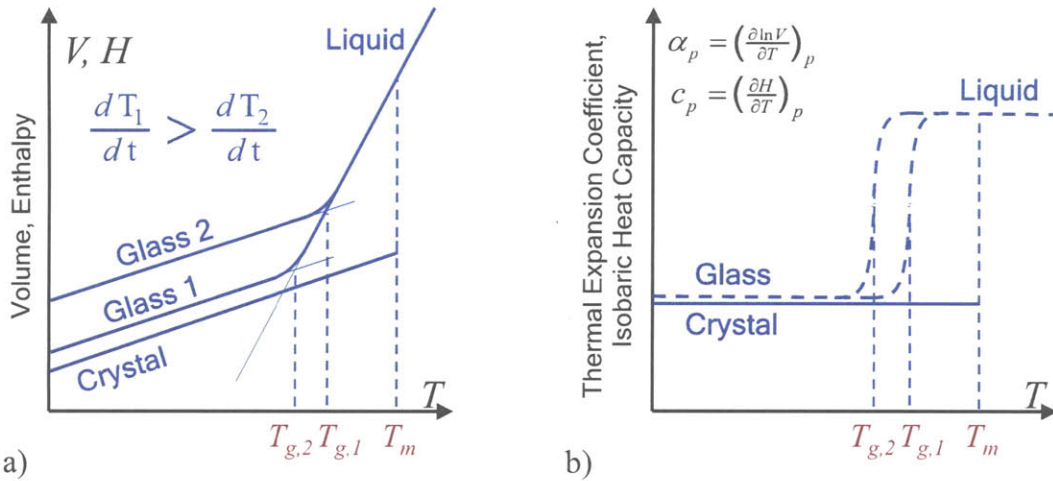


Figure 2-1: (a) Temperature dependence of the volume  $V$  and the enthalpy  $H$  of a liquid at constant pressure. When the liquid is cooled below its freezing point  $T_m$  quickly enough, crystallization can be avoided. When the liquid is cooled further, molecular motion slows down and eventually molecules cannot adequately sample configurations in the time allowed by the cooling rate. Depending on the cooling rate, the liquid falls out of quasi-equilibrium at different temperatures, e.g.  $T_{g,1}$  or  $T_{g,2}$ , and its structure appears ‘frozen’ on the laboratory timescale because. (b) At the respective temperatures, the rate of change of volume  $\alpha_p = (\partial \ln V / \partial T)_p$  and enthalpy  $C_p = (\partial \ln H / \partial T)_p$  with respect to temperature decreases abruptly (but *continuously*) to values comparable to those of the crystalline solid. The resulting material is a glass.

depend on the process by which it was formed. In reality, the dependence of  $T_g$  on the cooling rate is rather weak (a change in the cooling rate by an order of magnitude changes  $T_g$  by 3-5 K [Ang95]), so that the calorimetric glass transition temperature is a useful material characteristic.

Macroscopically, the most obvious indication of a glass transition is the dramatic change in shear viscosity by about 17 orders of magnitude up to  $10^{13}$  Poise, which constitutes the arbitrarily assigned value of viscosity at  $T_g$  [Ang95]. When the temperature of the liquid gets close to  $T_g$ , the viscosity  $\eta$  may become extremely sensitive to temperature. However, there are significant differences between various glass formers. For example, the temperature dependence of the shear viscosity for silica is described reasonably well by the Arrhenius law

$$\eta(T) = A \exp \frac{E_a}{k_B T}, \quad (2.1)$$

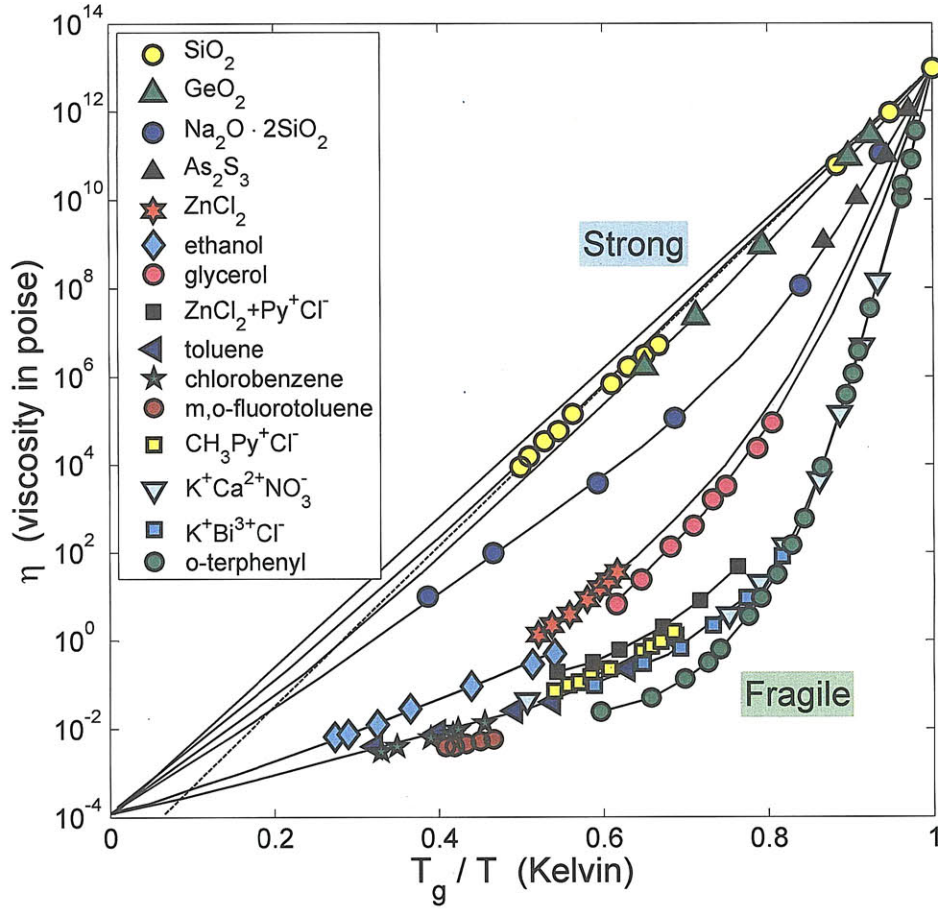


Figure 2-2: Scaled Arrhenius representation of the viscosity of various glass forming liquids showing Angell's strong-fragile pattern. The glass transition temperature  $T_g$  for each liquid is the temperature at which the liquid reach an arbitrarily defined viscosity of  $10^{13}$  Poise. Strong liquids (with a fragility index  $m$  defined by equation 2.3 of around 16) show approximately linear behavior (Arrhenius behavior) in the Angell plot, indicating a temperature-independent activation energy  $E = d \ln \eta / d(1/T) \approx \text{const}$ . Fragile liquids (with a fragility index up to over 100) show super-Arrhenius behavior which is characterized by an increase in the effective activation energy as the temperature decreases. For data sources see [Ang95] and [ANM<sup>+</sup>00].

where  $k_B$  is Boltzmann's constant,  $A$  a temperature independent parameter and  $E_a$  a characteristic activation energy. However, there are many liquids that exhibit a more pronounced viscous slow-down when approaching the glass transition, which can be well described, at least over a couple of orders of magnitude in viscosity, by the Vogel-Fulcher-Tammann (VFT) equation [Ful25]

$$\eta(T) = \eta_0 \exp \frac{D T_0}{(T - T_0)}, \quad (2.2)$$

where  $\eta_0$  and  $D$  are fitting parameters and  $T_0$  is a characteristic temperature. Note that for  $T_0 = 0$  K, the familiar Arrhenius equation results. Despite much effort, there is still little insight regarding the physical significance of the parameter  $T_0$ . Numerous other expressions have been posited to fit the temperature dependent viscosity, and equations with more parameters are better able at modeling a larger range of temperature dependent behavior. For an overview see section A.1.2 of reference [ANM<sup>+</sup>00].

A useful classification of liquids as ‘strong’, ‘intermediate’ and ‘fragile’ was proposed by Angell. Figure 2-2 shows an Arrhenius plot of various liquid viscosity data scaled by values of  $T_g$ , often referred to as an Angell plot [Ang95]. The so-called fragility index  $m$  is defined as the slope of the Arrhenius plot at  $T_g$

$$m = \left. \frac{\partial \log \eta}{\partial (T_g/T)} \right|_{T=T_g} \quad (2.3)$$

For ‘strong’ liquids (typically  $m \sim 20$ ) such as network oxides, like silica ( $\text{SiO}_2$ ), which exhibit tetrahedrally coordinated structures, both the viscosity and relaxation time show a nearly Arrhenius behavior, while the behavior of ‘fragile’ liquids (typically  $m \sim 80$ -90), like *o*-terphenyl (OTP), whose molecules exert mostly non-directional, dispersive forces on each other strongly deviates from the Arrhenius form. In this type of plot, curves for almost all materials fall between the curves of silica and OTP.

## 2.2 General Features of Liquid Relaxation

### 2.2.1 Correlation Functions and their Measurement

Macroscopic liquid properties, such as the static viscosity detailed above are governed by an average relaxation time during which molecular motion relax from some initial structure. However, a much more complex analysis is required to elucidate the detailed time dependent relaxation of the liquid. The general approach is to consider the evolution of an appropriate correlation function  $C_{GH}(\vec{r}', t'; \vec{r}, t) = \langle \delta G(\vec{r}, t) \delta H(\vec{r}', t') \rangle$ , where  $\delta G(\vec{r}, t)$  and  $\delta H(\vec{r}', t')$  represent local fluctuations away from the average value  $\delta G(\vec{r}, t) = G(\vec{r}, t) - \langle G(\vec{r}, t) \rangle$ . This can be for example the orientational-orientational correlation function

$$\phi(t) = \langle \delta\theta(0) \delta\theta(t) \rangle, \quad (2.4)$$

as probed by dielectric spectroscopy, where  $\delta\theta(t)$  is the angular displacement of a molecular glass-former’s dipole from its original orientation at time  $t = 0$ . The long time limit of the behavior of the correlation function determines macroscopic

transport properties. For example, the long time limit of the stress tensor correlation function determines the longitudinal viscosity.

Structural relaxation dynamics can also be described in the frequency domain by frequency dependent susceptibilities. These describe the response of a system to an external driving field  $g$  with amplitude  $g_0$  modulated at frequency  $\omega$  in terms of the induced change of the conjugate variable  $\delta\hat{G}$ . In the linear response regime, one can write

$$\delta\hat{G} = \hat{\chi}(\omega)g(\omega), \quad (2.5)$$

where  $\hat{\chi}(\omega) = \chi'(\omega) + i\chi''(\omega)$  represents the frequency dependent susceptibility of variable  $\hat{G}$ , which is independent of  $g_0$ . The real part  $\chi'(\omega)$  describes the reactive response while the imaginary part  $\chi''(\omega)$  describes dissipation phenomena. The two parts are connected through the Kramers-Kronig relation.

Regardless of whether a measurement of an observable  $G$  is carried out in the time-domain by determining the relaxation function  $\phi(t)$  or in the frequency-domain by measuring the dynamic susceptibility  $\hat{\chi}(\omega)$ , one obtains the same dynamical information of the system. Therefore, the investigation of the system response is largely determined by the experimental technique selected.

Since the transition from the liquid state to the glass is accompanied by an increase in viscosity of 17 orders of magnitude [EAN96], the characteristic relaxation time must show a similarly dramatic change. Therefore, it is desirable to utilize techniques that are capable of covering such a large frequency range. An excellent example is dielectric spectroscopy, shown in Figure 2-3 for glycerol [LL02], which permits an exceptional dynamic range of about 18 decades in frequency to be examined. Figure 2-3 (a) shows a schematic plot of broadband loss spectra at two different temperatures demonstrating the most common contributions for glass-forming materials which are described in detail in the following section. Note that dielectric spectroscopy is conducted through several measurement methods in order to cover such a wide frequency range [LL01].

## 2.2.2 The Susceptibility Spectrum

One might be initially led to assume that the disorder of the liquid state beyond any length scale greater than a given molecule's first two solvation shells would give rise to a featureless frequency-dependent susceptibility except for some signature of the short range order at very high frequencies [Tor08]. On the contrary, liquid relaxation spectra, such as the one depicted in Figure 2-3, show a rich variety of dynamical processes which each will be described below.



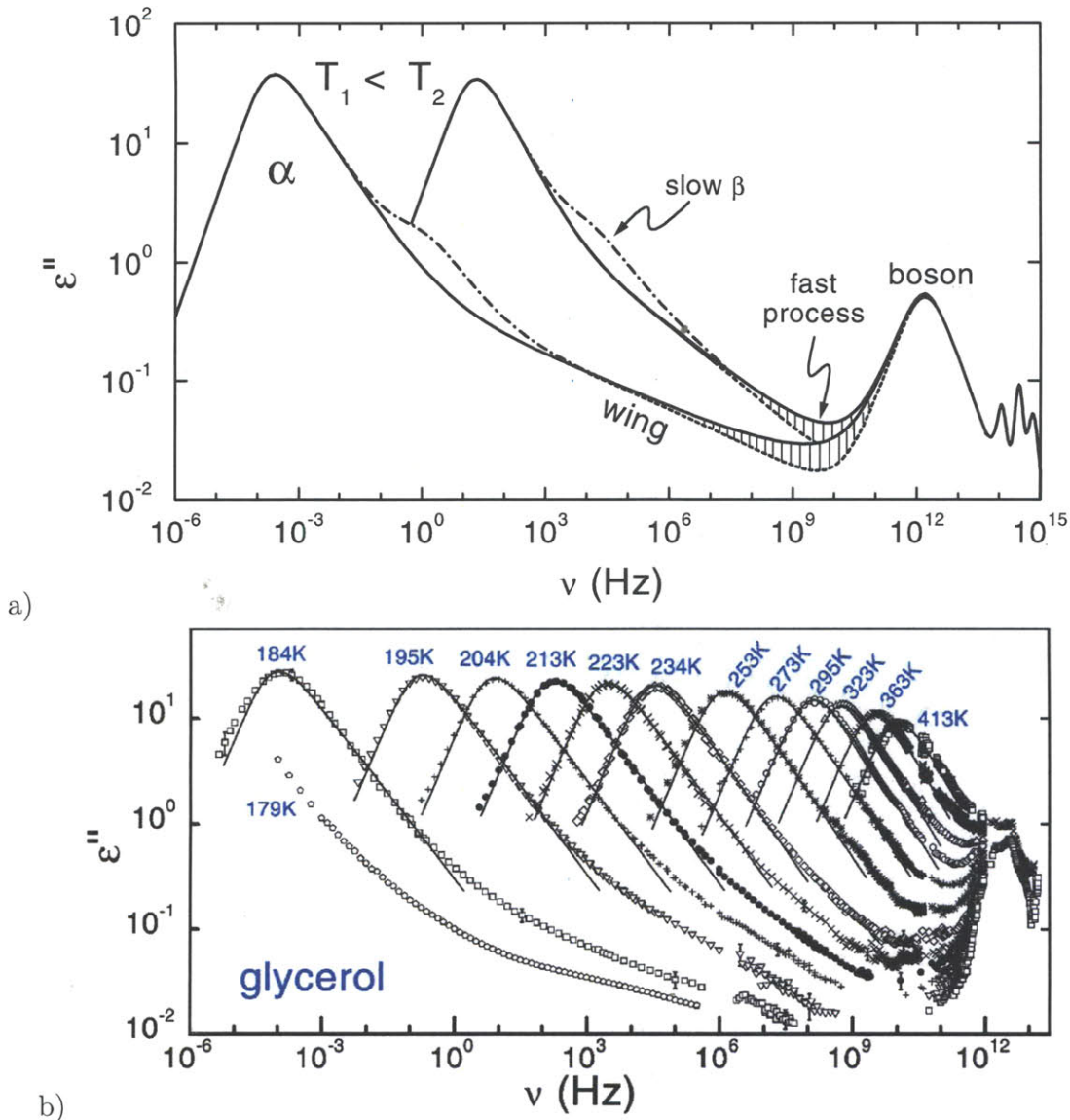


Figure 2-3: (a) Schematic representation of the frequency-dependent dielectric loss spectrum of a glass-forming material close to its glass transition temperature  $T_g$ . (b) Dielectric spectroscopy data for glycerol over a wide range of temperatures. The so-called  $\alpha$  process leads to a dominant loss peak at  $\nu_\alpha \approx 1/(2\pi/\langle\tau_\alpha\rangle)$ , where  $\langle\tau_\alpha\rangle$  is the average  $\alpha$  relaxation time. The  $\alpha$  relaxation is normally ascribed to collective structural rearrangement of the liquid and is strongly temperature dependent. Most glass formers have an asymmetrically-shaped  $\alpha$  peak that is much broader than expected from Debye relaxation theory. The  $\beta_{\text{fast}}$  relaxation occurs at frequencies in the gigahertz range, and shows little variation as the liquid temperature is changed. Adapted from Lunkenheimer *et al.*, [LL02].

### 2.2.2.1 Alpha Peak or Process

The  $\alpha$  relaxation process, which is attributed to the intermolecular structural rearrangements of the liquid molecules, is the most studied dynamical process in glass-forming liquids. It is manifested as a broad peak in the liquid's susceptibility spectrum as indicated in Figure 2-3 (a) and is characterized by a strong temperature dependence. Furthermore, the  $\alpha$  relaxation process is well known for its non-Debye behavior (the loss peak is usually much broader and more asymmetric than expected from Debye theory) and non-Arrhenius temperature dependence of the characteristic relaxation time  $\tau_c(T)$ . In particular, it can be described as the collective rearrangement of transient cages and is therefore a structural relaxation process. In fact,  $\alpha$  relaxation processes are posited to either originate i) from intrinsic non-exponential relaxation dynamics, ii) from a heterogeneous distribution of relaxation times, caused by variations of the local environment of the relaxing entities or iii) from a combination of both — a distribution of non-exponential relaxation times. The structural rearrangement dynamics of the  $\alpha$  process leads to a dominant loss peak in the susceptibility spectra at  $\nu_\alpha \approx 1/(2\pi \langle \tau_\alpha \rangle)$ , with  $\langle \tau_\alpha \rangle$  being the average  $\alpha$  relaxation time.

Due to the lack of a fitting form for the relaxation spectrum based on first principles, many researchers extend the approach of Debye by applying phenomenological functions such as the Cole-Davidson or the Fourier transform of the Kohlrausch-Williams-Watts relaxation function which are described in detail later in this section. At high frequencies, these empirical functions extrapolate to a power law,  $\chi''(\nu) \sim \nu^{-\beta}$ . However, they only provide adequate fits of the experimental data up to a few decades above the peak frequency, at best.

### 2.2.2.2 Excess Wing and Johari-Goldstein ( $\beta_{\text{slow}}$ ) Process

Many glass formers show an excess contribution to the high-frequency flank of the  $\alpha$  peak some decades in frequency above  $\nu_\alpha$  [Rös90, LPS<sup>+</sup>96]. This excess wing (also called the “tail” or “high frequency wing”), can be described reasonably well by a second power law,  $\chi''(\nu) \sim \nu^{-b}$  with  $b < \beta$  [LL01]. This feature was already described in the early work of Davidson and Cole [DC50], and appears to be a universal feature of glass forming liquids [LN97]. However, no consensus regarding the microscopic origin of this phenomenon has been reached.

In addition, many glass-forming materials exhibit a  $\beta_{\text{slow}}$  relaxation feature as indicated by the dash-dotted lines in Figure 2-3 (b). Originally, the  $\beta$  relaxation was linked to a change of the internal molecular conformations, e.g. the rearrangement of a molecular side-group. Johari and Goldstein showed that these additional relaxation processes might be inherent to glass-forming liquids in general [JG70]. The micro-



scopic processes underlying these  $\beta_{\text{slow}}$  relaxation processes are, again, controversial (since its universality means that it cannot depend on a specific molecular structure) and, until recently, it was assumed that the excess wing and the  $\beta_{\text{slow}}$  relaxations originate from different processes. However, experimental evidence that has emerged suggests that the excess wing is merely the high-frequency flank of the  $\beta_{\text{slow}}$  peak which is often hidden under the dominating  $\alpha$  peak [LSBL00].

### 2.2.2.3 Susceptibility Minimum and the Beta ( $\beta_{\text{fast}}$ ) Process

A minimum in the  $\chi''(\nu)$  spectrum [LL02] is clearly observed in various scattering experiments between the slow, strongly temperature dependent processes described above and the high frequency, temperature independent boson peak described below. A large number of experiments indicate the presence of fast processes in this range, since the spectrum around the minimum cannot be explained by a simple superposition of the  $\alpha$  peak (including excess wing) and the boson peak. The interest in this range is mostly due to the additional relaxation contributions in this region, now commonly termed the  $\beta_{\text{fast}}$  or simply beta processes, predicted by the mode-coupling theory. This fast relaxation process is attributed to sampling of multiple local potential minima that exist within a given intermolecular “cage” without molecular diffusion or changes in nearest neighbor molecules.

### 2.2.2.4 Boson Peak and Infrared Region

Another peak is apparent in the dynamic response of glass-forming liquids, in the terahertz region. This so-called boson peak is a universal feature of glass-forming materials and corresponds to an excess contribution (increase in the density of states over the Debye predictions) commonly found in specific heat measurements at low temperatures [AHcMV72, Kli06]. Many explanations for the boson peak have been proposed, for example, in terms of phonon localization models [TE97], or in terms of the soft potential model [RFM<sup>+</sup>05, VCF05]. The term “boson peak” is only used to denote a high-frequency peak that is caused by oscillatory excitations. In contrast, if the peak is assumed to originate from the cage effect, i.e. the fast movement of individual particles in the cages formed by their nearest neighbors, the term “microscopic peak” is used. Interestingly, there are indications for the superposition of two peaks in the terahertz regime in some materials [RNS97]. Mode-coupling theory also considers a contribution leading to a peak in the terahertz regime [FGMS97] which will be described below.

Finally, in the infrared region, various resonant absorption features can be expected which are due to vibrational, librational (hindered rotations), and phonon-like modes of the materials.

### 2.2.3 Models for Liquid Relaxation

A variety of empirical formulas have been used to qualitatively describe the features in the susceptibility spectra described above. The simplest of these functions, which was proposed by Debye, assume an exponential relaxation behavior having a single relaxation time  $\tau_D$  for all molecules given by

$$\hat{\chi}(\omega) = \chi_\infty + \frac{\chi_0 - \chi_\infty}{1 + i\omega\tau}, \quad (2.6)$$

where  $\omega$  is the angular frequency, and  $\chi_0$  and  $\chi_\infty$  are the low- and high-frequency limits of the susceptibility. The real and imaginary part of  $\hat{\chi}(\omega)$  are given by

$$\chi'(\omega) = \chi_\infty + \frac{\chi_0 - \chi_\infty}{1 + \omega^2\tau^2} \quad \text{and} \quad \chi''(\omega) = \frac{(\chi_0 - \chi_\infty)\omega\tau}{1 + \omega^2\tau^2}. \quad (2.7)$$

Usually, the Debye model is not sufficient to account for the experimentally measured susceptibility curves which are generally much broader and more asymmetric than those described by equation 2.7. Various modifications of the Debye model have been proposed to account for the observed deviations. Two of these are the Cole-Cole (CC) equation [CC41]

$$\hat{\chi}(\omega) = \chi_\infty + \frac{\chi_0 - \chi_\infty}{1 + (i\omega\tau)^{\alpha_{CC}}}, \quad (2.8)$$

and the Cole-Davidson (CD) equation [DC50]

$$\hat{\chi}(\omega) = \chi_\infty + \frac{\chi_0 - \chi_\infty}{(1 + i\omega\tau)^{\beta_{CD}}}, \quad (2.9)$$

both of which are combined in the Havriliak-Negami (HN) equation [HN67]

$$\hat{\chi}(\omega) = \chi_\infty + \frac{\chi_0 - \chi_\infty}{[1 + (i\omega\tau)^{\alpha_{HN}}]^{\beta_{HN}}}. \quad (2.10)$$

The exponents  $\alpha$  and  $\beta$  range between 0 and 1. While the exponent  $\alpha$  serves as a variance parameter by broadening the Debye distribution, the exponent  $\beta$  acts as a skew parameter. Examples for the shape of Debye and Havriliak-Negami relaxation functions are shown in Figure 2-4 (a).

Consider the dissipative (imaginary) part of the susceptibility,  $\chi''$ , e.g. the dielectric susceptibility of glycerol as depicted in Figure 2-3. For frequencies above

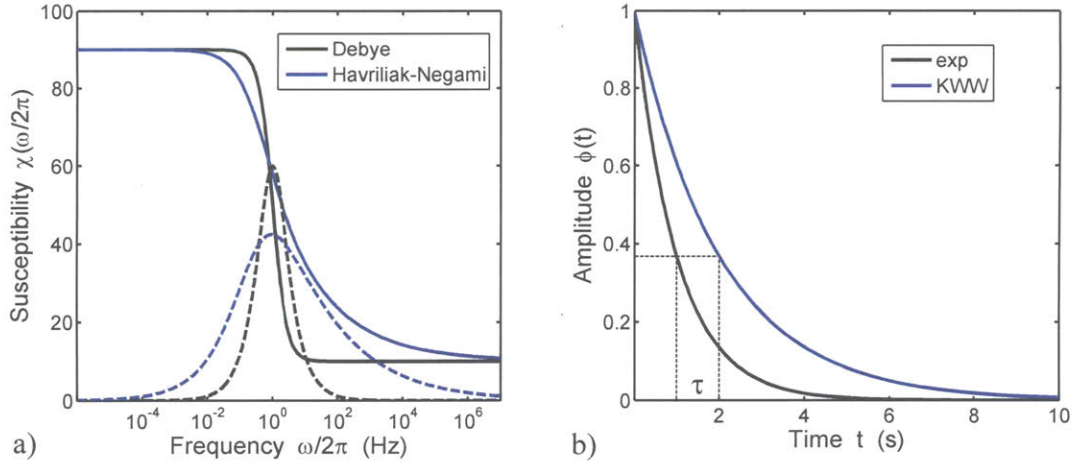


Figure 2-4: (a) Examples of phenomenological susceptibility fitting functions. Real part  $\chi'$  (full lines) and imaginary part  $\chi''$  (dashed lines) of Debye and Havriliak-Negami ( $\alpha_{HN} = 0.5$  and  $\beta_{HN} = 0.5$ ) forms. Low and high frequency limiting values are arbitrarily chosen as  $\chi_0 = 90$  and  $\chi_\infty = 10$ . Note the stretched and asymmetric shape of the Havriliak-Negami form. (b) Comparison of exponential and stretched-exponential (KWW with  $\beta_{KWW} = 0.5$ ) functions with different effective relaxation times  $\tau$ .

and below the  $\alpha$  peak,  $\nu \ll \nu_\alpha$  and  $\nu \gg \nu_\alpha$ , all curves exhibit power law behavior in the double-logarithmic representation. Let  $m$  and  $n$  be the power law exponents below and above  $\nu_\alpha$ , respectively. Then the Debye model has  $m = 1$  and  $n = -1$ . The Cole-Cole equation leads to a symmetric peak with  $m = \alpha_{CC}$  and  $n = -\alpha_{CC}$  while the Cole-Davidson response is characterized by  $m = -\beta_{CD}$  and  $n = 1$ . For the Havriliak-Negami equation,  $m = \alpha_{HN}$  and  $n = -\beta_{HN}\alpha_{HN}$ .

The broadening of the loss peak which is found in most materials in comparison with the Debye response is often ascribed to a distribution of relaxation times which may arise due to heterogeneity of the material under investigation, i.e. variations in the local environment of the relaxing entities. An alternative scenario is that of a homogeneous non-exponential response of the relaxing entities in the time domain. Independent of the underlying physical origin of the observed non-exponentiality, good fits can typically be obtained by the so-called stretched exponential or Kohlrausch-Williams-Watts (KWW) relaxation function [Koh54, WW70]

$$\phi(t) = \phi_0 \exp \left[ - (t/\tau_{KWW})^{\beta_{KWW}} \right], \quad (2.11)$$

where  $\phi$  is an amplitude function, e.g. the decay of the orientational-orientational correlation function of equation 2.4. The parameter  $0 < \beta_{KWW} \leq 1$  is used to account

for the stretching in time as manifested in the relaxation when contrasted with a pure exponential decay. Examples of both functions are shown in Figure 2-4 (b).

## 2.3 The Landscape Paradigm

A convenient and qualitative (and recently, increasingly quantitative) way of interpreting the complex phenomenology described above is provided by the potential energy surface representation of a liquid [Sti95]. This multidimensional viewpoint offers an intuitive picture for the non-Arrhenius viscosity and relaxation times, the bifurcation between the  $\alpha$  and  $\beta_{\text{slow}}$  relaxation processes, and the breakdown of the Stokes-Einstein relation for self-diffusion.

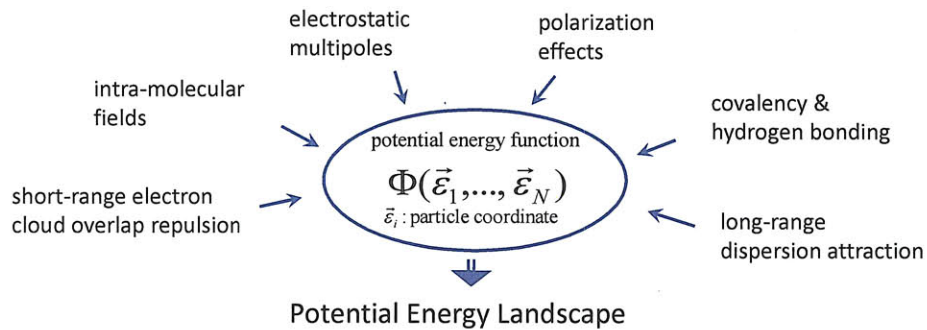


Figure 2-5: The potential energy function  $\Phi$  of a condensed phase system determines the shape of the multidimensional energy landscape.

### 2.3.1 Potential Energy Function

Condensed matter (whether crystalline, amorphous or liquid) is characterized by the interactions between the constituent particles: atoms, ions or molecules. These interactions can be expressed by the potential energy function of a given  $N$ -body system  $\Phi(\vec{\epsilon}_1, \dots, \vec{\epsilon}_N)$ , where the vectors  $\vec{\epsilon}_i$  comprise the positions, orientational and vibrational coordinates. In particular, this potential energy includes contributions from polarization effects and electrostatic multipoles, hydrogen and covalent bonding, short-range electron-cloud-overlap repulsion and longer range dispersion attractions, and intermolecular forces (Figure 2-5).

A useful approach for understanding supercooling and glass formation is to adopt a topographic view of the potential energy function  $\Phi$  which shows the ‘elevation’ of



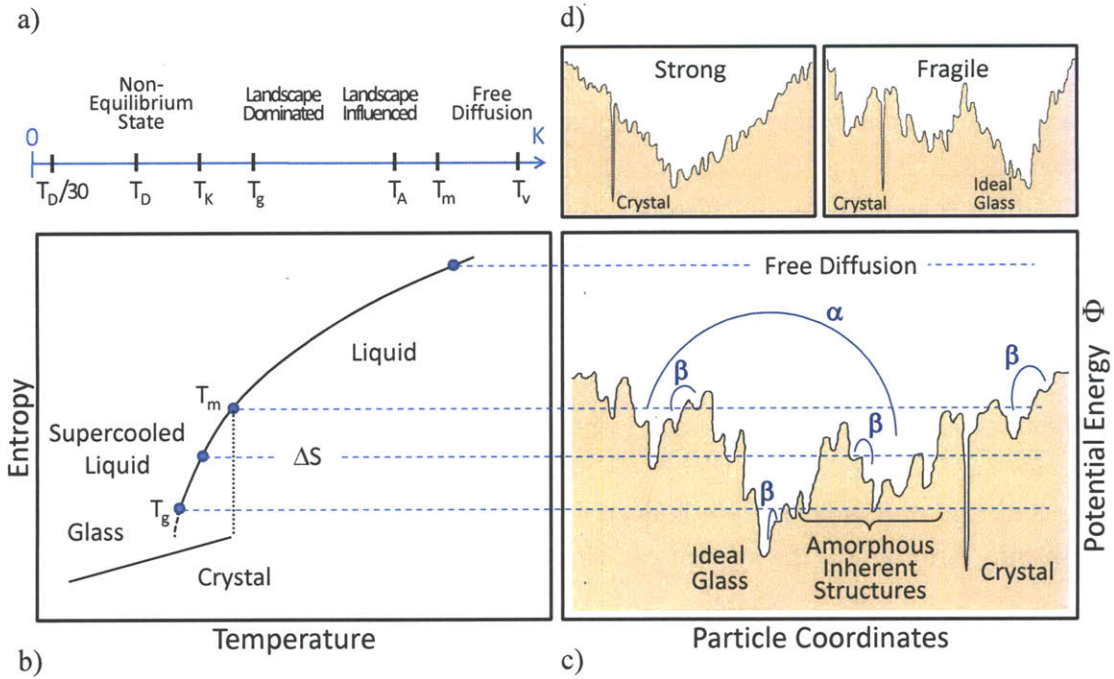


Figure 2-6: (a) Schematic representation of regimes of condensed phase ranging from the liquid state to frozen glass.  $T_v$  is the vaporization temperature,  $T_m$  the melting point.  $T_A$  represents the crossover temperature to activated motion, which is usually below  $T_m$ .  $T_g$  is the glass transition and  $T_K$  is the Kauzmann temperature.  $T_D$  is the Debye temperature which signals the quantization of vibrational motions. Below about  $T_D/30$ , the thermal properties of the system can be phenomenologically described as arising from a collection of two level systems. Just above this point, additional quantum excitations (Boson peak) are present. (b) Temperature dependent entropy of a liquid and (c) its corresponding possibility to sample its potential energy landscape (multidimensional configuration space for a many-particle system). At high temperatures, the system ‘sees’ no energy wells or barriers and can freely diffuse. When cooled quickly below  $T_m$ , the system may be able to avoid being trapped in the deep crystalline potential energy well and can thus continue to sample the landscape until it ‘freezes’ into its ideal glass state at  $T_g$ . (d) Energy landscape of strong and fragile substances. Strong landscapes consist of a single megabasin, while fragile landscapes show a proliferation of well-separated megabasins.

$\Phi$  at any ‘location’  $\vec{R} \equiv (\vec{\epsilon}_1, \dots, \vec{\epsilon}_N)$  in the configuration space of the  $N$  particle system.  $\vec{R}(t)$  at a given time is called a configuration point. A schematic illustration of this multidimensional topographic map is shown in Figure 2-6 (c). The topographical points of interest on the  $\Phi$ -surface are the maxima (mountain tops), minima (valley bottoms), and saddle points (mountain passes). The minima correspond to mechanically stable arrangements with minimal torque and force on every particle and in

which every displacement from such a configuration results in restoring forces. The way in which a material system samples its energy landscape as a function of temperature provides information on its dynamics. For example, the mechanical properties of a system are determined by the way a landscape deforms as a result of a change in density.

At high temperature, the system has sufficient energy to sample its entire energy landscape. It does not see any wells at all or relaxes by mechanisms which avoid them. When the temperature is decreased, the system is unable to surmount the highest energy barriers, and is therefore forced to sample the deeper minima. The kinetics of structural relaxation change from exponential to stretched exponential. When this happens, the activation energy (and entropy) connected with structural relaxation become super-Arrhenius. In the glassy state, the system resides in a local minimum (a basin) and can only execute collective vibrational motions and relaxation within the basin. Around  $T_g$ , the system can slowly sample nearby low energy minima.

### 2.3.2 Decoupling and Bifurcation between $\alpha$ and $\beta_{\text{slow}}$ relaxation

When a glass-forming liquid is cooled, a decoupling of the relaxation times is observed by several spectroscopic techniques in the moderately supercooled range, as illustrated in Figure 2-7 for ortho-terphenyl (OTP). In the equilibrium liquid regime (high temperatures), the liquid shows a single relaxation peak in frequency. When cooled to the moderately supercooled regime, however, the peak splits into a slow  $\alpha$  (primary) and a faster  $\beta_{\text{slow}}$  (secondary) relaxation. Another secondary process is marked as the  $\beta_{\text{fast}}$  process. The  $\alpha$  process is strongly non-Arrhenius and kinetically frozen out at  $T_g$ , while the  $\beta_{\text{slow}}$  relaxation process is more nearly Arrhenius and remains operative at  $T_g$ . In these experiments, the  $\alpha$  process roughly corresponds to molecular reorientation (no free rotations in the condensed phase) while the  $\beta_{\text{slow}}$  process is believed to be due to partial reorientation of the ortho-groups. The  $\beta_{\text{fast}}$  process is thought to arise from complex collective anharmonic cage rattling process.

The bifurcation can be readily interpreted in terms of the  $\Phi$ -topography picture. As the system is cooled, the configuration point  $\vec{R}(t)$  is forced into increasingly rugged and heterogeneous regions of the landscape in order to seek out the deeper basins which get increasingly rare and more widely separated. The  $\beta_{\text{slow}}$  processes are identified with elementary transition processes between contiguous basins that require only local rearrangements of small numbers of particles, while the  $\alpha$  relaxation is thought to correspond to configurational sampling of neighboring megabasins. Because the latter needs a large number of directed elementary transitions, it involves

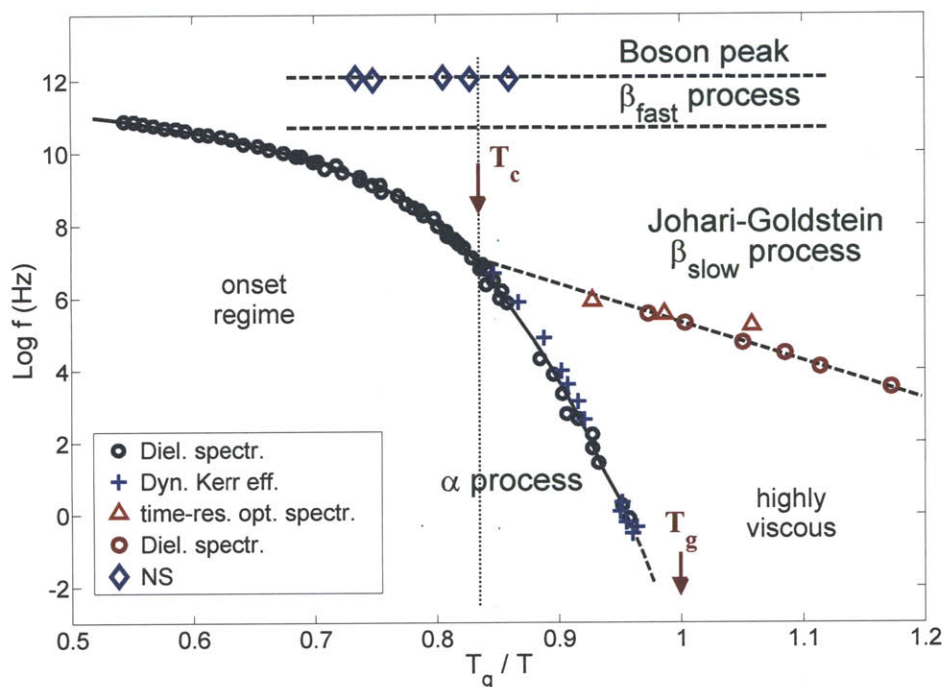


Figure 2-7: Temperature dependence of peak relaxation frequencies for the glass forming liquid OTP (*o*-terphenyl) as recorded by different spectroscopic techniques. At high temperatures, liquids show a single relaxation peak frequency which splits into slower ( $\alpha$ ) and faster ( $\beta_{\text{slow}}$ ) relaxations at a critical temperature  $T_c$ . While the  $\alpha$  relaxation exhibits non-Arrhenius behavior and disappears at  $T_g$ , the  $\beta_{\text{slow}}$  process continues below  $T_g$  and displays Arrhenius behavior. Data sources are given in references [Rös90] and [EAN96].

a much larger net change in elevation (activation energy) than the former. Examples of  $\alpha$  and  $\beta_{\text{slow}}$  relaxation processes are depicted in the schematic representation of the potential energy landscape in a liquid in Figure 2-6 (c).

### 2.3.3 Strong and fragile glass-formers

The variation in behavior of different glass-forming liquids can also be traced back to differences in topography in their respective energy landscapes. As described above and depicted in Figure 2-2, the deviation of the shear viscosity  $\eta$  from Arrhenius behavior ( $\eta = \eta_0 \exp(E/k_B T)$ ) forms the basis of the classification of liquids as either strong or fragile. Silica ( $\text{SiO}_2$ ) is considered the prototypical strong glass-former and has an almost constant activation energy of  $750 \text{ kJ mol}^{-1}$  [Ang95]. This suggests that the underlying mechanism (probably the breaking and reformation of Si-O bonds) is operative across the entire landscape. As sketched in Figure 2-6 (d), strong glass formers exhibit a uniformly rough topography in which only the  $\beta_{\text{slow}}$  transitions are

relevant. Little or no coherent organization of individual basins into the large and deep craters associated with the low-temperature  $\alpha$  transitions are present in strong glass formers, leading to very little or no  $\alpha/\beta_{\text{slow}}$  bifurcation in these materials.

In contrast, fragile glass formers exhibit significant landscape cratering and distinctive  $\alpha/\beta_{\text{slow}}$  bifurcation, as shown in Figure 2-7 for OTP. The viscosity of fragile glass formers deviates strongly from Arrhenius behavior (see Figure 2-2). In addition, the activation energy increases 20-fold between a temperature above the melting point and  $T_g$  [GT67]. Both properties indicate a very heterogeneous landscape. While sampling of different basins at high temperature only involves the rearrangement of small numbers of molecules (relaxation by surmounting low barriers), the very large activation energy around  $T_g$  corresponds to cooperative rearrangements of many molecules.

### 2.3.4 Breakdown of Stokes-Einstein relation for self-diffusion

Another decoupling occurs between i) translational and rotational diffusion, ii) and the translational diffusion and viscosity [Edi00] as a glass-forming liquid is cooled below approximately  $1.2 T_g$ . At higher temperatures, both translational and rotational diffusion coefficients are inversely proportional to the viscosity, in agreement with Stokes-Einstein and Debye equations. This inverse relationship between translational motion and viscosity breaks down below  $\sim 1.2 T_g$ , while that between rotational motion and viscosity does not [Sti95]. Near  $T_g$ , molecules have been found to translate faster (by as much as two orders of magnitude) than expected based on viscosity.

This behavior is most pronounced for fragile glass formers and may be explained by the cratering characteristics of their potential energy surface  $\Phi$  (Figure 2-6 (d)). When the temperature is lowered, the system gets trapped in one deep crater and, as emphasized above, a long sequence of elementary interbasin transitions is necessary to escape it. In real space, this sequence would look like a structural excitation in a local environment moving around in a microscopic domain that contains many particles, temporarily causing this domain to be more fluid compared with its surroundings. Since these domains have long lifetimes, and are large on a molecular scale near  $T_g$ , translational diffusion is enhanced compared with rotational diffusion.

### 2.3.5 Conclusion

A quantification of the potential energy landscape approach to the relaxation mechanisms and the thermodynamics of supercooled liquids is necessary and is being rapidly developed [SD04, MBN<sup>+</sup>05, Mat07, MABM10]. Although this approach is rather complex, it may be ultimately the most precise way to describe the many-body systems under consideration. The success of such schemes depends on the ability to formulate



real space models at a simpler level while approximately incorporating all essential features of the collective behavior.

## 2.4 Mode-Coupling Theory of the glass transition

### 2.4.1 Introduction

Various phenomenological models have been used to describe the relaxation dynamics of glass-forming liquids [ANM<sup>+</sup>00, Dyr06]. In most cases, these approaches begin with a rather simple physical idea (such as configurational entropy, free volume or short-time elastic constants) and experimental data are fit using equations derived from such a physical model such that the proposed physical picture can be investigated more quantitatively. Even though this approach is undoubtedly useful to rationalize and describe experimental results, often it is only qualitative and has only a rather limited capacity to make predictions. Unfortunately, a theory of the glass transition that makes nontrivial predictions of the evolution of relaxation across all temperature and frequency regimes, and also allows a quantitative comparison with experimental data, has yet to be formulated. However, there exists one theoretical approach, the so-called mode-coupling theory of supercooled liquids that not only permits quantitative calculations for the dynamics of supercooled liquids but has also made many predictions about these dynamics [Göt99].

Mode-coupling theory provides an intuitively appealing physical picture involving caging effects and retardation. This results in the trapping of particles inside cages formed by their neighbors as the temperature is lowered and makes the liquid-glass transition a purely dynamical effect, unrelated to any thermodynamical phase transition. Particles rattle around in their cages before they can diffuse (i.e. move away), and in order for a single particle to move, other particles around it must rearrange, requiring the motions of other particles, and so on. This leads to a feedback mechanism and nonlinear effects. When particles in the liquid collide, they transfer energy and momentum which, through subsequent collisions, are redistributed to surrounding particles. This results in the buildup of collective motion which returns to the original particle at a later time. The decay of the local disturbance in density is slow compared with the rate of binary collisions, making it difficult for a particle to actually move away and temporarily trapping the particle in a cage. Mathematically, these effects are expressed by a nonlinear coupling between density fluctuations and the velocity autocorrelation function of the particles.

The following section briefly outlines the derivation of the theory as originally developed by Bengtzelius, Götze and Sjölander [BGS84] and Leutheusser [Leu84].

An overview of recent developments and extensions is also given before a concluding summary regarding the predictions of the mode coupling theory is presented. The emphasis of the following discussion is on the aspects of the theory most relevant to the experiments presented in this thesis. The following discussion closely follows the tutorial paper of W. Kob in reference [FKMN97].

## 2.4.2 Mode-Coupling Equations

In the sixties and seventies, theoretical efforts were undertaken to quantitatively describe the dynamics of dense simple liquids [Kaw66]. Equations of motion for the density correlation function were derived by using mode-coupling approximations, which were shown to provide good descriptions of the dynamics of simple liquids at the triple point. In particular, they were shown to quantitatively correctly describe the cage effect. The cage effect is the trapping of a tagged particle of a dense liquid by its neighbors before it can escape the cage. Bengtzelius, Götze and Sjölander later simplified these equations by neglecting certain terms which they argued were irrelevant at low temperature [BGS84]. They then showed that if the temperature falls below a critical value  $T_c$ , the time dependence of the solution of the modified equations changes in a discontinuous fashion. This singularity was identified as the glass transition since this discontinuity was accompanied by a diverging relaxation time.

The density autocorrelation function  $F_{\mathbf{q}}(t)$  for wave vector  $\mathbf{q}$  is usually used to describe the dynamics of a liquid. For an assembly of  $N$  particles located at  $\mathbf{r}_1(t), \dots, \mathbf{r}_N(t)$  the intermediate scattering function  $F_{\mathbf{q}}(t)$  is defined as

$$F_{\mathbf{q}}(t) = \langle \delta\rho_{\mathbf{q}}(t)\delta\rho_{-\mathbf{q}}(0) \rangle \quad \text{with} \quad r_{\mathbf{q}}(t) = \sum_{j=1}^N \exp(i\mathbf{q} \cdot \mathbf{r}_j(t)). \quad (2.12)$$

Considering an *isotropic* system so that  $F_{\mathbf{q}}(t)$  only depends on the modulus of  $\mathbf{q}$ , the equations of motion can then be written as

$$\ddot{F}_{\mathbf{q}}(t) + \Omega_q^2 F_{\mathbf{q}}(t) + \int_0^t [M_q^0(t-t') + \Omega_q^2 m_q(t-t')] \dot{F}_{\mathbf{q}}(t') dt' = 0, \quad (2.13)$$

where the squared frequency  $\Omega_q^2$  follows directly from the short time expansion of the equations of motion for the particle and is given by

$$\Omega_q^2 \equiv \frac{q^2 k_B T}{m S_q}, \quad (2.14)$$

where  $S_q \equiv F_q(0) = \langle |\delta\rho_q(0)|^2 \rangle$  is the static structure factor,  $m$  is the mass of the particles and  $k_B$  is Boltzmann's constant. The only relevant contributions to the integral at temperatures close to the triple point come from the kernel  $M_q^0(t)$ , which describes the dynamics at short (i.e. microscopic) times, whereas in the supercooled regime, the memory kernel  $m_q(t)$  becomes important.

The equations of motion derived above are exact since the kernels  $M_q^0(t)$  and  $m_q(t)$  have not yet been specified. It can be assumed that  $M_q^0(t)$  is sharply peaked at  $t = 0$  and it is therefore often modeled by a  $\delta$ -function, i.e.  $M_q^0(t) = \frac{\Omega_q}{2\pi} \delta(t)$ . The long time behavior of the correlation function is ruled by the memory kernel  $m_q(t)$ . Within the approximations of the idealized mode-coupling theory, this kernel is a quadratic form of the correlation function  $F_q(t)$ ,

$$m_q(t) = \frac{1}{2(2\pi)^2} \int d\mathbf{k} V^{(2)}(q, k, |\mathbf{q}-\mathbf{k}|) F(k, t) F(|\mathbf{q}-\mathbf{k}|, t). \quad (2.15)$$

The vertex  $V^{(2)}$  can be computed from static quantities and is given by

$$V^{(2)}(q, k, |\mathbf{q}-\mathbf{k}|) = \frac{n}{q^2} S_q S_k S_{|\mathbf{q}-\mathbf{k}|} \left( \frac{\mathbf{q}}{q} [\mathbf{k} c(k) + (\mathbf{q} - \mathbf{k}) c(|\mathbf{q}-\mathbf{k}|)] \right)^2, \quad (2.16)$$

where  $n$  is the particle density, and  $c(k) = n(1 - 1/S_q)$  is the direct correlation function. The mode-coupling equations 2.12-2.16 form a closed set of coupled equations for  $F_q(t)$ . These equations can be considered the starting point for the mode-coupling theory of supercooled liquids. The product of density autocorrelation functions in equation 2.15, which describes the nonlinear feedback mechanism, constitutes the core of the mode-coupling theory. The magnitude of this feedback is determined by the strength of the vertex  $V^{(2)}$  whose value is in turn controlled by the amplitude of the static structure factor contained therein. The solutions to these mode-coupling equations through which the full time dependence of the intermediate scattering function can be obtained are precisely the above mentioned equations proposed and studied by Bengtzelius, Götze and Sjölander (BGS) [BGS84].

The quantities  $M_q^0(t)$ ,  $\Omega_q^2$  and  $V^{(2)}(q, k, |\mathbf{q}-\mathbf{k}|)$  also depend on temperature but it is assumed that this dependence is smooth over the entire temperature range. This means that any singularities in the equations of motion are a result of their intrinsic nonlinearity and not a result of a singularity in the input parameters.

Due to their complexity, solutions of the mode-coupling theory equations can only be obtained numerically. Therefore, Leutheusser [Leu84] approximated the structure factor by a  $\delta$ -function at the wave vector  $q_0$  where  $S_q$  has its main peak. This procedure transforms equation 2.13 into a single equation describing the correlation function for  $q_0$  as all other equations vanish. Equation 2.13 can be rewritten based on

this approximation as

$$\ddot{\Phi}(t) + \Omega^2 \Phi(t) + \nu \dot{\Phi} + \Omega^2 \int_0^t m[\Phi(t-t')] \dot{\Phi}(t') dt' = 0, \quad (2.17)$$

where  $\Phi(t)$  is the normalized density autocorrelation function

$$\Phi(t) = \frac{F_q(t)}{S_{q_0}} = \frac{\langle \delta \rho_{q_0}(t) \delta \rho_{-q_0}(0) \rangle}{S_{q_0}}, \quad (2.18)$$

and  $m[\Phi]$  is a low order polynomial in  $\Phi$ . Equations for a single correlation function such as equation 2.17 are called schematic models and are believed to describe some essential, i.e. universal, features of the full theory. Götze and Sjögren [GS88] calculated the correlation functions for a model with  $m[\Phi] = \lambda_1 \Phi + \lambda_2 \Phi^2$ , with  $\lambda_i > 0$ , the results of which are shown in Figure 2-8. For these curves, the coupling parameters are chosen such that their distance to the critical values decreases like  $0.2/2^n$  for  $n = 0, 1, \dots$  (liquid, curves A, B, ...) and increases like  $0.2/2^n$  for  $n = 0, 1, \dots$  (glass, curves F', D', ...). A change in temperature in the physical system corresponds to a change in the coupling constants  $\lambda_i$  in these schematic models. In particular, the temperature dependence of the full mode-coupling equations is given by the temperature or pressure dependence of the structure factor. The effect of the structure factor on the coefficients of the memory kernel  $m_q(t)$  also contributes to the temperature dependence of the mode-coupling equations. Cooling or compression of the system results in a more sharply peaked static structure factor  $S_q$ . This in turn increases the degree of coupling between the density fluctuations, resulting in a concomitant increase in the retarded viscosity of the liquid. This viscosity regulates the relaxation of the system back to its unperturbed state.

The solutions of the schematic models show that if the nonlinearity of the memory kernel  $m[\Phi(t)]$  exceeds a certain threshold, the density correlator does not decay to zero, even at infinite times. This means that the system is no longer ergodic since density fluctuations which were present at time zero do not disappear even at long times. Consequently, the dynamic transition can be identified with the liquid-glass transition. It was later found that such trends were due to the terms neglected in the original mode-coupling equations 2.13, with  $m_q(t)$  given as a quadratic function of  $F_q(t)$  as in equation 2.15. These terms become important at low temperature and result in qualitatively different behavior of the time dependent solution of the equations of motion [DM86]. In particular, the singularity of the solution disappears and the correlation functions decay to zero even at low temperatures. One of the main mechanisms that restores ergodicity to the system at all times is a thermally activated process, such as coupling to transverse current modes, which allows one

particle to overcome the walls of its cage. Therefore, such processes are generically called hopping processes which are taken into account in the extended version of mode-coupling theory. A detailed mathematical derivation of the equations of motion for both the idealized and the extended versions of the theory can be found in references [BK05] and [RC05].

Even though the solutions of the schematic models may not be quantitative (due to the elimination of the details of all the microscopic information), a wealth of qualitative and quantitative predictions for the temperature dependent behavior of the density correlator can still be obtained through them. These will be described in the following section.

### 2.4.3 Predictions of the Mode-Coupling Theory

The pertinent predictions of mode-coupling theory include the important prediction regarding the existence of a critical temperature  $T_c$  at which the  $\alpha$  relaxation time of the system diverges. All predictions presented below only hold, strictly speaking, close to  $T_c$ , i.e. it is assumed that the separation parameter  $\sigma = (T_c - T)/T_c$  is small.

#### 2.4.3.1 Glass Transition Singularity

The infinite time limit of  $\Phi(t \rightarrow \infty)$  is called the non-ergodicity parameter or Debye-Waller factor,  $f_q(T)$ . For high temperatures, where the vertices (coupling constants)  $V^{(2)}(q, k, |\mathbf{q}-\mathbf{k}|)$  are small, the correlation function  $\Phi(t)$  rapidly decays to zero following the initial microscopic transient. In addition,  $f_q$  is zero and the system is ergodic. In the idealized theory, the coupling constants increase when the temperature is lowered until the critical temperature  $T_c$  is reached and  $\Phi(t)$  does not decay to zero, even at infinite time. This is called the glass transition singularity and is an indication that the system remains out of equilibrium for all times, not just the time scales relevant for observation (see solutions B', D', F' in Figure 2-8 A). This mathematical divergence in the idealized mode-coupling theory is unphysical and was believed to be due to the approximation that only longitudinal acoustic modes were expected to contribute to the relaxation. However, recent work by Mayer *et al.* [MMR06] showed that the divergence originates from mathematical approximations introduced by BGS [BGS84] and ergodicity can be restored without the need to incorporate more variables than the original density fluctuations. Readers are referred to the discussion in reference [MMR06] for further details.

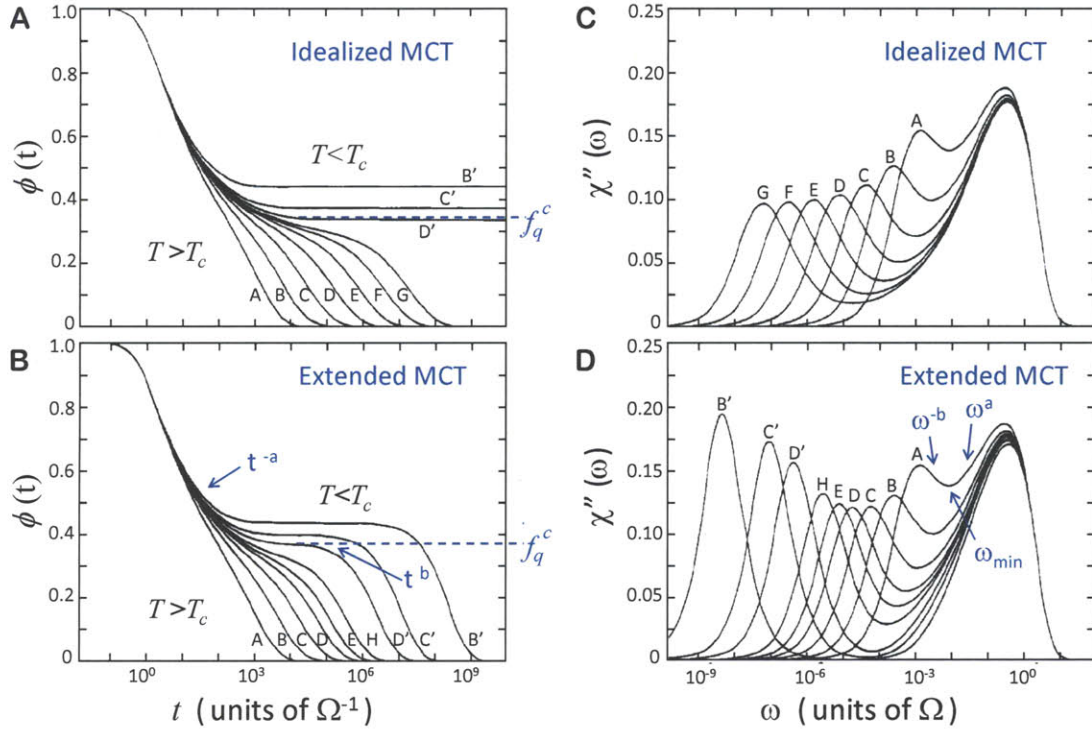


Figure 2-8: Mode-coupling theory calculations of the density-density relaxation function  $\phi(t)$  (A, B) and their corresponding Fourier transforms, the susceptibility spectra  $\chi''(\omega) = \omega\phi''(\omega)$  (C, D). A and C are solutions to the idealized mode-coupling theory equations. As the temperature is cooled toward a critical temperature  $T_c$  (solutions A-G), the relaxation functions show an increasingly pronounced two-step decay. The early decay corresponds to the  $\beta$  relaxation, while the second decay corresponds to the  $\alpha$  relaxation. Below the critical temperature (solutions B', C', D') the second decay never occurs, leading to a finite value of the non-ergodicity parameter  $f_q^c$  at long times. This behavior is reflected in the susceptibility in which the  $\beta$  peak at high frequencies scarcely changes with temperature, while the  $\alpha$  peak moves to much lower frequencies as the temperature is reduced before disappearing at  $T < T_c$ . B and D are solutions to the extended mode-coupling theory equations which include activated hopping processes through which the density correlation function  $\phi(t)$  is able to completely relax below the critical temperature. Immediately before the plateau, asymptotic formulas show a  $t^{-a}$  power law dependence for all temperatures while a  $t^b$  dependence is predicted at longer times. These power laws also hold true in the frequency domain where  $\chi''(\omega)$  has the form  $\omega^a$  and  $\omega^{-b}$  right above and below the minimum  $\omega_{min}$ . Adapted from Götze et. al. [GS88].

### 2.4.3.2 The Two-Step Relaxation Scenario

As temperature decreases, the smooth variation of the coupling constants leads to a critical temperature  $T_c$  at which  $f_q$  changes discontinuously from zero to a non-zero critical value  $f_q^c$ . Close to the bifurcation, where  $T - T_c/T_c \ll 1$ , the mode-coupling theory equations can be expanded in terms of  $\Phi(t) - f_q^c$ . The analysis of this asymptotic behavior yields the derivation of several central predictions of mode-coupling theory. First, the factorization

$$\Phi(t) = f_q^c + h_q G(t) \quad (2.19)$$

predicts that the  $q$ -dependence of  $\Phi(t) - f_q^c$  in the asymptotic region is completely specified by  $h_q$ , while the time dependence of all correlation functions is given by the  $q$ -independent function  $G(t)$ .  $G(t)$  is the  $\beta$ -correlator and is also the solution to the equation

$$\lambda G^2(t) + \sigma = \frac{d}{dt} \int_0^t G(t-t')G(t')dt' , \quad (2.20)$$

where  $\sigma$  is the separation parameter as previously defined. The solution to equation 2.20 shows that  $G(t)$  first decays as  $t^{-a}$  (the critical decay), and then decreases as  $-t^b$  (Von Schweidler law). The two exponents  $a$  and  $b$  are related to each other by the exponent parameter

$$\lambda = \frac{\Gamma^2(1-a)}{\Gamma(1-2a)} = \frac{\Gamma^2(1+b)}{\Gamma(1+2b)} , \quad (2.21)$$

where  $\Gamma$  is the standard  $\Gamma$ -function. For  $t \rightarrow \infty$ , one finds that the amplitude of the non-ergodicity parameter increases below the critical temperature  $T_c$ ,

$$f_q(T) = \begin{cases} f_q^c & (T > T_c) \\ f_q^c + h_q [(T_c - T)/T_c]^{1/2} & (T < T_c) \end{cases} , \quad (2.22)$$

where  $h_q$  is called the critical amplitude. This square-root cusp in  $f_q(T)$  is another general prediction of mode-coupling theory and has been shown experimentally to be present in several glass formers [YN95] while absent in others [PN00].

One of the most important predictions of mode-coupling theory, apart from the existence of a critical temperature  $T_c$ , is the existence of three different relaxation processes. The first one is a trivial relaxation on the microscopic time scale. Calculations of the correlation functions (depicted in Figure 2-8 (A)) show a quadratic dependence at short times due to the ballistic motion of the particles on those time scales. At high temperatures (e.g. curve A), the relaxation directly crosses over to a behavior

which can be well described by an exponential decay. If the temperature is decreased (curve D), there is an intermediate time regime, the so called  $\beta$  relaxation regime, where the correlation function decays only very slowly and the  $\Phi(t)$  plot exhibits an inflection point. At even lower temperatures (curve G) the correlation function shows a plateau and only decays to zero after very long times. This second decay is called the  $\alpha$  relaxation regime.

The existence of the plateau can be rationalized in the following way: At short times, the motion of the particle is essentially ballistic. After a microscopic time the particle remains trapped in a cage formed by its nearest neighbors, and thus the correlation does not decay any further. At much longer times, towards the end of the  $\beta$  relaxation, this cage starts to break up and the particle begins to explore an increasing volume of space. At this point, the motion becomes collective as the correlation function enters the time scale of  $\alpha$  relaxations and resumes its decay.

As described above, within the framework of idealized mode-coupling theory, the correlation function does not decay to zero when the critical temperature  $T_c$  is reached. In the extended version of the theory [RC05] this issue is addressed by taking thermally activated processes into account, such as coupling to transverse current modes, which restore ergodicity below  $T_c$ . The system can then relax back to equilibrium at long times. However, the plateau or inflexion point between fast and slow relaxation processes still serves as an effective non-ergodicity parameter  $f_q^c$  and follows the description of equation 2.22. Below  $T_c$ , the height of the plateau increases and the time scale for which it can be observed shortens. Mode-coupling theory predicts that for temperatures below  $T_c$ , this increase in the height of the plateau is proportional to  $\sqrt{T_c - T}$ , which was experimentally confirmed by neutron scattering [FFR90]. One might conclude that the concept of a critical temperature does not make sense anymore, since there is no temperature at which the relaxation times diverge. This is, however, not the case. If the hopping processes are not too strong, there still exists a temperature range in which the relaxation times show power-law behavior having a critical temperature  $T_c$ . However, this power law does not extend down to  $T_c$  but deviates in the vicinity of  $T_c$  such that the temperature dependence of  $\tau$  will be weaker than a power-law. Thus, despite the presence of the hopping processes, it is still possible to identify a  $T_c$  for the system.

### 2.4.3.3 The $\beta$ scaling regime

The  $\beta$  correlator  $G(t)$  defined by equation 2.20 obeys the scaling laws

$$G(t) = \begin{cases} \sqrt{|\sigma|} g_-(t/t_\sigma) & \text{for } \sigma < 0 \\ \sqrt{|\sigma|} g_+(t/t_\sigma) & \text{for } \sigma > 0. \end{cases} \quad (2.23)$$



The scaling time  $t_\sigma$  is given by

$$t_\sigma = t_0/|\sigma|^{1/2a}, \quad (2.24)$$

where  $t_0$  is the microscopic time scale calculated by  $t_0 = \Omega_0^{-1}$ . The master functions  $g_\pm(t/t_\sigma)$  are solutions to equation 2.20 with  $\sigma = \pm 1$ . While for short times ( $t \ll t_\sigma$ ), both master functions follow the critical decay law  $g_\pm(t/t_\sigma) = t/t_\sigma^{-a}$ , for longer times ( $t \gg t_\sigma$ ), the liquid master functions follows the von Schweidler law  $g_-(t/t_\sigma) = -B(t/t_\sigma)^b$  and the glass master function has a constant value  $g_+(t/t_\sigma) = 1/\sqrt{1-\lambda}$  (where  $\lambda$  is the exponent parameter from equation 2.21).

#### 2.4.3.4 The $\alpha$ scaling regime, Time-Temperature Superposition

The solutions of the mode-coupling theory equations for  $\Phi_q(t)$  can be scaled so that the  $\alpha$  decays for different temperatures can be depicted in a single plot. This  $\alpha$  scaling is the mode-coupling theory equivalent of the time-temperature superposition principle (e.g., see Figure 2-3 (B), which states that relaxation spectra (with their characteristic relaxation times  $\tau$ ) of the highly temperature dependent  $\alpha$  feature can be superimposed by scaling the time as  $t/\tau$  for different temperatures. The asymptotic analysis of the mode-coupling theory equations for  $\sigma < 0$  and  $(T - T_c)/T_c \ll 1$  gives the scaling relation

$$\Phi_q(t) = F_q^\alpha(t/\tau) \quad \text{for } t \gg t_\sigma \quad (2.25)$$

with  $F_q^\alpha$  being the temperature independent  $\alpha$  master function. Numerical simulations show that the  $\alpha$  relaxation can be well described by the phenomenological Kohlrausch-Williams-Watts stretched-exponential function

$$\Phi_q(t) = f_q^c \exp \left[ -(t/\tau_q)^\beta \right]. \quad (2.26)$$

When the temperature approaches the critical temperature  $T_c$ , the  $\beta$  relaxation regime increasingly stretches out in time and the  $\alpha$  relaxation time  $\tau_\alpha$  diverges with a power law,

$$\tau_\alpha(T) = \tau_0(T - T_c)^{-\gamma}. \quad (2.27)$$

The theory predicts an interesting connection between the exponents  $a$  and  $b$  (both of which are important for the  $\beta$  relaxation) as being coupled to the exponent  $\gamma = 1/2a + 1/2b$  which governs the time scale of the  $\alpha$  relaxation. Thus, according to mode-coupling theory, measurements of the temperature dependence of the  $\alpha$  relaxation

time yield information about the time dependence of the relaxation in the  $\beta$  regime and vice versa.

### 2.4.3.5 The susceptibility spectrum

The power spectrum  $S_q(\omega)$  is obtained by the Fourier transform of the time correlation function  $\Phi_q(t)$  and the susceptibility spectrum  $\chi''(\omega)$ , and a subsequent multiplication by  $\omega$ . Similar scaling laws as for  $\Phi_q(t)$  are valid for the susceptibility spectra, as indicated in Figure 2-8.

In the  $\beta$  relaxation regime, the  $\chi''(\omega)$  spectra should scale as

$$\chi''_{\pm}(\omega) = h_q \sqrt{|\sigma|} \hat{\chi}''_{\pm}(\omega t_{\sigma}), \quad (2.28)$$

where  $\hat{\chi}''_{\pm}$  is the susceptibility master function. Above  $T_c$ , the shape of  $\chi''_{-}$  in the vicinity of the minimum is described approximately by the interpolation equation:

$$\chi''(\omega) = \chi''_{min} \left[ a \left( \frac{\omega}{\omega_{min}} \right)^{-b} + b \left( \frac{\omega}{\omega_{min}} \right)^a \right] \frac{1}{a+b}. \quad (2.29)$$

Critical  $T$ -dependent behavior is predicted for both the value and the frequency of the minimum  $\chi''_{min}(\omega_{min})$  between the  $\alpha$  and  $\beta$  susceptibility peaks,

$$\chi''_{min}(\omega_{min}) \propto |T - T_c|^{1/2} \quad \text{and} \quad \omega_{min} \propto |T - T_c|^{1/2a}. \quad (2.30)$$

More generally, the asymptotic power-law frequency dependences of the  $\alpha$  and the  $\beta$  regimes are predicted to be:

$$\chi''(\omega) \propto \omega^{+a} \quad (\omega_{\sigma} \ll \omega \ll \Omega_q) \quad (2.31)$$

on the low-frequency side of the  $\beta$  peak,

$$\chi''(\omega) \propto \omega^{-b} \quad (\omega_{\alpha} \ll \omega \ll \omega_{\sigma}) \quad (2.32)$$

on the high-frequency side of the  $\alpha$  peak, and

$$\chi''(\omega) \propto \omega^{+1} \quad (0 < \omega \ll \omega_{\alpha}) \quad (2.33)$$

on the low-frequency side of the  $\alpha$  peak. The critical exponents  $a$  and  $b$  should range within  $0 < a < 0.5$  and  $0 < b < 1$  respectively with  $\omega_{\sigma} = 1/t_{\sigma}$ .

A summary of important mode-coupling theory predictions is given on the following page.

## Mode-Coupling Theory Predictions

Two relaxation steps,  $\beta_{\text{fast}}$  (fast) &  $\alpha$  (slow)

separation parameter :  $\sigma = (T_c - T)/T_c$

microscopic time scale :  $t_0 = \Omega_0^{-1}$

scaling time :  $t_\sigma = t_0/|\sigma|^{1/2a}$

Asymptotic power-law relations around  $t_\sigma$  and  $\omega_{\text{min}}$ :

$\beta$  relaxation:  $\phi_q(t) = f_q^c + h_q(t/t_0)^{-a}$        $\chi'' \sim (\omega/\omega_{\text{min}})^a$

$\alpha$  relaxation:  $\phi_q(t) = f_q^c + h_q(t/t_0)^b$        $\chi'' \sim (\omega/\omega_{\text{min}})^{-b}$

$\chi''_{\text{min}}(\omega_{\text{min}}) \propto |T - T_c|^{1/2}$        $\omega_{\text{min}} \propto |T - T_c|^{1/2a}$

exponent relations :  $\lambda = \frac{\Gamma^2(1-a)}{\Gamma(1-2a)} = \frac{\Gamma^2(1+b)}{\Gamma(1+2b)}$     and     $\gamma = \frac{1}{2a} + \frac{1}{2b}$

Susceptibility minimum :  $\chi''(\omega)/\chi''_{\text{min}} = \left[ a\left(\frac{\omega}{\omega_{\text{min}}}\right)^{-b} + b\left(\frac{\omega}{\omega_{\text{min}}}\right)^a \right] / (a + b)$

Low-frequency side of  $\alpha$  peak :  $\chi'' \sim \omega^{+1}$

Scaling laws :  $\tau_\alpha \propto \eta = t_0|\sigma|^{-\gamma} = t_0|\sigma|^{-(1/2a+1/2b)}$

Debye-Waller factor :  $f_q(T) = \begin{cases} f_q^c & (T > T_c) \\ f_q^c + h_q[(T_c - T)/T_c]^{1/2} & (T < T_c) \end{cases}$

(non-ergodicity parameter)

## 2.5 Conclusions

Insights into relaxation in glass forming liquids via both thermodynamic and kinetic approaches were presented in this chapter. While phenomenological models allow a qualitative description of certain features of the liquid-glass transition, only the first principles based mode-coupling theory can provide a wealth of predictions regarding the dynamics of a liquid as it is cooled down. Many of these predictions have been tested by various experiments that probe liquid dynamics by means of dielectric, longitudinal, bulk or shear mechanical and neutron or spin measurements. Nonetheless, since the natural variable of mode-coupling theory is fluctuations in density, and the extended versions of mode-coupling theory further include transverse currents, the obvious choices for experimental techniques to test mode-coupling theory predictions are methodologies that directly probe these variables. The high frequency region of the susceptibility spectrum is particularly important with regards to the many predictions of the theory, as shown by the discussions in this chapter. Acoustic measurements presented in the following chapters extend the previous experimentally accessible frequency range by one order of magnitude, thereby granting access to significant portions of the previously unexplored  $\beta$  relaxation regime.

# CHAPTER 3

---

## Experimental Methods

---

In the past few decades, a variety of mechanical spectroscopic techniques have been developed and applied to study the microscopic structure and dynamics of glasses and glass-forming materials over a broad range of frequencies. The predominant methods in the megahertz frequency range are piezoelectric techniques [KBL01] and impulsive stimulated light scattering experiments [YN87]. Brillouin light scattering experiments can investigate frequencies up to several gigahertz [CFMR02], and, in recent years, the frequency range has been extended up to several tens of gigahertz by ultraviolet Brillouin light scattering [BCE<sup>+</sup>04]. The terahertz frequency regime — the region around the boson peak — is well investigated by Raman spectroscopy [UY96], inelastic neutron scattering (INS) [WHL<sup>+</sup>94] and inelastic x-ray scattering (IXS) [GC06]. However, the extraction of elastic parameters from some of these methods has often been controversial since the nature of the excitation that gives rise to the scattering may be uncertain. For instance, Raman scattering measurements occasionally observe two-phonon processes which are difficult to deconvolve from the data. Similarly, INS and IXS do not always produce distinct phonon sidebands. In addition, the region in between the methods listed above — most of the gigahertz frequency range — is rather difficult to access but nevertheless of great importance in the study of liquid dynamics as this is the regime where the fast  $\beta$ -relaxation processes occur.

In the past two decades, photo-acoustic techniques have been developed that allow optical generation and detection of acoustic waves from several gigahertz up to a few terahertz. For example, acoustic waves in the 700 GHz to 1.5 THz range may be generated by femtosecond optical irradiation of multiple quantum well (MQW) structures [CLS04]. Here, the spatial periodicity of the wells determines the frequency of the acoustic wave, thus a different structure must be fabricated for each

individual frequency. A more versatile technique, Picosecond Ultrasonics (PU), uses a thermoelastic approach to generate high frequency ultrasound by ultrashort light pulses [Mar98]. It is a non-contact, non-destructive technique for generation of picosecond acoustic pulses, thereby allowing study of thin films or nanostructures to reveal internal features or to study relaxation processes.

Depending on the experimental geometry, the polarization of the acoustic pulses can be either longitudinal or shear, and the frequency can cover a range from several gigahertz up to about 500 GHz (when soliton formation is studied, frequencies as high as 1 THz can be reached). A large number of studies can be found in the literature concerning phonon mean free path measurements in crystals and amorphous solids [MTZM96], phonons in superlattices [EGR<sup>+</sup>07, WCK<sup>+</sup>08], the generation and detection of shear acoustic waves [HWM<sup>+</sup>00, RRP<sup>+</sup>05, PRG<sup>+</sup>07], etc. However, these investigations are usually performed on solid samples and there are only a very limited number of reports — less than a dozen — in which phonon propagation in liquids has been studied [MWM07, YAD<sup>+</sup>07]. These investigations use either Brillouin scattering directly in the liquid or a broadband approach similar to conventional ultrasonics. The highest acoustic frequencies reported are about 20 GHz [SN04, SYFM05] and only the longitudinal polarization has been observed.

The present chapter introduces the main experimental techniques used in this doctoral work that allowed the extension of the frequency window by over an order of magnitude for longitudinal waves (>200 GHz) and facilitated, for the first time, the observation and study of PU shear wave propagation in liquids. This chapter starts with an overview of the pump-probe setup, describes the acoustic wave generation within the framework of PU, in particular of multiple-cycle narrowband acoustic waves, and discusses various detection techniques for longitudinal and shear waves. The chapter concludes with a description of temperature-dependent measurements performed in two different cryostats. A lengthy discussion of the liquid sample cell developed and used in our investigations, together with a detailed study of laser heating, may be found in the subsequent chapter.

### **3.1 The Picosecond Ultrasonics Pump-Probe Setup**

One means by which to capture fast processes is to use a very short flashing light that freezes the process at a desired time. A sequence of these images acquired at different times will lead to a complete image of the dynamics of the process. Using such a technique, the photographer Eadweard Muybridge was the first to capture the components of a high-speed motion. This was done in 1872 at the request of Leland Stanford, who wanted to know whether all four hooves were ever off the ground at the

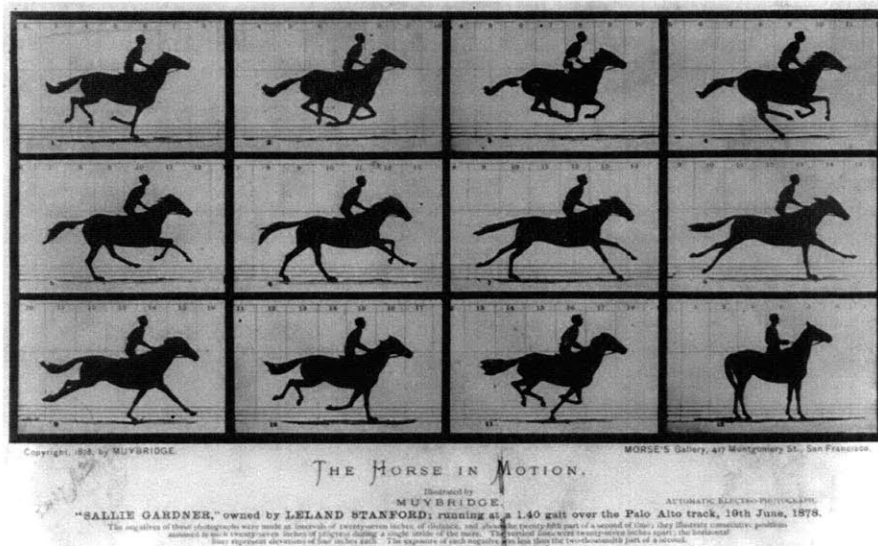


Figure 3-1: The Horse in Motion - by Eadweard Muybridge. One of the first stop-motion photographs, owned by Leland Stanford; A horse running at a 1:40 gait over the Palo Alto track, 19th June 1878. Source: *Library of Congress Prints and Photographs Division*; <http://hdl.loc.gov/loc.pnp/cph.3a45870>.

same time during a horse's trot. Muybridge set up 12 still cameras along a racetrack, each with a string-activated shutter. The strings were held taut across the infield and when the horse passed it broke each string in succession, triggering a sequence of images (see Figure 3-1). It turned out that there is a moment during a horse's trot during which all four hooves are off the ground at the same time. This triggered capture was the forerunner of modern stroboscopes.

Based on a stroboscopic approach, and to some extent similar to the technique developed by Muybridge, pump-probe techniques have been employed in studying ultrafast processes and dynamics on time scales inaccessible by conventional electronics. Here, an ultrashort stimulus (usually an optical pulse, called the *pump*) is used to trigger a process in the system of interest. A much weaker, concurrent pulse (called the *probe*) is used to capture the dynamics of this system at the chosen moment. The problem with such an approach is that it involves a perturbation of the system under investigation, meaning that the system is moved away from equilibrium. As we are interested in the equilibrium properties of that system, such an effect is not desirable. However, statistical physics provides a solution to this problem through the fluctuation-dissipation theorem, which states that there is a direct connection between molecular dynamics at thermal equilibrium and the macroscopic response observed in a dynamical measurement. This connection holds as long as the perturbation is infinitesimally small. More precisely, if a thermodynamic system responds

linearly to an external perturbation, the dynamics of the response are the same as those that govern the fluctuating properties of the thermodynamic system. This is relevant as it tells us that using an experiment with a small perturbation, such as an acoustic wave propagating through a liquid, we can probe equilibrium fluctuations of the liquid. The infinitesimal perturbation prerequisite is satisfied when the perturbing fields are weak relative to the potential of the intermolecular interaction, so that the applied field does not affect the rates of relaxation. The relationship between equilibrium fluctuations and out-of-equilibrium quantities is the essence of the fluctuation-dissipation theorem.

### 3.1.1 The Femtosecond Laser System

The experiments presented in this work were performed with a Coherent Inc. commercial laser system consisting of

- a Verdi V-18 (18 W, 532 nm, CW) pump laser,
- a Mira-900 mode-locked Ti:sapphire oscillator,
- and a RegA-9000 regenerative amplifier (1 W, 200 fs, 250 kHz).

The seed laser is the Coherent Mira-900 oscillator. This mode-locked femtosecond laser system is pumped by about 5 W split off from the Verdi V-18 (18 W). In our experiments, the laser system is tuned to a center wavelength of  $\sim 790$  nm. The output consists of pulses with a Gaussian temporal profile with a Full Width at Half Maximum (FWHM) of about 150 fs, at a repetition rate of 76 MHz with a pulse energy of around 2 nJ.

To obtain higher pulse energy, the oscillator pulses are amplified using a Coherent RegA-9000 regenerative amplifier, which is pumped by the remaining 13 W of the Verdi V-18 output. The average output power of the pump laser is 1 W at a repetition rate of 250 kHz. Even though this is the standard operating repetition rate where the trade-off between average power and pulse power is most favorable, it is possible to adjust the laser repetition rate between about 70 kHz and 300 kHz. After ejection from the laser cavity, the pulse is compressed down to a minimum duration of 200 fs. However, extremely short pulses are not advantageous for the photo-acoustic experiments presented below because longer duration pulses do not come as close to the damage threshold of the acoustic generation transducer films. For more information, see the notes in Subsection 3.2.3.



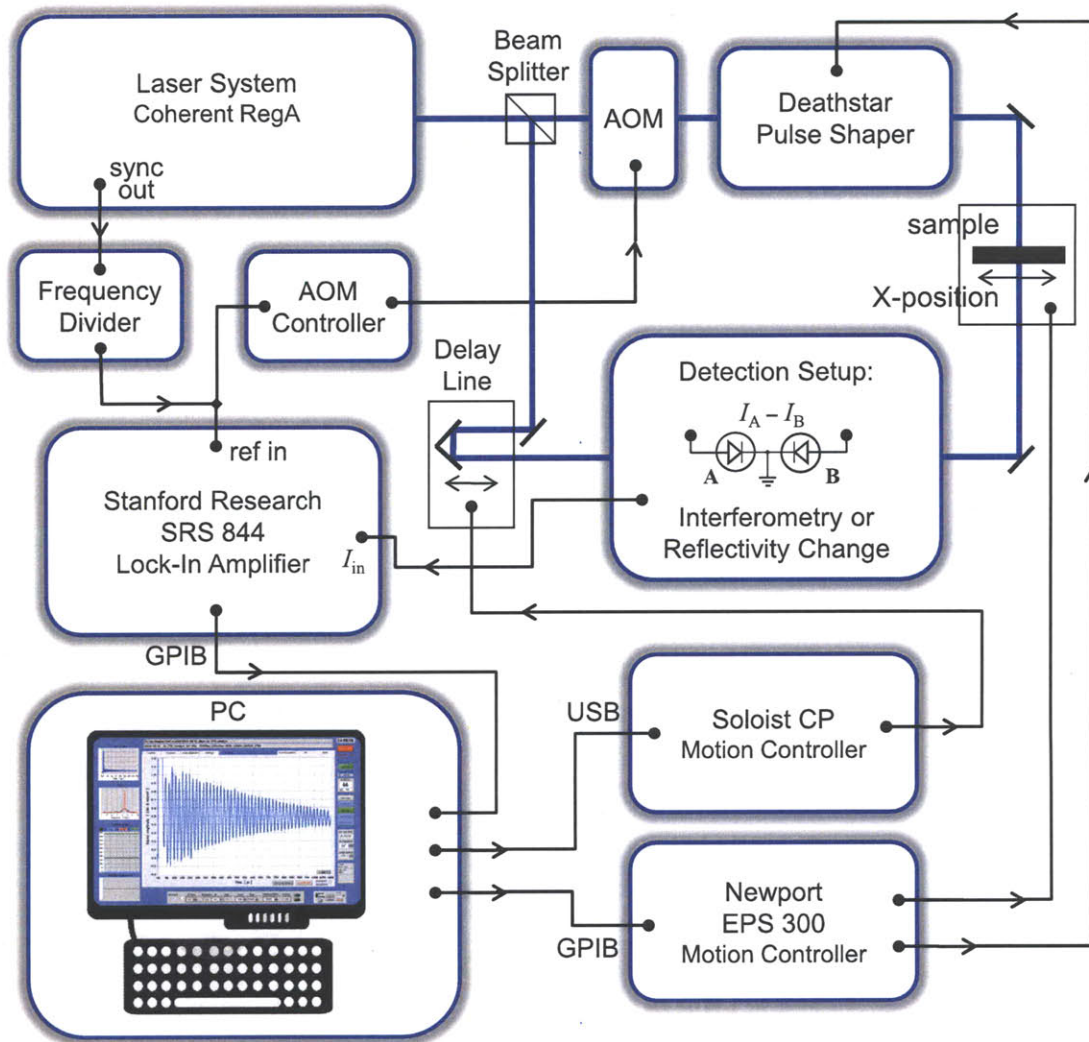


Figure 3-2: Block diagram of the time-resolved pump-probe experimental setup used to study liquid dynamics. The output of an amplified femtosecond laser is split in two beams: an intense laser beam, the *pump beam*, used to generate acoustic waves, and a much weaker laser beam, the *probe beam*, used to monitor the interaction of the acoustic wave with the liquid. A pulse shaper in the pump arm, the Deathstar, allows for an evenly spaced optical pump sequence of pulses by computer-controlled adjustment of a single delay line. Signal to noise levels on the order of  $10^{-5}$  to  $10^{-7}$  require lock-in detection which is implemented by chopping the pump beam with an acousto-optic modulator (AOM). Further signal enhancement is achieved by balanced detection either with an interferometer or by measurement of the induced reflectivity change. The time resolution of these experiments is assured by a computer controllable variable delay-line that moves the retroreflector and thus delays the probe pulses with respect to the pump pulses.

### 3.1.2 The Pump-Probe Setup

Liquid dynamics were investigated using a time-resolved all-optical pump-probe setup. A block diagram of this setup is depicted in Figure 3-2. The amplified 790 nm laser pulses emitted by the amplified Ti:Sapphire laser system were split into two beams of unequal intensity by a beam splitter. The more intense laser beam, the pump, was used to generate acoustic waves by opto-acoustic conversion at a metal transducer film. The significantly weaker laser beam, the probe, was used to monitor the interaction of the acoustic wave with the liquid. For most experiments, the probe laser beam was frequency doubled through second harmonic generation in a 100  $\mu\text{m}$  BBO crystal to 395 nm. When the system was aligned well, typical maximum powers were 200 mW for the pump arm reaching the sample (after losing half the pump energy through chopping as described below) and 4 mW for the probe arm. However, both powers were normally strongly attenuated to levels where data acquisition was barely possible in order to minimize heating and other unwanted effects (as discussed in Chapter 4).

For the data acquisition, a Stanford Research Systems SRS 844 Lock-In amplifier was used in order to record the low signal levels typical for these kind of photo-acoustic measurements. The reference signal was provided by dividing the sync output of the regenerative amplifier by a factor of 2. This signal was also used to trigger the driver of an acousto-optic modulator (AOM) which was placed in the pump arm and which ‘chopped’ the beam by rejecting every other laser pulse. As will be explained in this section, such modulation is crucial for a good signal-to-noise ratio in the lock-in based detection technique.

To enhance the signal, a pulse shaper is placed in the beam path of the pump to allow the generation of narrowband acoustic waves. The shaper comprises a multiple recirculation-reflection design which is discussed in detail later in this chapter. It allows the generation of an optical pulse sequence with repetition rates as low as 1 GHz and as high as 1 THz through the movement of a single automated delay line (the shaper can also be operated in single-pulse mode). The pulse shaper output is then focused onto the sample, where a beam diameter of about 100  $\mu\text{m}$  at the focus was typical. The pump power was continuously adjustable between 0 and about 200 mW via changing the AOM driver voltage between 0 and 5 V which changes the diffraction efficiency. A typical value for the pump beam fluence used in the experiment was 5  $\text{mJ}/\text{cm}^2$ .

The acoustic waves were detected either by interferometry, which is sensitive to the displacement of an interface caused by transmission of an acoustic pulse, or by reflectometry, which directly monitors the propagation of the acoustic pulse through the photoelastic effect. Both methods will be discussed in detail later in this chapter.

In both cases, a balanced photodetection scheme with two large-area, low-noise photodiodes was used to minimize noise (mostly laser noise and air fluctuations) that is present in the signal. For that, the two diodes were connected with opposite polarity, as shown in the circuit diagram in Figure 3-2, and before each measurement, the intensities on both diodes  $I_A$  and  $I_B$  were balanced such that  $I_A = I_B$ . The common output was then fed into the lock-in detector.

### 3.1.3 Data Acquisition

Temporally resolved monitoring of acoustic waves is achieved by variably delaying the probe beam by means of a linear air-bearing translation stage, purchased from Aerotech Inc. and sketched in Figure 3-2. It provides continuously variable motion with  $< 1 \mu\text{m}$  resolution (corresponding to a time resolution of  $2 \times 3.3 \text{ fs}$ ) over one meter of path length. This provides up to two meters, or over 6 ns, of variable delay between the pump and the probe pulses. The controller for the translation stage has been recently updated to a Soloist CP Motion Controller, also purchased from Aerotech. To make use of the motor driven translation stage, a retroreflector was mounted on it. A beam falling on a retroreflector is reflected parallel to the direction of incidence. Due to this retroreflector, once the alignment of the delay line is done, the probe can be focused on the sample at a fixed place, which will not change with the shortening and lengthening of the probe optical path. In fact, this alignment is crucial for the all-optical pump-probe setup since the objective is to achieve overlap between pump and probe beams at all times. Therefore, the probe beam diameter was increased with telescopes for the pass through stage to minimize beam walking and divergence effects, and the proper alignment of the delay stage/retroreflector assembly was often controlled.

In contrast to most pump-probe setups which use a motorized stage, the one used for our experiments was an air bearing stage that operates most efficiently by setting a starting and ending position and then letting it move between them at a constant velocity. This approach was used for all our measurements and many such cycles were done for each particular data acquisition. In synchrony with the start of each new cycle of the stage, the lock-in was triggered to sample and buffer data at a predefined rate. The effective time step of a measurement was calculated from the speed of light, the stage velocity and the lock-in sampling rate. After all the data were acquired and read into the buffer of the computer, they were time-averaged in order to further reduce random noise. An individual data acquisition run with up to several hundred cycles typically took between 1 min to 1 hour or more.

The particular geometry in which the sample was placed in the beam paths (normal or oblique incidence) or whether opposite or same side pump-probe geometry

was used depended on the particular experiment and will be discussed for each type of experiment in the following chapters.

## 3.2 Generation of Gigahertz Frequency Acoustic Waves

In optically absorbing samples, acoustic responses can be initiated by ultrafast lasers through sudden electronic excitation and subsequent lattice thermalization and expansion [TGMT86]. Such techniques are capable of generating higher frequencies than conventional ultrasonic techniques and also permit probing in a noncontact fashion [SNM01]. Laser generated acoustic waves are limited in their high-frequency content by either the optical pulse duration  $\tau$ , through the condition  $\omega\tau \leq 1$ , or the spatial extent  $\zeta$  of the thermal driving force, through the condition  $k\zeta \leq 1$ , where  $\omega$  is the acoustic frequency,  $k$  the corresponding acoustic wavevector and  $\omega/k = c$  the speed of sound. With a typical optical pulse duration on the order of  $\tau \approx 100$  fs for femtosecond laser pulses, the first condition is always met for even the highest acoustic frequencies supported by the sample. This means that the second condition determines the high-frequency limit and the maximum acoustic wave vector is then given by  $k_{max}\zeta \approx 1$ , where  $\zeta$  is again the size of the heated region. In the case of through-plane acoustic waves, the frequency content is determined by the profile and depth of the heated region, which for most metals is on the order of 10-100 nm. Since this depth typically also depends slightly on laser wavelength, varying the excitation wavelength allows modification of the generated acoustic frequency spectrum to some extent. A second adjustable parameter is the thickness of the absorbing material. Reducing it to values smaller than the heated region may increase the acoustic bandwidth. For example, the acoustic wave packet generated in a 10 nm aluminum film by 800 nm femtosecond pulses includes substantial frequency components up to over 400 GHz [MTZM96]. The relevant optical and acoustic parameters can be found in Appendix A.

### 3.2.1 Acoustic Generation (Opto-Acoustic Conversion)

At the heart of picosecond ultrasonic measurements is the conversion of electromagnetic energy into acoustic energy. This conversion is usually mediated through energy deposition of laser light and the resulting rapid thermal expansion which takes place in a very thin top region of a metal film, i.e. the acousto-optic transducer. Even though there are other mechanisms for high-frequency acoustic generation, e.g. piezo-electricity, the work of this thesis is based on this thermal effect. The series of

steps by which a laser pulse is converted into a mechanical strain will be described below.

An ultra-short laser pulse with energy  $Q$  penetrates some distance into a thin metal film with an optical skin depth  $\zeta$ , where it gets partially absorbed and transfers its energy to the electron gas. This creates an electron distribution out of equilibrium with the lattice. The electrons rapidly thermalize and transfer their energy to the lattice, and the increase in temperature causes the material to expand. Typical electron-phonon relaxation times are on the order of a few picoseconds, e.g. 3.5 ps in an aluminum thin film [SDJM03].

From a macroscopic point of view, the absorption of the laser pulse leads to the total energy deposition per unit volume at a distance  $z$  into the film of

$$\Delta W(z) = (1 - R) \frac{Q}{A\zeta} \exp(-z/\zeta), \quad (3.1)$$

where  $R$  is the reflectivity and  $A$  the irradiated area of the film [TM94]. There are two main assumptions in this energy distribution: first, the laser spot size is assumed to be very large compared with the film thickness (which is usually the case), and second, the temperature rise occurs instantaneously (which we will see later is usually not the case). This heating causes a temperature rise  $\Delta T(z)$  with a profile that can be approximated by

$$\Delta T(z) = W(z)/c_V, \quad (3.2)$$

where  $c_V$  is the specific heat at constant volume. Under the assumption that the film is elastically isotropic, this temperature distribution sets up an isotropic thermal stress  $\sigma(z)$  given by

$$\sigma(z) = -3K\alpha\Delta T(z), \quad (3.3)$$

where  $K$  is the bulk modulus and  $\alpha$  the linear expansion coefficient. The resulting sudden thermal expansion of the thin metal film launches two counter-propagating longitudinal acoustic waves through the plane of the film. The outward propagating strain pulse is immediately incident at the boundary of the generation surface and the magnitude of its reflection determines the shape of the resulting acoustic pulse.

Let us examine the shape of the strain pulse in more detail. Since we assume the film to be elastically isotropic, the stress  $\sigma$  only depends on  $z$ . The resulting motion is parallel to  $z$  and the only non-zero component of the elastic strain tensor is  $\eta_{33}$ .

By solving the equations of elasticity [TGMT86]

$$\sigma_{33}(z) = 3 \frac{1-\nu}{1+\nu} K \eta_{33}(z) - 3K\alpha\Delta T(z), \quad (3.4)$$

$$\rho \frac{\partial^2 u_3(z)}{\partial t^2} = \frac{\partial \sigma_{33}(z)}{\partial z}, \quad \text{and} \quad (3.5)$$

$$\eta_{33}(z) = \frac{\partial u_3(z)}{\partial z}, \quad (3.6)$$

we can derive the following equation for the time dependent strain  $\eta_{33}(z, t)$  in the  $z$ -direction:

$$\begin{aligned} \eta_{33}(z, t) = & (1 - R) \frac{Q\alpha}{A\zeta c_V} \frac{1 + \nu}{1 - \nu} \\ & \times \left[ \exp\left(\frac{-z}{\zeta}\right) \left(1 - \frac{1}{2} \exp\left(\frac{-c_1 t}{\zeta}\right) - \frac{1}{2} \exp\left(-\frac{|z - c_1 t|}{\zeta}\right) \text{sign}(z - c_1 t)\right) \right], \end{aligned} \quad (3.7)$$

where  $\nu$  is the Poisson ratio,  $u_3(z)$  the displacement, and  $\rho$  the density. The longitudinal speed of sound is given by

$$c_l^2 = 3 \frac{1-\nu}{1+\nu} \frac{K}{\rho}. \quad (3.8)$$

If the transducer film is thin, the launched strain pulses in the forward and backward direction bounce back and forth within the film and get partially transmitted into the adjacent materials each time they hit an interface. The acoustic reflectivity  $r_{12}$  of an acoustic pulse incident at an interface between two different materials with acoustic impedances  $Z_1 = \rho_1 c_1$  and  $Z_2 = \rho_2 c_2$  (where  $\rho_i$  and  $c_i$  are the density and the sound velocity of materials  $i = 1$  and  $2$ , respectively) is given by

$$r_{12} = \frac{Z_2 - Z_1}{Z_1 + Z_2}. \quad (3.9)$$

The shape of the transmitted acoustic pulse generated in a transducer film (material 1) of thickness  $d$  into a semi-infinite substrate (material 2) is depicted in Figure 3-3. At the free interface of the transducer film, the acoustic pulse gets totally reflected with a sign change while the absolute value of the acoustic amplitude stays the same. However, successive oscillations of the strain transmitted into the substrate have different amplitudes, which are determined by the transmission coefficient

$$t_{12} = 1 - r_{12} = \frac{2 Z_2}{Z_1 + Z_2}. \quad (3.10)$$

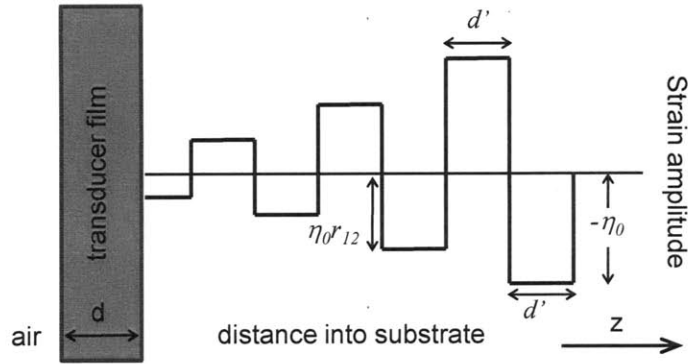


Figure 3-3: Shape of acoustic strain pulse generated in a transducer film of thickness  $d$  and transmitted into the substrate.  $r_{12}$  is the acoustic reflection coefficient of the transducer-substrate interface, and  $d'$  and  $\eta_0$  are defined in the text.

The period of the oscillation  $d' = d(c_2/c_1)$  in the substrate is different from that in the transducer  $d$  because of the change in sound velocity when going from the film into the substrate.

The amplitude  $\eta_0$  of the first strain front entering the substrate is

$$\eta_0 = \frac{1 + \nu}{1 - \nu} \alpha \Delta T \frac{2Z_1}{Z_1 + Z_2} \frac{c_1}{c_2}, \quad (3.11)$$

where  $\nu$  is the Poisson's ration of the transducer film.

### 3.2.1.1 Acoustic boundary conditions

Three boundary conditions at the generation interface are possible:

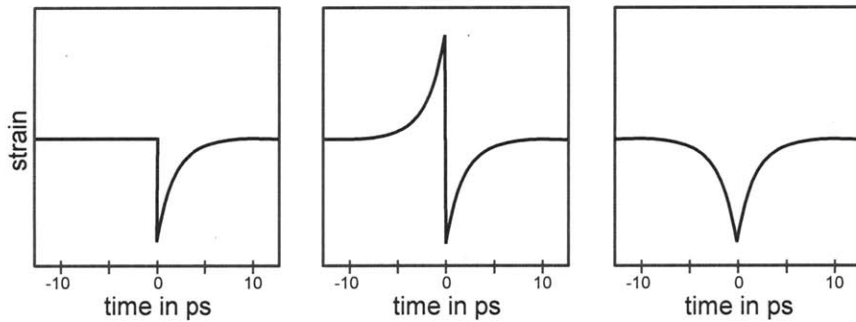


Figure 3-4: Different strain pulse profiles due to various acoustic boundary conditions of the generation interface as seen inside the transducer film. Good acoustic matching of substrate and transducer film (left), free boundary (middle) and stiff substrate with high acoustic impedance (right).

$Z_{\text{transducer}} \approx Z_{\text{substrate}}$  In case of perfect acoustic matching of the substrate and the transducer film, the generated strain pulse  $\eta(z, t)$  will be completely transmitted and can be ideally described by

$$\eta(z, t) = \eta_0 \exp \left[ \frac{-(z - c_l t)}{\zeta} \right] \Theta(z - c_l t), \quad (3.12)$$

where  $\Theta(z - c_l t)$  is the Heaviside step function, and  $c_l$  the longitudinal acoustic velocity in the material. This unipolar pulse has the maximum producible bandwidth, as the spatial extent of the strain pulse will be cut in half. It can be approximately generated by using a combination of a glass substrate and an aluminum transducer film with a reflectivity coefficient of  $r_{\text{glass-Al}} \approx -0.10$ .

$Z_{\text{transducer}} \gg Z_{\text{free boundary}}$  At a free boundary, the outwards propagation strain pulse will be completely reflected with inversion and therefore has a bi-polar shape:

$$\eta(z, t) = \eta_0 \exp \left[ \frac{-(z - v_l t)}{\zeta} \right] \text{sign}(z - v_l t). \quad (3.13)$$

$Z_{\text{transducer}} \ll Z_{\text{substrate}}$  A third possibility is a substrate much denser than the metal film. In this case, the outwards propagating strain pulse will be almost completely reflected at the interface with no inversion. This generates a unipolar pulse of the form:

$$\eta(z, t) = \eta_0 \exp \left[ \frac{-(z - v_l t)}{\zeta} \right]. \quad (3.14)$$

The true strain profile may be significantly broadened by thermal and hot electron diffusion out of the excitation region, and thus the acoustic bandwidth may be correspondingly reduced. For this reason it is important to use a thin film to limit the extent across which thermal and carrier diffusion can occur in order to generate high bandwidth acoustic pulses. These effects are taken into account in the widely used Two-Temperature Model [TM94] which considers a different temperature distribution for the electrons and for the lattice. It is assumed that a short laser pulse instantaneously transfers its energy to the electron gas and raises it to a temperature which very quickly ( $\sim 100$  fs) comes to internal equilibrium via electron-electron interactions. Over a few hundred femtoseconds, excited electrons travel ballistically some distance into the film at supersonic speed (those electrons move at the Fermi velocity,  $\sim 10^6$  m s<sup>-1</sup>, for a few hundred femtoseconds) before they transfer their energy into the acoustic (and optical) phonon modes of the lattice and raise its temperature. The contribution of this effect significantly broadens the acoustic strain pulse to a



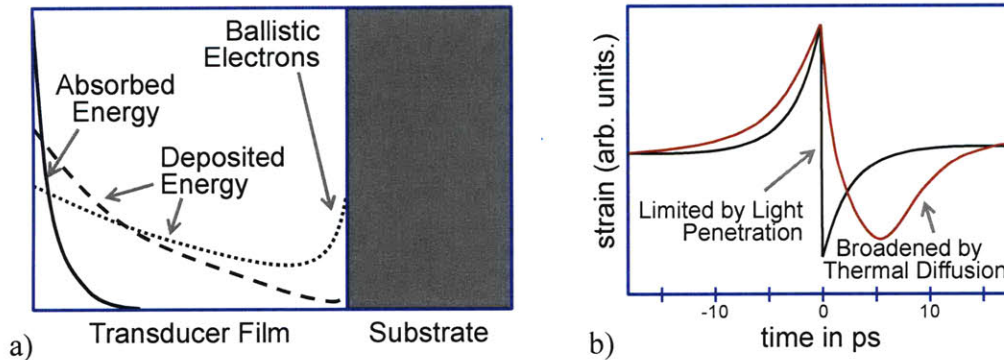


Figure 3-5: (a) Temperature profile of the lattice as a function of distance into the film after the thermal equilibration of the electrons with the lattice. The solid curve shows the temperature profile when electron diffusion is negligible. The dashed curve indicates the temperature profile when some electrons are able to diffuse deep into the film before losing their energy to the lattice. If the effect of electron diffusion is very strong and the film thickness is of the same order, then the hot electrons can diffuse all the way through the film until they are stopped by the insulating substrate. This can dramatically alter the strain profile and in certain cases can even give rise to a distinct second acoustic feature. (b) Electron diffusion significantly broadens the acoustic strain pulse thereby reducing its bandwidth. Reproduced from reference [Sla02].

duration given by the acoustic transit time across the heated region (to about 10 ps to 15 ps in the case of aluminum), as shown in Figure 3-5. A detailed discussion can be found in [WG95].

### 3.2.2 Narrowband Acoustic Generation

Frequency-resolved acoustic spectroscopy requires signal-to-noise ratios (SNR) sufficient for reliable spectral decomposition of the detected acoustic signal, and this often presents a challenge. One approach to achieve this requirement is the excitation of narrowband (multiple-cycle) acoustic wavepackets, thus selecting certain frequency components in the propagating acoustic wave. For most of the measurements of this thesis, a sequence of excitation pulses was used to generate a train of acoustic pulses. The system we designed for this purpose relies on a multiple recirculating reflection design illustrated in Figure 3-6 and is called the *Deathstar* [CFY<sup>+</sup>05]. A single pulse is introduced into the system of retroreflectors of the pulse shaper. It traverses this path seven times around, each time slightly displaced, so that seven pulses emerge. Each time the pulse passes a custom designed variable reflector, some portion of the pulse is transmitted. The partial reflectivities of the different parts of the variable

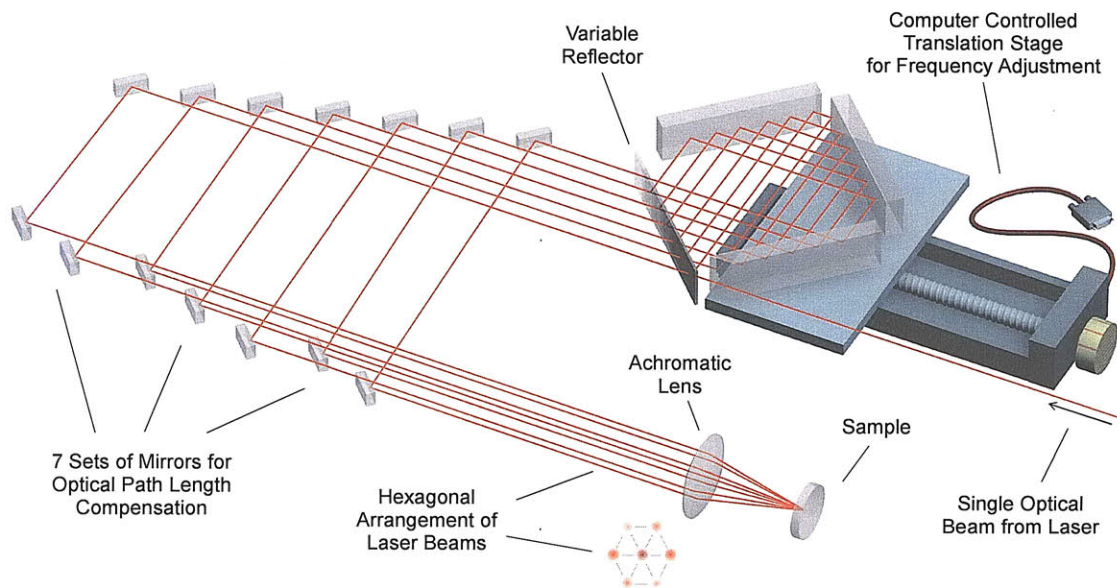


Figure 3-6: Deathstar pulse shaper: Schematic drawing of recirculating reflective pulse shaper, for evenly spaced pulse sequences with repetition rates in the 1 GHz to 1 THz range. A single delay line is adjusted to change the repetition rate. The output pulses are arranged in a hexagon with the most intense pulse in the center. The way in which they are focused down to one spot on the sample bears resemblance to the Death Star in the motion picture Star Wars, giving the pulse shaper its name.

reflector were chosen so that the envelope of the transmitted pulse intensities roughly forms a Gaussian profile\*. An array of ‘twin mirrors’ following the pulse shaper compensates for the additional travel distance of about 15 cm for each additional round trip that successive pulses traverse. The position of each set of mirrors in the array is carefully adjusted to ensure that each pulse has travelled exactly the same distance when it is focused down by a 40 cm focal length achromat onto a single spot on the sample. This distance adjustment, together with the focusing of the lens, results in a temporal and spatial re-overlap of all pulses at the sample.

By adjusting the position of the motorized stage in the pulse shaper (on which one of the retroreflectors is mounted) the spatial, and, therefore, temporal separation between all of the pulses is changed evenly. This setup allows us to generate pulse sequences with repetition rates as low as 1 GHz and as high as 1 THz by tuning the repetition rate (and thereby the frequency) through movement of one single automated delay line. The lowest repetition rate is given by the delay line length, while the highest repetition rate is limited by the optical pulse duration. In fact, the

\* The seven transmitted pulses roughly have the following intensities: 6.2 %, 12.7 %, 19.7 %, 22.8 %, 19.7 %, 12.7 %, and 6.2 %.



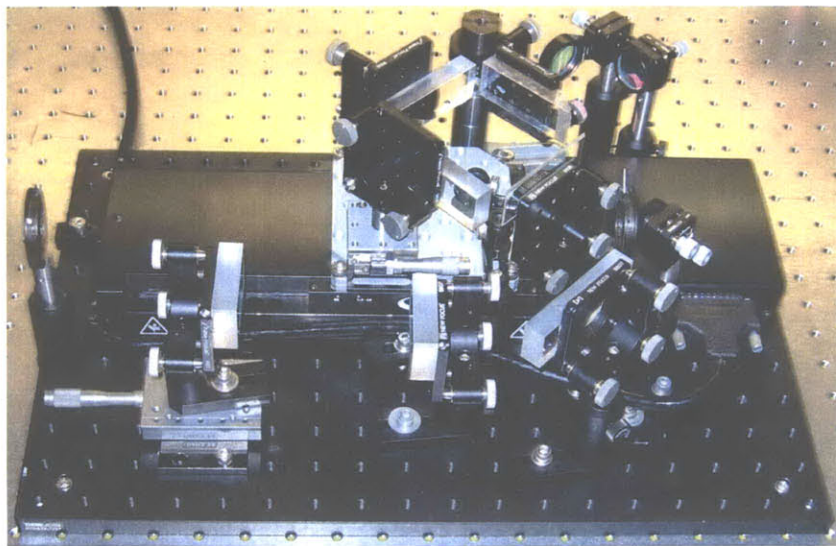
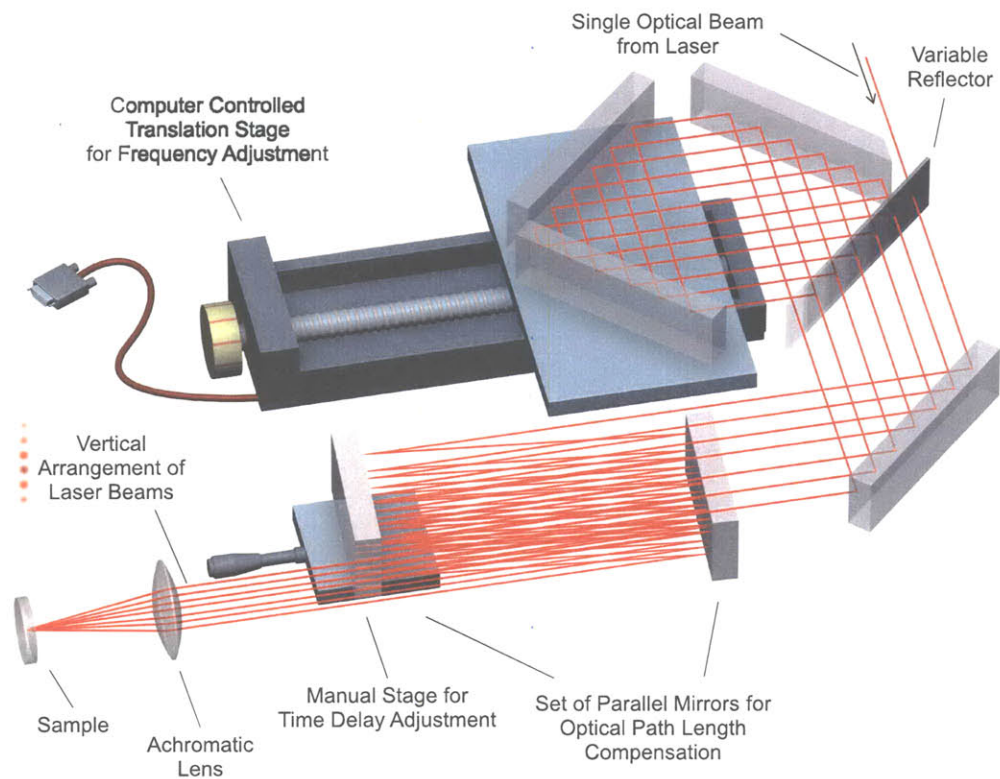


Figure 3-7: Schematic drawing (top) and photograph (bottom) of Deathstar Compact (DSC) pulse shaper: The array of twin mirrors is replaced by two parallel mirrors that compensate for additional round trip distance and the output pulses are arranged in a vertical line. This modification reduces the size of the pulse shaper significantly and allows everything to fit on a small breadboard.

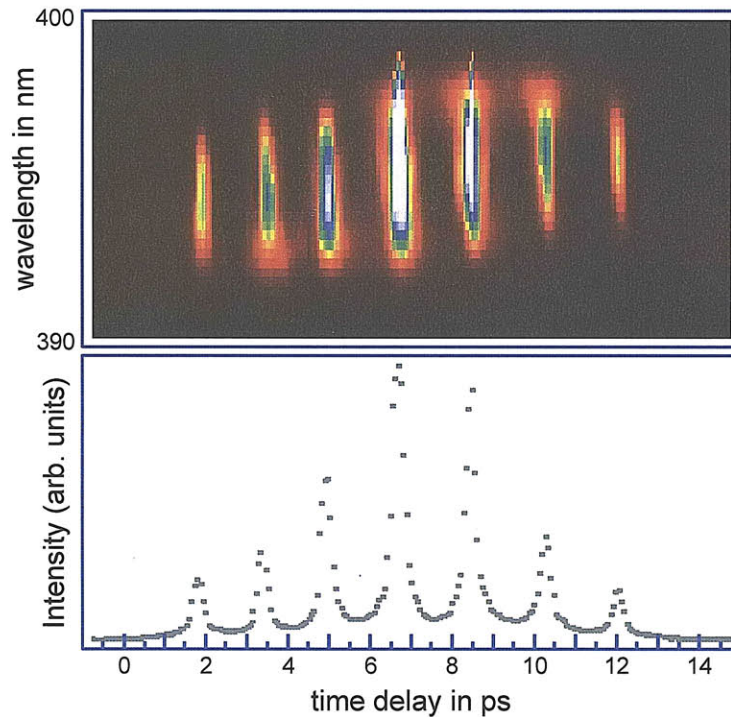


Figure 3-8: Deathstar Compact output characterization by a two-dimensional FROG trace (top) and its integrated intensity (bottom). The spacing between the pulses is 1.7 ps which corresponds to frequency of about 580 GHz.

temporal separation between the pulses can be reduced to zero (as mentioned for the alignment above) so that they all overlap in time. This is very convenient, as it allows the experimentalist the ability to switch the setup between single pump (broadband) and multiple pump (narrowband) configurations without any actual change of the setup except for the computer controlled movement of the delay line.

In the latest version of the pulse shaper, a pair of parallel mirrors compensates for the difference in travel distance of the individual pulses. Their distance exactly matches half the round trip length in the re-circulating system when the delay line is set to its minimum delay. The positions and orientations of these mirrors with respect to the incoming laser beams is such that the beams that initially pass over the first mirror hit the second mirror, which slightly steers them downwards and displaces them sideways. This results in a zigzag pattern of the beams before they finally exit the pulse shaper setup in a vertical alignment. Again, a lens focuses all the beams onto one spot on the sample. This modification replaces the array of twin mirrors and reduces the size of the pulse shaper by a factor of about 3. This new pulse shaper is called the *Deathstar Compact* (DSC) and can fit on a  $1' \times 1\frac{1}{2}'$  breadboard. A schematic drawing of the setup together with a photograph are depicted in Figure 3-7.

The pulse shaper output is characterized by recording a FROG trace (frequency-resolved optical gating) and is shown in Figure 3-8 for a frequency of 580 GHz. The two-dimensional picture (time delay versus optical wavelength) clearly shows all seven, equally spaced output pulses. The slight perceived chirp is an artifact of the cross-correlation measurement where the beams are crossed in a second harmonic generation crystal (which, in our case, happens at slightly different angles).

### 3.2.3 Notes on Amplified Laser System

Most picosecond ultrasonic experiments are performed with an oscillator laser system. Such systems normally operate at repetition rates slightly below 100 MHz, corresponding to a time interval of about 10 ns between consecutive pulses. This is usually not enough time for the sample to fully cool back down to equilibrium, and some residual heat will still be present when the next excitation pulse arrives. This leads to cumulative heating effects (which, in case of unsynchronized chopping, may have a frequency dependence) that must be accounted for in temperature sensitive measurements [SCC08]. Amplified laser systems, like the one used here, offer several advantages. Their repetition rate is much lower and therefore the system will sufficiently cool before the next pulse arrives. In addition, the higher pulse energy permits the use of longer focal length lenses (versus the microscope objectives that are often necessary in oscillator experiments) as it is not necessary to focus the beams down as tightly to reach sufficient excitation fluence. This not only makes the alignment easier, but also reduces the effect of beam steering issues. However, the significantly higher fluence in experiments with amplified laser systems (in our case the pulse energy is several hundred times higher compared with an oscillator) deposits more heat per shot, which has to be considered in sample design and analysis. A detailed study of heating issues is presented in the following chapter.

Pump fluence for measurements presented in this thesis is determined in the following way: The fluence  $F$  at a pump power  $P$  at a repetition rate  $\nu$  and a pump laser spot diameter of  $d$  is given by

$$F = 0.58 \cdot \frac{P/\nu}{\pi(d/2)^2} . \quad (3.15)$$

The factor 0.58 is the fractional area of a two-dimensional Gaussian beam within its full width of half maximum.

Under standard experimental conditions, the excitation beam hits the sample at a repetition rate of  $\nu = 125$  kHz (half the pulses are rejected by the optical chopper) and has a spot diameter of  $d = 100$   $\mu\text{m}$ . The conversion between measured pump

power  $P$  (in [mW]) incident on the sample and fluence  $F$  (in [ $\frac{\text{mJ}}{\text{cm}^2}$ ]) is thus given by

$$F \left[ \frac{\text{mJ}}{\text{cm}^2} \right] = 0.0591 \times P [\text{mW}] . \quad (3.16)$$

### 3.3 Concepts of Acoustic Strain Detection

Gigahertz acoustic strain pulses can be detected in many different ways. Most of them fall into two general categories: monitoring a reflected/transmitted probe laser intensity and interferometry measurements. In our experiments, we take advantage of both approaches and use whatever is best suited to extract the desired information from an experiment. The following section introduces the general ideas behind both approaches; the precise manner in which they are applied is described in the context of each experiment in the following chapters.

#### 3.3.1 Reflectivity Change and Brillouin Scattering

The first detection scheme is based on the coupling of mechanical strain with the laser light through the so-called photoelastic effect. A detailed treatment of this problem was done by Lin and coworkers [LSMT91]. We summarize the main steps in the following.

A time delayed probe pulse relative to the generating pump pulse with a delay  $\Delta t$  is used to detect the propagation and attenuation of the strain pulse as shown in Figure 3-9. The reflected probe light consists of a number of superposing beams with a principal reflection  $r_A$  and a couple of minor beams  $r_B$  and  $r_C$  reflected at the strain pulse. We consider only these two first-order reflections. These reflections can be considered to be off of a local change in refractive index produced by the presence of the strain pulse through the photoelastic effect. Depending on the distance  $d = \Delta t c_l$  of the strain pulse from the transducer film, the three reflected beams A, B and C interfere either constructively or destructively. This results in an oscillatory modulation of the total reflected intensity as a function of time, which can be used to determine the acoustic velocity  $c_l$  of the strain pulse in the sample while the amplitude of the modulation can be related to the amplitude of the strain.

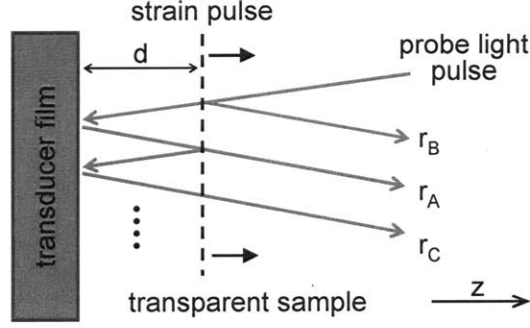


Figure 3-9: Schematic diagram of Brillouin scattering detection. After generation of the acoustic strain pulse in the transducer film, it propagates inside a transparent substrate. Incident probe light reflects off of the transducer film  $r_A$  but also off the propagating strain pulse  $r_B$  and  $r_C$  due to acoustically induced local changes in the refractive index.

Following the general concepts of photoacoustic strain detection given in [TGMT86], the reflection coefficients of the amplitudes of the three reflected beams are

$$r_A = r_{trans} + \delta r_{trans} \quad (3.17)$$

$$r_B(t) = ik_0 \int_0^\infty dz \delta n_s(z, t) \exp(-2ikz) \quad (3.18)$$

$$r_C(t) = ir_{trans}^2 k_0 \int_0^\infty dz \delta n_s(z, t) \exp(2ikz). \quad (3.19)$$

In these equations,  $k_0$  and  $k$  are the wave numbers of the light in vacuum and in the sample, respectively, and  $r_{trans}$  is the reflection coefficient for the probe light pulse at the transducer film-sample interface.  $\delta r_{trans}$  is the change in reflectivity of the transducer film  $r_{trans}$  due to the change in temperature caused by the pump pulse and decreases smoothly as time increases. In the remainder of this thesis it will be referred to as the *thermal background*.  $\delta n_s(z, t)$  is the time dependent strain pulse induced change in the refractive index as a function of position  $z$  in the sample, and equations 3.18 and 3.19 assume that this change in the refractive index  $\delta n_s(z, t)$  is small.

The total time dependence of the change in the optical reflectivity is then given by

$$\Delta R(t) = |r_A + r_B(t) + r_C(t)|^2 - |r_{trans}|^2. \quad (3.20)$$

Together with equation 3.17, we find that the first order effects caused by the propagating strain pulse are

$$\Delta R(t) = r_{trans}^* (\delta r_{trans} + r_B(t) + r_C(t)) + \text{c.c.} \quad (3.21)$$

We are interested in the acoustic information about the transparent sample contained in  $r_B$  and  $r_C$  which are integrals over the time-dependent strain distribution within the sample. The strain  $\eta_{33}(z, t)$  in the  $z$  direction as a function of position and time was derived in equation 3.7 and determines the change in refractive index  $\delta n_s(z, t)$  at a distance  $z$  into the sample at time  $t$  as

$$\delta n_s(z, t) = \frac{\partial n_s}{\partial \eta_{33}} \eta_{33}(z, t). \quad (3.22)$$

From this, the acoustic contribution to the time-dependent change in reflectivity can be calculated as

$$\Delta R(t) = 2 \frac{\eta_0}{n_s} \frac{\partial n_s}{\partial \eta_{33}} \frac{[1 - \cos(2kd')] \sqrt{R}(1 - R) \cos(2kc_l t - \psi)}{|1 + r_{12} \exp(4ikd')|}. \quad (3.23)$$

$\eta_0$  (as defined by equation 3.11) is the amplitude of the first step of the strain entering the transparent sample material,  $r_{12}$  the reflection coefficient of the transducer-sample interface (as defined by equation 3.9), and  $R$  is the intensity reflection coefficient  $|r_{trans}|^2$  of the transducer-sample interface. The functions  $\psi$  and  $\phi$  are defined by

$$\psi = \pi + 2kd' - \phi - \arctan \left\{ \frac{r_{trans} \sin(4kd')}{[1 + r_{trans} \cos(4kd')]} \right\}, \quad \text{and} \quad (3.24)$$

$$r_{trans} = |r_{trans}| \exp(i\phi), \quad (3.25)$$

where  $d'$  is the same as in Figure 3-3.

Lin *et al.* [LSMT91] have pointed out that the properties of the transducer film and its thickness are very important, i.e.:

- i) Equation 3.23 contains the factor  $(1 - R)$ , which means that for a perfectly reflecting transducer film,  $\Delta R$  would vanish. The reason for this is that in the case that  $R = 1$ , the amplitudes of  $r_B$  and  $r_C$  would be the same but with a  $\pi$  phase difference and therefore cancel each other at all times. Thus, the first order in the amplitude of  $r_B$  and  $r_C$  of the interfering beams B and C would cause no change in the total reflected intensity, i.e.  $\Delta R = 0$ .
- ii) As we saw in Figure 3-3, the spatial period of the strain pulse in the substrate is  $2d'$ . For the series of strain interfaces to be an efficient reflector of light, the spatial periodicity  $2d'$  should be close to half the wavelength of light in the substrate.
- iii) When the transducer film thickness is comparable to the optical penetration depth  $\zeta$ , the total optical reflectivity  $R$  of the film goes down and the intensity



of the reflectivity change  $\Delta R$  goes up. This is again because of the factor  $(1 - R)$  which favors thinner films.

The period  $\tau_{ac}$  of the acoustic oscillation can be extracted from equation 3.23 as

$$\tau_{ac} = \frac{\lambda}{2 n c_l}, \quad (3.26)$$

where  $n$  is the refractive index in the sample medium and  $\lambda$  the probe light wavelength. So far, we have only considered the probe beam as being at normal incidence to the transducer film. It is easy to include a different scattering angle in equation 3.26 and rewrite it in terms of the phonon frequency that is studied

$$f_{BS} = \frac{2 n c_l}{\lambda} \sin(\theta/2). \quad (3.27)$$

$\theta$  is the angle between the incoming probe beam and the normal to the plane of the transducer film and  $f_{BS}$  is normally called the Brillouin scattering frequency. A measurement of this frequency can thus give the sound velocity when the refractive index of the sample is known.

So far, our analysis has not included any attenuation of the propagating strain pulse, but this is straightforward to do. The acoustic strain pulse  $\eta(z, t)$  can be written in terms of its Fourier transform  $\eta(q)$ ,

$$\eta(z, t) = \int_{-\infty}^{\infty} dq \eta(q) \exp i(qz - c_l t). \quad (3.28)$$

Comparing this equation with equations 3.18 and 3.19 shows that the amplitude of the acoustic oscillation is determined by the Fourier components  $\eta(2k)$  and  $\eta(-2k)$ . This simply means that the decrease of the amplitude of the acoustic oscillation is given by the rate of attenuation of these Fourier components. In other words, a measurement of this type, often referred to as *time-domain Brillouin scattering* (TDBS), is sensitive to the ultrasonic attenuation rate  $\Gamma(f)$  of phonons of frequency  $2\pi f = 2kc_l$ . This attenuation rate is related to the Half Width at Half Maximum (HWHM)  $\Delta f/2$  of the Brillouin peak in a frequency-domain Brillouin Scattering measurement (BLS) by

$$\Gamma(f) = 2\pi \frac{\Delta f}{2}. \quad (3.29)$$

### 3.3.2 Interferometry

The second detection scheme, used in this work to study broadband and high-frequency narrowband longitudinal acoustic waves, is interferometry. Laser interferometers are

used in numerous applications, as they are sensitive, non-destructive probes. Interferometric techniques have the ability to measure independently both phase and amplitude changes to an optical probe pulse. The general principle of laser interferometry is to split a spatially coherent light beam into probe and reference beams, usually through partial reflection [Mal92]. The probe beam is reflected off of, or transmitted through, the sample while the reference beam, often called local oscillator, is sent along a path of almost the same length (the distance difference must be smaller than the coherence length or spatial extent of the laser beam). When the two beams are recombined, usually again through partial reflection, a small difference in their optical path lengths results in intensity changes of the interferometrically recombined beams. These can either be used for determination of topology by observing the spatial variations in a fringe pattern, or to study mechanical dynamics by monitoring the time-dependent changes in intensity. In both cases, resolution of displacements or phase shifts with sub-angstrom accuracy is possible.

The relative path lengths of the reference and probe beams must be held constant to within a small fraction of the light wavelength to optimize resolution and SNR. Interferometric fluctuations decrease the sensitivity of the interferometer. These can be caused, e.g. by air currents, laser pointing instability, and vibrations of the optical elements in either beam path. However, there exists a wide range of methods available to compensate for them. For example, active feedback based on automated tracking of fringe intensities and piezoelectric modulation of the reference beam phase can yield  $\lambda/100$  accuracy in a Michelson interferometer [BECW02].

The two interferometer designs used in this work for the detection of small, acoustic strain induced displacements are both passive and minimize the effects of vibrations and air currents by a common path design and a small number of optical components. Both interferometers are usually operated with 395 nm light as this increases the sensitivity (shorter optical wavelength) and are described below.

### 3.3.2.1 Grating interferometer

The first type of interferometer is based on a robust time-resolved transient grating, or four-wave mixing approach [RMBN00] and is illustrated in Figure 3-10. In this diffraction-based interferometer [GBB<sup>+</sup>04], a binary phase mask pattern with spatially periodic trenches of a specified spacing is used to separate a single incoming beam into  $\pm 1$  orders of diffraction to produce the probe and reference beams. The phase mask is designed to maximize energy in these orders by having an etch depth of the trenches specific to the light wavelengths of interest. A lens recollimates the probe and reference beams and the sample is placed in the Fourier plane  $f$  of the lens. The reference and probe beams arrive at the sample parallel and focused, be-

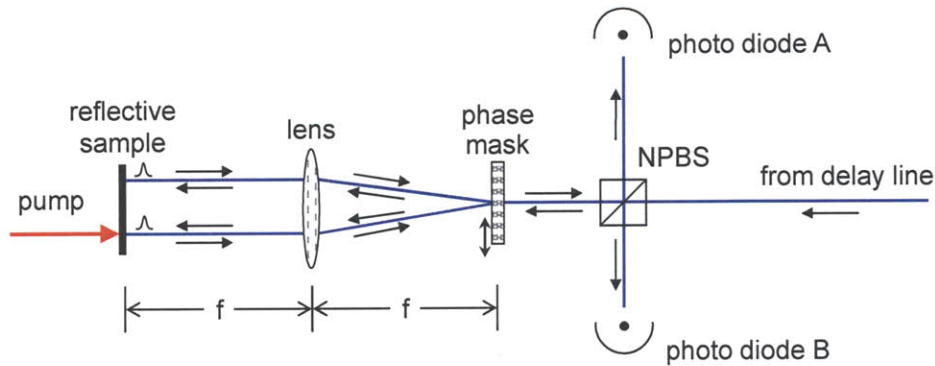


Figure 3-10: Grating interferometer: Probe and reference arms are generated through a phase mask and a lens brings them parallel and focuses both onto the sample. The pump beam induces a perturbation of the sample in the area of the probe arm which results in a small optical phase shift while the reference arm stays unaltered. Both recombine at the same phase mask and the phase change is recorded as an intensity change on photodiode A. The static phase can be adjusted by moving the phase mask perpendicularly to the incident probe beam.

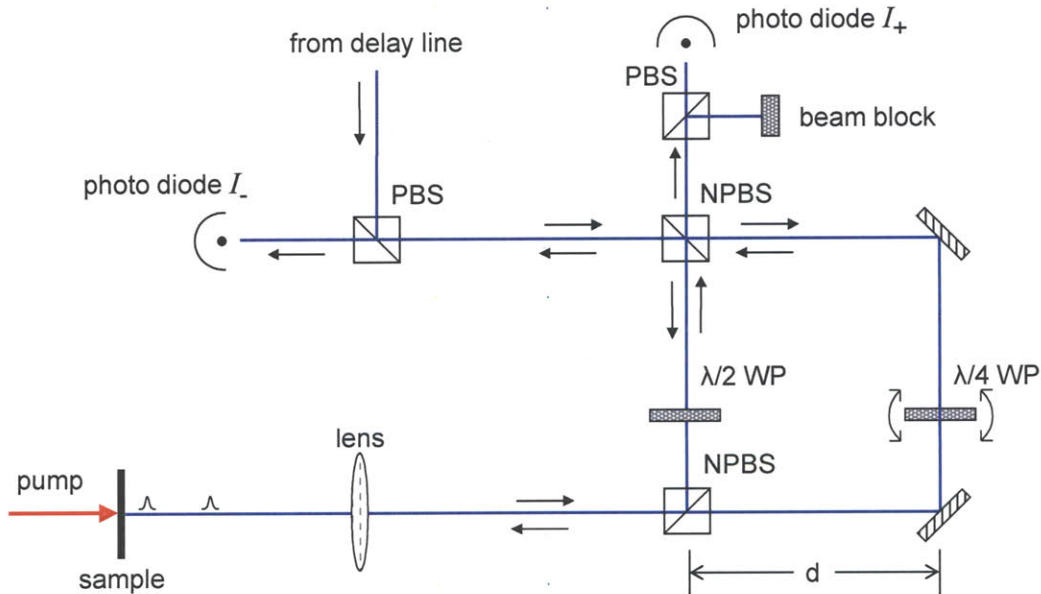


Figure 3-11: Sagnac interferometer: A non-polarizing beam splitter (NPBS) splits the incoming beam into two equally intense parts that travel on a closed trajectory in opposite directions. The sample is placed at a temporally asymmetric position within this loop so that the counter-clockwise traveling beam (reference) hits the sample first and the clockwise traveling beam (probe) arrives at the same spot at a later time. The time delay is determined through the distance  $d$  by  $\Delta t = d/c$  ( $c$  is the speed of light) which determines the maximum operational time interval of the interferometer.

cause the phase mask is in the focal plane  $f$  of the lens. The spot size on the sample is determined by the choice of the focal length  $f$  of the lens, while the interbeam spacing  $D$  is determined by the phase mask period  $\Lambda$ . This spacing can be computed by using the diffraction formula  $\sin(\theta/2) = \lambda/\Lambda$ , where  $\lambda$  is the optical wavelength and given by  $D = 2f \tan(\theta/2) = 2f(\lambda/\Lambda)/\sqrt{1 - (\lambda/\Lambda)^2}$ .  $D$  should be minimized to optimize the stability of the interferometer and was typically a couple of millimeters in our experiments. After reflection of probe and reference beams from the sample, the same lens recollimates both and recrosses them onto the phase mask. On this second pass through the phase mask, the probe and reference beams are diffracted into many orders. The newly diffracted +1 order of the probe and -1 order of the reference are collinear with the original beam and recombine interferometrically. This interferometric signal beam is split off by a non-polarizing beam splitter (NPBS) and directed onto photodiode A. The original reflection off of this beam splitter (before the beam enters the interferometer) is directed onto the second photodiode B whose signal is used for balanced detection.

The probe beam collects time-dependent information about the laser induced material response by monitoring the surface position. A displacement of the surface by an acoustic strain pulse modulates the intensity of the interferogram. The static phase difference of the probe and reference beams determines the sensitivity of the interferometer. This static phase can be controlled by translating the phase mask perpendicular to the initial laser beam.

This interferometer design is very compact and only involves two optical elements, a phase mask and a lens. None of the optical components need to be aligned with more than ordinary precision and the phase stability and robustness against vibrations are enhanced by the symmetry of the probe and reference optical paths. The only asymmetry is the displacement induced by the pump laser in the region where the probe beam interacts with the sample. In contrast, most other interferometer geometries include reflections of separated probe and reference beams which result in higher sensitivity to air currents and vibrations of the reflecting elements.

### 3.3.2.2 Sagnac Interferometer

The second type of interferometer is based on the Sagnac design [Sag13, Pos67] and is illustrated in Figure 3-11. The Sagnac effect is the relative rotation-induced phase shift between two beams of light that have traveled an almost equal distance on a closed trajectory in opposite directions. It was first applied in gyroscopes to measure the rotation of an object, and allows highly accurate measurements of rotation rates down to about  $0.1^\circ$  per hour. In our case, instead of measuring a rotation, it detects very small relative displacements by interfering two beams, a reference beam that hits

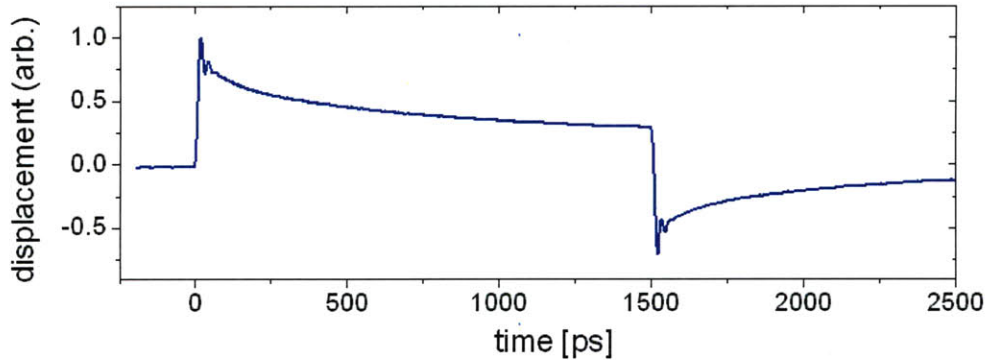


Figure 3-12: Single pulse excitation of a 20 nm thick aluminum film and its interferometric detection with the Sagnac interferometer. The ‘long arm’ of the interferometer starts to detect the displacement at  $t = 0$  ps, while the ‘short arm’ starts detecting the same feature after a delay of  $t = 1500$  ps.

the unperturbed sample first, and a time-delayed probe beam that hits the same spot some time after the perturbation by the pump beam has occurred [HW99, PRBJ99, NLW00]. For this reason, this type of interferometer is called a common-path time division interferometer.

Vertically polarized laser light enters the setup by reflecting off a polarized beam splitter (PBS) toward a non-polarizing beam splitter (NPBS). There, the incident beam is split into two equal parts, one of which travels clockwise (reference) and the other one counter-clockwise (probe) in the same loop. The sample is placed at a temporally asymmetric position within this loop so that the reference beam reaches the sample first while the probe beam arrives at the same spot at a later time. The time delay is determined through the distance  $d$  by  $\Delta t = d/c$ , where  $c$  is the speed of light. This time delay determines the maximum operational time interval of the interferometer as shown in Figure 3-12. The lens used here is a 10 cm achromat that focuses the probe beam to a spot of about 20  $\mu\text{m}$ . After finishing a full loop, both beams interfere at the same NPBS and the pump induced optical phase changes are monitored as intensity modulation on photodiodes A and B.

As a result of the common path design, both beams, reference and probe, experience the same optical path on passing through the interferometer apart from a fixed phase difference. This fixed phase can be adjusted by rotation of the quarter wave plate ( $\lambda/4$ -WP) which allows the delay of one beam with respect to the other. Values of  $\varphi_0 = \pm\pi/2$  correspond to the setting of maximum sensitivity of the interferometer output as depicted in Figure 3-13.

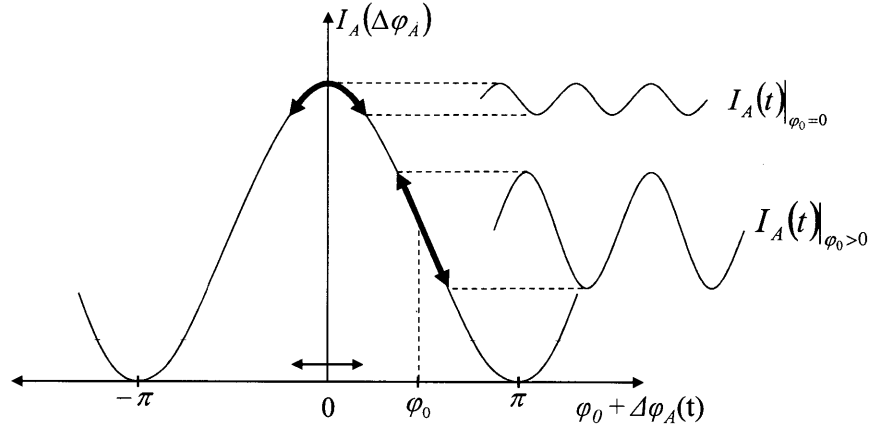


Figure 3-13: Sensitivity of the Sagnac interferometer for diode A. The constant phase shift  $\varphi_0$  can be adjusted by rotation of the  $\lambda/4$ -WP in Figure 3-11 to maximize the sensitivity of the interferometer at  $\varphi_0 = \pm\pi/2$ .

The laser induced changes of the real and imaginary parts of the reflectance are generally very small ( $10^{-4} - 10^{-5}$ ). We can define the reflectance change as  $\delta r = r' - r$ , where  $r = r_0 \exp(i\varphi_0)$  is the complex amplitude reflection coefficient of the sample seen by the reference beam while the complex amplitude reflection coefficient seen by the probe pulse is  $r'(\tau) = r_0(1 + \rho(\tau)) \exp[i(\varphi_0 + \Delta\varphi(\tau))]$ , where  $\tau$  is the delay time between the pump and probe pulse,  $\rho(\ll 1)$  is the change in reflectance and  $\Delta\varphi(\ll 1)$  is the change in phase induced by the pump pulse ( $\delta r/r \approx \rho(\tau) + i\Delta\varphi(\tau)$ ). With these definitions, the  $\varphi_0 = +\pi/2$  and  $-\pi/2$  outputs of the photodetector are proportional to

$$I_+ \approx E^2 r_0^2 (1 + \rho - \Delta\varphi) \quad \text{and} \quad I_- \approx E^2 r_0^2 (1 + \rho + \Delta\varphi), \quad (3.30)$$

where  $E$  is the electric field amplitude of the probe and reference beams at the input to the interferometer (they have the same intensity).  $\rho$  and  $\Delta\varphi$  can be extracted by recording the sum and the difference of these two equations. This means that the Sagnac interferometer in the  $I_+ - I_-$  configuration allows us to only measure the phase change (imaginary part) of the reflectivity which may be purely due to displacement signal.

However, as Thomsen *et al.* [TGMT86] have pointed out, the photoelastic effect changes not only the real part of the reflectivity, but also acts on the imaginary part. A general equation for the complex change of reflectivity  $\delta r/r$  can be derived by

simple extension of the method presented in reference [TGMT86],

$$\frac{\delta r(\tau)}{r} = -2ik_0\delta z + \frac{4ik_0\tilde{n}}{(1-\tilde{n}^2)} \int_0^\infty dz \left[ \frac{d\tilde{n}}{d\eta}\eta(z,\tau) + \frac{d\tilde{n}}{dT}T(z,\tau) \right] \exp(2ik_0\tilde{n}z), \quad (3.31)$$

which includes the effect of the surface displacement  $\delta z = u(0, t)$  on the phase. Here,  $\tilde{n} = n + ik$  is the complex refractive index,  $k_0 = 2\pi/\lambda$  is the light wavevector in air, and  $\eta(z, t) = \partial_z u(z, t)$  and  $T(z, t)$  are the longitudinal strain and lattice temperature distribution in the film, e.g. as defined by equations 3.2 and 3.7.

Considering the imaginary part of equation 3.31 shows that that phase change  $\Delta\varphi$  cannot be regarded to be solely due to surface displacement. However, Hurley and Wright [HW99] have carefully studied both contributions,  $\rho$  and  $\Delta\varphi$ , of a gold sample and estimated from their ratio that the contribution from the terms of the integral in equation 3.31 contribute less than 10% to the overall phase shift. This means that by far the dominant contribution of the phase shift is due to displacement and all future discussion of interferometric measurements in this thesis treats it as purely due to displacement.

### 3.3.2.3 Advantages and Disadvantages of each Interferometer

Neither of the interferometers requires active stabilization due to their common path designs. During operation, the Sagnac interferometer allows data to be recorded with a somewhat better SNR due its completely common path design. The differential detection configuration allows selective recording of the phase change  $\Delta\varphi$ , as discussed above (which is mostly sensitive to pure displacement and reduces the influence of strain induced reflectivity change to the signal). These are the main advantages of this type of interferometer. However, the Sagnac is considerably more difficult to align. In addition, a clean light polarization (the two beams that travel in opposite direction are perpendicularly polarized) is critical for its performance. This is a particularly important aspect to consider when using samples that consist of anisotropic materials, either the transducer film or the substrate that holds it.

The grating interferometer is very simple to align. However, the spatial separation of the probe and the reference beam makes it very sensitive to air currents which decrease SNR. Using this interferometer, it should be possible to map out precisely the topography (thickness profile) of a sample at the same time as the measurements of the acoustic parameters — or slightly before or after — though this has not yet been attempted. This is discussed in the future directions chapter at the end of this thesis.

## 3.4 Setup Characterization

Initial experiments were carried out on simple samples to test the experimental setups for Brillouin scattering from a transparent substrate and interferometric detection from a transducer-air interface.

### 3.4.1 Brillouin Scattering

The sample by which we characterized Brillouin scattering was an optical quality BK7 glass substrate from CVI-Melles Griot (PW-1025-C). It was coated with a 40 nm aluminum film by e-beam physical vapor deposition. An example of the induced reflectivity change is shown in Figure 3-14. The sound velocity  $c_l$  and ultrasonic attenuation rate  $\Gamma$  can be extracted from the period and rate of damping of the oscillatory part of the response. The Brillouin scattering oscillation can be described by the simple functional form

$$\Delta R(t) = A_0 \exp(-\Gamma t) \cos[2\pi f t + \phi] , \quad (3.32)$$

where  $A_0$  is an arbitrary amplitude,  $\Gamma$  the attenuation rate for an oscillatory frequency  $f$  and  $\phi$  is an arbitrary phase (which just indicates the choice of zero time). The frequency is given by

$$f = 2n(\lambda)c_l/\lambda , \quad (3.33)$$

which allows extraction of the longitudinal sound velocity  $c_l$  when the refractive index  $n(\lambda)$  of the transparent sample at the wavelength  $\lambda$  of the probe light is known. However, the procedure for extracting the desired information by fitting the functional form of equation 3.32 to the recorded data is always complicated by the presence of a smoothly varying background. This background is caused by the term  $\delta r_{trans}$  in equation 3.17 and is due to the slow cooling of the transducer film.

There are two strategies to remove this background. The first consists of taking the time derivative of the recorded reflectivity change. While this operation removes the slowly decaying background almost completely, it preserves the periodicity and rate of decay of the original signal. The disadvantage of this strategy is that numerical differentiation of experimental data always increases the noise level significantly. Therefore, this procedure is normally only used together with the subsequent Fourier transform of a selected interval of the Brillouin oscillation to get a quick and rough estimate of the oscillation frequency.

A better approach is to include terms in the functional form used in the fitting procedure that account for the decaying background. A simple exponential decay is



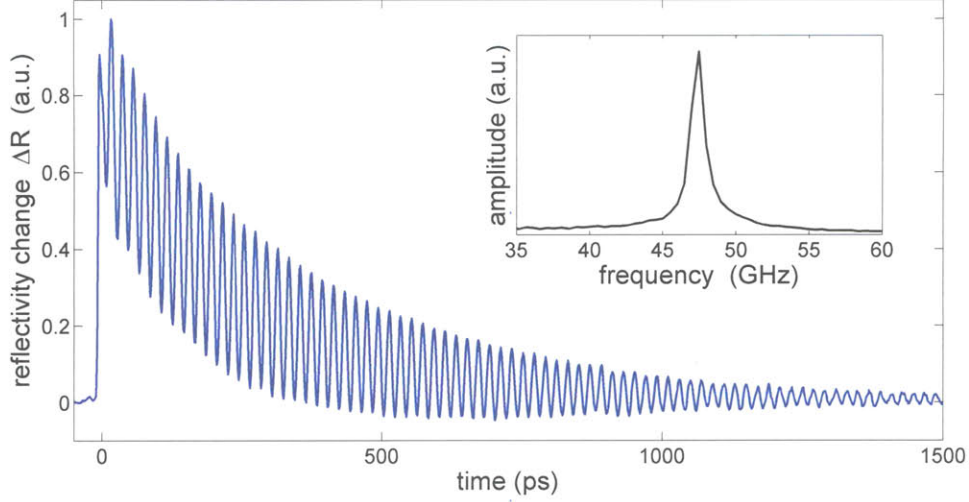


Figure 3-14: Change of the optical reflectivity  $\Delta R$  as a function of time. The strain pulse is generated in an aluminum transducer film and then propagates inside a transparent sample (here BK7 glass) as shown in Figure 3-9. The detection light wavelength is 395 nm and the inset shows the Fourier transform of the oscillation of a selected interval as described in the text.

usually good enough to fit the experimental data well. The functional form typically used for the analysis of Brillouin oscillation data is given by

$$\Delta R(t) = A_0 \exp(-\Gamma t) \cos(2\pi f t + \phi) + B_0 \exp(-t/\mu) + \delta, \quad (3.34)$$

where  $B_0$  is the initial amplitude of the temperature induced reflectivity change of the transducer film (given by  $\delta r_{trans}(t=0)$ ) that cools with a time constant  $\mu$ . Usually, an offset  $\delta$  also must be included that accounts for a signal baseline offset (an artifact of the lock-in detection). These three additional fit parameters,  $B_0$ ,  $\mu$  and  $\delta$ , decrease the accuracy of all fitted values. To reduce the errors in the two parameters of interest, the frequency  $f$  and the acoustic attenuation rate  $\Gamma$ , we usually do a first fit of the reflectivity data with functional form 3.34 in which we allow all parameters to vary. Once this is done, we repeat the fit with the same functional form but only allow the frequency  $f$  and the acoustic attenuation  $\Gamma$  to vary. All other parameters are kept constant at the values determined by the first fit.

### 3.4.2 Interferometric Detection

To test the quality of our interferometric detection setup and also to illustrate the optical pulse shaper, we study the response of the transducer-air interface of a 20 nm

aluminum film on a sapphire substrate. The film is always excited at the sapphire-aluminum interface.

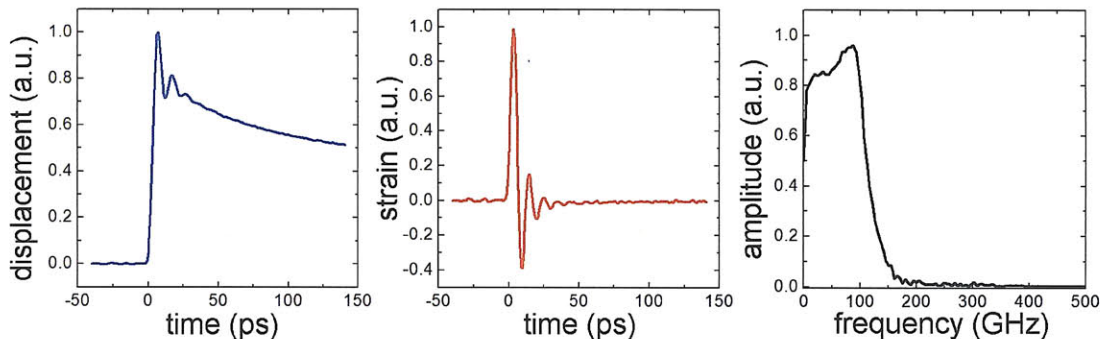


Figure 3-15: Single Pulse Excitation: Displacement (left) and corresponding strain (middle) of a 20 nm aluminum film on a sapphire substrate. The opto-acoustic conversion takes place at the interface between aluminum and sapphire, and the displacement is detected interferometrically on the opposite side, at the film-air interface. Because of the higher acoustic impedance of sapphire, the part of the acoustic wave propagating into the sapphire is reflected with no inversion. Fourier transform of the strain (right).

### 3.4.2.1 Single Pulse Excitation

In Figure 3-12 we saw the recorded signal of the Sagnac interferometer for a long time interval where an acoustic pulse was excited by a single optical excitation pulse. The signal shows two main features: a sudden increase at  $t = 0$  ps followed by a sudden decrease at  $t = 1500$  ps. The second feature is the result of the time delay getting long enough for the ‘short’ arm to overlap with the signal. From this time delay on, both the ‘short’ and ‘long’ arm overlap with the signal and the recorded signal is a convolution of both. This is an unwanted effect and limits the useful time window of the Sagnac interferometer in our configuration to 1500 ps. Figure 3-15 shows the section of interest of Figure 3-12, namely the first displacement and several echoes measured by the interferometer’s ‘long’ arm. The strain pulse  $\eta(t)$  is calculated from the measured displacement  $u(t)$  by

$$\eta(z, t) = \frac{1}{c_l} \frac{\partial u(z, t)}{\partial t}, \quad (3.35)$$

where  $c_l$  is the longitudinal sound velocity.

One can distinguish at least three full oscillations, which can be used to determine the film thickness. The period of one oscillation is measured to be  $\tau_{rt} = 12.2$  ps and corresponds to two round trips of the acoustic strain pulse in the film. The acoustic

reflection coefficient of the film-air interface is -1, which causes the acoustic strain pulse to change sign upon reflection. Therefore, the acoustic strain pulse needs two round trips to give one full cycle of the interface displacement. This is indicated by the second factor of 2 in the equation for the film thickness given by

$$d_{al} = \frac{c_{Al} \cdot \tau_{rt}}{2 \cdot 2} \approx 19.5 \text{ nm} , \quad (3.36)$$

where the value for the longitudinal sound velocity in aluminum is  $c_{Al} = 6.4 \text{ nm ps}^{-1}$  (for references see Appendix A).

### 3.4.2.2 Multiple Pulse Excitation

A last test of the setup was performed using all seven pulses of the Deathstar pulse shaper with the frequency set to 200 GHz and 38 GHz.

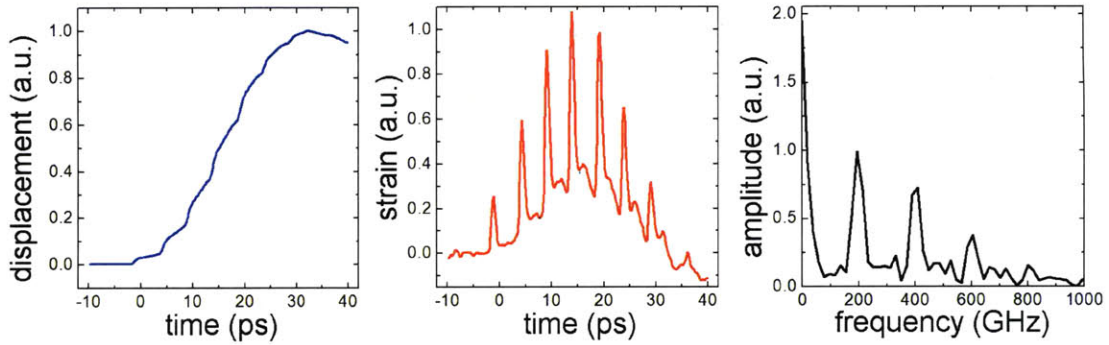


Figure 3-16: Multiple Pulse Excitation: Displacement (left) of the air interface of a 20 nm aluminum film resulting from shaped excitation at 200 GHz, together with corresponding acoustic strain (middle) and the frequency spectrum (right)

The strain in Figure 3-16 clearly shows the overall Gaussian profile of the seven pulses. The individual acoustic pulses are broader ( $\sim 3 \text{ ps}$ ) than the width of the input light pulses of the Deathstar output (Figure 3-8,  $\sim 300 \text{ fs}$ ) due to the excitation process described above. For excitation at 38 GHz in Figure 3-17, the round trip time of the echoes overlaps with the arrival of the next pulse and so the film is driven resonantly. The additional modulation of the strain subsequent to the last excitation pulse arrival is an indication that the acoustic echoes experienced constructive interference due to their temporal overlap.

A last notable feature is the steady increase in the displacement in both figures. This is due to the almost unipolar temporal profile of the acoustic strain pulse and a result of the higher acoustic impedance of the sapphire substrate at which the pulse is generated.



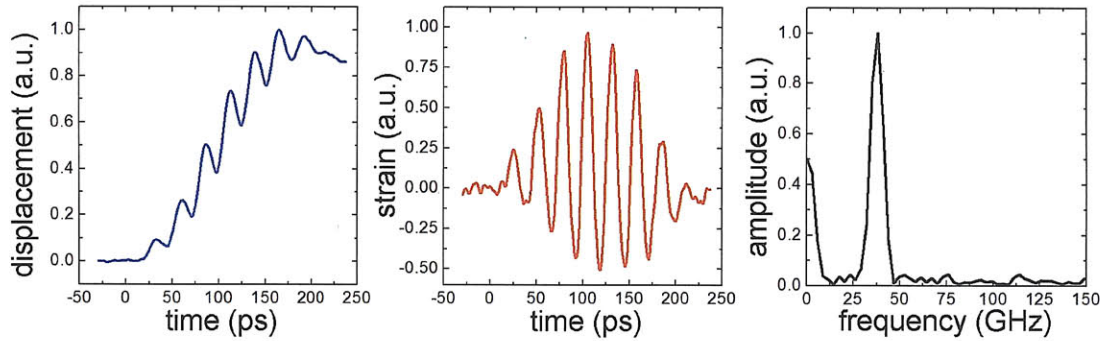


Figure 3-17: Multiple Pulse Excitation: Displacement (left) of the air interface of a 20 nm aluminum film resulting from shaped excitation at 38 GHz, together with corresponding acoustic strain (middle) and the frequency spectrum (right).

## 3.5 Temperature Dependent Measurements

Some of the experiments presented in Chapters 5 and 6 have been performed in air while other experiments have been performed in an optical cryostat in order to gain access to a wider range of temperatures. Either a cold finger or sample-in-vapor cryostat was used for these experiments:

### 3.5.0.3 Sample-in-Vapor Cryostat

The sample-in-vapor cryostat used here (Janis Co., Inc., STVP-100) is depicted in Figure 3-18. In this type of cryostat the sample is in a gas environment at atmospheric or slightly greater pressure. The sample jig is attached with several screws to a thermally insulated holder construction coming down from the top and is not in thermal contact with any other part of the cryostat. A temperature sensor, called ‘sensor B,’ is attached directly to the sample jig. Cold nitrogen gas is injected into the sample chamber through a valve at the top; it falls down and floats around the sample. A heater block containing a resistive heater with a feedback temperature sensor, called ‘sensor A,’ is located at the bottom of the sample chamber and controls the gas temperature. An exhaust opening at the top of the sample chamber allows warmed up nitrogen gas to flow out of the chamber. Good thermal insulation of the cold sample chamber with respect to the ambient is ensured by a vacuum jacket. One inch diameter optical windows at the four sides of the cryostat allow access to the sample at a 90 degree or 180 degree pump-probe geometry.

Advantages of the sample-in-vapor cryostat include:

- High mechanical stability of the sample. The cryostat is very heavy and can be mounted very rigidly.

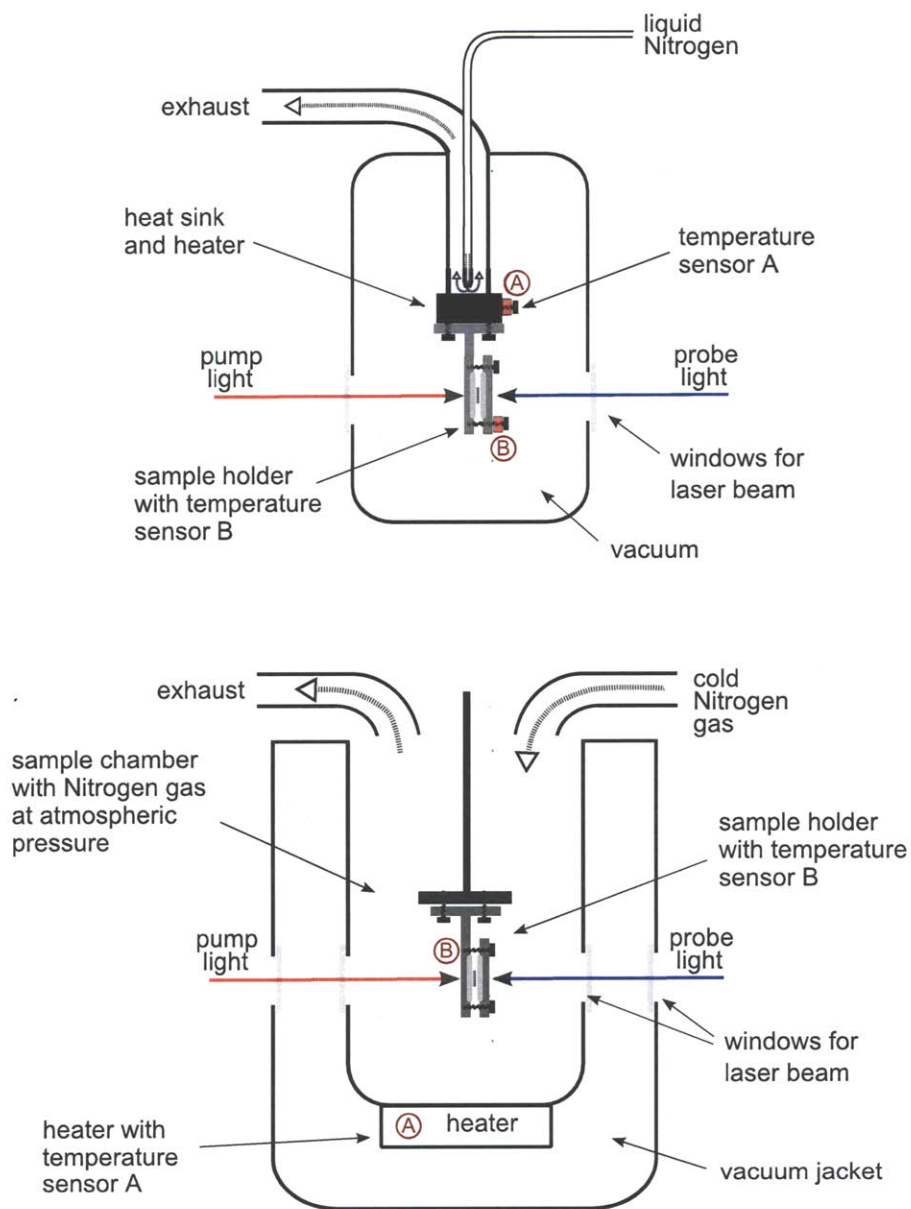


Figure 3-18: Sketch of cold finger cryostat (Janis Co., Inc., ST-100(500K)) (top) and sample-in-vapor cryostat (Janis Co., Inc., STVP-100) (bottom). The main difference between the cryostats is that in the case of the cold finger cryostat, the sample itself is in a vacuum chamber and heat transfer happens through conductive transport to or from the heat sink. Good thermal transfer properties of the sample holder and a sample suitable for vacuum are essential requirements. In the case of a sample-in-vapor cryostat, the sample is floating in a nitrogen gas environment at about atmospheric pressure and a vacuum jacket ensures good thermal insulation from the surroundings. The two mentioned requirements for a cold finger cryostat are of minor importance for a sample in vapor cryostat; however, flowing nitrogen gas might reduce the stability of optical experiments, and the size of the cryostat makes it more difficult to work with.

- The sample is at atmospheric pressure. This is particularly important for volatile liquid samples like water because the sample cell is not closed.
- Even if there is some evaporation of the liquid, the constant gas flow removes most of the liquid vapor before it can condense on the cryostat windows and require cleaning.

Disadvantages of the sample-in-vapor cryostat:

- The cryostat is very big and therefore difficult to handle.
- The optical windows are quite small, which make the initial setup of the sample difficult. Measurements in which the sample has to be translated a large distance or measurements at oblique incidence are particularly difficult.
- The flowing/floating gas creates turbulence which causes distortion of the laser beams and thereby decreases the optical stability. This is especially problematic for interferometric detection.
- This type of cryostat has long temperature equilibration times (1 hour or longer) because of the solely convective heat transport.
- Our model of the sample-in-vapor cryostat is limited to temperatures below room temperature.

#### 3.5.0.4 Cold Finger Cryostat

In our cold finger cryostat (Janis Co., Inc., ST-100-500K), the sample holder is attached to the end of the cold finger which is cooled by liquid nitrogen as shown in the top sketch of Figure 3-18. The temperature of the copper heat sink block is controlled by a feedback loop consisting of temperature sensor A and a 50 W resistive heater. The whole sample chamber is evacuated to a high vacuum of  $10^{-5}$  to  $10^{-7}$  Pascal to ensure thermal insulation from the environment. To ensure good thermal contact of the sample holder with the heat sink, Indium foil <sup>†</sup> is used and temperature sensor B monitors the temperature of the sample holder.

Advantages of the cold finger cryostat:

- Small size, easy to handle.
- Large chamber windows and therefore easy access to large areas of the sample at a wide range of angles.

---

<sup>†</sup>LakeShore Cryotronics, Inc., Indium foil IF-5 (2"×2"×0.005")

- No turbulence due to gas as is the case for the sample-in-vapor cryostat; therefore higher optical stability.
- Usually fast temperature equilibration time; this strongly depends on the thermal conductivity of the different substrates the sample consists of.
- The ST-100 (500 K) cold finger cryostat has a temperature range from 4 K up to 500 K.

Disadvantages of the cold finger cryostat:

- Poor mechanical stability due to slim design.
- Sample chamber has to be evacuated for thermal insulation. Our open sample cell design often results in fast evaporation of the liquid and condensation of that vapor on the inside of the cryostat windows making them cloudy and requiring the cryostat to be dismantled and cleaned.

### 3.5.0.5 Cryogenic measurements

Each cryostat has its pros and cons and the more suitable one was chosen for each experiment. For example, when a temperature range up to 400 K was studied, the cold finger cryostat was used. For the experiments on water, the sample-in-vapor cryostat was the better choice. With both cryostats, the same sample jig which was used will be discussed in the next chapter. Temperature sensor B was always directly attached to a point on the sample holder furthest away from the heat sink, as shown in Figure 4-3. A Lakeshore temperature controller was used to control the heater feedback loop and to monitor the temperature of the sample and the heater. The temperature stability was usually better than 0.2K and the accuracy of the temperature at the sample region of the measurement was estimated to be known within 2K.





# CHAPTER 4

---

## Liquid Sample Cell

---

Special sample preparations are required for the study of mechanical relaxation processes in supercooled liquid samples at gigahertz frequencies. Acoustic waves with frequencies in the tens to hundreds of gigahertz have corresponding wavelengths that are on the order of a couple hundreds nanometer down to ten nanometers. These acoustic waves have typical sound velocities of 1000 to 3000 m s<sup>-1</sup> in supercooled liquid samples. At temperatures much higher than the glass transition temperature, typical mean free paths of the gigahertz acoustic waves in the liquids are only a few wavelengths. However, close to and below the glass transition temperature, the mean free paths increase drastically. Consequently, in order to study liquid mechanical properties via transmission measurements, samples with liquid thicknesses ranging from a few nanometers up to several microns are necessary. In order to access the wide range (4 orders of magnitude) of sample thicknesses required for these measurements, novel and versatile liquid cells have been developed. The liquid cell design used for these experiments is discussed and characterized in detail in this chapter.

### 4.1 Liquid Cell Design

Three general liquid samples structures have been developed for the work presented in this thesis. Schematics of these structures—labeled as (I), (II) and (III)—are illustrated in Figure 4-1. The first sample configuration (I) is used for interferometric detection analogous to conventional picosecond ultrasonic measurements, the details of which are provided in Chapter 3. Two thin metal films act as an acoustic transducer and receiver with the liquid sample sandwiched between them. The frequency content of acoustic wavepackets is determined not only by the optical pulse excitation sequence, but also by the transducer film (i.e. film thickness and hot electron

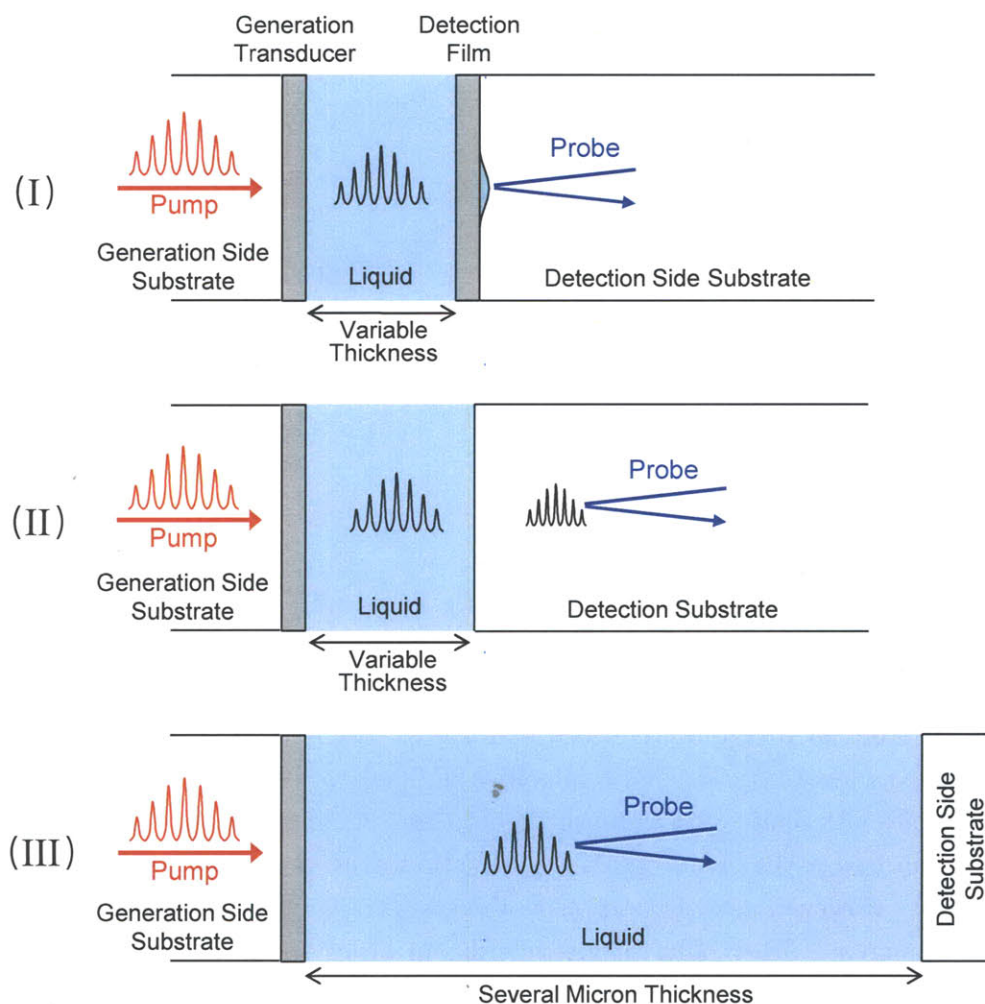


Figure 4-1: The three different experimental geometries for liquid samples used in all the experiments of this thesis. Liquid thicknesses ranging from a few nanometers to several hundreds of nanometers (or even microns when the damping is very low) are necessary for the measurement of liquid relaxation dynamics. In sample configuration (I), a liquid sample is sandwiched between two metal thin films: an acoustic generation transducer thin film on a generation side substrate and receiver thin film on a detection side substrate. This configuration is used for interferometric measurements similar to conventional transmission ultrasonics. Configuration (II) is similar to (I), but consists of only one metal generation transducer thin film. The propagation of the acoustic wave is monitored by time-domain Brillouin scattering after transmission into a transparent detection substrate placed after the liquid sample. In the third configuration (III), the propagating acoustic wave is monitored by time-domain Brillouin scattering directly in the liquid. This imposes a limit on the sample liquid thicknesses to be at least several microns. The detection side substrate in this case is solely for holding the liquid sample in place.

diffusion) as has been discussed in the previous chapter. The acoustic waveform generated by the transducer propagates into and through the adjacent liquid sample layer before entering the second metallic thin film. After traversing this film, the strain wavepacket causes a displacement of the metal film along the acoustic propagation direction, which can be detected interferometrically. The frequency dependent acoustic speed and attenuation rate are obtained by comparing Fourier spectra of acoustic waves that have been transmitted through different liquid thicknesses. The first configuration (I) is the most versatile in terms of acoustic frequencies that can be accessed and therefore permits the determination of mechanical parameters of liquid samples over a large range of frequencies from a few gigahertz up to several hundred gigahertz and into the terahertz regime. However, many parameters must be chosen carefully to tune the bandwidth of a given sample, which in turn limits the frequency range of that sample. In principle, this sample configuration permits measurements of both longitudinal and shear relaxation. However, ongoing experimental work is underway to realize measurements of shear relaxation in this manner.

The second configuration (II) is similar to the first one except that it features only a single metal generation transducer thin film. After an acoustic wavepacket has traversed a liquid sample it is partially transmitted into an optically transparent detection substrate. Brillouin scattering is then used to monitor the propagation and attenuation of a given acoustic frequency component (as determined by Equation 3.27). The analysis of the oscillatory phase and amplitude of the Brillouin scattering of the propagating acoustic wave in the transparent detection substrate allows extraction of the desired information about the liquid by comparing liquid samples with different liquid thicknesses. Chapter 6 further describes the essential role of sample configuration (II) in the measurement of shear waves.

The simplest and most robust sample cell geometry is the third configuration illustrated in Figure 4-1 (III). The desired acoustic wavepacket is generated in the transducer film and propagates through a sufficiently thick layer of liquid, where it is monitored by time-domain Brillouin scattering. If the temperature and wavelength dependent refractive index of the liquid are known, the acoustic speed  $c_l$  and attenuation  $\Gamma$  of the liquid at a given frequency can be directly extracted by fitting the recorded data with the functional form of Equation 3.32. In contrast to configuration (II) where the Brillouin scattering parameters of the detection substrate (speed of sound and refractive index) determine the frequency of the measured acoustic wave, only the pertinent parameters of the sample liquid (speed of sound and refractive index of the liquid at the experimental conditions) are relevant. The typically low refractive indices and speeds of sound in liquids limit the accessible frequencies in the same way as for spontaneous frequency domain Brillouin scattering [CFMR02].

However, the current strategy for analyzing the data obtained from the first two configurations (described in detail in Chapters 5 and 6) require, as an input parameter, the longitudinal speed of sound in the liquid to determine the liquid layer thickness. The third approach is often the only way to independently obtain the thickness of a sample liquid.

In the following two sections we discuss specific measurements of substrates, transducer and receiver thin films and the design of the sample cell holder, and the approach to access a large range of liquid thicknesses within a single sample.

## 4.2 Substrates and Transducer Films

Not only is a judicious choice of materials for the transducer and receiver thin films and the substrates important but their combination is crucial to:

- optimize the generation efficiency and bandwidth of the generation transducer film, and
- maximize the acoustic transmission of the generated acoustic wavepacket i) into the liquid and ii) into a detection thin film or a detection substrate.

### 4.2.0.6 Considerations for Substrate-Generation Transducer Assembly

The bandwidth of the generated acoustic wave is influenced by the acoustic impedance mismatch (expressed by the acoustic reflectivity) between the substrate material and the transducer film material as discussed in Section 3.2. The acoustic reflection coefficient  $r_{\text{substrate-film}}$  of the generation interface is given by Equation 3.9.

A small mismatch, as in case of glass-aluminum ( $r_{\text{glass-Al}} \approx -0.14$ ), maximizes the bandwidth of the pulse since the expansive portion of the strain is largely transmitted into the substrate. However, this also means that half of the acoustic energy is lost directly to the generation side substrate. One option to circumvent the substantial acoustic energy loss is to use a very stiff substrate, e.g. sapphire ( $r_{\text{sapphire-Al}} \approx 0.45$ ), where about half of the outwards propagating portion of the acoustic strain pulse is reflected without inversion at the interface between the transducer film and the stiff substrate. Consequently, the resulting strain pulse is purely compressional. In addition, since the reflection coefficient is positive but smaller than unity, the generated acoustic pulse is unipolar and asymmetrical. As a result of this, the bandwidth of the strain pulse is lower than in the case of a small mismatch. On the other hand, a totally symmetric and bi-polar pulse can be generated at an air-aluminum interface with a reflection coefficient of  $r_{\text{air-Al}} = 1$ , as shown in the strain pulses generated by irradiation of a 100 nm aluminum film and different boundary conditions

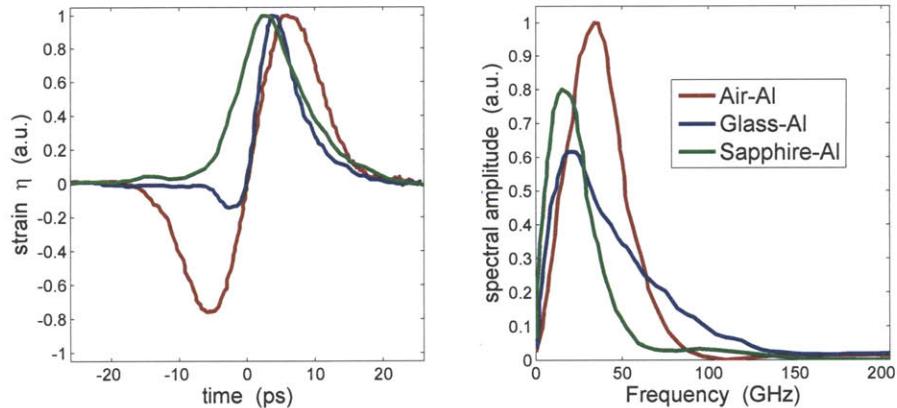


Figure 4-2: Longitudinal strain profiles and their corresponding Fourier spectra as generated by a single optical pulse in 100 nm aluminum at three different interfaces. In the case of the glass-aluminum and sapphire-aluminum traces, the strain was detected interferometrically at the air interface after a single traversal of the aluminum film. In the case of the air-aluminum trace, (which was only added for comparison since it could not be used in our sample geometry) the strain was detected interferometrically when it returned to the air interface after a full round trip in the aluminum film and reflection at the sapphire-transducer interface.

together with their corresponding Fourier spectra depicted in Figure 4-2. In these examples, the film thickness is significantly larger than the optical penetration depth  $\zeta_{\text{Al}}(790 \text{ nm}) \approx 7.5 \text{ nm}$  and also the electron diffusion length  $D \approx 24 \text{ nm}$  [Sla02] so that the film can be considered semi-infinite for the generation process. In order to generate acoustic wave packets with higher bandwidth, the film thickness must be decreased below these values [MTZM96].

Aluminum is the material of choice among all other transducer film materials considered for the longitudinal acoustic wave study of liquids up to about 150 GHz. The short optical penetration depths and electron diffusion length in aluminum enables the generation of acoustic pulses with significant bandwidth even in thick films (larger than its optical penetration depths and electron diffusion length). The low density of aluminum ( $\rho = 2.7 \text{ g cm}^{-3}$ ) leads to its fairly low acoustic impedance ( $Z \approx 17 \cdot 10^6 \text{ kg m}^{-2} \text{ s}^{-1}$ ) which is comparable to the impedance of liquids. As a result of this low impedance, not only the acoustic echoes in the transducer film are minimized but the acoustic transmission from the film into the liquid is also maximized. Similar considerations apply to shear wave generation which in addition requires a specific, anisotropic transducer film with broken transverse thermoelastic symmetry which will be described in detail in Chapter 6.1. For a list of acoustic

and optical parameters for many common transducer materials and substrates see Tables A.2 and A.1.

#### 4.2.0.7 Considerations for Detection-Substrate and Receiver Film

The sample geometries shown in (I) and (II) of Figure 4-1 require either a receiver transducer or a detection substrate for the detection of acoustic strain pulses transmitted through sample liquid of different layer thicknesses. Similar to what we discussed above regarding the generation transducer, the most important factor in optimizing the measurement is to maximize the acoustic transmission into the receiver film or the detection substrate. In other words, the transmission coefficient  $t_{12}$  as defined by Equation 3.10 should be maximized. In the case of experimental configuration (I) with a receiver thin film, the film should have a thickness such that the optical penetration depth of the probe light at the probe wavelength into the transducer film is small (usually  $\lambda = 395$  nm for interferometric detection). Aluminum is an excellent choice due to its small optical penetration depth at the probe wave length ( $\zeta_{Al}(395 \text{ nm}) \approx 7$  nm), though for some experiments, chromium ( $\zeta_{Cr}(395 \text{ nm}) \approx 9$  nm) was used because of its lower surface roughness. In the case of experimental configuration (II) with a detection substrate, in order to study the acoustic attenuation and speed at different frequencies of the sample, detection substrate materials with different Brillouin scattering parameters must be used. Because of this, from Equation 3.27, the Brillouin frequency is determined by the speed of sound  $c_l$  or  $c_s$ , the probe optical wavelength  $\lambda$  and the refractive index  $n(\lambda)$  of the material in which the acoustic wave propagates. In order to study the acoustic attenuation and speed at different frequencies, detection materials with different parameters are necessary, e.g. BK7 has a longitudinal Brillouin frequency of 47 GHz for a probe wavelength of 395 nm and normal incidence, while sapphire has about 100 GHz.

#### 4.2.0.8 Thin Film Fabrication

Most metal thin films were fabricated at the Research Laboratory of Electronics at MIT by fellow graduate student Kara Manke. Optical substrates were usually bought from CVI Melles Griot and Edmund Optics and cleaned in a piranha solution ( $\text{H}_2\text{SO}_4/\text{H}_2\text{O}_2$  mixture) before deposition. Various transducer films were deposited by electron beam physical vapor deposition or sputtering. Materials used include aluminum, gold, silver, chromium and amorphous silicon, all with wide range of thicknesses.

Specially prepared transducer films are required for shear wave generation due to symmetry considerations. Monocrystalline columnar layers of iron and cobalt were

obliquely grown by molecular beam epitaxy (MBE) at very small rates of condensation. This fabrication was done at the Laboratoire de Physique des Matériaux of the Université Henri Poincaré in Vandoeuvre, France by professor Stéphane Andrieu.

Profilometry of the films was used for precise thickness determination and atomic force microscopy was used for surface characterization. Aluminum films typically yielded a root mean square surface roughness of 5 nm while MBE iron thin films and chromium films usually ranged around 3 nm.

## 4.3 Sample Design and Sample Construction

As described in the previous section, it is necessary for sample cell configurations (I) and (II) to allow access to a wide range of liquid thicknesses, from single nanometer to several microns. In order to do this, a jig was designed and fabricated to hold two substrates in place to sandwich the sample liquid between them. In addition, the orientation of the two substrates with respect to each other needs to be adjustable in order to tune the thickness of the sample layer.

### 4.3.1 Sample Holder Design

A schematic of the sample holder jig constructed to achieve versatility of liquid sample thicknesses is sketched in Figure 4-3. A copper base part and a copper top part each has notches that allow 1" generation side (supporting the transducer film) and detection side (supporting the receiver film or serving as the detection medium) substrates to form a snug fit with the copper parts. Set screws in each copper part allow the substrates to be held firmly. Once a few drops of sample liquid are placed on one of the substrates, the other substrate is pulled over and subsequently secured using six screws. These screws not only hold the structure together but also allow adjustment of the two substrates orientation with respect to each other, such that the sample liquid thickness can be controlled. Once the jig is assembled, it is attached to the heat sink of a cryostat with indium foil in between to ensure good thermal contact.

### 4.3.2 Access to Wide Range of Liquid Thicknesses

Two flat substrates were used to form a liquid cell in an earlier attempt by R. Slayton [Sla02, SN04] to apply broadband picosecond ultrasonics to measure acoustic properties of liquids. However, liquid layers of glycerol thinner than 1  $\mu\text{m}$  were shown to be difficult to obtain and the acoustic frequencies studied were limited to below 20 GHz with poor SNR. A problem arises due to the increasing difficulty of a viscous liquid to flow outwards when two flat substrates are brought close together. Applying more



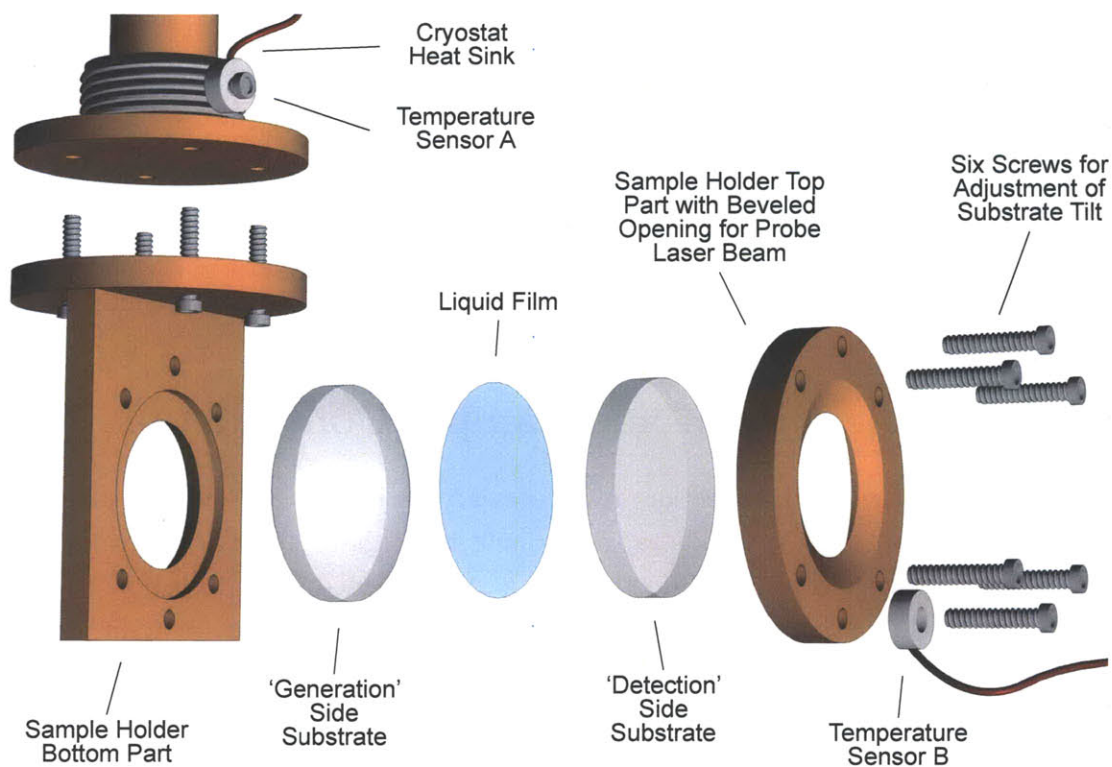


Figure 4-3: An illustration of the sample holder used to obtain liquid samples of different thicknesses. A copper jig was designed to hold two substrates in place with the sample liquid sandwiched in between. The whole construction is attached to a heat sink of a cryostat and a temperature sensor is placed on the jig to monitor sample temperature.

pressure with the jig causes even thick substrates (up to 1 cm thick) to bend slightly. The way the sample holder in the initial studies was constructed results in pressure being applied only in a ring pattern along the edges of the substrates. At some point, the two substrates touch in a similar ring pattern along the outside, trapping the liquid in the center and making it unable to flow out. A trick to achieve somewhat thinner liquid layers by this method is to heat up the liquid and hereby decrease its viscosity.

T. Hecksher [Hec06] fabricated sub-micron liquid layers by replacing one of the flat substrates with a plano-convex sapphire lens with radius of curvature  $R = 700$  mm, which is a slightly curved surface. This allowed her to study silicon oil (DC704) layers of 200-300 nm. However, the highest frequencies she was able to access were still only about 20 GHz. This limitation was due to the incompatibility between the curved surface and the pulse-echo analysis experimental approach. In a curved substrate sample cell design the two substrates will directly contact one another. In



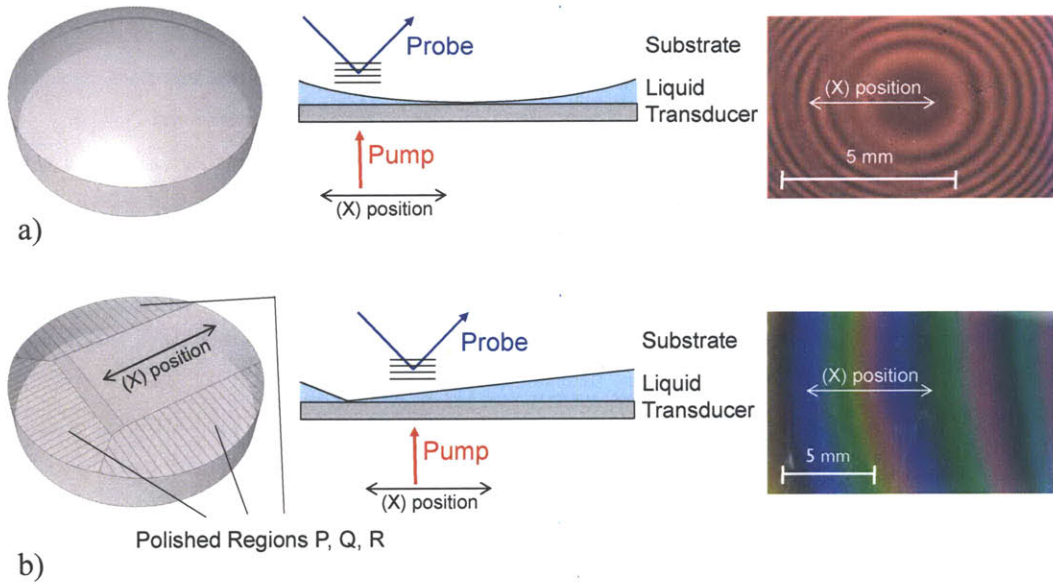


Figure 4-4: (a) Sketch of curved slope sample design, referred to as ‘flat-curved’ sample design, and usually constructed with a plano-convex lens with a radius of curvature of 2.5 m. (b) Linear slope sample design, referred to by ‘flat-polished’ sample design, and built with a specially prepared flat substrate (three areas polished, P, Q, and R, see Figure 4-6). Their respective images show Newton’s interference rings/fringes (photograph of (a) taken with 800 nm light and (b) with white light). Measurements are made at several lateral (X) positions on the sample, corresponding to different liquid layer thicknesses.

order to access liquid layers of a few hundred nanometers the experiment has to be conducted a certain distance away from the contact region. At that position, the two substrates could no longer be considered parallel and the liquid layer thickness varied significantly over the probe spot size diameter which resulted in the artificial broadening of the interferometrically detected strain pulse. In addition, the acoustic reflection occurs at an angle such that a tilted acoustic wave front of the echo results. This causes further broadening of the detected signal. This problem is more fully explained in Chapter 5.

In order to bridge the hitherto inaccessible frequency gap at high gigahertz acoustic frequencies for mechanical spectroscopy, we use a pulse-echo approach to measure the interaction of the acoustic wave with the liquid and compare different liquid thicknesses with each other. Measurements are therefore made at several lateral (X) positions on the same sample, which correspond to different liquid layer thicknesses. The advantages and disadvantages of this approach are discussed below.

First, a lens with the largest radius of curvature commercially available,  $R = 2500$  or  $5000$  mm, is used for experiments for which very thin liquid layers up to several tens of nanometer are sufficient. It is found that even with large curvatures of several meter, just a very small pressure is sufficient to cause the substrates to contact each other. An example of a flat-curved substrate sample cell design is shown in illustration (a) of Figure 4-4. The right image shows the interference fringes of light, called Newton's rings, between the flat and the curved substrate as a function of increasing liquid thickness.

In the second approach to construct thin liquid layers, we started with a flat substrate and polished three regions of one face (to the top, bottom and to the right in order to leave a rectangular untreated area) at an angle of a couple of degrees as shown in the left sketch of Figure 4-4 b). With some intuition and patience, it is possible to build a liquid sample cell having a liquid thickness increase of just a couple of tens of nanometers per millimeter by adjusting the orientation of this polished substrate with respect to the flat. By polishing off an additional 1-2 mm stripe of glass at a very small angle (indicated to the left side of the non-polished area in the lower left hand sketch of Figure 4-4 b), it is possible to gain access to liquid layers that are several microns thick within the same sample. In the areas with this thick liquid layer, Brillouin oscillations in the liquid can be directly measured as illustrated in configuration (III) of Figure 4-1, while the area with the smoothly increasing liquid thicknesses (from zero to several hundreds or thousands of nanometers) can be used for measurements with configurations (I) and (II).

It should be noted that sample configurations with the combination of a flat substrate and a curved substrate are much easier to build. They are thus very useful for the study of liquids in the high temperature regime where the mean free path of the acoustic wave in the liquids is generally small and very thin liquid layers are needed. However, as the frequency under investigation decreases (the acoustic wave length increases) and/or the acoustic mean free path increases (e.g., the attenuation gets smaller at lower temperature and lower frequency), a thicker liquid layer is needed for measurable damping to occur, and the local tilt of the acoustic wave over the curved substrate across the experimental detection cross-section (probe spot size diameter) may become problematic. Interferometric measurement (Figure 4-1 a) of a multiple-cycle acoustic wave after it has passed through the liquid layer should reveal time-dependent oscillations at the acoustic frequency, but these will be washed out if different regions of the probe spot encounter the acoustic wave at significantly different parts of the acoustic cycle, i.e. at significantly different acoustic phases. If a single-cycle, broadband acoustic pulse is used, its higher-frequency components will be suppressed by phase variation across the probe spot. Using a curved substrate,

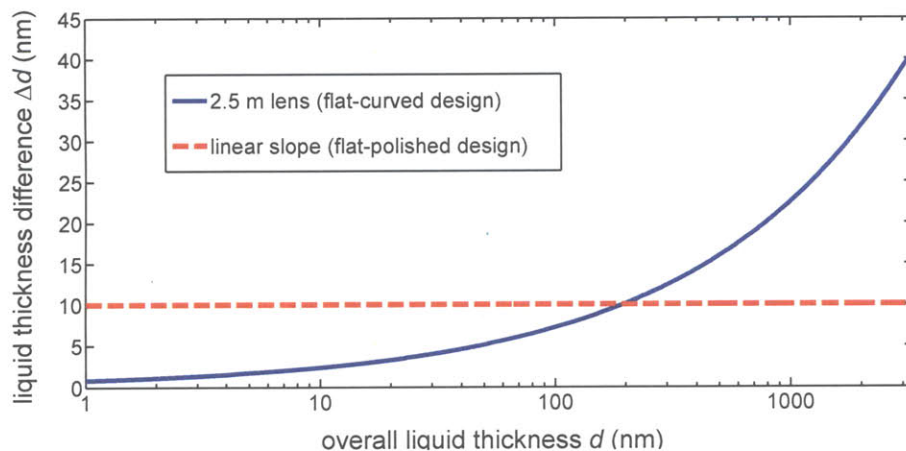


Figure 4-5: Variation of the thickness of the liquid layer over a typical laser probe spot size of  $25\ \mu\text{m}$  for i) a linear-slope sample and ii) a sample constructed using a substrate having a radius of curvature of 2.5 m. The liquid thickness difference  $\Delta d_{\text{linear}}$  remains constant across different liquid thickness  $d$  in the linear-slope case. On the other hand,  $\Delta d_{\text{curved}}$  is very small for thin liquid thickness areas in the curved substrate case, but rapidly increases with increasing liquid thickness. Thus, a curved substrate sample design is the structure of choice for liquids with high acoustic attenuation (e.g. measurements at high temperatures), while a linear slope sample should be used when the acoustic attenuation is weak and thicker layers are needed (e.g. near or below the glass transition temperature).

these effects increase as the liquid layer thickness increases, leading to overestimates of the attenuation rates determined through compared measurements at different thicknesses. If Brillouin scattering from a curved substrate is measured, then the refraction angle of the acoustic wave as it passes from liquid to substrate changes with liquid layer thickness, leading to changes in the Brillouin scattering signal intensity at the scattering angle that has been selected (and that is not changed as different liquid layer thicknesses are examined). This too introduces systematic error in the deduced attenuation rates. The sample cell design with the substrate polished on three sides was developed in order to overcome the problems for thick liquid layers.

## 4.4 Sample Preparation and Handling

It is common practice to vacuum distill the glass-forming liquids under study in conventional Brillouin scattering or dielectric spectroscopy directly into a dust-free cell before sealing the liquid under vacuum. Such an approach is incompatible with the open sample cell design detailed here. As a result, the following procedures were adopted. In most of our measurements, the liquid was heated under vacuum to



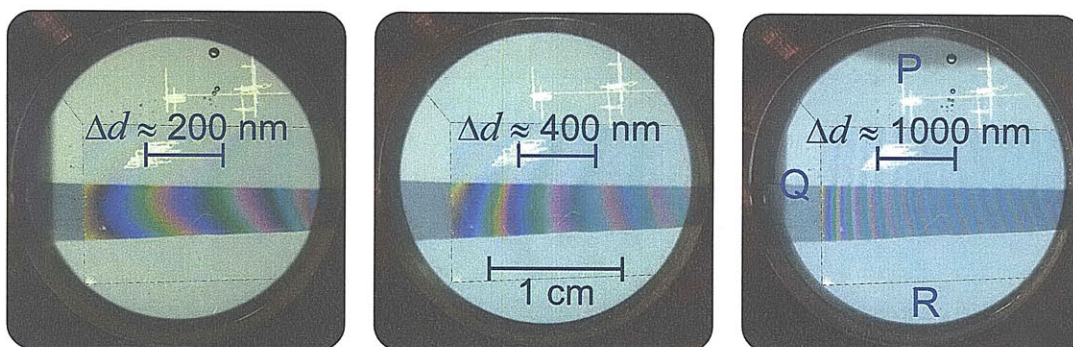


Figure 4-6: Photographs of three different linear slope samples. The liquid thickness increase is extremely small, ranging from about 300-1500 nanometers per centimeter. The liquid thickness can be easily adjusted as described in the text. Three polished regions marked P, Q, and R (between the lines and the edges of the circle) are visible in each sample. The samples were constructed with two substrates, both of which were partially coated by a thin aluminum film to increase the reflectivity so that the bright Newton interference fringes are visible. Note that the overlapping area of the coatings and therefore the intense Newton fringes only make up a strip in the center of the unpolished area.

allow volatile impurities to evaporate. For glycerol, the drying agent  $\text{MgSO}_4$  was also added. The removal of impurities such as alcohols, phenols and water is important to prevent any phase separation of the impurities from the liquid under study. These impurities may also trigger crystallization of the liquid sample. Upon removal of the impurities, the purified sample was then outgassed after which the liquid was forced through several linked  $0.2 \mu\text{m}$  teflon millipore filters to remove dust particles while the liquid was still hot and its viscosity was relatively low. It is important to remove dust particles because any particle present in the liquid may serve not only as a crystallization seed but also as a spacer, rendering the construction of very thin samples impossible.

Both liquids under study, glycerol and silicon oil (DC704), are extremely hydroscopic and can absorb up to tens of percent of water. In addition, their viscosity and other mechanical properties are very dependent upon the water content, e.g. addition of 1% water to pure glycerol reduces its viscosity by almost 20% [HL59]. Therefore, in order to prevent the outgassed liquid from further contamination by water, samples were usually constructed under  $\text{N}_2$  atmosphere using the following methods. First, both substrate surfaces used to build the sample were purged with dry nitrogen for up to half an hour to remove dust particles and any water molecules that may still have been adsorbed on the surfaces. This is particularly important for sample designs in which the liquid surface-to-volume ratio is large. The liquid, stored under dry nitro-

gen atmosphere at all times, was subsequently forced through a teflon millipore filter before a drop of the filtered liquid was deposited on one of the substrate surfaces. The second substrate was quickly placed on top of the drop(s) to seal the liquid. The assembly was then secured to the top copper part of the sample holder using several screws as indicated in Figure 4-3. The screws also allowed the adjustment of the tilt of one substrate relative to the other substrate. With patience, it was possible to center the contact area of a sample in the flat-curved substrate design or to adjust the tilt of a sample in the flat-polished substrate design such that increases in the liquid thickness were kept very small. Examples of sample cells with the flat-polished substrate design are shown in Figure 4-6.

## 4.5 Sample Heating

### 4.5.1 Steady State Heating

Due to the complex construction of our liquid sample cells, it is not possible for a temperature sensor to be placed directly in or next to the measurement volume of the liquid sample. This section describes the experiment conceived to determine and calibrate the temperature in the volume of the liquid sample where the measurement is conducted, a cylinder of about 100  $\mu\text{m}$  diameter with a thickness of some tenths of one nanometer up to several micrometers. Instead of placing the temperature sensor directly in the measurement volume, the temperature sensor **B** is placed about 1 to 2 cm away from the experimental volume, separated by the transducer films, optical substrates and copper sample holder as depicted in Figure 4-3.

The temperature calibration measurement takes advantage of the fact that the velocity of the acoustic waves in a liquid is strongly temperature dependent. Therefore, the speed of the acoustic wave can be used as a very sensitive probe to determine the temperature in the experimental region of the liquid. The measurement data shown in Figure 4-7 are obtained from a sample structure as sketched in configuration (III) of Figure 4-1. The sample structure consists of a flat generation side substrate with an acousto-optic transducer film, several microns of glycerol, and a flat detection side substrate. Figure 4-7 shows the time-dependent reflectivity change at several different pump powers of such a sample structure having glass as the generation side substrate and 80 nm of aluminum as the transducer film. The sample mount was held at a constant temperature of 230 K for all the scans of this measurement. The fit parameters for different pump powers show that the attenuation rate  $\Gamma$  and the Brillouin scattering frequency  $f_{BS} = \omega/2\pi$  change significantly as a function of pump

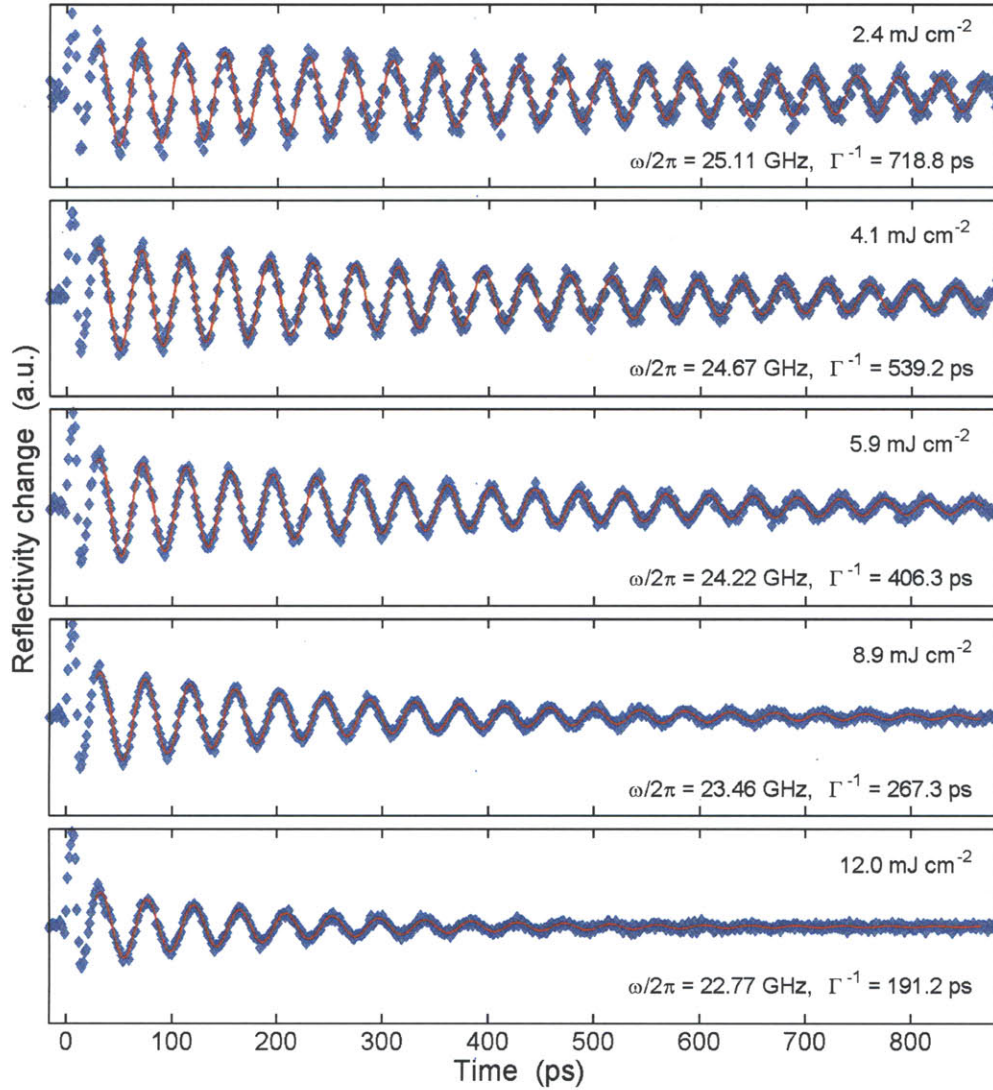


Figure 4-7: Recorded reflectivity change data (blue diamonds) for sample 1) of Table 4.1 which has 80 nm aluminum on glass and was measured at 230 K at five different pump powers. Fit of the experimental data is shown in red. The pump power for each plot is indicated together with the two fit parameters of interest: the oscillatory frequency and the exponential decay time constant. The Brillouin scattering oscillation frequency changed by over 10% and the time constant changed by a factor of almost 4.

power. Glycerol was chosen because it is a well characterized material with readily available temperature dependent speed of sound data in the literature.

Figure 4-9 shows the pump power dependence of the Brillouin scattering frequency  $f_{BS}$  and the attenuation rate  $\Gamma$  for a variety of different sample configurations at two different temperatures: 230 K and room temperature, 295 K. Equation 3.27 relates

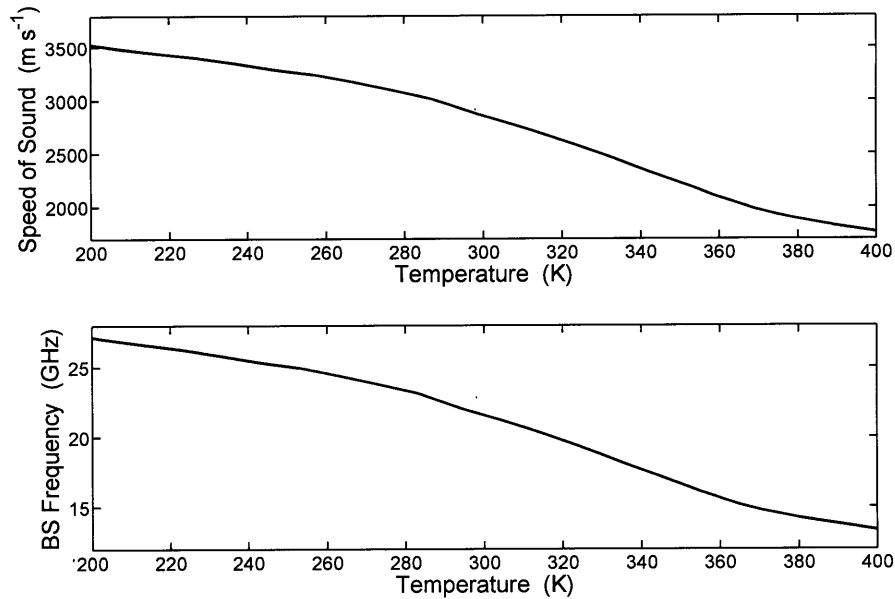


Figure 4-8: (top) Temperature dependence of the speed of sound in glycerol determined from conventional Brillouin scattering measurements with scattering wavevector  $q = 0.036 \text{ nm}^{-1}$ , taken from Comez *et al.* [CFSM03]. (bottom) This temperature dependent speed of sound allows us to estimate the expected temperature dependence of the Brillouin scattering frequency of our time domain Brillouin scattering measurement with wavevector  $q \sim 0.048 \text{ nm}^{-1}$ .

the Brillouin scattering frequency to the speed of sound. This frequency can then be related to the liquid temperature when reference data for the speed of sound at a similar acoustic wavevector,  $q_{\text{ref}} \sim 0.036 \text{ nm}^{-1}$  (from Comez *et al.*, [CFSM03], see Figure 4-8) compared to ours,  $q_{\text{BS}} \sim 0.048 \text{ nm}^{-1}$ , are taken into account. A summary of the sample configurations studied together with the parameters of interest can be found in Table 4.1. The first two samples both feature an 80 nm aluminum transducer film either on 1) glass or 2) sapphire generation side substrates. The next two samples feature canted, molecular beam epitaxially (MBE) grown iron thin films, also on either 3) glass or 4) sapphire substrates. These transducer films are used for shear wave generation as described in chapter 6. The last sample features a 25 nm strontium ruthenate ( $\text{SrRuO}_3$ , SRO) thin film on an off-axis cut strontium titanate ( $\text{SrTiO}_3$ , STO) substrate.  $\text{SrRuO}_3$  is a new generation transducer material well suited for high efficiency generation of large bandwidth longitudinal and shear acoustic waves. The probe power at each measurement was adjusted to account for differences in reflectivity, such that the power on the detection diode was kept constant for all measurements. As shown in Figures 4-9, similar trends are observed in both the Brillouin scattering frequency and the attenuation rate. Both parameters



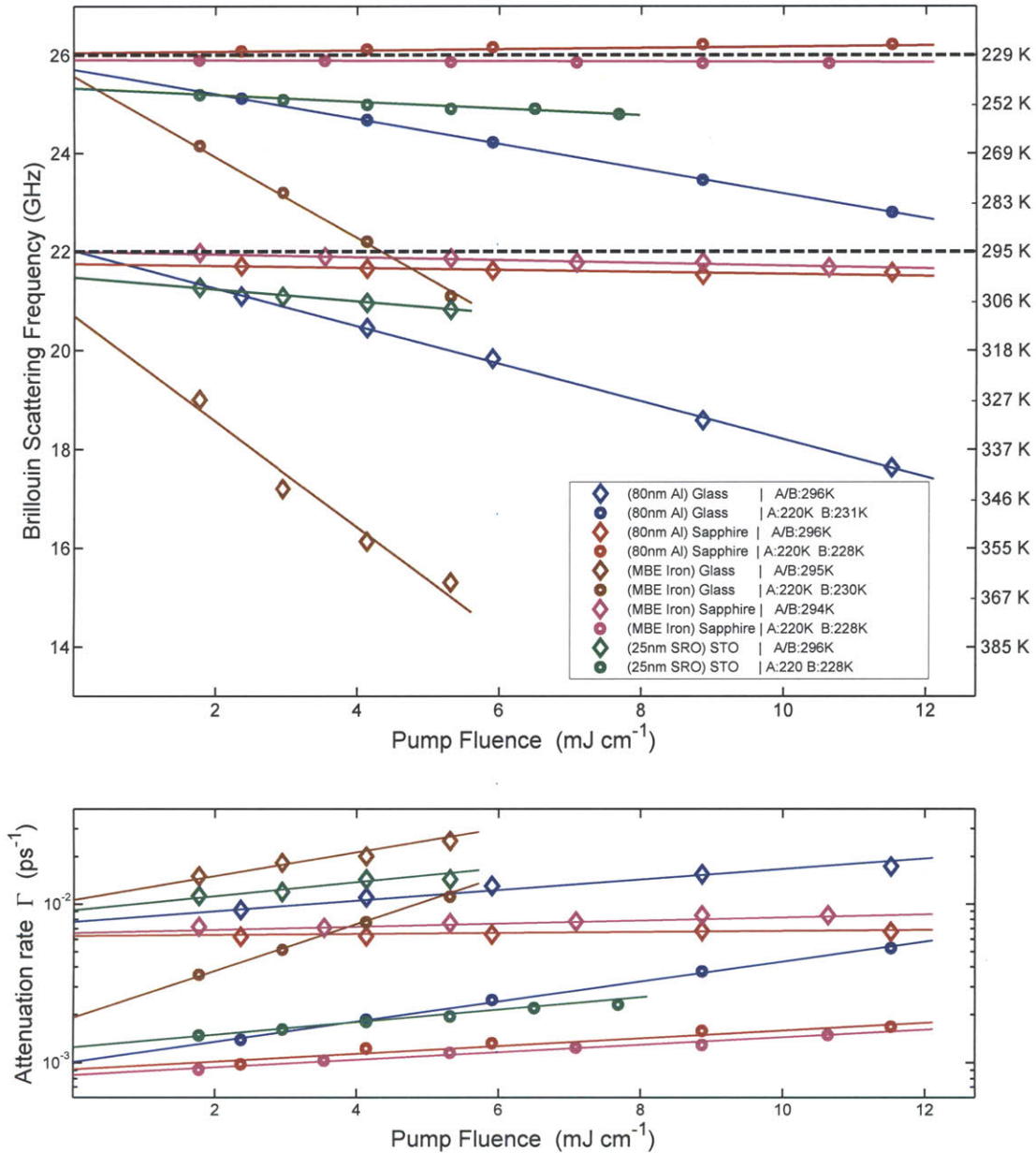


Figure 4-9: Brillouin scattering frequencies and attenuation rates measured in glycerol at various laser power levels reveal cumulative sample heating effects in different sample structures. Different generation side substrate materials and transducer films materials were studied with a glass detection side substrate present to hold the liquid in place. The fit parameters (Brillouin scattering frequency and acoustic attenuation rate) were extracted from the recorded Brillouin scattering oscillations of the acoustic wave after propagation 1 micron away from the transducer film. Measurements on each sample assembly were made at room temperature and with the set point (sensor A) and sample mount (sensor B) temperatures at 220 K and approximately 230 K respectively.



reflect the energy deposition caused by the pump pulse which results in an elevated steady-state temperature.

The strong cumulative heating effects are manifested differently depending on the sample structures. These differences are important and influence the choice of sample structures for the experiments detailed in the following chapters. Strong cumulative heating is always observed when glass, with a transducer film deposited on it, is used as the generation side substrate (as is the case for samples 1) and 3)):  $\sim 40$  K/10 mJ cm<sup>-1</sup> for glass-aluminum and over  $\sim 100$  K/10 mJ cm<sup>-1</sup> for glass-iron. The ratio of about 1:3 reflects the difference in optical absorbance of aluminum and iron at 790 nm of 13% and 39% respectively (see Table A.1 for a list of absorption coefficients for many relevant materials). In stark contrast to this is the cumulative heating observed in two sample configurations which have a transducer film on sapphire substrates (samples 2) and 4)). In this case, the pump power dependent heating is determined to be 3 to 5 K/10 mJ cm<sup>-1</sup>. The explanation of this large difference in cumulative heating lies in the difference in thermal conductivity,  $\kappa_{\text{glass}} \approx 1.4$  W m<sup>-1</sup>K<sup>-1</sup> and  $\kappa_{\text{sapphire}} \approx 45$  W m<sup>-1</sup>K<sup>-1</sup> for glass and sapphire, respectively (see Table A.3 for a list of thermal properties of relevant materials). Finally, SrTiO<sub>3</sub> is almost as good a thermal conductor as sapphire,  $\kappa_{\text{STO}} \approx 20$  W m<sup>-1</sup>K<sup>-1</sup> when subjected to a heating of  $\sim 10$  K/10 mJ cm<sup>-1</sup>. The only difference compared to the previous samples is the large offset at zero pump power which is probably caused by strong absorption of the 395 nm probe light (the probe was kept constant

Table 4.1: Cumulative heating study of five different sample structures: Summary of the relevant results from Figure 4-9. Distinct differences are also observed in the cumulative heating of glass, a poor thermal conductor when used as the generation side substrate compared to sapphire, one of the best thermally conducting insulators.

	Bottom Substrate	Transducer	Top Substrate	Probe Power	Sensor B	$\Delta T /$ Pump Power	Offset $\Delta T$
1)	Glass	80 nm Al	Glass	1.8 mW	296 K 231 K	40 K/10 $\frac{\text{mJ}}{\text{cm}}$ 42 K/10 $\frac{\text{mJ}}{\text{cm}}$	2 K 7 K
2)	Sapphire	80 nm Al	Glass	1.8 mW	296 K 228 K	3 K/10 $\frac{\text{mJ}}{\text{cm}}$ -3 K/10 $\frac{\text{mJ}}{\text{cm}}$	0 K 0 K
3)	Glass	MBE Iron	Glass	1.1 mW	295 K 230 K	120 K/10 $\frac{\text{mJ}}{\text{cm}}$ 110 K/10 $\frac{\text{mJ}}{\text{cm}}$	10 K 15 K
4)	Sapphire	MBE Iron	Glass	1.1 mW	294 K 228 K	5 K/10 $\frac{\text{mJ}}{\text{cm}}$ 5 K/10 $\frac{\text{mJ}}{\text{cm}}$	0 K 2 K
5)	STO	25 nm SRO	Glass	3.5 mW	296 K 228 K	8 K/10 $\frac{\text{mJ}}{\text{cm}}$ 10 K/10 $\frac{\text{mJ}}{\text{cm}}$	6 K 15 K

for all measurements). Note that the probe had at least twice as much power for measurements on SrTiO<sub>3</sub>/SrRuO<sub>3</sub> samples compared to the highly reflective metal films.

### 4.5.2 Simulation of Accumulative Heating

We verify our experimental observations by simulating the cumulative heating through modeling different sample structures and solving the time-independent heat equation in cylindrical geometry in COMSOL<sup>®</sup> Multiphysics. The sample structure used in all simulations includes a generation side substrate with a 50 nm iron transducer film deposited on it, glycerol, and a detection side substrate. A uniform absorption of 39% of a 100 mW laser beam with a Gaussian beam profile and a FWHM spot size of 100 micron (corresponding to a pump laser fluence of 5.9 mJ cm<sup>-1</sup>) throughout the depth of the transducer film was used as the heat input to the model system. The temperature profile obtained from these time-independent heat equation simulations gives an upper bound (because they were steady state and did not include the impulsive nature of heat deposition in real experiments) for the actual cumulative temperature rise and should be accurate to within a few percent.

Results from simulating three different substrate combinations, each having a 10 micron glycerol film, are depicted in Figure 4-10. The glass transition temperature of glycerol,  $T_g = 186$  K, was used as the initial temperature in all simulations. Acoustic waves at our detection wave vector propagate very far into the liquid (at least 10 to 15 microns) at low temperatures. The top plot shows the temperature distribution in a glass-glass configuration—the case with the highest temperature increase in our measurements—where the temperature close to the transducer film is elevated by 90 K. The dashed lines indicate the probe beam diameter and the temperature within this spatial range changes by about 5 K/micron of propagation distance. To quantify this effect, which should manifest as a frequency chirp in the measured Brillouin oscillation, we have to modify the functional form given in Equation 3.32 by allowing the oscillatory frequency to vary. The new functional form is then given by

$$\Delta R(t) = A_0 \exp(-\Gamma t) \cos [\omega(t) \cdot t + \phi] , \quad (4.1a)$$

$$\text{where } \omega(t) = 2\pi (f_0 + C \cdot t) \quad (4.1b)$$

represents a linearly chirped frequency, where  $f_0$  is the initial Brillouin oscillation frequency at zero time (i.e. close to the transducer film) and  $C$  is the linear chirp coefficient and reflects the change in Brillouin frequency away from the film (as a result of a temperature gradient in the liquid). Even though a linear chirp does not reflect

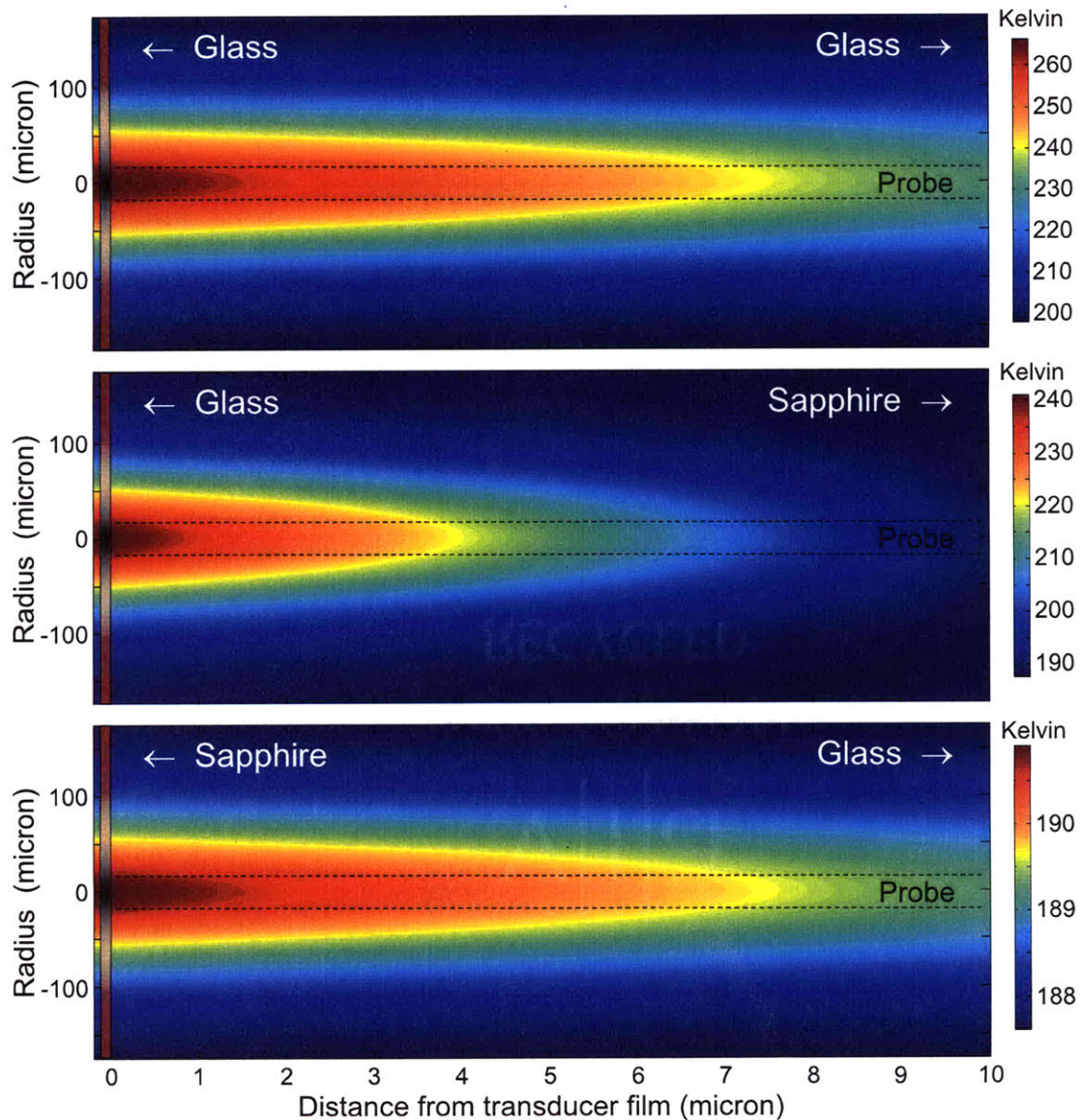


Figure 4-10: Results from simulations of cumulative heating in three different sample structures: A 50 nm iron transducer film on either glass (top and middle) or sapphire (bottom) generation side substrates (to the left) absorbs 40% of a 100 mW laser pulse with a FWHM spot size of 100 micron. The detection side substrate (to the right) can be either sapphire or glass. The resulting steady state heat distribution in a 10 micron glycerol film sandwiched between both substrates is calculated with the commercial software COMSOL® Multiphysics. The glass transition temperature of glycerol was chosen ( $T_g = 186$  K) as the initial temperature in all the simulations. At such a low temperature, Brillouin scattering can be easily monitored for more than 4 ns, which corresponds to an acoustic propagation distance of at least 15 micron away from the generation transducer. The dashed lines indicate the probe beam diameter. Note the different temperature scales in each plot.

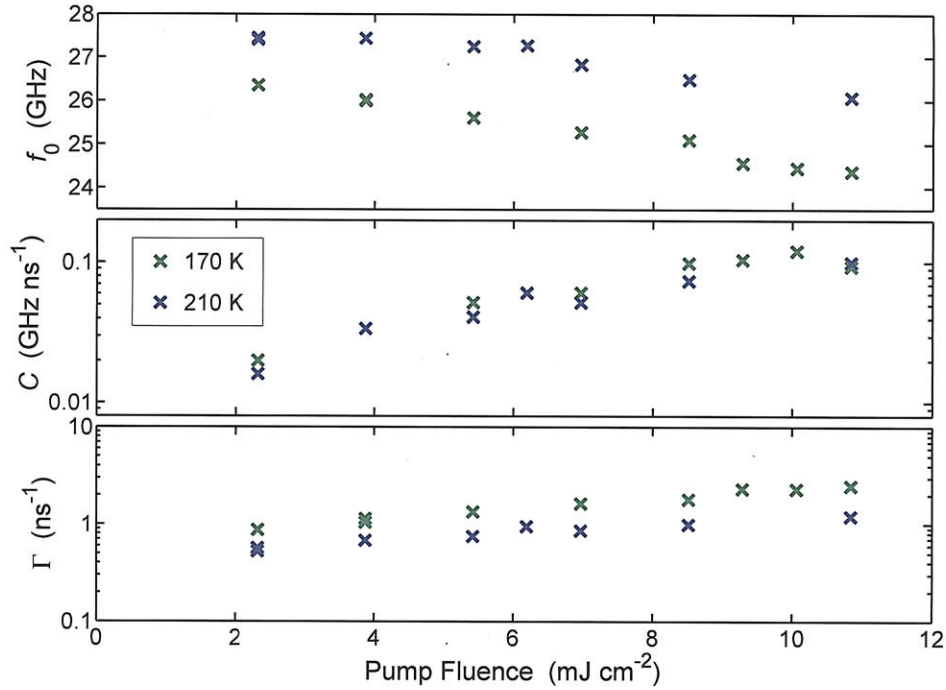


Figure 4-11: Pump fluence dependence of acoustic parameters in glycerol at 170 K and 210 K.  $f_0$  denotes the initial Brillouin oscillation frequency close to the transducer,  $C$  the linear chirp coefficient and  $\Gamma$  the acoustic attenuation as given in the functional form in Equation 3.32. The sample structure having a 20 nm aluminum transducer film on a glass generation side substrate shows strong steady state heating (several tens of degrees as seen in the simulations) which is reflected in the pump fluence dependence of these parameters. Stronger cumulative heating causes the initial Brillouin oscillation frequency  $f_0$  to decrease while the acoustic attenuation  $\Gamma$  increases slightly as the pump fluence is increased. Higher temperatures of the liquid close to the transducer film at higher pump fluences lead to a higher temperature gradient away from this film and result in an increase of the chirp coefficient  $C$  with pump fluence.

the true change in frequency (which has to model the temperature dependence of the Brillouin frequency) it is deemed sufficient for the present analysis. The extracted fit parameters (from Equation 4.1) for a 20 nm aluminum transducer film on a glass generation side substrate at two different temperatures are depicted in Figure 4-11. The results from the simulations confirm our hypothesis that a strong temperature gradient is present in our liquid sample. In addition, the chirp increases as a function of pump fluence due to the steeper temperature gradient in the liquid as more heat is deposited at higher pump fluences.

Another adjustable parameter of interest in the three sample structures studied is the liquid thickness. The temperature distribution along the center axis of the sample



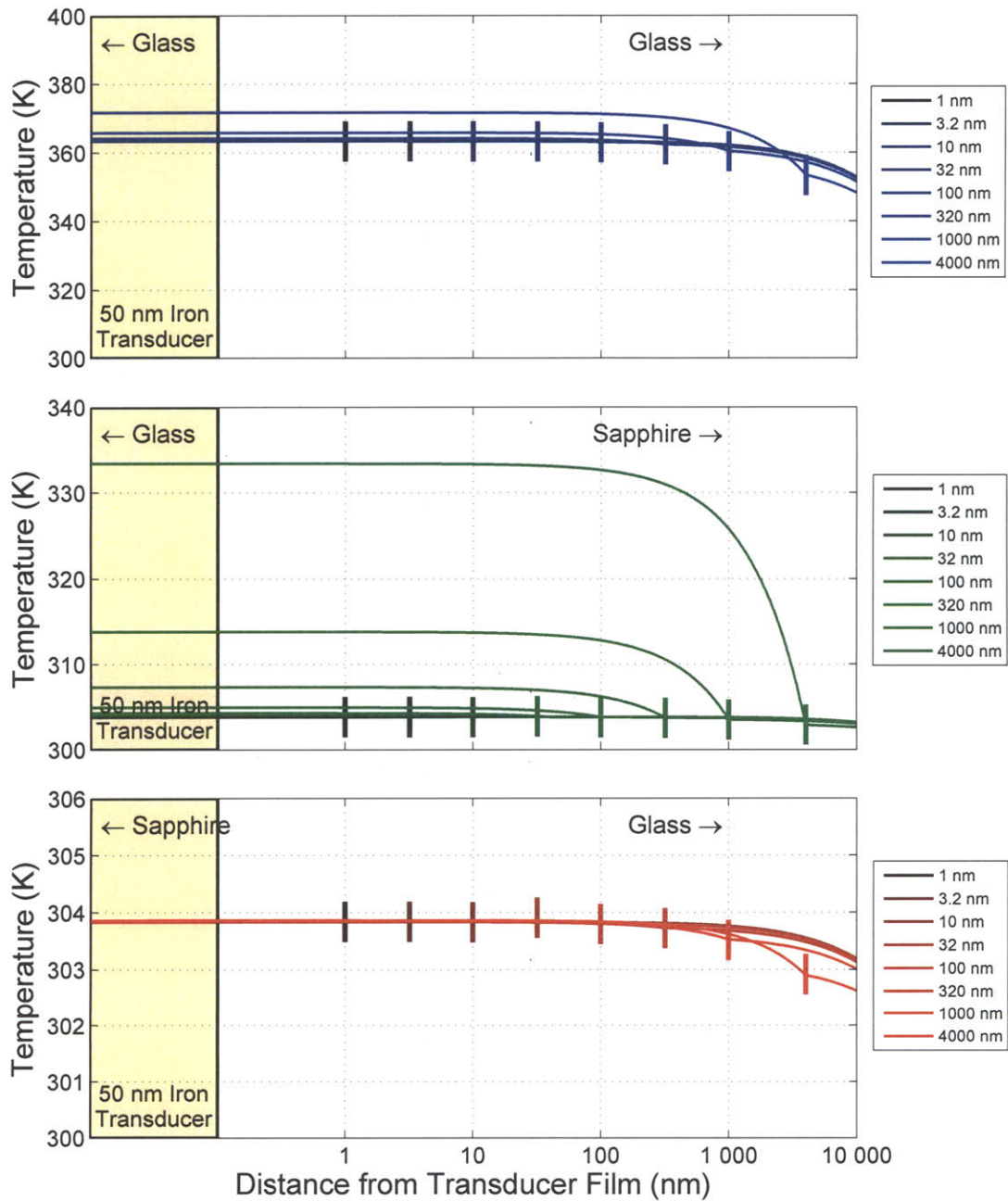


Figure 4-12: Simulation results of cumulative heating in the same three sample structures as in Figure 4-10 but having different liquid thicknesses. The temperature indicates the temperature along the center axis of the cylindrical symmetry of the sample. The liquid thicknesses range from 1 nm up to 4 micron and are indicated by a vertical bar for each temperature trace.

structure having liquid thicknesses between 1 nm and 4 micron is depicted in Figure 4-12. While the physical meaning of a 1 nm liquid film in this type of simulation is debatable, at such a thickness, the generation and detection side substrates of the sample are effectively in contact. The results presented in the figure show that for a glass-glass structure, the cumulative heating effect is again very high—about 65 K across the whole liquid film. On the other hand, a sapphire-glass structure (or even more so a sapphire-sapphire structure, which is not shown) exhibits very low and approximately constant cumulative heating of just a few Kelvin throughout the liquid thickness. An interesting and important point in terms of sample construction is the thermal properties of a sample configuration having a glass-sapphire structure. At small liquid thicknesses, the cumulative heating is similar to a sapphire-glass structure, but for increasingly thick liquid layers the liquid behaves like as thermal insulator between the heat absorbing transducer film and the excellent thermally conducting sapphire. The thermal insulating behavior of the liquid causes the cumulative effect to become stronger with increasing liquid thicknesses.

The main conclusion we draw from the simulations and experimental studies of different sample structures is that the cumulative heating effects can be minimized by using a good thermally conducting transducer side substrate, like sapphire. Unfortunately, this is not always possible, for example, in the measurements presented in Chapter 6 where for some configurations a glass lens had to be used to hold the generation transducer.

### 4.5.3 Single-Shot Heating

Heating on a shot-to-shot basis is generally of no major concern for the experiments presented in this thesis. Typically, the optical pump pulse energy gets absorbed by the transducer film which launches a coherent acoustic wavepacket that leaves the generation region more quickly than the ‘incoherent’ heat. In other words, an acoustic pulse always propagates ahead of heat. Therefore, the acoustic wave always travels through unheated (by the current laser shot) material.

## 4.6 Conclusions

Different sample configurations which allow us to study interactions of gigahertz longitudinal and shear acoustic waves with liquids were introduced in this chapter. We described the sample holder design and carefully examined cumulative heating effects due to the absorption of the optical pump and probe pulses in the sample liquid. Such heating can be minimized through the use of thermally conducting substrates, such

as sapphire, on the generation side. In addition, experiments should be conducted at the lowest possible optical pump powers.

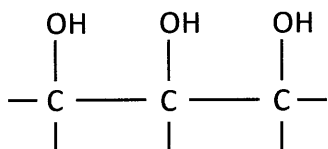




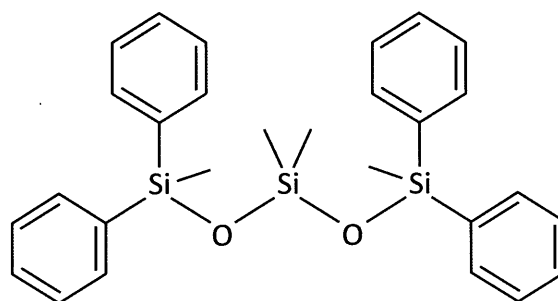
---

# Acoustic Spectroscopy of Glycerol and DC704

---



glycerol



tetramethyl tetraphenyl trisiloxane

In the previous chapters, we described how different laser picosecond ultrasonic approaches may be used to effectively characterize various phenomenological aspects of the glass transition and how to test predictions of the mode-coupling theory. In the following two chapters we present results obtained when we applied these developed spectroscopic strategies to the study of longitudinal (Chapter 5) and shear (Chapter 6) mechanical properties of two glass forming liquids: glycerol ( $C_3H_5(OH)_3$ ) and tetramethyl tetraphenyl trisiloxane; tetramethyl tetraphenyl trisiloxane, commonly used as diffusion pump oil, was developed by the Dow-Corning company and is sold under the trade name of DC704.

Glycerol, a trihydric alcohol, is an associated liquid which forms weak hydrogen-bonding networks and has a fragility index of  $m = 53$  [Ang95], making it intermediate

between fragile and strong systems (see Section 2.1 for details about this classification). Glycerol has a boiling point  $T_b \approx$  of 565 K, which is rather high in comparison to alkanes with similar molecular weights such as hexane and heptane which boil at 342 K and 371 K, respectively [BR05]. Glycerol supercools easily below its melting temperature  $T_m = 291$  K and forms a glass at  $T_g \approx 186$  K, making it one of the prototypical and extremely well studied glass formers. The wealth of available physical information obtained from a variety of spectroscopic techniques makes glycerol a particularly interesting candidate for comparison of results obtained from different spectroscopic techniques.

Broadband spectra from glycerol are available from neutron and light-scattering experiments which qualitatively agree with mode-coupling theory predictions [RSKQ94, WHL<sup>+</sup>94, FGMS97, BR05] — in contrast to spectra obtained by dielectric spectroscopy which show significant deviations [LPS<sup>+</sup>96, LL02, LWSL05, BR05]. Mechanical spectra are also available from ultrasonics investigations [JNB86], impulsive stimulated scattering studies [YCN88, PN00], and initial picosecond acoustic transmission measurements [SN04]. The results from all these techniques are pieced together in Chapter 5 to compile broadband longitudinal relaxation spectra. Even though shear acoustic relaxation is much more difficult to investigate, in Chapter 6, results from our shear measurements of glycerol are compared with literature data obtained from glycerol at around 1 kHz [Jeo87], in the tens of megahertz range [PL57], and in the gigahertz range from depolarized Brillouin scattering measurements made at temperatures close to  $T_g$ . Glycerol is thus the ideal candidate for both our longitudinal and shear studies.

Like glycerol, DC704 is a molecular glass former. It has a glass transition temperature  $T_g$  of  $\approx 210$  K [NJO05, HO10] and a boiling point of  $T_b \approx 496$  K [DC7]. It has a fragility index of  $m = 95$  [JNO05] and therefore belongs to the group of fragile glass formers. It is likely to be entirely van-der-Waals bonded due to the presence of four phenyl groups; since oxygens are bonded to silicon, hydrogen bonding is absent in DC704. Silicone oils are extremely resistant to decomposition. In addition, their extremely low vapor pressure makes them especially well suited as pump fluids in diffusion pumps for high vacuum and ultra high vacuum applications where there are stringent requirements concerning resistance against oxidization and decomposition.

DC704 was chosen by our collaborators [Hec, Tor] and us because its dielectric and shear mechanical spectra do not show any secondary relaxation features (often interpreted as a Johari-Goldstein or  $\beta_{\text{slow}}$ -relaxation) at frequencies above the  $\alpha$  relaxation, simplifying the analysis of compiled spectra. In addition, like glycerol, it supercools easily and rarely crystallizes which is particularly important for our measurements in which acoustic waves are generated through the heating and subsequent

thermal expansion of a transducer metal film that is directly adjacent to the liquid. This cycles the temperature of the transducer film by up to 100 K and the liquid in the vicinity to the film by tens of Kelvin, and may facilitate crystallization.

Special precautions are required in the sample preparation of these materials since both glycerol and DC704 absorb large quantities of gases and glycerol is extremely hygroscopic. Even though the lab in which our experiments were carried out does not have humidity control, the humidity in the room was closely monitored and samples were typically assembled in a nitrogen purge box only when the room humidity of the lab fell below 20%. After samples were built, they were quickly transferred to the cryostat, which was either purged with dry nitrogen (for the sample-in-vapor cryostat) or evacuated (for the cold finger cryostat). This procedure may not eliminate all possible contamination but the excellent reproducibility observed in time-domain Brillouin scattering experiments makes us confident that contamination has been kept to a minimum.



# CHAPTER 5

---

## Longitudinal Waves Study of Glycerol and DC704

---

In this chapter we discuss measurements of the density response of glycerol and DC704 at temperatures from below their respective glass transition temperatures up to 400 K and at frequencies from below 10 GHz up to 200 GHz. We start by illustrating how spectroscopic approaches of time-domain Brillouin scattering and interferometry are applied to obtain speed of sound and acoustic attenuation information for these two liquids. Thereafter, our results are first discussed individually and later pieced together with data from several other techniques to create broadband mechanical relaxation spectra, ranging from 2 MHz to 200 GHz for glycerol and 15 mHz (millihertz) to over 100 GHz for DC704. Our data allow the viscous slowdown in these liquids to be followed and characterized over many orders of magnitude through the use of phenomenological models and also enable analysis in terms of the mode-coupling theory. In particular, the predicted power-law behavior of the fast dynamics in glass forming liquids and its connection to the slow dynamics are tested.

### 5.1 Experimental Methods and Data Analysis

The general concepts of the experimental configurations that were used for these measurements have been described in Chapters 3 and 4. In order to span as broad a frequency range as possible, we combined time-domain Brillouin scattering in a large liquid volume with transmission measurements using interferometric detection of the transmitted strain wave packet across different liquid thicknesses. In the first approach, optically generated longitudinal acoustic waves were monitored via time-domain Brillouin scattering while the waves propagated through very thick liquid layers. This enabled the direct extraction of acoustic speeds and attenuation rates at

fixed wavevectors which could be varied by changing the probe wavelength or scattering angle. Subsequently, the experiment was repeated with both single-cycle and multiple-cycle acoustic waves and, instead of monitoring propagation in the liquid, the arrival of the acoustic wave at a receiver metal film was measured using an interferometric detection setup. We describe the analysis we performed, which compared transmitted strain pulses through different liquid thicknesses with each other in order to extract the liquid response at a fixed frequency that can be varied by changing the excitation pulse sequence timing. In the following two subsections we present the details of both experimental approaches and the means by which we extracted information about the liquid responses from each of these techniques.

### 5.1.1 Time-Domain Brillouin Scattering in Liquid

The general concepts of and the theoretical background for monitoring the propagation of gigahertz frequency longitudinal acoustic strain pulses in a transparent medium via time-domain Brillouin scattering have been elaborated in Section 3.3.1. As detailed in Section 4.5, we have taken advantage of the fact that time-domain Brillouin scattering in a liquid can be utilized as a very sensitive probe of the effects of cumulative heating. The outcome of those measurements suggested the use of sapphire substrates with aluminum transducer films and the lowest possible pump fluence for these measurements in general.

For the purpose of compiling broad relaxation spectra, we first recorded at many different temperatures time-domain Brillouin scattering data sets for both liquids using the laser fundamental wavelength, centered at 790 nm, and frequency doubled light, centered at 395 nm. One of those data sets, recorded from DC704 with 395 nm light, is shown in Figure 5-1. The sample was constructed from a 20 nm aluminum transducer film on a sapphire generation-side substrate and a many-micron thick liquid layer held by a glass lens. This construction allowed us to monitor the propagation of the acoustic strain pulse until the strain pulse was attenuated to below our detection limit.

Figure 5-1(c) shows raw data as time delay vs. temperature, with the amplitude of the derivative of the recorded signal color-coded. Selected raw data at several different temperatures are shown in Figure 5-2 and clearly illustrate the strong acoustic attenuation at temperatures above the glass transition temperature  $T_g \approx 210K$ . The derivative was only taken for ease of display, but the fits were made directly on the recorded reflectivity-change data. As pointed out above, this required the more complicated fitting form of Equations 3.34 with seven parameters. In order to reduce the uncertainty of the two parameters of interest, the Brillouin frequency  $f$  and the attenuation rate  $\Gamma$ , a two-step fitting procedure was used. A first fit was done allowing

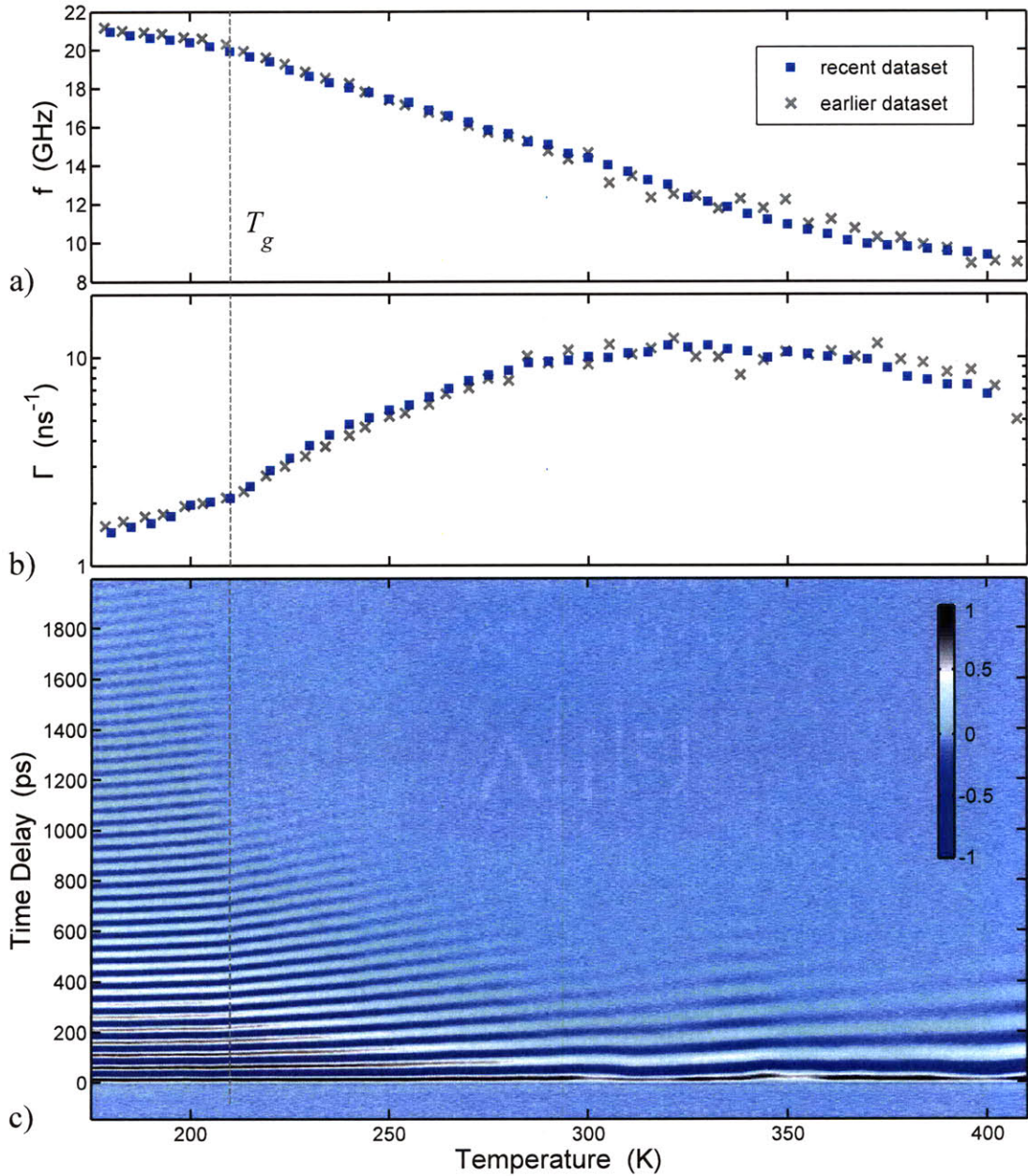


Figure 5-1: Brillouin scattering raw data (recorded with 395 nm light) from DC704 (c) and the extracted fit parameters for the acoustic frequency  $f$  (a) and attenuation rate  $\Gamma$  (b). The data shown as ( $\square$ ) in (a) and (b) were extracted from the raw data in (c) which were recorded at very low pump fluence,  $\sim 2.8 \text{ mJ cm}^{-2}$ , while the ( $\times$ ) come from another data set recorded one year earlier. Even though all experimental conditions were modified (different liquid source, transducer film, and newly built detection setup), the fit parameters of both sets are in excellent agreement within experimental uncertainty, demonstrating the excellent reproducibility of this type of measurement. Note the change in behavior at the glass transition temperature  $T_g \approx 210 \text{ K}$  (indicated by a dashed line) in all three plots.



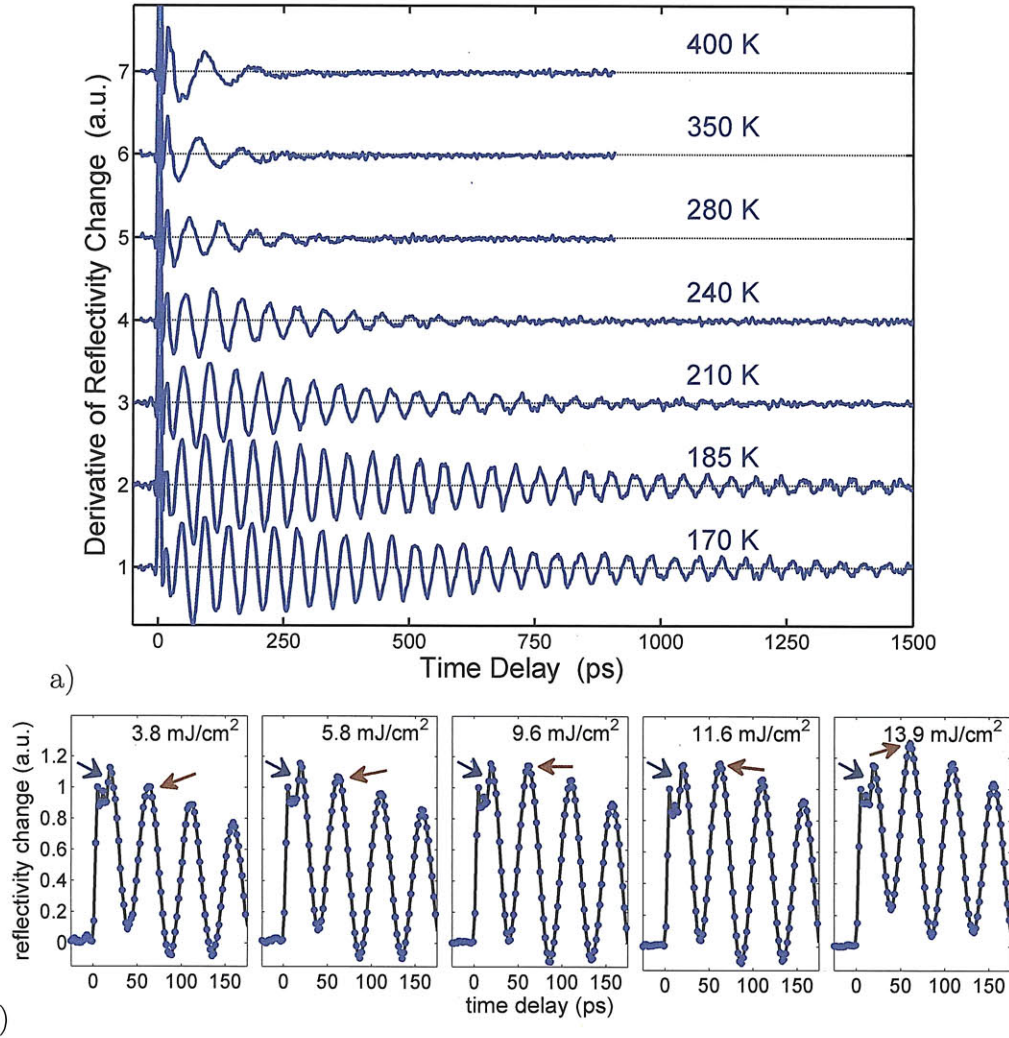


Figure 5-2: (a) Selection of Brillouin scattering data in DC704 at various temperatures. (b) Brillouin scattering raw data from DC704 at an initial temperature of 200 K and various pump fluences recorded in a sample with a 20 nm aluminum transducer film on a sapphire substrate. The acoustic excitation at  $t = 0$  ps and the first couple of Brillouin oscillations are shown. The procedure for data analysis is to normalize the recorded reflectivity data using the very sharp peak at  $t = 0$ , the so-called electronic peak which is caused by the change in reflectivity of the transducer film due to the heated electron gas upon pump pulse absorption. The relative amplitudes of the first Brillouin oscillation peak (indicated by the first blue arrow) and the second Brillouin oscillation peak (indicated by the second red arrow) change depending on pump fluence, suggesting that such a data analysis procedure should be used with caution. However, the initial amplitude of the Brillouin oscillation seems to scale reliably with the electronic peak amplitude and in addition, the pump fluences were typically kept constant and at a minimal level for measurements of acoustic attenuation and dispersion.



all seven parameters to vary. In a second step, we repeated the fit with the same functional form but only allowed the frequency  $f$ , the attenuation rate  $\Gamma$ , and the phase  $\phi$  to vary while keeping all other parameters constant at the values determined by the first fit. This procedure was automated in a Matlab routine and typically reduced the fit uncertainties of the values significantly.

Results for the extracted Brillouin scattering frequency and attenuation rate are shown in Figures 5-1 (a) and (b) respectively. We also include results from another experiment on DC704 which contained a little more noise but are overall in excellent agreement with the present data. Together, these results demonstrate the reproducibility of this type of measurement. The glass transition temperature  $T_g$  is indicated in all three subplots of Figure 5-1, and a clear change in behavior around this temperature is observed.

### 5.1.2 Interferometry: Displacement Detection at Receiver

In most picosecond ultrasonics measurements aimed at studying mechanical properties (typically of solids), the damping rate of the sample is determined by comparing the ratio of the amplitudes of successive ultrasonic echoes [TGMT86]. This type of data analysis requires knowledge of the acoustic impedances and reflectivities of the various interfaces in a given sample. However, even when the reflection coefficients are known, the acoustic attenuation is often overestimated because of additional damping caused by roughness of the reflecting interfaces or surfaces. This is particularly significant for the high frequency components of the wavepacket where the acoustic wavelengths are on the order of tens of nanometers, a length scale on which typical interface/surface roughness is not negligible.

An alternative approach is to compare signals transmitted through different thicknesses of sample material, as done by Choi *et al.* [CFY<sup>+</sup>05]. This is, however, often difficult to implement in complex samples since all other parameters besides the sample thickness have to be kept constant.

In both cases, signals are typically analyzed in the frequency domain by exploiting the fact that any waveform  $h(t)$  can be decomposed into its Fourier components  $\tilde{h}(\omega)$ :

$$h(t) = \frac{1}{2\pi} \int \tilde{h}(\omega) e^{-i\omega t} d\omega. \quad (5.1)$$

Through this procedure, it is possible to compare the amplitudes and phases at a given frequency by Fourier transformation of the two time-domain signals  $h_1(t)$  and  $h_2(t)$ , which either constitute a signal and its corresponding echo (e.g.  $\eta_1$  and  $\eta'_1$  in Figure 5-3), or two different signals transmitted thorough different sample thicknesses

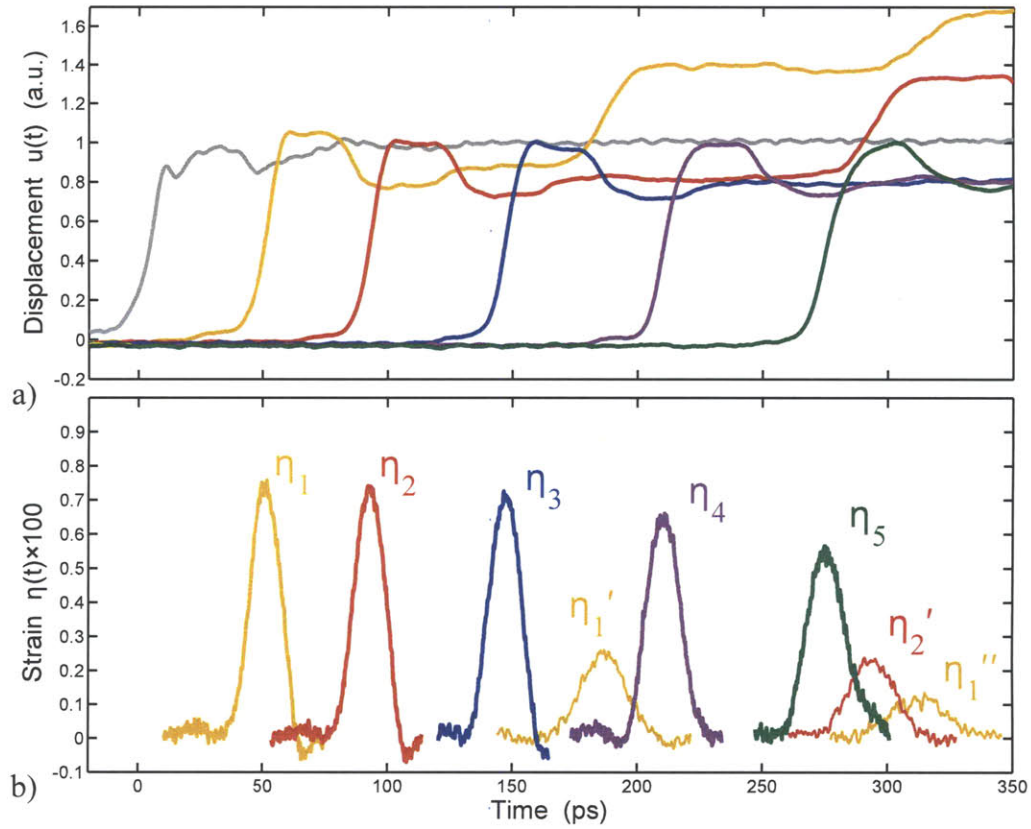


Figure 5-3: Measured and normalized displacement data (a) and the derived strain (b) after transmission through different layer thicknesses of DC704 at 200 K. The acoustic strain was produced by a 30 nm aluminum transducer film on a sapphire generation side substrate and detected interferometrically at the back side of a 100 nm aluminum film on a sapphire detection side substrate. Signals labeled  $\eta_1 - \eta_5$  are from acoustic waves transmitted through progressively greater liquid thicknesses, 117 nm, 225 nm, 355 nm, 512 nm, and 670 nm, respectively;  $\eta'_1$  and  $\eta'_2$  are echoes of  $\eta_1$  and  $\eta_2$ ; and  $\eta''_1$  is the second echo of  $\eta_1$ .

$d_1$  and  $d_2 > d_1$  (e.g.  $\eta_1$  and  $\eta_2$  in Figure 5-3). The complex Fourier transformations of both signals  $\tilde{h}_1(\omega)$  and  $\tilde{h}_2(\omega)$  are then given by

$$\tilde{h}_1(\omega) = \int h_1(t)e^{-i\omega t} dt \quad \text{and} \quad \tilde{h}_2(\omega) = \int h_2(t)e^{-i\omega t} dt. \quad (5.2)$$

Figure 5-3 (a) shows the measured displacements for five different thicknesses of DC704 recorded with a linear slope sample. A signal (in gray) from the part of the sample assembly where the transducer films were in contact is added to the plot which shows a rise at  $t = 0$  followed by a weak oscillatory signal caused by Brillouin scattering in the detection substrate. We did not use this signal amplitude for our

analysis since the acoustic strain in this case did not experience exactly the same conditions (due to the contact between the metal thin films) as in the other cases, but the signal provided calibration for essentially zero liquid thickness.

We assume that the displacement can be described by a plane wave equation. The time-derivative of the displacement  $u(t, x)$  is then proportional to the strain  $\eta(t, x)$ ,

$$\eta(t, x) = \frac{d}{dx}u(t, x) = \frac{1}{c} \frac{d}{dt}u(t, x), \quad (5.3)$$

where  $c$  is the acoustic phase velocity. Figure 5-3 (b) shows the transmitted strain through five different liquid thicknesses, 117 nm, 225 nm, 355 nm, 512 nm, and 670 nm, labeled  $\eta_1$  through  $\eta_5$ . The first echoes  $\eta'_1$  and  $\eta'_2$  are included for liquid thicknesses 1 and 2, in addition, the second echo  $\eta''_1$  is also included for liquid thickness 1. The reduction in amplitude originating from acoustic attenuation and broadening from dispersion and other potential sources (e.g. frequency dependent damping) are clearly visible.

The shape of the strain after transmission through different liquid thicknesses is simply related to a set of acoustic parameters which includes the complex speed of sound or equivalently the complex longitudinal modulus. After traveling through an additional distance  $\Delta d = d_2 - d_1$  in the liquid, the Fourier domain ‘output’ strain  $\tilde{\eta}_2(\omega)$  is related to the ‘input’ strain  $\tilde{\eta}_1(\omega)$  by the complex wavevector,  $\hat{k}(\omega) = \omega/\hat{c}(\omega)$ ,

$$\tilde{\eta}_2(\omega) = e^{i\hat{k}(\omega)\Delta d} \tilde{\eta}_1(\omega). \quad (5.4)$$

While the real portion of the wavevector shifts the phase of the input strain, the imaginary component of the wavevector dampens the amplitude. If we denote the transmitted strain as

$$\tilde{\eta}_{trans}(\omega) = \frac{\tilde{\eta}_2(\omega)}{\tilde{\eta}_1(\omega)}, \quad (5.5)$$

we can write the complex acoustic velocity as

$$\hat{c}(\omega) = \frac{\omega}{\hat{k}} = \frac{i\omega\Delta d}{\ln(\tilde{\eta}_{trans}(\omega))}. \quad (5.6)$$

From this, we obtain the following formula for determining the frequency dependent damping coefficient  $\alpha(\omega)$ :

$$\alpha(\omega) = \frac{1}{\Delta d} \ln |\tilde{\eta}_{trans}(\omega)|, \quad (5.7)$$

where  $\Delta d$  is either the round trip distance or the difference in sample thickness when comparing two different signals. The Fourier angle can also be used to extract dispersion information.

In the case of signal-echo analysis, Equation 5.7 must also include the overall reflection coefficient  $R$  for the echo, resulting in:

$$\alpha(\omega) = \frac{1}{\Delta d} \ln [R |\tilde{\eta}_{trans}(\omega)|]. \quad (5.8)$$

The complex acoustic modulus  $\hat{M}(\omega)$  and the acoustic susceptibility/compliance spectrum  $\hat{J}(\omega)$  can be determined directly from a broadband measurement or multiple narrowband measurements of the transmitted strain:

$$\hat{M}(\omega) = -\rho \left[ \frac{\Delta d \omega}{\ln(\tilde{\eta}_{trans}(\omega))} \right]^2 \quad \text{and} \quad (5.9)$$

$$\hat{J}(\omega) = \frac{1}{\hat{M}(\omega)} = -\rho^{-1} \left[ \frac{\ln(\tilde{\eta}_{trans}(\omega))}{\Delta d \omega} \right]^2. \quad (5.10)$$

In order to account for different attenuation strengths at different frequencies in the most reliable manner, we conducted our analysis on data sets having 15 to 50 strain profiles, each recorded at a different liquid thickness using a fixed excitation pulse shape (single-cycle or multiple-cycle pulse at a fixed frequency) and at a constant sample temperature. In most of the interferometric measurements conducted for the work presented in this thesis we either used single-pulse or multiple-pulse excitations having no more than 3 pulses. A complication with multiple-cycle pulse excitation in our sample configuration is the following: high acoustic attenuation rates (with typical mean free paths on the order of a few wavelengths) limit most of the experiments to very thin liquid layers which are significantly below the mean free path. Multiple cycle pulses restrict this minimal thickness since the thickness must be large enough to allow a full multiple-cycle wave form to ‘fit in’. In other words, the acoustic transit time through the liquid thickness must be equal to or larger than the time duration of the full acoustic waveform. In most cases, this is not possible since seven — or even only five — pulses exceed the acoustic attenuation time at that particular frequency by several times. Measurements can be carried out with multiple-cycle acoustic waves whose total length exceeds the liquid path length, but in that case acoustic cavity effects due to interference among reflected acoustic wave components add uncertainty to the analysis.

## 5.2 Results

In the following two subsections, we present the spectral results obtained by our combined time-domain Brillouin scattering and interferometry studies on glycerol and DC704. In the third subsection we present and discuss results from high pump fluence time-domain Brillouin scattering measurements of large amplitude acoustic waves as they propagate through a liquid.

### 5.2.1 Results: Glycerol

The extracted acoustic velocity and attenuation coefficient results vs. frequency are shown in Figures 5-4 (a) and (b), respectively. The acoustic velocity is constant over the displayed frequency range for most temperatures and only shows some dispersion for the highest temperatures. The variation in data point density of the interferometric measurements at different temperatures originates from different time step sampling of the raw displacement data like the ones shown in Figure 5-3. The discrete Fourier transform treatment then passes those on to the frequency domain.

Due to the lack of a generally accepted model for the relaxation behavior of viscous liquids for the high frequency regime, let alone the entire spectrum, as described in Chapter 2, we can only rely on a theoretical prediction obtained from a classical calculation for the frequency dependence of the absorption coefficient  $\alpha(\omega)$  in a liquid as derived by Herzfeld and Litovitz [HL59]:

$$\alpha(\omega) = \frac{2}{3} \frac{\omega^2}{c^3 \rho} \left( \eta + \frac{3}{4} (\gamma - 1) \frac{\lambda}{c_p} \right), \quad (5.11)$$

where  $\gamma = c_V/c_p$ , in which  $c_V$  and  $c_p$  are the volume specific isochoric and isobaric heat capacities, respectively,  $\lambda$  is the acoustic wavelength,  $c$  is the adiabatic longitudinal speed of sound and  $\rho$  is the density. The first term in this formula for the absorption is related to the static viscosity  $\eta$  while the second term comes from heat diffusion. Under the assumption that all parameters in Equation 5.11 are independent of frequency, the expression predicts a absorption coefficient proportional to the square of the frequency

$$\frac{\alpha(\omega)}{\omega^2} = \text{constant}. \quad (5.12)$$

Figure 5-4 (c) shows the ratio of damping to frequency squared vs. frequency across all measured temperatures and frequencies. For the five lowest reported temperatures, 180 K - 240 K,  $\alpha(\omega)/\omega^2$  shows very little frequency dependence, in agreement with the prediction of Equation 5.12. The data points determined by interferometry (diamonds) at 180 K which lie below the indicated line (at frequencies up to

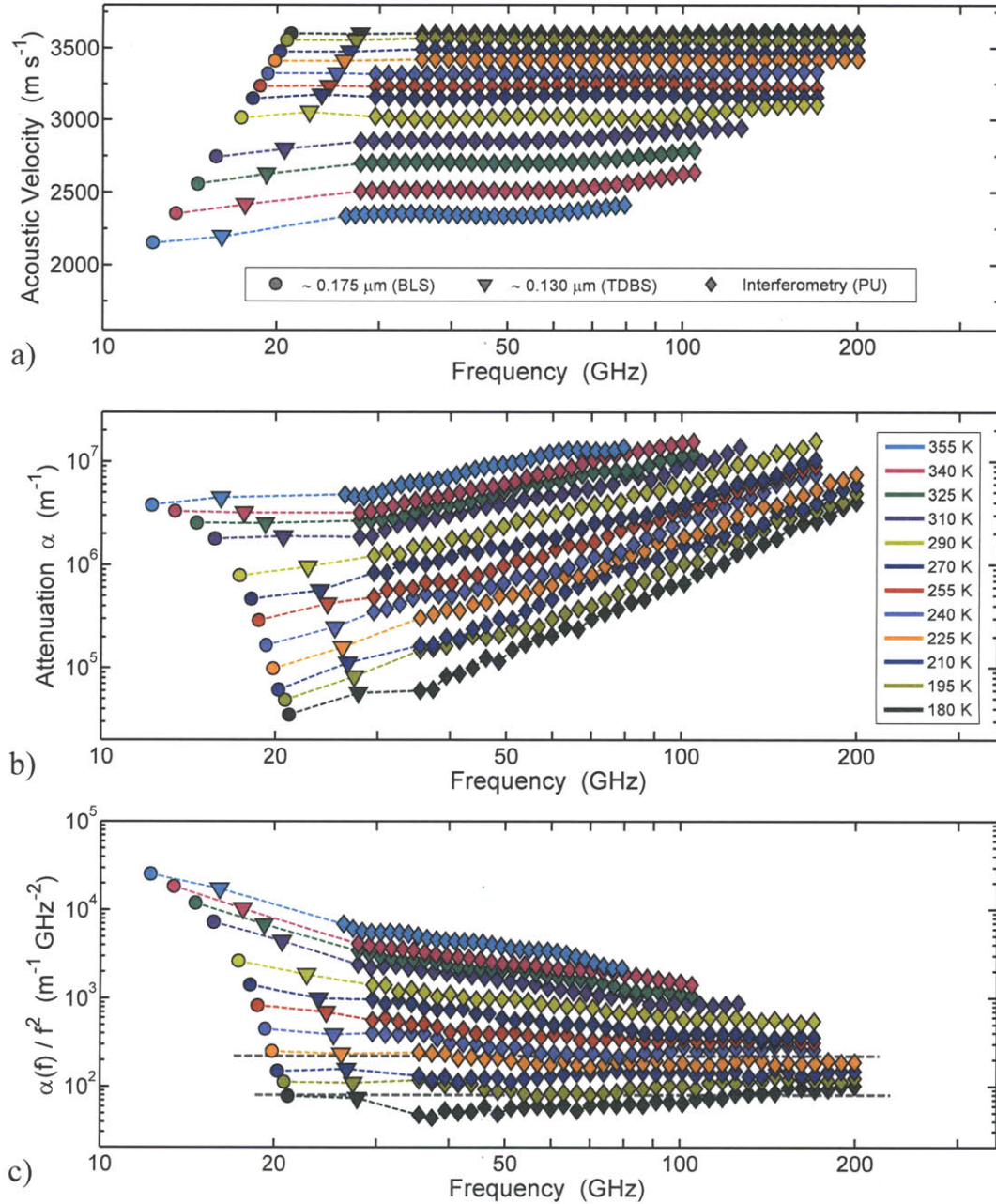


Figure 5-4: Acoustic velocity (a) and attenuation coefficient (b) vs. frequency for glycerol. The displayed data show temperature dependent results from our interferometric ( $\diamond$ ) and time domain Brillouin scattering ( $\nabla$ ) measurements. Results from Brillouin light scattering ( $\circ$ ) (BLS) [CFMS03] at frequencies lower than ours are also included. (c) Attenuation rate ( $a(f)$ ) divided by the square of frequency ( $f$ ) vs. frequency (i.e.,  $a(f)/f^2$  vs.  $f$ ). The somewhat lower attenuation at low temperatures and low frequencies is an artifact of the data extraction algorithm as described in the text. Note that in case of Brillouin scattering measurements the wavevector is fixed while the frequency is changed as a function of temperature and vice versa for the interferometric measurements.

about 100 GHz) probably result from an underestimation of the acoustic attenuation coefficient due to the limited attenuation within the accessible propagation distance. The mean free path in this range,  $\ell(\omega) = 1/\alpha(\omega)$ , is on the order of 10  $\mu\text{m}$ , which is greater than the largest liquid thickness, at slightly more than 3 microns. At higher temperatures, the slope becomes increasingly negative, indicating a sub-square dependence of the acoustic attenuation with frequency. This can be explained by the appearance of an additional relaxation feature as the strongly temperature dependent  $\alpha$ -relaxation shifts to higher frequencies with increasing temperature enters our spectral range from the low frequency side.

Acoustic velocities and damping rates, as a function of temperature, are shown for glycerol in Figure 5-5. We display the present data measured by interferometry and time-domain Brillouin scattering together with literature data from impulsive stimulated scattering measurements [YCN88] and ultrasonics [JNB86]. All features in the data are consistent with the material undergoing a transition from liquid to glass. For high temperatures where  $1/\tau_R \gg \omega$  and the acoustic damping rate is low, the velocity increases linearly with temperature. A value for the zero frequency limiting speed  $c_0^l$ , which describes the adiabatic propagation of longitudinal acoustic waves in an equilibrated liquid, can be extrapolated from this low frequency side of the relaxation. By further assuming a linear dependence on the temperature, points from different techniques in the region from 270 K to 440 K can be fitted. This analysis yields

$$c_0^l(T) = (2610 \pm 5)[\text{m/s}] - (2.30 \pm 0.02)[\text{m/s}] \times T[\text{K}] , \quad (5.13)$$

as depicted in Figure 5-5 (a) by the dashed line. The parameters determined by the linear fit of Equation 5.13 are in excellent agreement with the ones reported by Comez *et al.* in [CFM03] and determined  $c_0^l(T) = (2593 - 2.286 \cdot T) [\text{m/s}]$  for the low frequency limit of the longitudinal velocity in the temperature 307 – 390 K.

A significant change in the sound speed and a peak in the damping rate is observed around  $1/\tau_R \sim \omega$ . For the different displayed frequencies this appears in the temperature range 250 K - 370 K. At low enough temperatures or high enough acoustic frequencies where  $1/\tau_R \ll \omega$ , the damping reduces to low values, and again the acoustic velocity increases approximately linearly with decreasing temperature. A fit of the velocity vs. temperature in this range yields a phenomenological expression for the evolution of the instantaneous longitudinal sound speed  $c_\infty$ ,

$$c_\infty^l(T) = (4635 \pm 10)[\text{m/s}] - (5.45 \pm 0.5)[\text{m/s}] \times T[\text{K}] . \quad (5.14)$$



The large frequency range available allows us to extrapolate the expressions for low and high-frequency acoustic velocities over a broad temperature range.

Close to the glass transition,  $T_g = 186$  K, and below, the material shows a solid-like response for all measured frequencies, and a crossover to another linear behavior is observed:

$$c_{glass}(T) = (3750 \pm 3)[\text{m/s}] - (0.85 \pm 0.02)[\text{m/s}] \times T[\text{K}] . \quad (5.15)$$

Equations 5.13 and 5.14 together with the temperature dependence of the density, given by Equation A.3, allow us to determine the two limiting elastic moduli, the relaxed longitudinal elastic modulus  $M_0$  and the unrelaxed modulus  $M_\infty$ :

$$M_0(T) = (8.49 \pm 0.04)[\text{GPa}] - (1.28 \pm 0.03) \cdot 10^{-2}[\text{GPa}] \times T[\text{K}] \quad (5.16)$$

$$M_\infty(T) = (26.9 \pm 0.2)[\text{GPa}] - (5.2 \pm 0.1) \cdot 10^{-2}[\text{GPa}] \times T[\text{K}] . \quad (5.17)$$

### 5.2.2 Results: DC704

Figure 5-6 shows the combined results obtained from our measurements on DC704 and data obtained at other frequencies by our collaborators. A similar analysis to that used for glycerol can be carried out. The data for DC704 also exhibit well-known features expected of the structural relaxation process: namely, a marked dispersion of the sound velocity, accompanied by a maximum peak in the absorption, a typical S-shape dispersion curve that is bounded by the limiting high (unrelaxed) and low (relaxed) frequency values of the velocity, and a change in the slope in  $c(T)$  at about 210 K which indicates the occurrence of a liquid-glass transition.

For high temperatures and low frequencies where the acoustic damping rate is low, the velocity increases linearly with temperature allowing us to extrapolate a value for the zero frequency sound velocity  $c_0^l$ . Here we have assumed linear dependence on the temperature, and data obtained from different techniques are fitted in the region from 220 K to 350 K. This analysis yields

$$c_0^l(T) = (2465 \pm 5)[\text{m/s}] - (3.52 \pm 0.02)[\text{m/s}] \times T[\text{K}] . \quad (5.18)$$

At temperatures lower than the temperature range 220 K - 300 K, in which a strong peak in the damping rate is observed for the different techniques, the damping once again drops, leading to an increase in acoustic velocity that is approximately linearly with the decrease in temperature. A fit of the velocity vs. temperature in this range yields a phenomenological expression for the evolution of the instantaneous



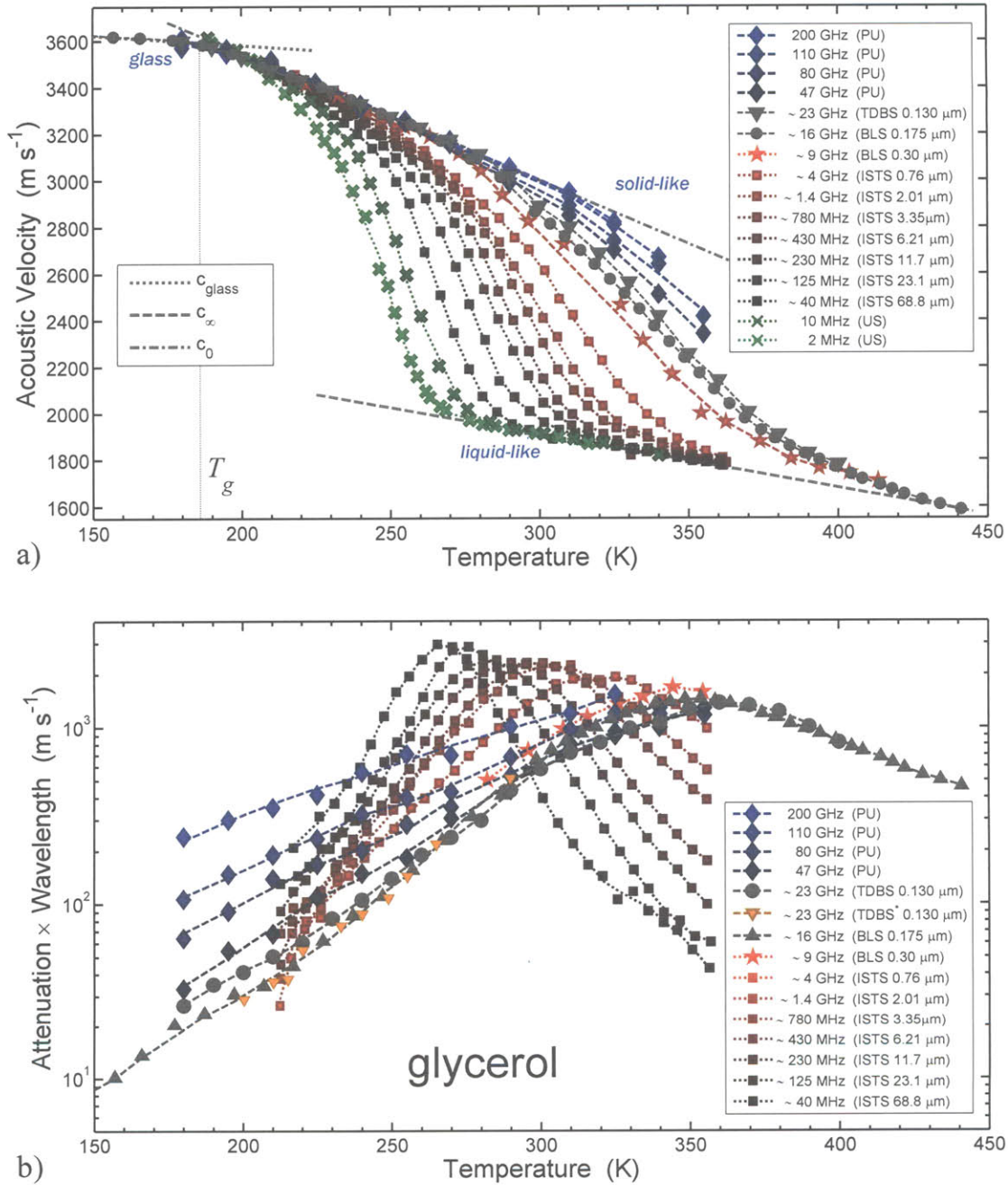
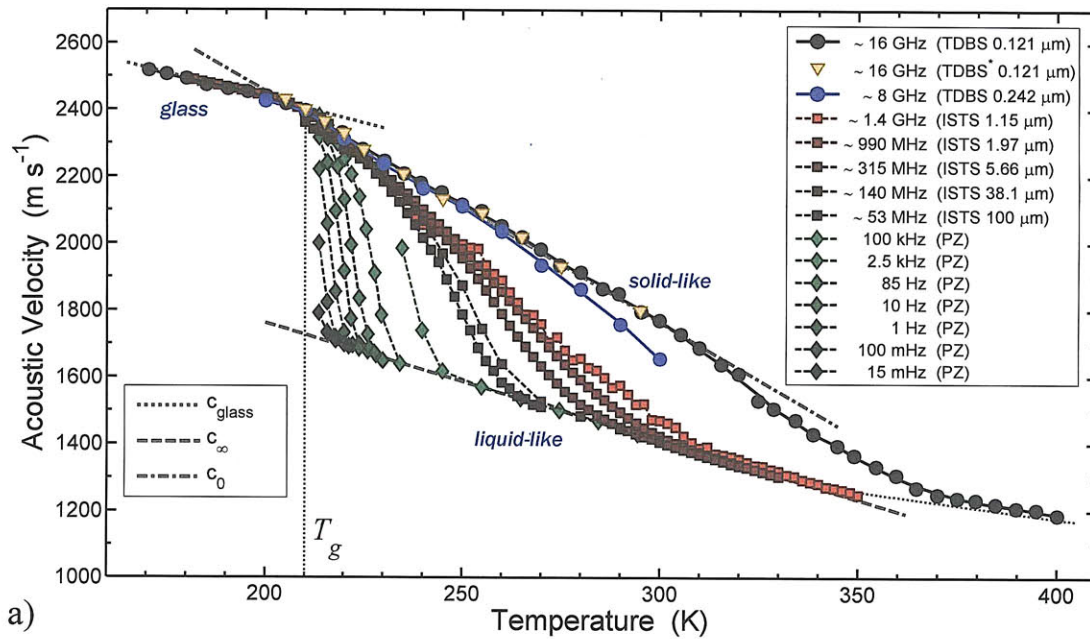
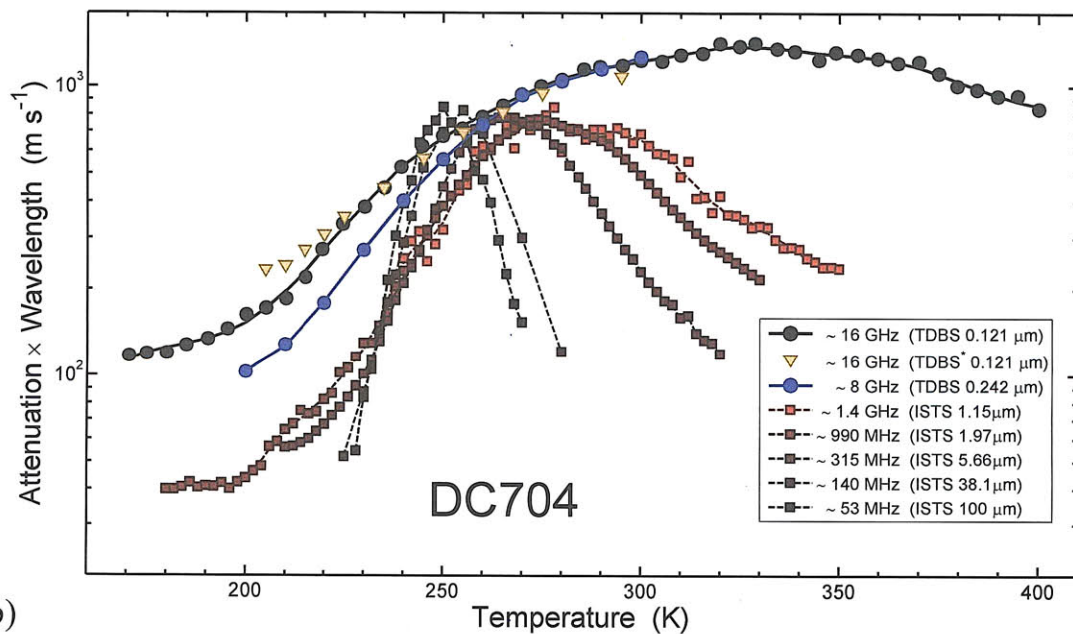


Figure 5-5: Acoustic velocity (a) and scaled damping rate (b) in glycerol as a function of temperature. Present results from interferometric measurements (PU) at four selected frequencies and time-domain Brillouin scattering (TDBS) are shown. In the acoustic damping plot we added data from a similar TDBS\* measurement as reported by T. Hecksher [Hec06] which are in excellent agreement with ours. We also show data from impulsive stimulated thermal scattering (ISTS) [YCN88] and conventional ultrasonics (US) [JNB86].



a)



b)

Figure 5-6: Acoustic velocity (a) and scaled damping (b) in DC704 as a function of temperature. Present results from time-domain Brillouin scattering (TDBS) at two different wave vectors are represented with full circles and similar TDBS\* measurements from T. Hecksher [Hec06] show excellent agreement. Impulsive stimulated thermal scattering (ISTS) data are from [Tor10] and [Joh10], and Piezo-Electric Modulus Gauge (PZ) data from [HO10].

(unrelaxed) longitudinal sound velocity  $c_{\infty}^l$ :

$$c_{\infty}^l(T) = (3835 \pm 10)[\text{m/s}] - (6.9 \pm 0.4)[\text{m/s}] \times T[\text{K}] . \quad (5.19)$$

The large frequency range made available by piecing together data obtained using various techniques enables the extrapolation of the expressions for both the low and high-frequency acoustic velocities over broad ranges of temperatures.

Close to the glass transition in DC704,  $T_g = 210$  K, and below, the material is solid-like for all measured frequencies and the aforementioned crossover to another linear behavior is observed, which approximately follows:

$$c_{glass}^l(T) = (3035 \pm 10)[\text{m/s}] - (3.05 \pm 0.04)[\text{m/s}] \times T[\text{K}] . \quad (5.20)$$

### 5.2.3 Non-Linear Interaction of Acoustic Wave with the Liquid

Based on what we learned from the cumulative heating studies presented in Section 4.5, we used sapphire generation side substrates whenever possible. This structure enables the cumulative heating effect to be kept low, ensuring that the liquid temperature is only increased to a couple of K above the initial temperature (as shown in the simulation results of Figure 4-10). For such a sample, the drop in temperature away from the transducer film is very small and should only manifest, if at all, in a very small positive chirp in the signal due to a small negative temperature gradient away from the transducer film.

However, a careful analysis of Brillouin scattering data at low temperature (below  $T_g$ ) shows a clear and rather strong increase in the initial Brillouin frequency  $f_0$  as a function of pump fluence. In addition, there is a strongly pump fluence dependent negative chirp constant  $C$ . Pump fluence dependent results for DC704 at 200 K are depicted in Figure 5-7. A trend opposite to that expected from cumulative heating is clearly observed.

#### 5.2.3.1 Possible Origin of Frequency Increase and Negative Chirp

Different origins for the observed behavior are conceivable, arising from either a change in refractive index or a change in the speed of sound in the liquid. The most plausible and relevant possibilities are listed below:

- Heat induced refractive index change of the local oscillator: The probe beam portion reflected by the transducer film could be affected in some way by

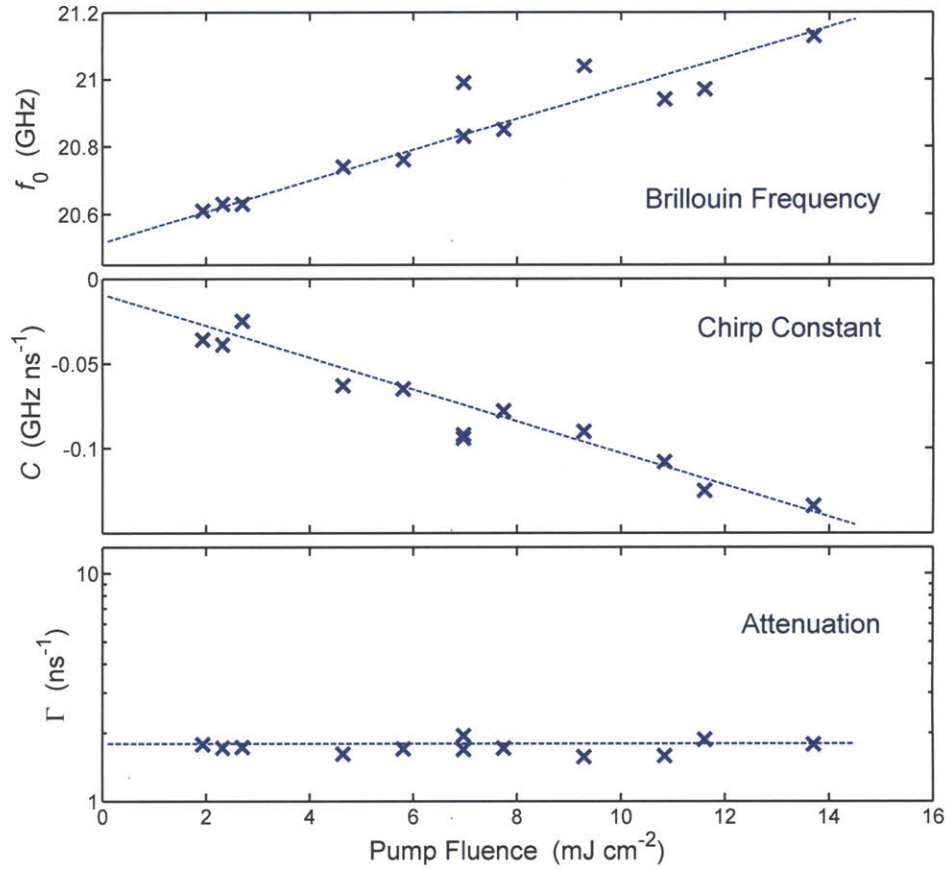


Figure 5-7: Brillouin scattering parameters obtained from fits by equation 4.1 for measurements on DC704 at 200 K. The sample structure features a 60 nm aluminum transducer film on a sapphire generation side substrate and a sapphire detection side substrate – the best possible structure from a thermal point of view (because of sapphire’s high thermal conductivity). Measurements at different pump fluences were recorded in random order over several days to eliminate any effects due to hysteresis or chemical changes of the liquid.

the shot-to-shot heating of the transducer film (up to several hundred degrees Kelvin) and its subsequent cooling on the timescale of the measurement.

- Heat induced pressure gradient in the liquid: Assuming a very viscous liquid at temperatures around  $T_g$ , such high viscosities might prevent the liquid from equilibrating a pressure gradient that resulted from a temperature gradient induced thermal expansion.
- Probe beam deflection at transducer film: Thermalization of the transducer film resulting from the energy absorption of the pump laser beam follows the spatial

Gaussian energy distribution of the optical pulse. Such thermal expansions cause a slight curvature of the transducer film surface.

- Wavevector shift of the local oscillator beam through the Doppler effect: pump pulse absorption (thermal expansion) causes an almost instantaneous displacement of the transducer film. The subsequent relaxation (cooling) of the transducer film back to its original position on the experimental timescale results in a slight shift in the optical wavevector of the local oscillator.
- Thermal lensing: The temperature gradient in the liquid changes the local refractive index, possibly creating a thermal lens in the liquid.
- Data acquisition problem: e.g. wobbling stage
- Data analysis problem: e.g. originating in problems with the fitting routine
- Non-linear interaction of the propagating acoustic wave with the liquid: high acoustic strain amplitudes require the inclusion of higher order elastic constants for modeling the propagating acoustic wave in the liquid.

We estimated the magnitudes of all these effects carefully and came to the conclusion that the magnitude of each effect (except for the last one) is at least one to two orders of magnitude too small to explain the observations, e.g. made in figure 5-7. A series of further investigations supports the assumption that the origin of the deviation of the Brillouin fit parameter (e.g. there should be no or a slightly positive chirp caused by the temperature gradient) lies in the nonlinear interaction between the acoustic waves and the liquid.

First, pump fluence dependent measurements were carried out at a number of different laser repetition rates and the obtained values for the linear chirp fit parameter  $C$  are shown in figure 5-8. These values all fall on the same curve in the pump fluence-chirp parameter plot, allowing all effects related to cumulative heating to be ruled out. Cumulative heating would result in a qualitatively similar dependence of the linear chirp fit parameter  $C$  with overall pump power and not with pump fluence. The initial Brillouin scattering frequency  $f_0$  and attenuation  $\Gamma$  show the same behavior. This set of measurements confirms that the values of the fit parameters are functions of the pump fluence, not of pump power. In contrast, measurements on glycerol in a glass/glass cell show a marked decrease in the amount of positive chirp at lower laser repetition rates, confirming that the effects described earlier are due to cumulative heating of the liquid.

Second, analysis of a temperature dependent study at a constant and low pump fluence of  $3.5 \text{ mJ cm}^{-2}$  suggests that the chirp parameter is related to the acoustic



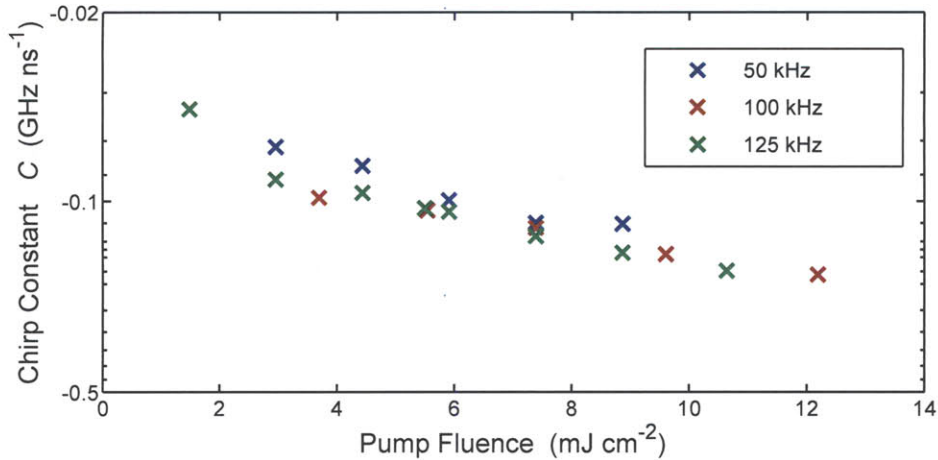


Figure 5-8: Pump fluence dependence of linear chirp constant  $C$  in DC704 at an initial temperature of 200 K at different laser repetition rates. The data points show the same pump fluence dependent behavior even though the amount of deposited heat varies for different laser repetition rates. A similar behavior is observed for the Brillouin frequency, i.e. the data points for similar pump fluences fall on the same curve. As a result, any possible origin of the negative chirp and frequency increase due to cumulative heating is ruled out.

attenuation rate. The temperature dependence of the three Brillouin fit parameters, frequency, chirp and attenuation, is plotted in figure 5-9. The acoustic attenuation rate increases by about an order of magnitude over the temperature range shown while the chirp constant increases by two orders of magnitude. This finding strongly suggests that the magnitude of the chirp is related to the acoustic strain amplitude. Figure 5-10 shows the comparison of Brillouin scattering parameters measured in a glycerol sample from either single pulse or multiple pulse excitation (by seven pulses at the Brillouin scattering frequency, labeled as Deathstar in Figure 5-10) at an initial temperature of 170 K. For similar pump powers, data recorded with multiple pulse excitation show significantly smaller effects than those recorded with a single pulse which is another clear evidence against cumulative heating as the source.

Finally, two additional measurements using multiple pulse excitation were carried out to further investigate the origin of the Brillouin scattering parameter. First, the excitation pulse train was used to ‘stretch’ the acoustic pulse duration launched into the liquid. For this, the sequence of optical pulses was set to a high frequency, in order to stretch the acoustic input pulse from about 8 ps up to almost 40 ps (limited by the Brillouin oscillation period of 47 ps), which are listed in Table 5.1. In this type of measurement, a constant acoustic strain amplitude can be maintained while the spectrum is shifted to lower frequencies. The Brillouin fit parameters shown

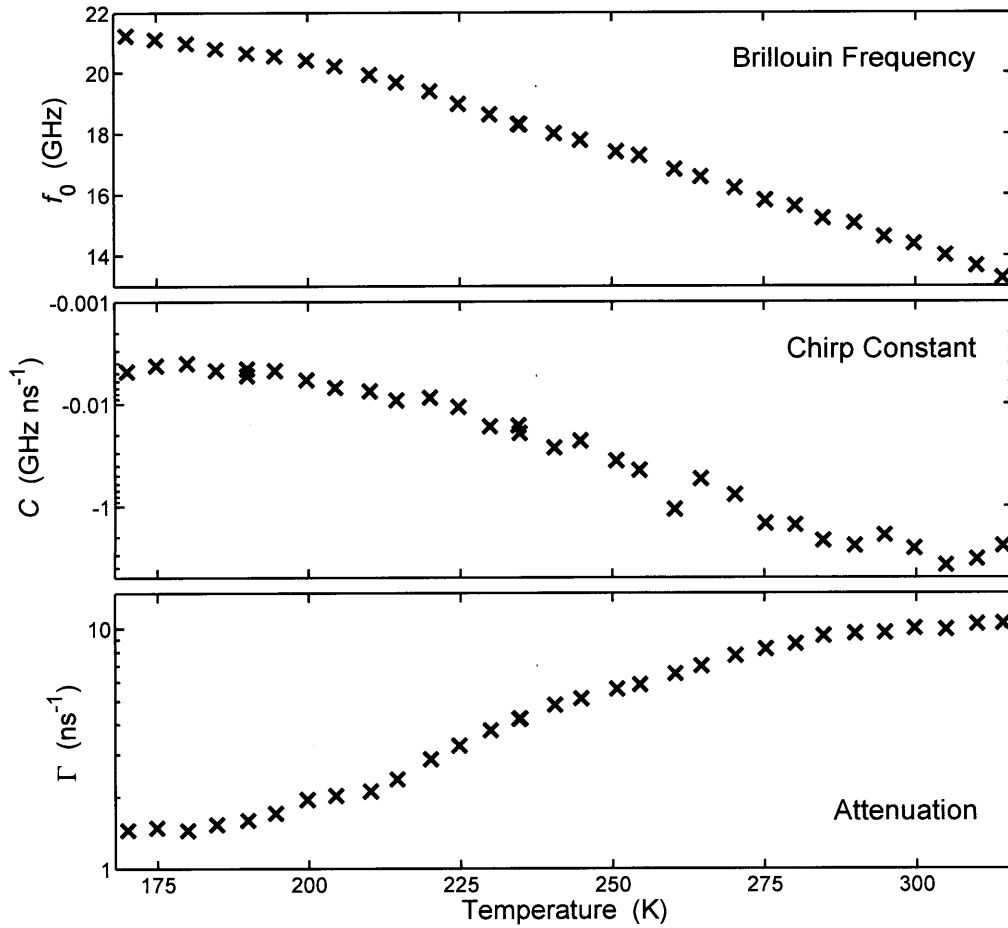


Figure 5-9: Brillouin scattering fit parameters for DC704 as a function of temperature at a relatively low fluence of  $3.5 \text{ mJ cm}^{-2}$ . The chirp fit parameter  $C$  changes by about two orders of magnitude over the displayed temperature range and follows a similar trend as the inverse of the attenuation rate  $\Gamma$ . This suggests that the chirp is related to the acoustic amplitude, hinting at an acoustic origin of the chirp.

in the table only vary within the experimental uncertainties of the measurements and therefore the results suggest no dependence of the observed negative chirping effect on the shape of the acoustic strain. In a second type of experiment using multiple pulse excitation, the frequency of the pulse sequence was set to match the frequency of the Brillouin oscillations. This allows the pump fluence to be kept constant while the acoustic energy is spread out into a series of pulses such that the strain amplitude per pulse is reduced. The extracted parameters can then be compared with parameters obtained from measurements recorded under the same conditions but with the excitation by a single pulse. Experiments were carried out on DC704 and glycerol at different temperatures over many different levels of pump



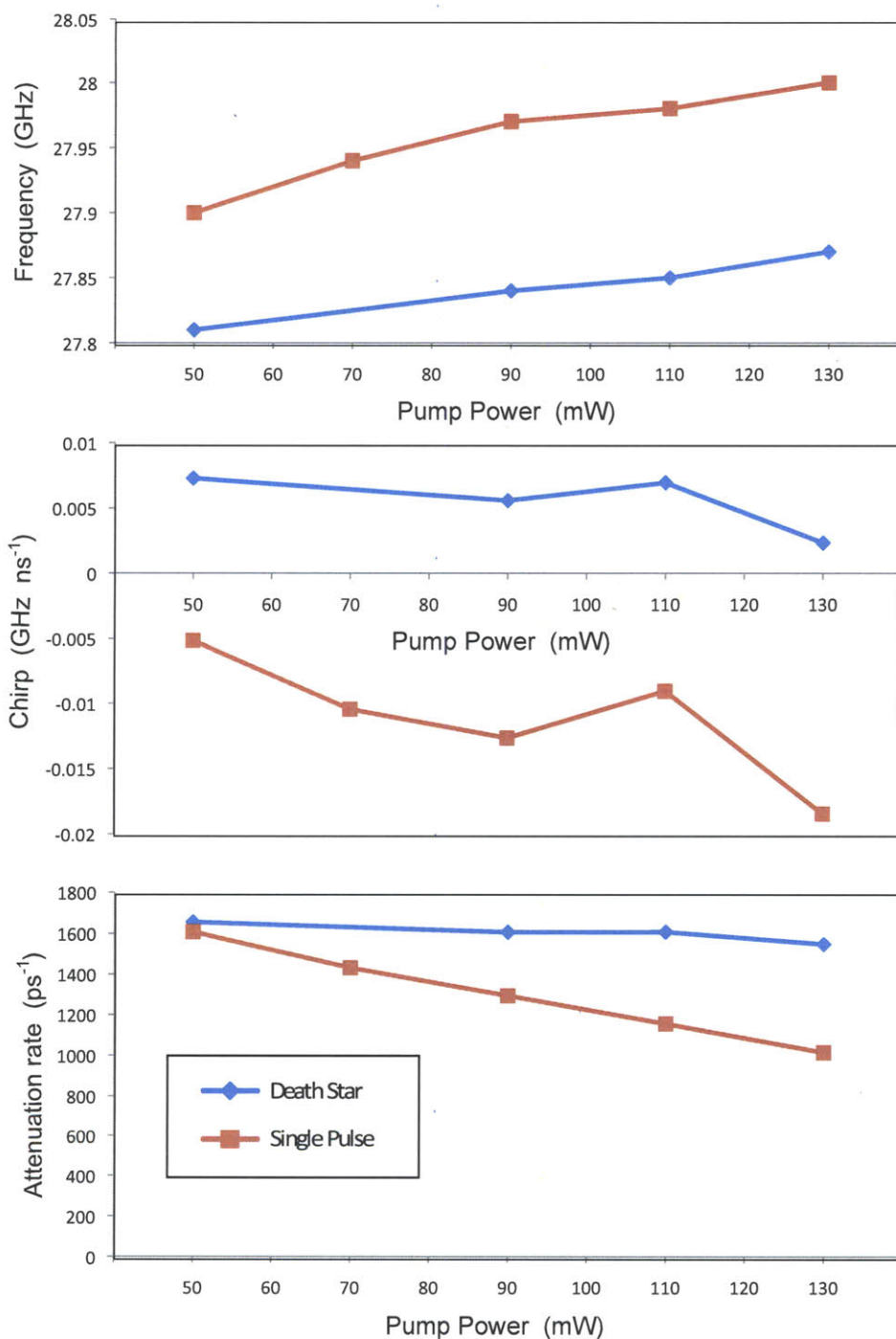


Figure 5-10: Brillouin scattering in glycerol at 170 K: Comparison of single pulse vs. multiple pulse excitation. A clear difference in all displayed parameters is visible. Note that the values of the chirp coefficient are significantly smaller than the ones in case of DC704, suggesting a weaker non-linear response at similar strain amplitudes.

Table 5.1: Brillouin scattering fit parameters for measurements on DC704 at various acoustic pulse widths. The ambient temperature was 200 K and the pump fluence was 10.5 mJ/cm<sup>2</sup>. The acoustic pulse duration can be tuned within a certain range using the Deathstar pulse shaper. A pump pulse train at a frequency above the natural bandwidth of the transducer film but within the range to broaden the generated acoustic output pulse can be generated by the Deathstar pulse shaper. The acoustic pulses are broadened by shifting the generated acoustic frequency spectrum to lower frequencies while keeping the overall acoustic amplitude constant. Even though the acoustic pulse duration is changed by a factor of about 5, the fit parameter only varies within the uncertainty of the experiment and shows no dependence on the acoustic pulse width.

Deathstar frequency [GHz]	<i>Inf</i>	<i>Inf</i>	400	200	125	125
acoustic FWHM [ps]	~ 8	~ 8	~ 15	~ 25	~ 38	~ 38
frequency $f_{BS}$ [GHz]	21.29	21.32	21.28	21.29	21.31	21.33
time constant $\tau$ [ps]	509	518	519	536	605	598
chirp $C$ [GHz/ns]	-0.114	-0.113	-0.087	-0.093	-0.103	-0.097

fluences. It was observed that the extracted fit parameters from measurements with multiple pulse input always contained smaller deviations of the Brillouin fit parameter for frequency, chirp and attenuation as a function of pump fluence.

The results from the experiments reported above support the hypothesis that the dependence of the Brillouin scattering fit parameters on pump fluence can be explained by a non-linear interaction of the propagating strain pulse with the liquid. At high strain amplitudes, the interaction of the propagating acoustic wave with the liquid cannot be considered linear anymore and higher order elastic constants must be taken into account. In a simple physical picture, high strain amplitudes elicit large deviations from equilibrium density, at which point the restoring force is out of equilibrium and the material effectively becomes stiffer [vCD06]. Therefore, in our measurement, the liquid's response to high strain amplitudes results in an increasing Brillouin frequency and an increasing negative chirp with increasing strain amplitudes, which can be expressed by modifying the time dependent frequency  $\omega(t)$  of equation 4.1a to the form

$$\omega(t) = 2\pi \cdot f_0 (1 + \Theta_0 \cdot \epsilon_{NL} \cdot \exp[-\Gamma \cdot t]) . \quad (5.21)$$

In this expression for the fitted time-dependent angular frequency  $\omega(t)$ ,  $f_0$  is the linear Brillouin frequency at sufficiently small acoustic strain amplitudes,  $\Theta_0$  is an amplitude proportional to the acoustic strain amplitude  $A_0$ ,  $\epsilon_{NL}$  the material's tem-

perature dependent non-linear coefficient and  $\Gamma$  the acoustic attenuation constant of equation 4.1a. The non-linear coefficient is related to the elastic coefficients by  $\epsilon_{NL} = 1 + b/2a$  where  $a$  is the linear elastic coefficient,  $a = C_{ijkl}$ , of the liquid and  $b$  is the second-order non-linear coefficient. The density of the material is then given by  $\rho = \rho_0 + a \partial_x \rho + b/2 \partial_x^2 \rho$  [Tou10].

Even though equation 5.21 describes the system adequately, it is not as robust as the linear chirp model given by equation 4.1 and thus we did not adopt this model. In order to properly apply this non-linear chirp model, not only iterations of the fitting form 5.21 to data recorded at a single pump fluence are necessary but also iterations within a data set of a number of pump fluences in which the frequency  $f_0$  and the non-linear coefficient  $\epsilon_{NL}$  converge to a single value that fits all the data from the set. The amplitude  $\Theta_0$  which is proportional to the acoustic strain amplitude  $A_0$  can be approximated as being proportional to the pump fluence. However, since the linear chirp model is sufficient to quantify the non-linear interaction of the acoustic waves at high strain amplitudes, we refrain from using a fit model with non-linearly chirped frequency.

### 5.2.3.2 Conclusion

The nonlinear responses observed here may open the door to versatile nonlinear acoustic spectroscopy in the GHz frequency range. This could be of considerable interest in connection with structural and polarization relaxation dynamics. The combination of a sapphire substrate and an aluminum transducer film might be the ideal choice for these kind of experiments for several reasons. First, the high thermal conductivity of sapphire ensures sufficient cooling of the transducer film in between consecutive laser pulses which is particularly important here since high pump fluences (with resulting large amounts of heat deposition in the transducer film) are desirable to generate large acoustic strain amplitudes. Second, aluminum is particularly well suited as the transducer material because its high thermal expansion allows it to generate higher strain amplitudes through the same amount of heat than other transducer materials. Finally, the large positive reflection coefficient of the sapphire-aluminum interface not only allows most of the acoustic energy to be transmitted into the liquid under study but the acoustic wave launched from this interface also has a unipolar shape. As a result, the strain pulse is only compressional, without a rarefying tail, and the steep repulsive part of the intermolecular potential might reach nonlinear regimes faster than the more slowly varying attractive potential.

For the purposes of linear acoustic spectroscopy in this chapter and chapter 6, the primary outcome of our present results shows that the lowest possible pump fluence should be used for these measurements in general.

## 5.3 Broadband Acoustic Spectra and Analysis

### 5.3.1 Composition of Broadband Acoustic Spectra

To compile acoustic spectra over a broad frequency range, the results from several different spectroscopic techniques have to be pieced together. In Figure 1-2 we gave an overview of various techniques available that all probe the mechanical (longitudinal, bulk or shear) responses of a liquid and the frequency range each of them covers. In the following subsection we briefly sketch the principles of the techniques used to compile the broadband spectra of glycerol and DC704 to be presented and discussed later in this section.

#### 5.3.1.1 Piezo-Electric Modulus Gauge Techniques

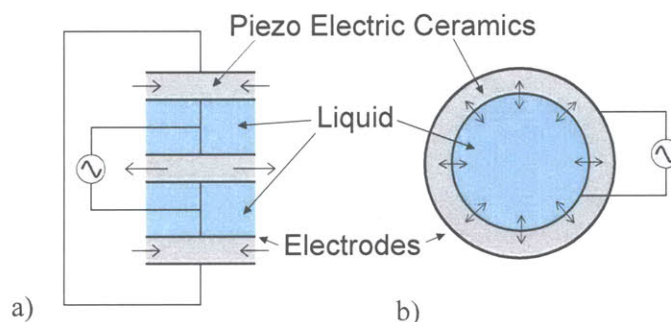


Figure 5-11: Sketches of (a) Piezoelectric shear modulus gauge (PSG) and (b) Piezoelectric bulk modulus gauge (PBG) which allow the shear and bulk elastic moduli of a liquid to be measured at frequencies from millihertz up to several tens of kilohertz. An oscillating electric field applied to piezoelectric ceramics in particular arrangements generates either nearly pure shearing or volume oscillations. Adding liquid to either configuration changes the frequency-dependent capacitance of each system which allows one to extract the complex shear or bulk modulus.

At low frequencies, from millihertz up to several tens of kilohertz, the PSG [CO95] and the PBG [CO94] can measure the complex frequency dependent shear and bulk moduli,  $\hat{G}(\omega)$  and  $\hat{K}(\omega)$ , respectively, allowing the complex longitudinal modulus  $\hat{M}(\omega)$  to be calculated through the relation  $\hat{M}(\omega) = \hat{K}(\omega) + \frac{4}{3}\hat{G}(\omega)$ . Their principles of operation are sketched in Figure 5-11. Both the PSG and the PBG rely on the piezoelectric effect, i.e. that certain materials deform when exposed to an electric field.

The PBG is made of a spherical ceramic shell of 1 to 2 cm in inner diameter with electrodes on both the inside and outside. Applying an oscillating electric field at a

set frequency  $\omega$  over the electrodes causes the shell to contract and expand radially, creating a volume oscillation. The capacitance of this system changes when the shell is filled with liquid since the liquid opposes this radial motion. The measured frequency-dependent capacitance can then be translated into the complex elastic modulus  $\hat{K}(\omega)$  of the liquid through modeling of the entire mechanical system.

The principle of operation of PSG relies on the same effect as PBG but in a different geometry. In this case, three piezo-ceramic discs with electrodes are connected electrically such that the two outer discs will expand radially when the inner disc contracts and vice versa. This gives a (almost) pure shear deformation of the two liquid layers between the discs. The measured capacitance of the system can be translated into the complex shear elastic modulus  $\hat{G}(\omega)$  of the liquid.

In both types of measurements, the frequency is fixed and respective complex moduli are measured.

### 5.3.1.2 Ultrasonic Techniques

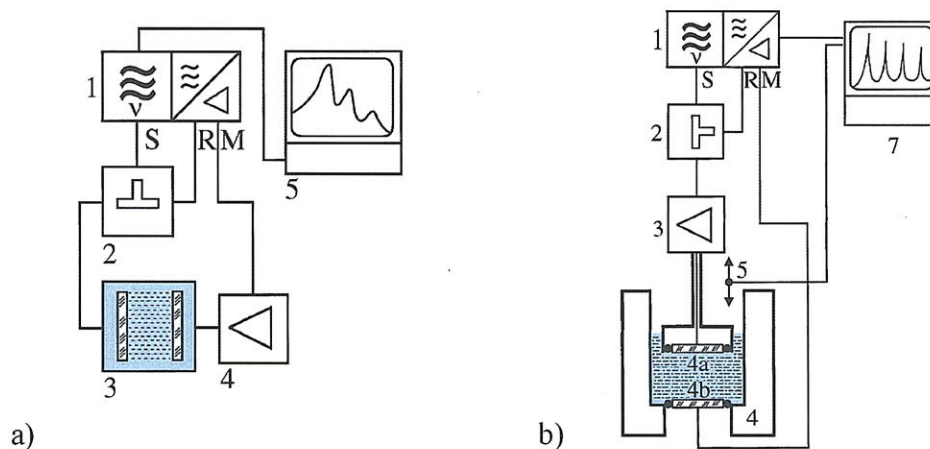


Figure 5-12: Block diagram for (a) ultrasonic resonator measurements and for (b) continuous wave transmission method. (a) A network analyzer (1) is used to generate a driving signal S that is split (2) into two parts and fed to the resonator cell (3) with the liquid and the reference input R of a superheterodyne receiver unit. A pre-amplifier (4) amplifies the signal before it is fed into the measurement channel M of the superheterodyne receiver unit. A computer (5) controls all processes. (b) The signal output S of a network analyzer (1) gets split into two parts by a signal splitter (2) and amplified by a broad-band amplifier (3) before being fed to the transmitter crystal (4a) in the sample cell (4). The transmitted acoustic signal gets detected by the receiver crystal (4b) and fed into the superheterodyne receiver unit. A stepping motor (5) controls the transducer spacing. From [KBL01].

At high kilohertz and megahertz frequencies, ultrasonic (US) techniques provide both longitudinal speeds and attenuation rates. Two different approaches are illustrated in Figure 5-12. In a cavity resonator cell measurement, a circular cylindrically shaped resonator cavity with fixed path length is completely filled with liquid. Plane waves, propagating in the direction of the cell axis, are excited and received by disc-shaped transducers forming the cell faces and form a standing acoustic wave. This technique is well suited for measurement of acoustic properties below a couple of megahertz down to about 10 kHz, where the attenuation is low.

Traveling wave transmission methods, as depicted in Figure 5-12, are the low frequency equivalent of our interferometric approach and well established for measurements of liquids at frequencies between about 1 MHz and 5 GHz. An acoustic wave (either pulsed or continuous-wave) is generated by a quartz transducer crystal on one side of a liquid cell and received by a receiver crystal after transmission through the liquid. The cell is provided with a computer controlled sliding carriage for smooth variation of the transmitter/receiver spacing, and the acoustic transmission through different liquid thicknesses is analyzed to extract the speed of sound and attenuation coefficients. Although the sample cells and parts of the electronic apparatus have to be exchanged due to their bandwidth limitations, the same principle of measurement is suitable over the entire frequency range. The pulse mode of operation requires a rather complicated apparatus that includes a receiver and amplifier unit with sufficiently broad detection bandwidth permitting the detection of the transmitted signals without significant distortion of the pulse shape. At hypersonic frequencies ( $> 1$  GHz), continuous-wave measurements using variable pathlength cells are preferable since the use of narrowband spectrum analyzers instead of broadband superheterodyne receivers will significantly enhance SNR. The reader may refer to [KBL01] for a detailed discussion of ultrasonic approaches and references.

In ultrasonic approaches the frequency is fixed and a complex wavevector is measured.

### 5.3.1.3 Impulsive Stimulated Scattering

In the megahertz frequency range, Impulsive Stimulated Scattering (ISS) techniques measure both longitudinal and shear sound velocities and damping, depending upon the experimental geometry [YN87]. In case of impulsive stimulated thermal scattering (ISTS) which is sensitive to longitudinal waves only, absorption of excitation laser pulses in the liquid results in a sudden heating and a thermal expansion in a spatially varying pattern. The expansion generates an acoustic response whose wavelength matches the excitation interference fringe spacing. In this manner, the wavevector magnitude  $q$  matches the wavevector difference between the excitation



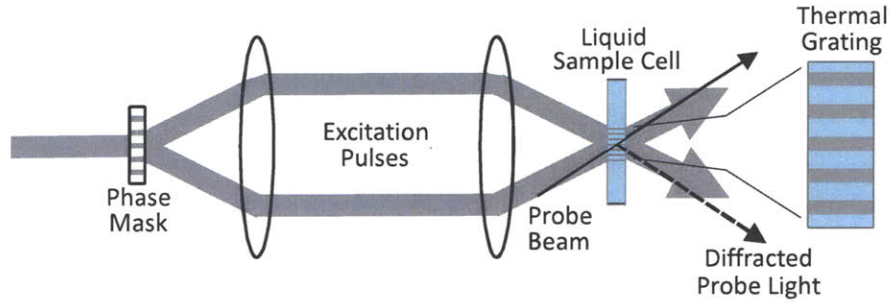


Figure 5-13: Sketch of impulsive stimulated thermal scattering (ISTS) technique. A diffractive optic (phase mask) generates the two excitation beams which are crossed inside the liquid sample. A probe beam incident on this grating gets diffracted and allows to probe both the acoustic and thermal responses of the material under study. Many mask patterns with different periods are etched onto a single glass substrate for rapid wavevector and acoustic frequency tuning.

pulses. The acoustic frequency of the generated longitudinal acoustic wave is given by the dispersion relation  $\omega(q)$  of the sample.

Diffraction of a probe laser pulse incident on the transient grating arises through acoustically induced changes in the refractive index (generally only the real part), which is particularly sensitive to density. The signal shows time-resolved acoustic oscillations which eventually decay due to acoustic damping. This transient acoustic response has frequency  $\omega_{ac}(q)$  at the selected wavevector, allowing the speed of sound  $c_{ac}(q) = \omega_{ac}(q)/q$  and the decay of the acoustic oscillation envelope which is related to the acoustic attenuation  $I(t) \sim \exp(-\Gamma_{ac}t)$  to be determined.

There is also a quasi-steady-state density modulation which decays at long time due to diffusion of the heat from the grating peaks to the nulls. At low temperatures but above the glass transition, structural relaxation dynamics extend to time scales significantly longer than that of the acoustic response, resulting in reduced acoustic damping and slow components of thermal expansion that are observed directly in the data. Its dynamics can typically be well described by the stretched exponential or Kohlrausch-Williams-Watts functional form of equation 2.11, yielding additional information about the relaxation dynamics in the kilohertz to low megahertz regime.

In this type of measurement, the wavevector is fixed and a complex frequency is measured.

#### 5.3.1.4 Frequency-Domain Brillouin Scattering

Brillouin light scattering (BLS) studies acoustic waves with frequencies between high hundreds of megahertz up to about 10 GHz [CFSM03]. Thermal fluctuations in the



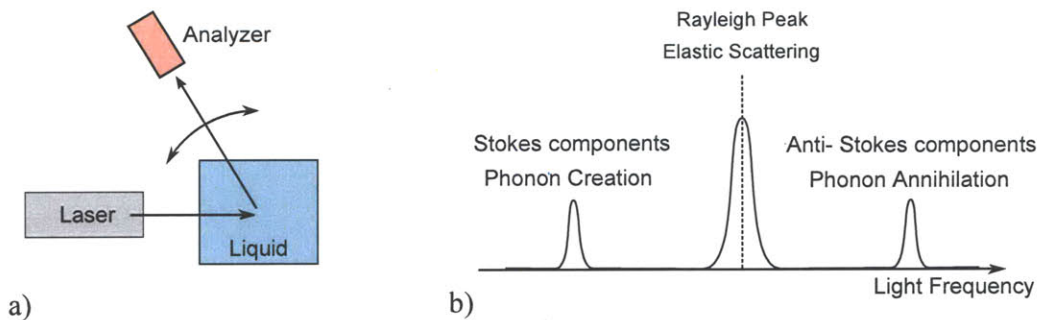


Figure 5-14: (a) Sketch of Brillouin scattering setup. Photons from a monochromatic laser beam are scattered in all directions upon interaction with thermal phonons present in the liquid. An analyzer with high spectral resolution, typically a Sandercock-type multi-pass Fabry-Pérot interferometer, analyzes the frequency spectrum of the scattered light. (b) Schematic illustration of a Brillouin spectrum. The Rayleigh peak originates from quasi-elastically scattered light that has not shifted in its center peak frequency. If the resolution of the analyzer is sufficient, two weak side peaks (typically on the order of  $10^{-6}$  with respect to the Rayleigh intensity) are visible. They come from an inelastic scattering process of the coherent laser light with incoherent thermal phonons, either from the creation (Stokes) or annihilation (anti-Stokes) of a phonon whose frequency and wavevector with respect to the incoming laser light determine the shift frequency and scattering angle.

density are studied directly as a result of the interactions between a coherent beam of photons with thermally driven phonons. The general concept of BLS is sketched in Figure 5-14 (a).

According to Debye's theory of specific heat (originally developed as a crystal lattice theory), the thermal fluctuations of a system can be considered as a superposition of acoustic modes that include all directions of wave propagation across a broad distribution of wavelengths. If a beam of monochromatic light is scattered from a thermal spectrum of acoustic modes onto a detector with a small aperture, conservation of momentum in the scattering processes leads to a selection of particular acoustic waves from the thermal spectrum. These waves propagate in both directions of the bisector of the scattering angle and their wavelength has to obey Bragg's law of scattering. Due to energy conservation, scattering of photons by the thermally driven acoustic waves leads to frequency-shifted lines in the light spectrum. In correspondence with the two possible directions of wave propagation along the bisector of scattering angle, a down-shifted Stokes line and an up-shifted anti-Stokes line exist in addition to the central (unshifted) Rayleigh line, as depicted in Figure 5-14 (b). The magnitude of the shift  $\delta f_{\text{light}}$  equals the frequency  $f_{BLS}$  of the acoustic wave under consideration, so the sound velocity of the liquid can be determined by measuring the scattering angle

and the shift in the light spectrum. When sufficiently high spectral resolution of the Brillouin spectrometer is available, the half-width  $\Delta f_{BLS}$  of the Brillouin (Stokes and anti-Stokes) lines can be used to evaluate the acoustic attenuation coefficient  $\alpha$  of the selected acoustic modes which are related to one another according to

$$\alpha(f_{BLS}) = \pi \Delta f_{BLS} / c, \quad (5.22)$$

where  $c$  is the speed of sound. In order to achieve this high resolution, almost all Brillouin scattering experiments use a Fabry-Pérot interferometer. However, conventional Fabry-Pérot interferometers do not achieve the contrast needed to resolve the weak Brillouin doublets. Sandercock first showed that a multipass spectrometer significantly improves contrast. In addition, it was recognized that coupling of two synchronized Fabry-Pérots helps to eliminate the overlap of different orders of interference signal.

Inelastic X-ray scattering and Neutron scattering measurements both rely on the same physical principle as BLS and only differ in the type of radiation used in the scattering experiment. Both allow to probe significantly higher acoustic frequencies. The wavevector is fixed and the complex frequency is measured in all types of scattering measurements.

### 5.3.1.5 Concluding Remarks on different techniques

Strictly speaking, the results obtained from the different techniques are not exactly equivalent since in some of them, i.e. ISS, BLS and TDBS, a (real) wavevector is specified and a (complex) frequency is measured while in others, i.e. PSG, PBG, US and interferometry, a (real) frequency is specified and a (complex) wave vector is measured. This important distinction has to be kept in mind when comparing data from different techniques. In practice, except in the limit of extremely strong damping, the results are invertible.

## 5.3.2 Broadband Spectrum Analysis of Glycerol

### 5.3.2.1 Broadband Spectrum: Speed of Sound

First, we combine the data obtained from our measurements in glycerol using ISTS and ultrasonics to compile the mechanical spectra from 2 MHz up to 200 GHz. We start by analyzing the temperature and frequency dependence of the acoustic velocity. While going from the viscous to the elastic regime, energy losses affecting acoustic propagation are considerably reduced. Therefore, we expect an increase in the sound velocity with both reduction in temperature and increase in frequency, as shown in

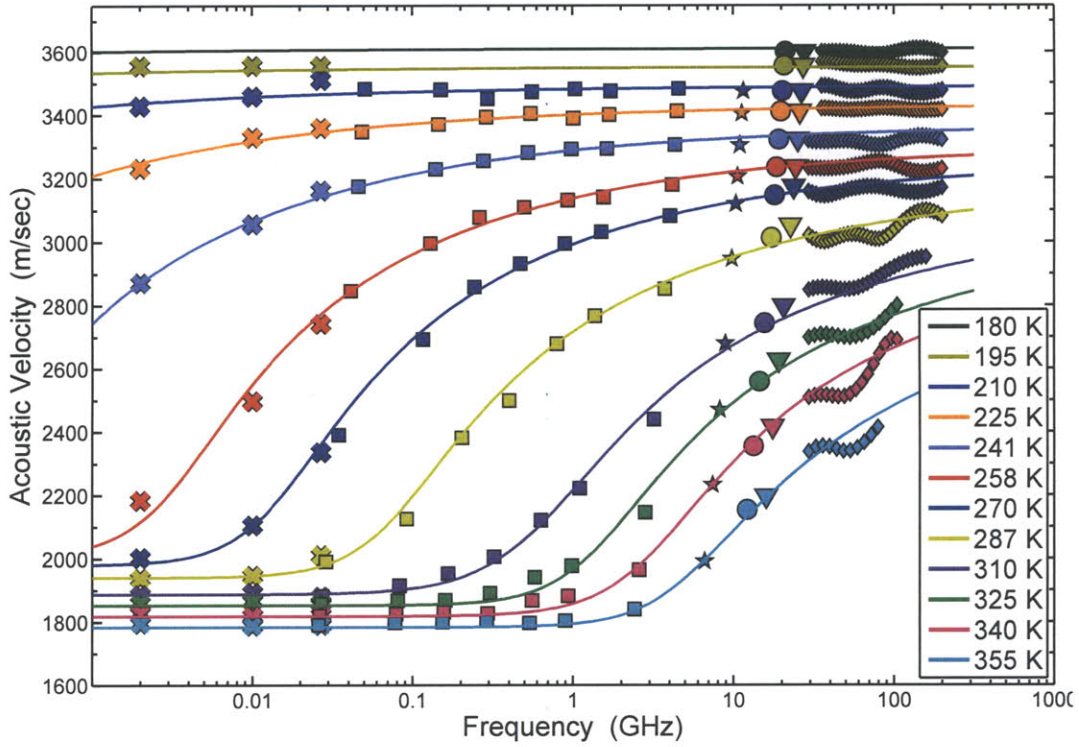


Figure 5-15: Acoustic velocity of glycerol as a function of frequency at several temperatures. (✕) represents data from ultrasonics, (■) represents data from ISTS, (★ and ●) represents data from BLS, (▼) represents data from TDBS and (◆) represents data from interferometric measurements. Data sources are given in Figure 5-5. The solid curves are fits by a Cole-Davidson form with an exponent parameter of  $\beta_{CD} = 0.3$ . The slight wave behavior in the data points from interferometry measurements is an artifact of the data extraction algorithm as described in Section 5.1.2.

Figure 5-15. Various phenomenological models have been developed in an attempt to describe such viscoelastic crossover. One of the most popular models is based on the assumption that the time decay of fluctuations in density and other quantities can be well approximated by a KWW stretched exponential having the form  $\exp(-\frac{t}{\tau})^\beta$ . The corresponding frequency dependence can be derived from such a distribution through a Laplace transform and can be fairly well approximated by a Cole-Davidson (CD) function (Equation 2.9), giving the frequency-dependence of the sound velocity as:

$$c^2(\omega) = c_\infty^2 - (c_\infty^2 - c_0^2) \operatorname{Re} \left[ \left( \frac{1}{1 + i\omega\tau} \right)^{\beta_{CD}} \right] \quad (5.23)$$

where  $c_0$  and  $c_\infty$  can be used from the fits given in Equations 5.13 and 5.14, respectively. We have performed such fits for data sets at all temperatures as shown in Figure 5-15. Excellent agreement is obtained for  $\beta_{CD} = 0.3$ .

### 5.3.2.2 Broadband Spectrum: Modulus

The complex longitudinal acoustic modulus  $\hat{M}(\omega)$  can be calculated by

$$\hat{M}(\omega) = \rho \left( \frac{1}{c(\omega)} - i \frac{(\Gamma \cdot \lambda)(\omega)}{2\pi c^2(\omega)} \right)^{-2} \quad (5.24)$$

from the speed of sound  $c(\omega)$  and scaled acoustic attenuation rate  $(\Gamma \cdot \lambda)(\omega)$  given in Figure 5-16 (a) and (b), respectively. The real part of the elastic modulus is a measure of the stiffness of a material. In Figure 5-16 (a) we see that for a liquid in the supercooled regime this quantity shows dispersion. At low frequencies and high temperatures the value of the modulus  $M'(\omega)$  is small, indicating a soft (liquid-like) material, while at high frequencies and low temperatures the value of the modulus increases, indicating a higher stiffness of the material. The limiting value at low frequencies is given by  $M_0(T)$  while the limiting value at high frequencies is determined by  $M_\infty(T)$ . The temperature dependence of both quantities is given by the linear interpolations of Equations 5.16 and 5.17, respectively.

### 5.3.2.3 Broadband Spectrum: Compliance

From the real and imaginary parts of the complex modulus,  $\hat{M}(\omega) = M'(\omega) + iM''(\omega)$ , determined by Equation 5.24 and shown in Figure 5-16, we can calculate the longitudinal compliance  $\hat{J}(\omega)$  which is simply the inverse of the modulus:

$$\hat{J}(\omega) = \frac{1}{\hat{M}(\omega)} = \frac{1}{M'(\omega) + iM''(\omega)}. \quad (5.25)$$

Compliance is a linear response function and is thus a susceptibility. The longitudinal compliance  $\hat{J}(\omega)$  is chosen for the following analysis over the modulus since mode-coupling theory predictions are usually expressed in terms of susceptibility.

### 5.3.2.4 Mode-Coupling Theory Analysis

Figure 5-17 shows the longitudinal compliance spectrum for glycerol at different temperatures. The figure shows that the maximum of the susceptibility spectra, a signature of the  $\alpha$ -relaxation process, is only visible down to 258 K in the available frequency range. Above a critical temperature  $T_c$  and at frequencies above the  $\alpha$ -relaxation peak up to a minimum in the susceptibility, mode-coupling theory predicts

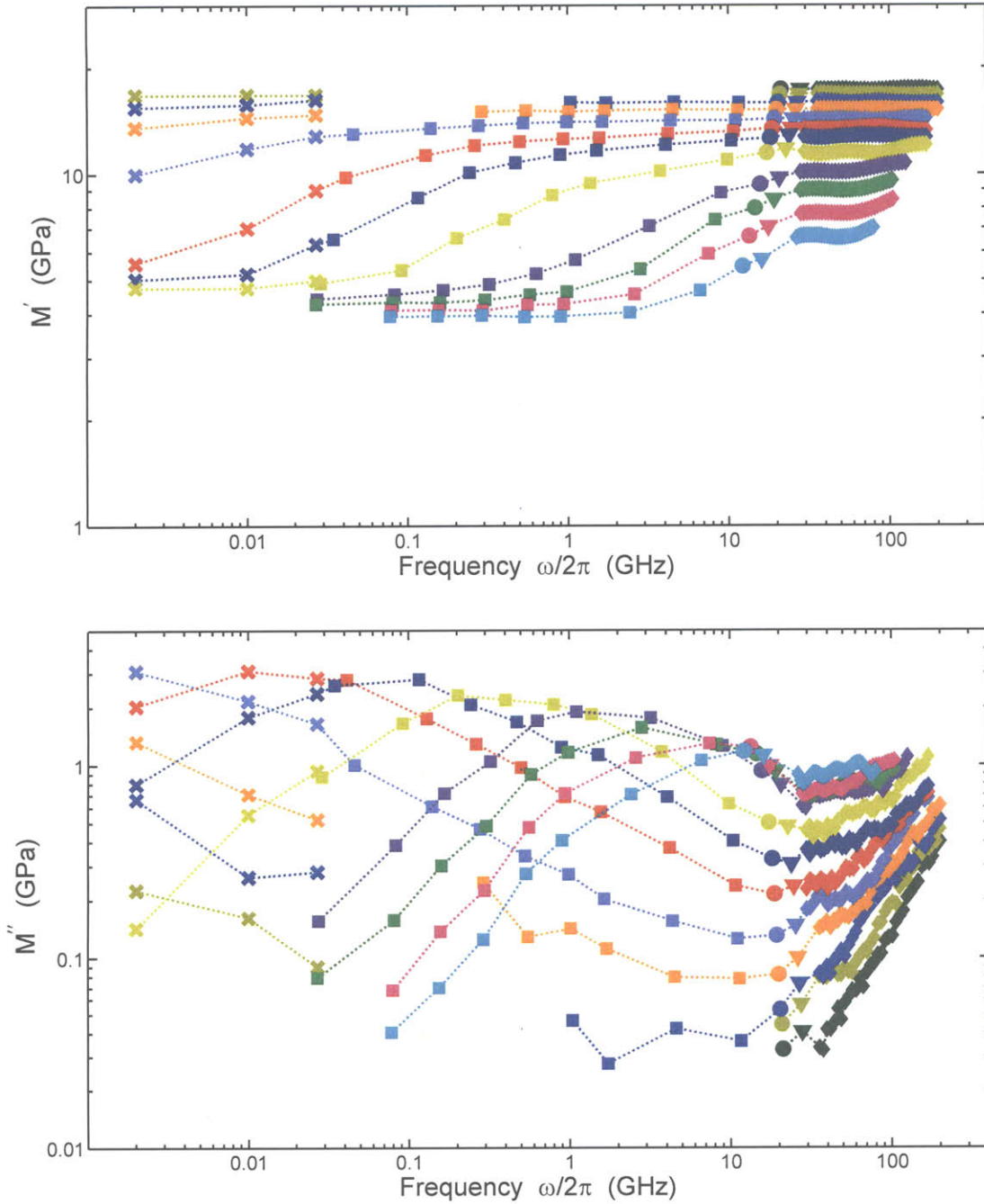


Figure 5-16: Real and imaginary parts of the longitudinal modulus of glycerol vs. frequency. The same data sources are used as in Figures 5-15. The real part of the elastic modulus measures the stiffness of a material. For a liquid in the supercooled state this quantity shows dispersion; the limiting value at low frequencies is given by  $M_0$  while the limiting value at high frequencies is  $M_\infty$ .



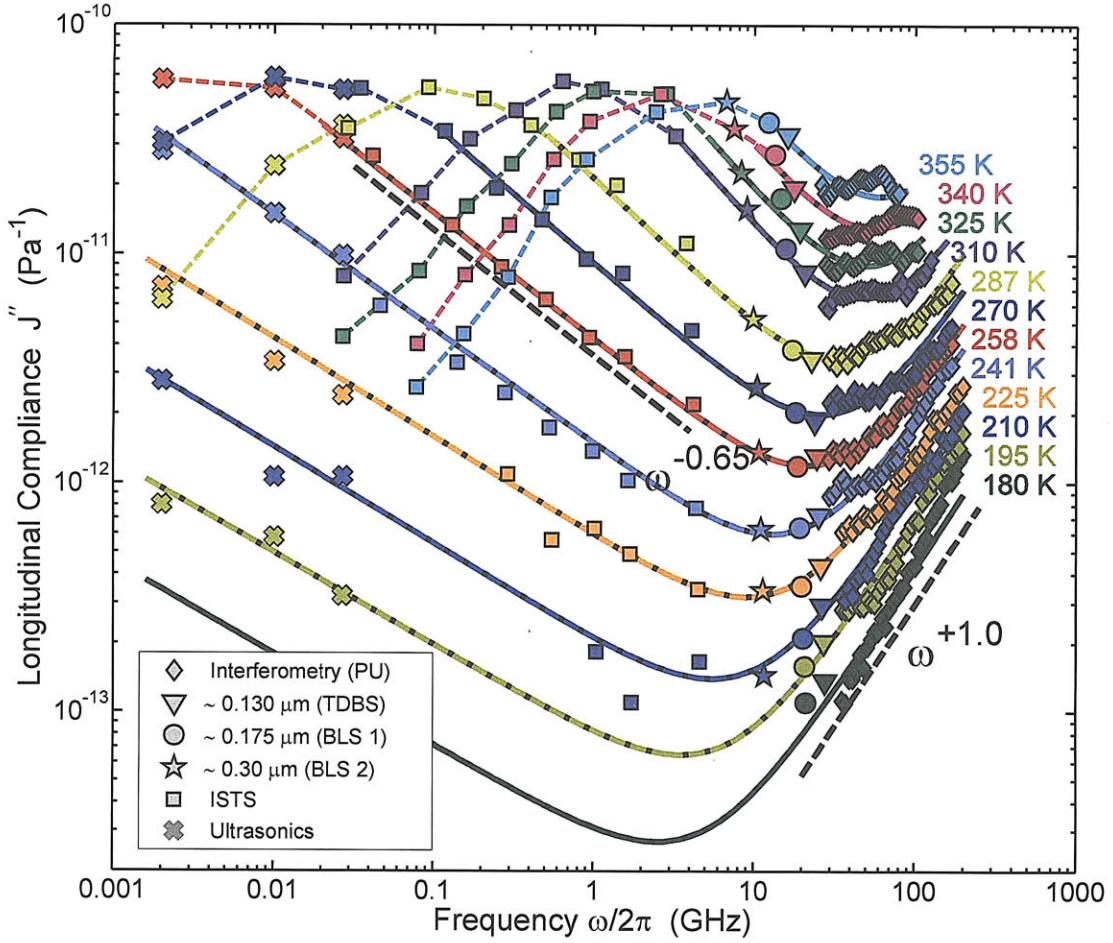


Figure 5-17: Longitudinal compliance spectrum  $J''(\omega)$  of glycerol. The thick lines are fits by the mode-coupling theory power-law prediction for the minimum in the susceptibility given by Equation 5.27. The exponent  $b = 0.65 \pm 0.03$  is determined for  $J'' \sim \omega^{-b}$  at the low frequency and  $a = 1.0 \pm 0.03$  is determined for  $J'' \sim \omega^a$  at the high frequency side of the minimum of the susceptibility at temperatures above 241 K.

that the  $\alpha$ -relaxation tail in the susceptibility spectrum has a power-law frequency dependence of  $J''(\omega) \sim \omega^{-b}$ , where the values of  $b$  vary within the range  $0 < b \leq 1$ . At frequencies above the minimum, the spectrum is predicted to resume a sub-linear power-law frequency dependence,  $J''(\omega) \sim \omega^a$ , where values of  $a$  and  $b$  are subjected to the MCT constraint

$$\lambda = \frac{\Gamma^2(1-a)}{\Gamma(1-2a)} = \frac{\Gamma^2(1+b)}{\Gamma(1+2b)}, \quad (5.26)$$

which implies  $a < b$  and limits  $a$  to  $a \leq 0.395$  when  $b \leq 1$ .

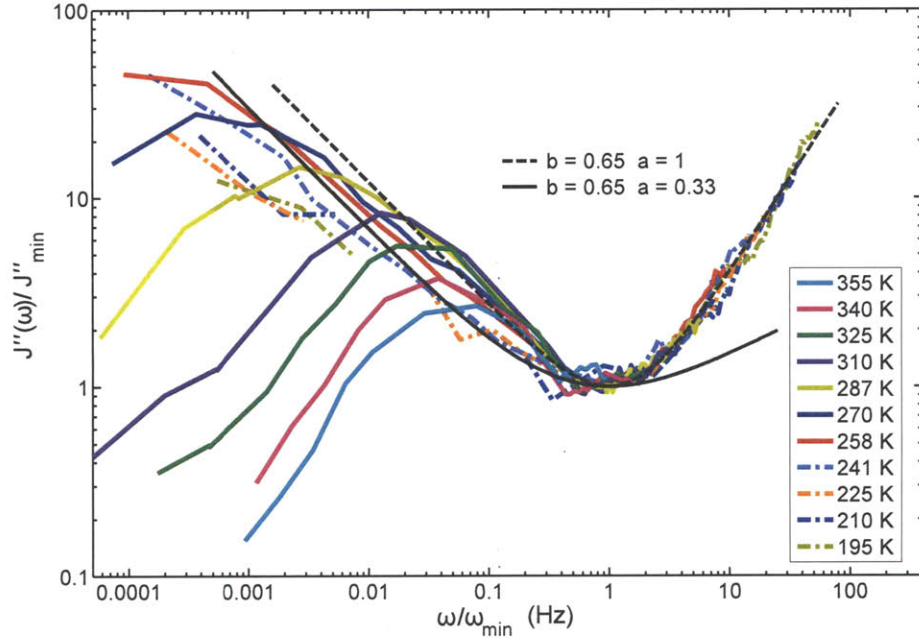


Figure 5-18: Susceptibility spectra of Figure 5-17, rescaled so that their minima  $J''_{min}$  at  $\omega_{min}$  coincide. Solid line: theoretical curve predicted by mode-coupling theory with  $a = 0.33$  and  $b = 0.65$ , dotted line: best fit to temperatures above 258 K with  $a$  and  $b$  not fixed,  $a = 1$  and  $b = 0.65$ .

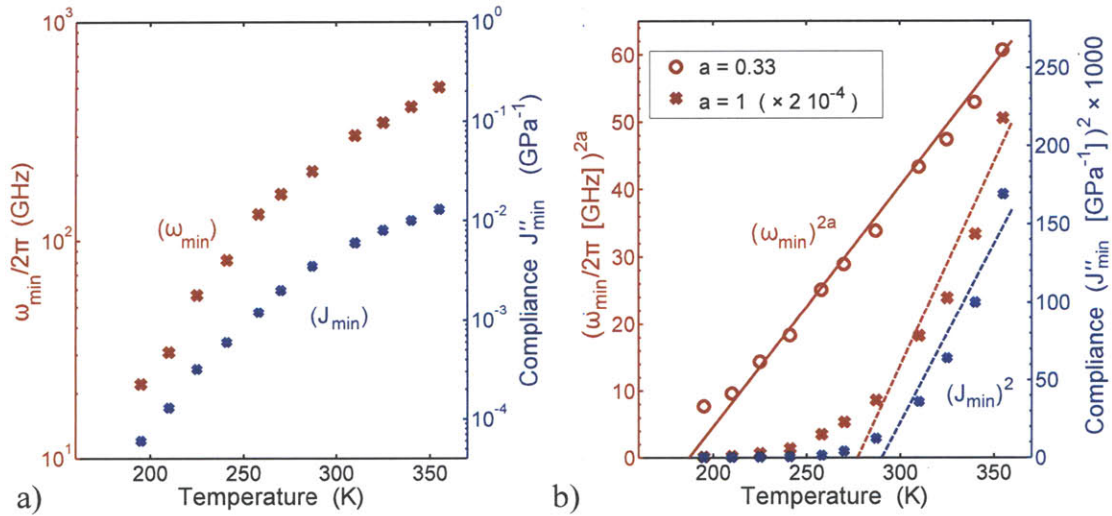


Figure 5-19: (a) Temperature dependence of frequency  $\omega_{min}$  and magnitude  $J''_{min}$  of the susceptibility minimum as determined by fits of Equation 5.27 to the data in Figure 5-17. (b)  $(\omega_{min})^{2a}$  and  $(J''_{min})^2$  vs.  $T$ . While the extrapolation of the critical temperature with the free fit parameter  $a = 1$  ( $\star$ ) gives  $T_c \approx 285$  K for both the frequency and magnitude of the minimum, the use of the MCT predicted value of  $a = 0.33$  (o) yields a significantly different critical temperature of  $T_c \approx 190$  K.



At temperatures well above  $T_c$ , the  $\alpha$ -relaxation occurs fast enough so that the high-frequency wing of the  $\alpha$  susceptibility spectrum overlaps with the low-frequency wing of the  $\beta$ -relaxation, and the susceptibility minimum between  $\alpha$  and  $\beta$ -relaxation features can be described by an interpolation of the form

$$J''(\omega) = \frac{J''_{min}}{a+b} \left[ b \left( \frac{\omega}{\omega_{min}} \right)^a + a \left( \frac{\omega}{\omega_{min}} \right)^{-b} \right]. \quad (5.27)$$

Free fits of this form to the data in Figure 5-17 at all temperatures are indicated by the solid lines and yield values for  $b$  of  $\approx 0.65$  and  $a$  close to or slightly above 1. With the position obtained for the frequency at the compliance minimum  $\omega_{min}$  and the minimum compliance value  $J''_{min}$  we can rescale the data around the minimum which is shown in Figure 5-18.

Assuming a value for  $b$  of 0.65, the restriction imposed on the exponents by Equation 5.26 fixes  $\lambda$  to be 0.69 and  $a$  to be 0.33. Values of  $a$  and  $b$  very similar to those obtained from our fits of the susceptibility minimum by Equation 5.27 were observed by Wuttke *et al.* in a neutron scattering study of glycerol [WHL<sup>+</sup>94]. In particular, they also found a value of  $a = 1$  in the temperature range 273 – 363 K and they attributed the deviation from the MCT prediction to a “white noise or Debye-density-of-states-like behavior which leads up to the boson peak”.

The fits of Figure 5-17 also provide us with the temperature evolution of the frequency  $\omega_{min}(T)$  and the magnitude of the susceptibility minimum  $J''_{min}(T)$  as shown in Figure 5-19 (a). A critical temperature  $T_c$  can be deduced from the temperature dependence of these two parameters. From the scaling relation of mode-coupling theory:

$$\omega_{min}(T) \sim (T - T_c)^{1/(2a)} \quad (5.28)$$

$$J''_{min}(T) \sim (T - T_c)^{1/2}. \quad (5.29)$$

To directly obtain the critical temperature we plot  $(\omega_{min})^{2a}$  and  $(J''_{min})^2$  vs.  $T$  in Figure 5-19 (b). When the value of  $a = 1$  from the free fits is used, a critical temperature of  $T_c \approx 285$  K for both, the frequency and magnitude of the minimum are obtained. This yields  $T_c \approx 1.55 \cdot T_g$  which is quite high compared with typical values of fragile glass-formers around  $T_c \approx 1.2 \cdot T_g$ . When the mode-coupling theory predicted value of  $a = 0.33$  is used, a significantly different value for the critical temperature,  $T_c \approx 190$  K is obtained.

### 5.3.2.5 Conclusion

Our data around the minimum can be described, at least qualitatively in a restricted scaling range, by the mode-coupling theory predictions for the susceptibility minimum. For frequencies above the minimum,  $J''$  increases much more steeply than predicted by the theory. However, our results for  $a$  and  $b$  are in reasonable agreement with the results from neutron scattering by Wuttke *et al.* [WHL<sup>+</sup>94], especially the exponent parameter  $a$  for which they also found a value around 1. Their postulate regarding this deviation from the predictions of mode-coupling theory is that the boson peak in glycerol, as in other network materials, is generally more pronounced than in fragile systems due to an increased strength of the microscopic dynamics, possibly enhanced by the network hydrogen bonds, which extends to relatively low frequencies. It should be also noted that the predictions used above come from schematic models of mode-coupling theory which considers a fluid made of shapeless particles for which the only dynamical variables are the positions of the centers of mass. This does not describe well the situation in glycerol which exhibits directional forces due to hydrogen bonding.

## 5.3.3 Broadband Spectrum Analysis of DC704

### 5.3.3.1 Broadband Spectrum of DC704

Next, we analyze the longitudinal acoustic results for DC704. Figure 5-20 shows the longitudinal compliance spectrum  $J''(\omega)$  vs.  $\omega$  including our data obtained from interferometry, TDBS at two optical detection wavelengths, 790 nm and 395 nm, and ISTS. The solid lines are free fits having a combined form, consisting of the Fourier transform of the Kohlrausch-Williams-Watts function (KWW, Eq. 2.11) for the  $\alpha$ -peak and the mode-coupling theory interpolation formula (Eq. 5.27) for the minimum.

In Figures 5-21 and 5-22 we show the real and imaginary parts of the longitudinal compliance of DC704 for various temperatures across a very broad frequency range. The data sources are the same as those used in Figure 5-20, but low frequency data from piezo-electric techniques are now added.  $J''(\omega)$  in Figure 5-22 follows the  $\alpha$ -relaxation, which exhibits the typical asymmetrically shaped relaxation peak across more than 12 decades in frequency. As mentioned above, the relaxation behavior at frequencies around the  $\alpha$ -peak is described by a KWW equation. The choice of a KWW functional form over another form is arbitrary and the purpose of the fits is mainly to qualitatively compare the peak behavior at different temperatures. Since the same stretching parameter  $\beta = 0.53 \pm 0.01$  can be applied to fit the peak at all tem-

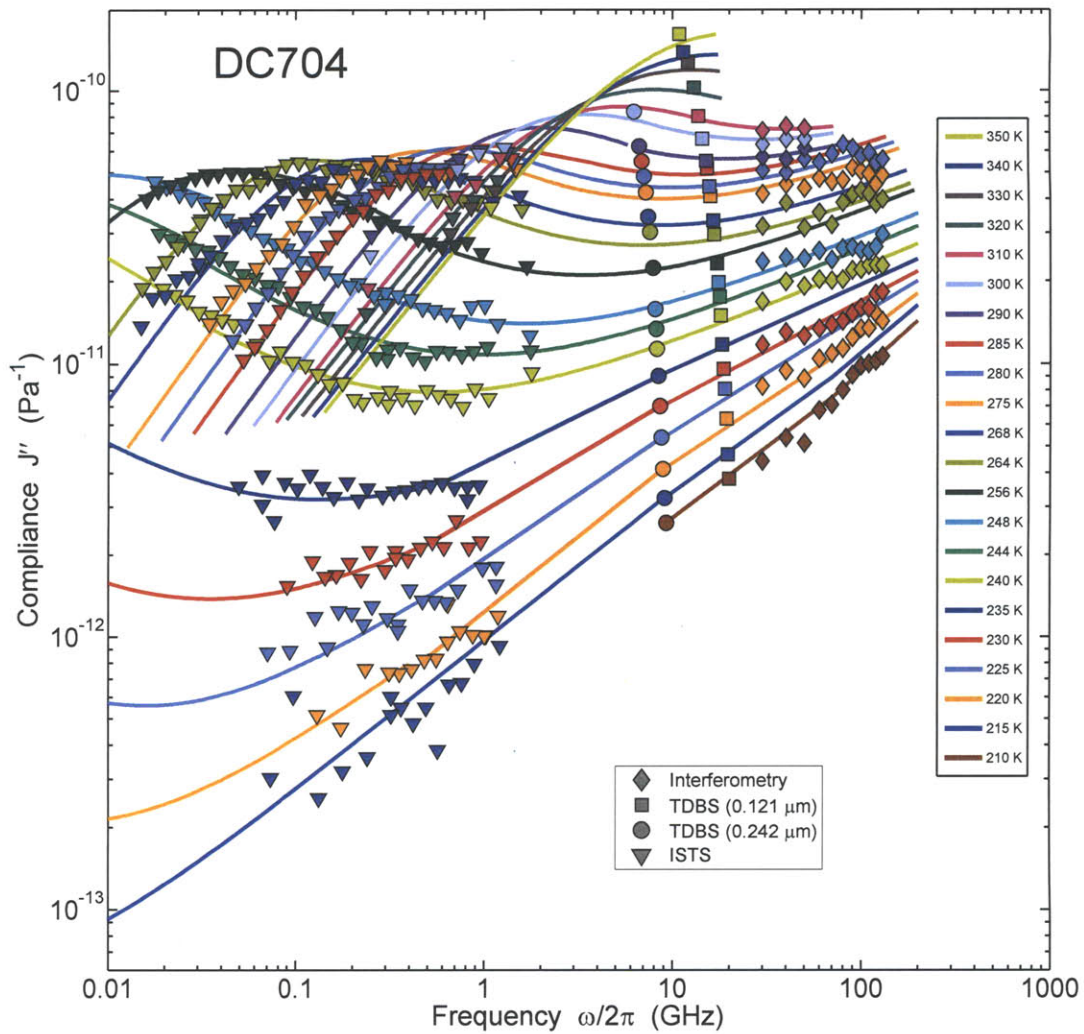


Figure 5-20: Frequency dependence of the longitudinal compliance spectrum  $J''(\omega)$  vs.  $\omega$  of DC704 at various temperatures. The solid lines are fits based on the mode-coupling theory prediction for the susceptibility minimum which satisfy well the predicted relationship between  $a$  and  $b$  at temperatures above 235 K.

peratures, the so-called time-temperature superposition principle clearly holds over the entire temperature range. The inverse of the peak frequencies, the  $\alpha$ -relaxation times  $\langle\tau_\alpha\rangle$ , and the magnitudes  $J''_\alpha$ , are shown in Figure 5-23 (a). The relaxation feature in  $J''$  is accompanied by a relaxation step in  $J'$  as seen in Figure 5-21. The lines are Cole-Davidson fits (Equation 2.9) where the zero and infinite frequency limiting values for the speed of sound from Equations 5.18 and 5.19 are used to calculate  $J_0$  and  $J_\infty$ , respectively. The same relaxation times as for the KWW fits to the  $\alpha$ -peaks of Figure 5-22 were used. Although the fits reproduce the general behavior of the data, the quality of the agreement is poor.

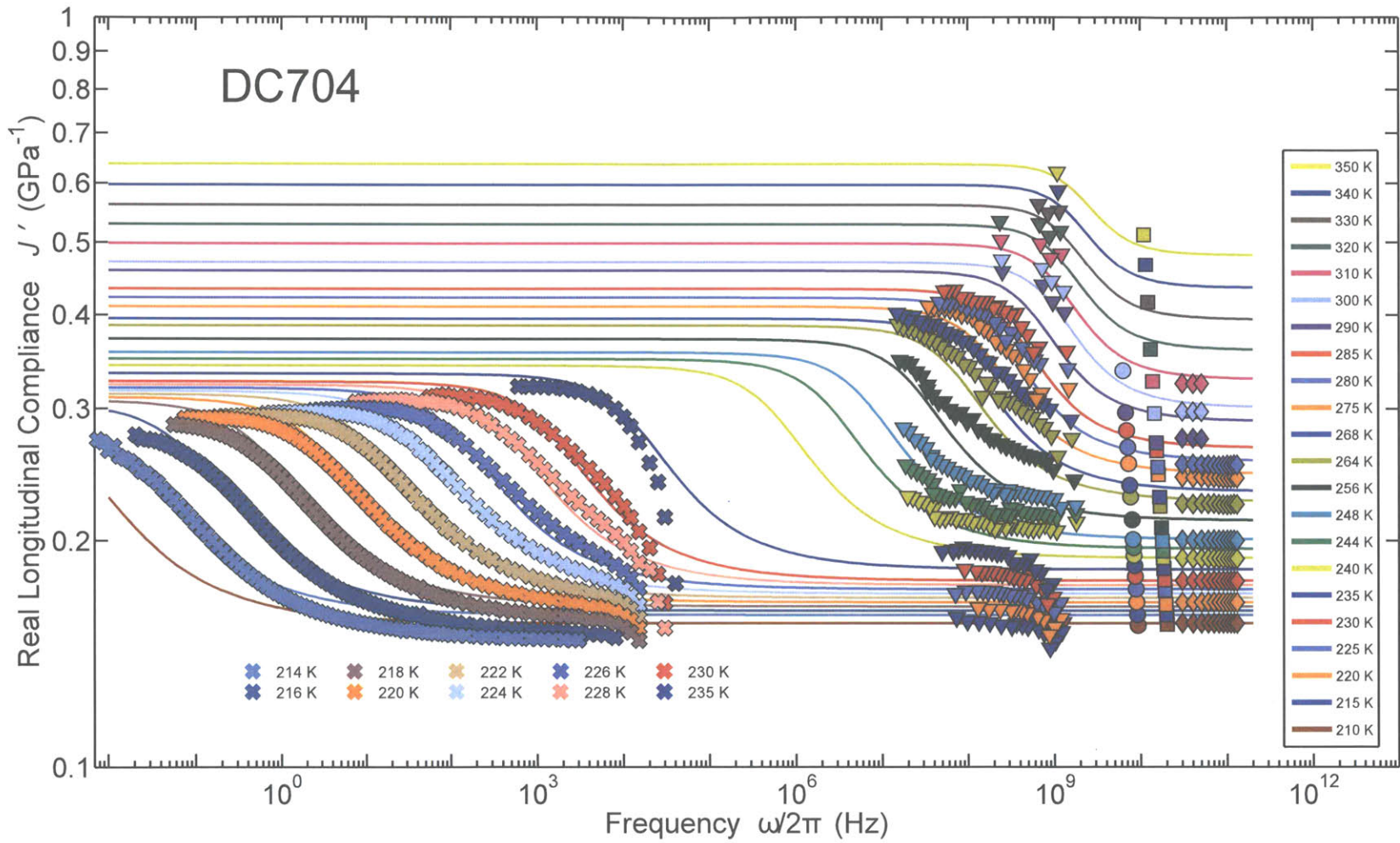


Figure 5-21: Extremely broadband relaxation spectrum of DC704: Reactive part of longitudinal compliance as measured by PZ: Piezo-Electric Modulus Gauge [HO10], ISTS: Impulsive Stimulated Thermal Scattering [Tor10], TDBS: Time-Domain Brillouin Scattering and Interferometry (both novel results). Solid curves are fits to a Cole-Davidson form as described in the text.



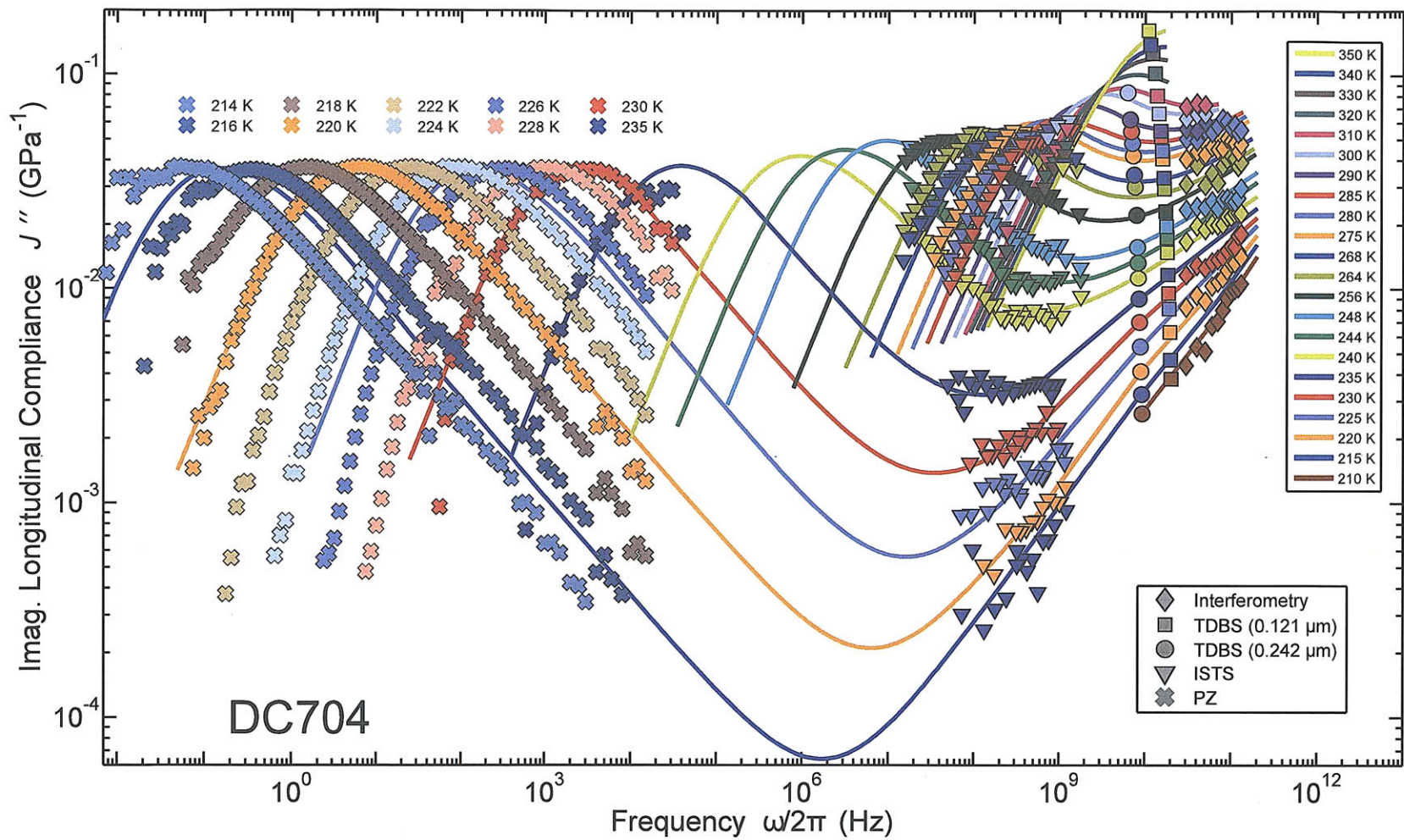


Figure 5-22: Extremely broadband relaxation spectrum of DC704: Dissipative part of longitudinal compliance. Data sources are given in Figure 5-21. Lines are fits with KWW form for the  $\alpha$ -peak region and the MCT interpolation formula for the minimum. In regions which contain no data they merely serve as visual aids and do not necessarily reflect the true relaxation behavior.

The susceptibility minimum in  $J''$  is described by the mode-coupling theory extrapolation formula of Equation 5.27. At all temperatures  $T \geq 240$  K, fits with the same power exponents were possible and yielded the following values for the exponents:  $a = 0.28$  and  $b = 0.48$ . These parameters are in excellent agreement with the mode-coupling theory prediction, as given by Equation 5.26 which yields a value of  $a = 0.278$  is obtained when  $b$  is fixed at the experimentally determined value from above. For the lowest temperatures,  $T \leq 230$  K, the minimum falls in a frequency range inaccessible to us (frequencies between  $\sim 30$  kHz and  $\sim 60$  MHz). As mentioned above, some of this frequency range is accessible by ultrasonic techniques. We are hoping to obtain reliable ultrasonics data through ongoing collaborative effort. Therefore, the fits in this range should only be treated as a visual aid. The fits of the minimum of Figure 5-22 provide us with the temperature evolution of the frequency  $\omega_{min}(T)$  and the magnitude of the susceptibility minimum  $J''_{min}(T)$  which are shown in Figure 5-23 (b).

### 5.3.3.2 Phenomenological and Mode-Coupling Theory Analysis of DC704

In Figure 5-23 (a) we report the temperature dependence of the  $\alpha$ -relaxation time and magnitude, and in Figure 5-23 (b) we report the temperature dependence of the position and magnitude of the minimum of the susceptibility.

In the following, a similar analysis is carried out for the susceptibility minimum as it was done for glycerol in Section 5.3.2.4. In Figure 5-24 we plot  $(\omega_{min})^{2a}$  vs.  $T$  and find an approximately linear  $T$  dependence extrapolating to  $T_c = 237 \pm 3$  K, or  $\simeq 1.13 \cdot T_g$ . The amplitudes  $J_{min}$  also follow a linear behavior with the same  $T_c$  as for  $\omega_{min}$  for the temperature range  $230 \text{ K} < T < 280 \text{ K}$ . At higher temperatures, the second linear fit exhibits a slope that is about twice as high and suggests  $T_c \sim 257$  K. This deviation can be interpreted as an increase in the overall relaxation strength at high frequencies, as seen in the susceptibility spectrum of Figure 5-22. The increase in the overall relaxation strength probably originates from an additional relaxation feature.

For the high temperature range, the temperature dependence of the  $\alpha$ -relaxation peak frequency  $\nu_\alpha = 1/\langle\tau_\alpha\rangle$  can be described by an Arrhenius law,

$$\frac{1}{\tau_\alpha(T)} = \nu(T) = \nu_\infty \exp\left(-\frac{E_a}{k_B T}\right), \quad (5.30)$$

where  $\nu_\infty$  is the relaxation rate in the high temperature limit,  $E_a$  is the characteristic activation energy and  $k_B$  is the Boltzmann constant. Figure 5-25 (a) shows the inverse of the relaxation times vs. inverse temperature from Figure 5-23. As expected, our high temperature data are well described by the Arrhenius law, as indicated by the

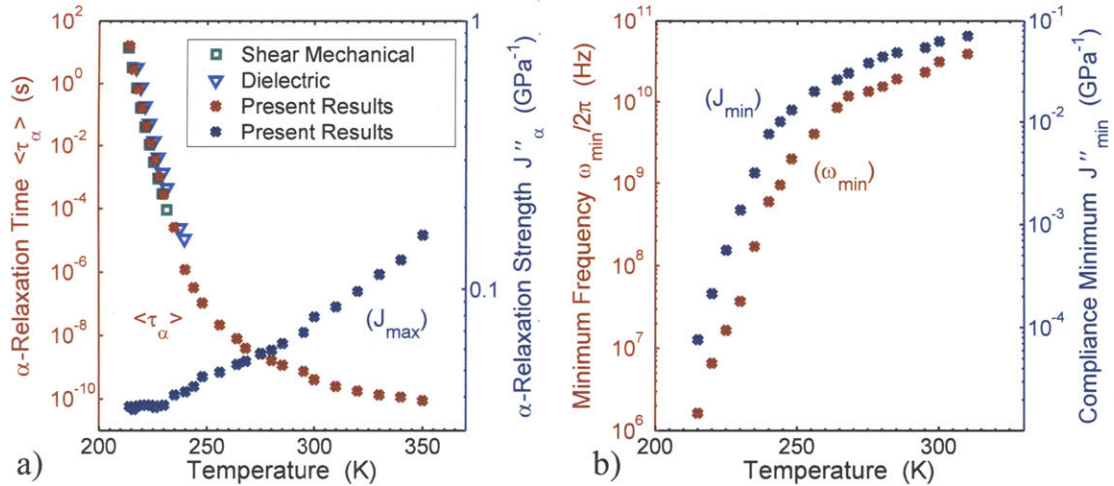


Figure 5-23: (a) Longitudinal mechanical loss peak relaxation time  $\langle \tau_\alpha \rangle$  and strength  $J''_{max}$  vs.  $T$  as extracted from the fits in Figure 5-22. For comparison, shear and dielectric loss data from [JNO05] are included. (b) Frequency  $\omega_{min}$  and magnitude  $J''_{min}$  of the susceptibility minimum in Figure 5-22 as a function of  $T$  also from the fits in Figure 5-22. Both  $\omega_{min}$  and  $J''_{min}$  show two distinct regimes of almost linear behavior having different crossover temperatures. Their analysis in terms of mode-coupling theory is shown in Figure 5-24.

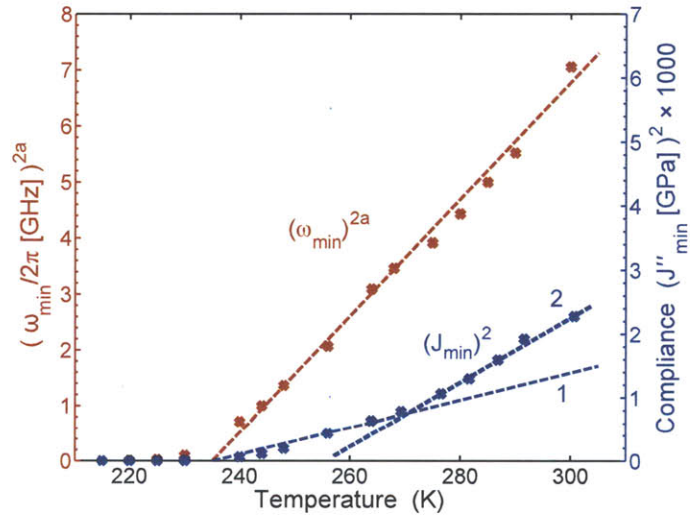


Figure 5-24: Test of mode-coupling theory predictions for the evolution of the susceptibility minimum  $J''_{min}(\omega_{min})$ :  $(\omega_{min})^{2a}$  and  $(J''_{min})^2$  vs.  $T$ . For the former, we observe an approximately linear  $T$  dependence, extrapolating to  $T_c = 237 \pm 3$  K, or  $\simeq 1.13T_g$ . The amplitudes  $J_{min}$ , however, deviate from the predicted behavior. Linear fit 1 with the same  $T_c$  values as for  $\omega_{min}$  only provides satisfactory fits to the data up to  $\sim 280$  K. At higher temperatures, linear fit 2 exhibits a slope that is twice as high and suggests a  $T_c \sim 257$  K. This deviation can be interpreted as an increase in the overall relaxation strength at high frequencies, as seen in the susceptibility spectrum of Figure 5-22, probably originating from an additional relaxation feature or the extension of microscopic relaxation processes down to these relatively low frequencies.



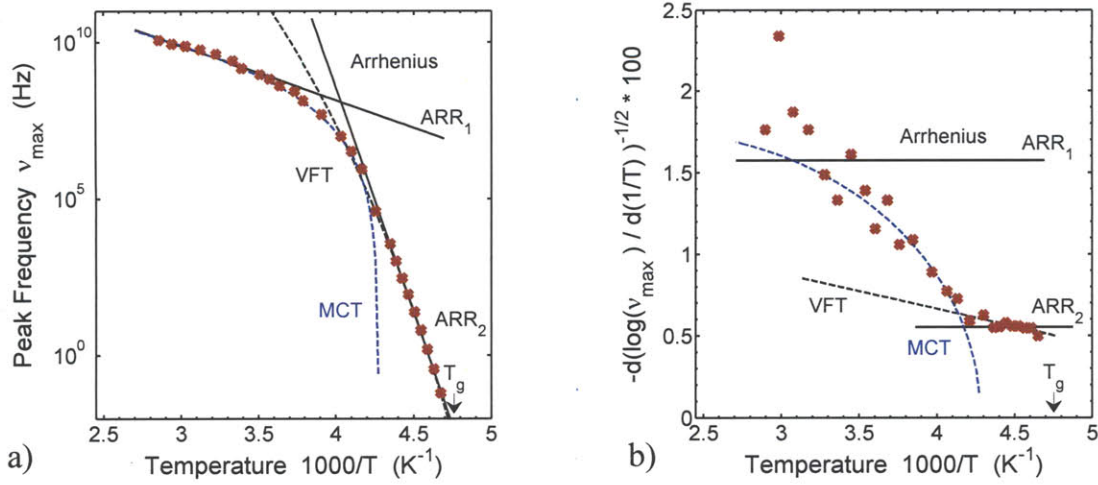


Figure 5-25: (a) Activation plot for DC704. The glass transition temperature is at  $T_g = 210$  K. Arrhenius fits with  $\nu_\infty = (1.45 \pm 0.73) \times 10^{15}$  Hz,  $E_a = (33.6 \pm 0.5)$  kJ mol $^{-1}$  for ARR $_1$  and  $\nu_\infty = (1.0 \pm 1.32) \times 10^{66}$  Hz,  $E_a = (275 \pm 3)$  kJ mol $^{-1}$  for ARR $_2$ . VFT fit with  $\nu_\infty = (3.1 \pm 1.5) \times 10^{14}$  Hz,  $D = 1.986 \pm 0.93$  and  $T_0 = (207 \pm 16)$  K. Mode-coupling theory fit with  $\nu_\infty = (1.58 \pm 0.34) \times 10^{11}$  Hz,  $\gamma = 3.5 \pm 0.8$  and  $T_c = (234 \pm 7)$  K. (b) Results from (a) in a differential quotient  $[-d(\log(\omega_\alpha/2\pi))/d(1/T)]^{-1/2}$  vs.  $1000/T$  representation where ARR and VFT laws are transformed to constant and linear functions, respectively.

fit ARR $_1$ . However, the low temperature data measured by PZ techniques should exhibit super-Arrhenius behavior (with a temperature-dependent activation energy) but appear to also be satisfactorily well described by an Arrhenius law, as indicated by a second fit ARR $_2$ .

In the temperature region close to the dynamic glass transition, an empirical dependence according to the Vogel-Fulcher-Tammann (VFT) equation should be ob-

Table 5.2: The table below summarizes the various functional forms of temperature laws and their respective fit parameters.  $\log \nu$  stands for  $\log_{10}(\nu_{max}/Hz)$  and  $A = \log_{10}(\nu_\infty/Hz)$ . The values for  $B = E_a/k_B$ ,  $D$ ,  $T_0$ ,  $T_c$  and  $T$  are given in K, and the temperature range refers to the temperature window across which the parameters are optimized.

	Name	Function	A	B, D, $\gamma$	$T_0, T_c$	T Range
Arrhenius	ARR $_1$	$\log \nu = A - B/T$	15.2	4050	0	285–350
Arrhenius	ARR $_2$	$\log \nu = A - B/T$	66.0	33000	0	214–235
Vogel-Fulcher	VFT	$\log \nu = A - D T_0 / (T - T_0)$	24.5	30.3	207	214–248
Mode-Coupling	MCT	$\log \nu = A + \gamma \log[(T - T_c)/T]$	11.2	3.5	234	237–350

served:

$$\frac{1}{\tau_{\alpha}(T)} = \nu(T) = \nu_{\infty} \exp\left(-\frac{D T_0}{(T - T_0)}\right), \quad (5.31)$$

where  $D$  is a constant and  $T_0$  is the Vogel-Fulcher temperature. A VFT fit is indicated by a black dashed line in Figure 5-25 (a) and shows excellent agreement with the data at temperatures up to about 260 K. The Vogel-Fulcher temperature from our fits is  $T_0 = (207 \pm 16) \text{ K}$ , which is consistent (within the uncertainty) with the Vogel-Fulcher temperature determined by D. Torchinsky of  $T_0 = (218 \pm 8) \text{ K}$  [Tor08] from KWW fits to the slowly varying thermal signal observed in ISTS measurements at a restricted temperature range from 230 K to 248 K.

A further approach to describe the evolution of the  $\alpha$ -relaxation is given by the mode-coupling theory. For temperatures above a critical temperature  $T > T_c$  it is predicted that the relaxation rate scales as

$$\frac{1}{\tau_{\alpha}(T)} = \nu(T) = \nu_{\infty} \left(-\frac{D T_0}{(T - T_0)}\right)^{-\gamma}, \quad (5.32)$$

where  $\gamma$  is a constant. A fit to our  $\alpha$ -peak data is shown as a blue dashed line in Figure 5-25 (a), and fits our data well over the large temperature range from 237 K to the highest temperatures measured, 350 K. The fit yields a critical temperature  $T_c = 234 \text{ K}$  and a value for the exponent  $\gamma = 3.5$  which will be compared to differently obtained values for the same parameters in Sections 5.3.3.3.

As we see from the y-scale of Figure 5-25 (a), the supercooled liquid dynamics span an extraordinarily wide time scale ranging from microscopic relaxation time ( $\sim 10^{-11} \text{ s}$ ) to ultraslow fluctuations ( $> 10^2 \text{ s}$ ). In order to analyze its temperature dependence in detail, the derivative of the relaxation rate with respect to  $1/T$  is calculated as

$$\left[\frac{-d \log \nu}{d(1/T)}\right]^{-1/2}. \quad (5.33)$$

Stickel *et al.* [SFR95] proposed and pioneered the use of such types of plot, which are aptly called Stickel plots. For the Arrhenius-dependence of Equation 5.30, the VFT-dependence of Equation 5.31, and the temperature dependence suggested by the mode-coupling theory, Equation 5.32 for  $T > T_c$ , the conditions described by the following equations hold:

$$\text{Arrhenius: } \frac{d \log \nu}{d(1/T)} = \frac{E_a}{k_B} \log e \quad (5.34)$$

$$\text{VFT: } \frac{d \log \nu}{d(1/T)} = -(D T_0) \left(1 - \frac{T_0}{T}\right)^{-2} \log e \quad (5.35)$$

$$\text{MCT: } \frac{d \log \nu}{d(1/T)} = \frac{\gamma \log e}{T_c/T^2 - 1/T} \quad (5.36)$$

Hence in a plot of  $[d(-\log \nu)/d(1/T)]^{-1/2}$  vs.  $1/T$  the Arrhenius-dependence is a constant and the VFT dependence manifests itself as a straight line having a nonzero slope. Such a derivative plot enables a detailed analysis of the scaling with temperature and works particularly well for the temperature range with strong variation of the frequency. Even though the data at high temperature follow Arrhenius behavior well in Figure 5-25 (a), the quality of the fit in Figure 5-25 (b) is relatively poor. This can be attributed to the small variation of the peak frequency in the high temperature range which causes significant scattering due to the numerically calculated derivative. Therefore, it is interesting to look at the low temperature data when the  $\alpha$ -relaxation slows down rapidly and approaches the glass transition at  $10^{-2}$  Hz. In this region, we have indicated a second Arrhenius dependence  $\text{ARR}_2$  in Figure 5-25 (a) which also describes very well the data close to  $T_g$  in Figure 5-25 (b). This is surprising as already mentioned above, since DC704 is a fragile glass-former and should more clearly show a temperature dependent activation energy as described by the VFT equation. However, the VFT fit in Figure 5-25 (b) shows a very small slope which is another indication for a small temperature dependence of the activation energy. Finally, as expected, the mode-coupling theory fit agrees exceptionally well over a large temperature range at high temperatures.

### 5.3.3.3 Conclusion

In the previous paragraphs we described first the analysis of the susceptibility minimum and second the analysis of the  $\alpha$ -peak by of mode-coupling theory predictions for our results on DC704. The results and evaluation of the accuracy of the mode-coupling theory predictions are summarized below.

First, the analysis of the peak frequency of the  $\alpha$ -relaxation feature yielded a critical temperature of  $T_c = (234 \pm 7)$  K which is in excellent agreement with the critical temperature obtained from the fits to both the susceptibility minimum frequency and peak frequency of  $T_c(237 \pm 3)$  K. In addition, it is also in close agreement to the critical temperature obtained by D. Torchinsky [Tor08] from KWW fits of ISTS data which was reported to be  $T_c = (227 \pm 5)$  K.

Second, from the fits of the compliance minimum  $J''_{min}(\omega_{min})$  in Figure 5-22 by the interpolation formula Equation 5.27, we obtained for the power-law exponents below and above the minimum  $b = 0.48 \pm 0.01$  (for all temperatures) and  $a = 0.28 \pm 0.02$  for temperatures  $\geq 240$  K. An alternative way to calculate one of the exponents from the other is provided by mode-coupling theory's exponent relation (Equation 5.26) which explicitly connects the slow,  $\alpha$ -relaxation to the fast,  $\beta$ -relaxation dynamics:

$$\lambda = \frac{\Gamma^2(1-a)}{\Gamma(1-2a)} = \frac{\Gamma^2(1+b)}{\Gamma(1+2b)}. \quad (5.37)$$

Inserting the experimentally determined value for  $b$  of 0.48 determines  $\lambda$  to be 0.79 and  $a$  to 0.278 which exceptionally well agrees with the experimentally determined value of 0.28 above the critical temperature.

Third, from the analysis of the  $\alpha$ -relaxation peak we not only obtain the critical temperature but also the critical exponent  $\gamma$  through Equation 5.32 which we determined to  $\gamma = 3.5 \pm 0.8$ . This critical exponent is predicted to also follow the relationship:

$$\gamma = \frac{1}{2a} + \frac{1}{2b}. \quad (5.38)$$

Inserting the experimentally determined values for  $a$  and  $b$  from above yields  $\gamma = 1/(2 \times 0.48) + 1/(2 \times 0.28) = 2.8$ . Both values of  $\gamma$  agree well within the experimental uncertainty.

In conclusion, our mode-coupling analysis of the longitudinal compliance spectrum of DC704 describes all aspects of the spectrum above a critical temperature extremely well. In particular, mode-coupling theory predictions for the connection of the slow to the fast relaxation dynamics can be confirmed. Another remarkable aspect of the analysis of the broadband compliance spectrum of DC704 is that the data obtained by several different techniques show excellent consistency over the whole examined temperature and frequency range.

## 5.4 Conclusions

In this chapter, we described the approach we use to measure the density responses of glycerol and DC704 from below their respective glass transition temperatures up to 400 K and at frequencies from below 10 GHz up to 200 GHz. We started by illustrating how spectroscopic approaches of time-domain Brillouin scattering and interferometry are applied to obtain speed of sound and acoustic attenuation information for these two liquids. Our experimental setup and the analysis of the measured displacement/strain data have proven to be very robust, and the measurements show

excellent experimental reproducibility. In case of interferometric detection we averaged data obtained from 15 to 50 liquid thicknesses in order to achieve extremely high data accuracy over the examined frequency range.

In the second section we presented our results obtained by time-domain Brillouin scattering and interferometry on glycerol and DC704. We also show that they with our time-domain Brillouin scattering approach we can generate and detect sufficiently high-amplitude acoustic strain pulses that interact with the liquid in a non-linear fashion. For the studies presented in this thesis, this non-linear effect is minimized by conducting our measurements at the lowest possible optical pump powers. However, these results are very interesting and promising since they may open the door to study higher order mechanical properties of liquids.

In the final section we pieced together data obtained from various mechanical techniques to create a broadband relaxation spectrum, ranging from 2 MHz to 200 GHz for glycerol and 15 mHz (millihertz) to over 100 GHz for DC704. The viscous slowdown in these liquids over many orders of magnitude are characterized by phenomenological models and analyzed in terms of the mode-coupling theory. Overall, the obtained susceptibility spectra for both glycerol and DC704 exhibit a shape and temperature dependence typical of glass formers. We find that for glycerol, the shape of the susceptibility minimum is incompatible with the generic asymptotic laws of mode-coupling theory while the shape of the minimum and the evolution of the  $\alpha$ -relaxation peak for DC704 above a critical temperature of  $T_c \sim 235$  K are well described by the theory. In particular, the predicted connection of mode-coupling theory between the fast and slow dynamics is established for DC704.





# CHAPTER 6

---

## Shear Acoustic Waves Study of Glycerol and DC704

---

It is widely believed that pure shear waves do not propagate in liquids due to the absence of a restoring force. However, this general assumption is not correct. In contrast to longitudinal waves, shear waves do not cause any change in density  $\rho$  [HL59],

$$-\rho \frac{\partial \eta}{\partial t} = \text{div } \vec{w} = 0 \quad (6.1)$$

or for two-dimensional motion

$$\frac{\partial w_1}{\partial x} + \frac{\partial w_2}{\partial y} = 0 \quad (6.2)$$

with  $\eta$  being a strain and  $\vec{w} = w_1 + w_2$  a macroscopic flow velocity. When we define the direction of propagation in the  $x$ -direction and the direction of motion in the  $y$ -direction, then  $w_1 = 0$  and the equation of motion becomes

$$\rho \frac{\partial w_2}{\partial t} = \frac{\partial}{\partial x} \sigma_{yx} = \frac{\partial}{\partial x} \eta_s \frac{\partial w_2}{\partial x} = \eta_s \frac{\partial^2 w_2}{\partial x^2}, \quad (6.3)$$

where  $\eta_s$  is the static shear viscosity.

In classical theory  $w_2$  is proportional to

$$\exp \left[ i\omega t - i\omega x \left( \frac{1}{c_s} + \frac{\alpha}{i\omega} \right) \right] \quad (6.4)$$

where  $c_s$  is the shear sound velocity and  $\alpha$  the shear absorption coefficient per unit length. Inserting equation 6.4 into 6.3 gives

$$\begin{aligned} i\rho\omega &= -\eta_s\omega^2 \left( \frac{1}{c_s} + \frac{\alpha}{i\omega} \right)^2, \\ \frac{\alpha}{\omega} = \frac{1}{c_s} \quad \text{and} \quad \frac{\rho}{\eta_s\omega} = \frac{2\alpha}{\omega c_s} = \frac{2}{c_s^2}, \quad \text{or} \\ c_s &= \sqrt{\frac{2\eta_s\omega}{\rho}} \quad \text{and} \quad \alpha = \sqrt{\frac{\rho\omega}{2\eta_s}}. \end{aligned} \quad (6.5)$$

The waves described by these equations behave very much like electromagnetic waves penetrating a metal (in which case  $1/\alpha$  resembles the *skin depth*) and the amplitude decreases by the factor  $\exp(-2\pi) \sim 1/535$  within one wavelength.

In the relaxation theory for a viscoelastic medium, for example a liquid which exhibits a shear modulus of rigidity, one relates the deviatoric part of stress  $\sigma_{ij}$  to strain  $s_{ij}$  by the shear modulus  $G$ ,

$$\sigma_{ij} = 2G\eta_{ij}. \quad (6.6)$$

The differential equation governing the propagation of shear waves is then given by

$$\rho \frac{\partial w_i}{\partial t} = \rho \frac{\partial^2 u_i}{\partial t^2} = G \sum_{k=1}^3 \frac{\partial^2 u_i}{\partial x_k^2}, \quad (6.7)$$

where  $u_i$  is the displacement of a volume element in the  $x_i$  direction. Considering the direction of propagation in the  $x$ -direction and the direction of motion in the  $y$ -direction, the equation of motion becomes

$$\rho \frac{\partial^2 u_y}{\partial t^2} = G \frac{\partial^2 u_y}{\partial x^2}. \quad (6.8)$$

If viscous losses are present,  $u_y$  is proportional to  $\exp[i\omega t - i\omega x(1/c_s + \alpha/i\omega)]$  and the density can be expressed as

$$\rho = G \left( \frac{1}{c_s} + \frac{\alpha}{i\omega} \right)^2, \quad (6.9)$$

which has a complex and frequency dependent shear modulus. Comparing this equation with equation 6.5, one sees that both equations become identical in the limit of low frequencies,  $\lim_{\omega \rightarrow 0} G(\omega) = i\omega\eta_s$ . Relaxation theory further predicts a crossover frequency at which the dynamical properties of liquids move from the hydrodynamic regime (classical theory), with liquid-like or viscous behavior, to the elastic regime

(relaxation theory). At high frequencies, where the behavior is solid-like,  $G(\omega)$  approaches a limiting value,  $\lim_{\omega \rightarrow \infty} G(\omega) = G_\infty$ . In this regime, the average shear relaxation time,  $\langle \tau \rangle$ , is then given [Bra85] by Maxwell's expression

$$\langle \tau \rangle = \eta_s / G_\infty . \quad (6.10)$$

When the acoustic frequency exceeds the relaxation rate for viscous effects,

$$f_{shear} \geq G_\infty / 2\pi\eta , \quad (6.11)$$

shear waves may propagate over a notable distance in liquids. At room temperature, this crossover frequency is  $\sim 0.5$  GHz for glycerol,  $\sim 10$  GHz for DC704, and  $\sim 150$  GHz for water [MWM07].

The present chapter describes our picosecond ultrasonic shear wave measurements on these liquids. The next two sections provide theoretical background and introduce the modifications to the experimental approach discussed in Chapter 3 that are necessary for optical generation and detection of shear acoustic waves. Subsequently, we discuss results obtained at various frequencies and temperatures and provide an interpretation in the context of previous results from the literature at other frequencies and temperatures. This chapter concludes with a summary and an outlook regarding application of the newly developed technique for generation and detection of shear acoustic waves in liquids.

## 6.1 Theoretical Background on Shear Waves

### 6.1.1 Optical Generation of Plane Coherent Shear Acoustic Waves

In picosecond ultrasonics, as described in Section 3.2, plane longitudinal acoustic waves at gigahertz frequencies can be generated by absorption of femtosecond laser pulses and subsequent thermal expansion. Due to symmetry considerations and as a consequence of the isotropy of the thermal expansion of each volume element in the heated region, this generation mechanism is restricted to the longitudinal acoustic mode, as shown in Figure 6-1 a). Mathematically, this results from the spherical symmetry of the thermoelastic stress tensor  $\sigma_{ij} = K\alpha\Delta T\delta_{ij}$ , where  $K$  is the bulk elastic modulus,  $\Delta T$  is the temperature rise,  $\alpha$  is the thermal expansion coefficient, and  $\delta_{ij}$  is Kronecker's delta. However, around the edges of the heated region this spherical symmetry is no longer preserved and non-planar shear waves can be excited. Even though this possibility of shear wave generation has been pursued [RRP<sup>+</sup>05] (but lim-

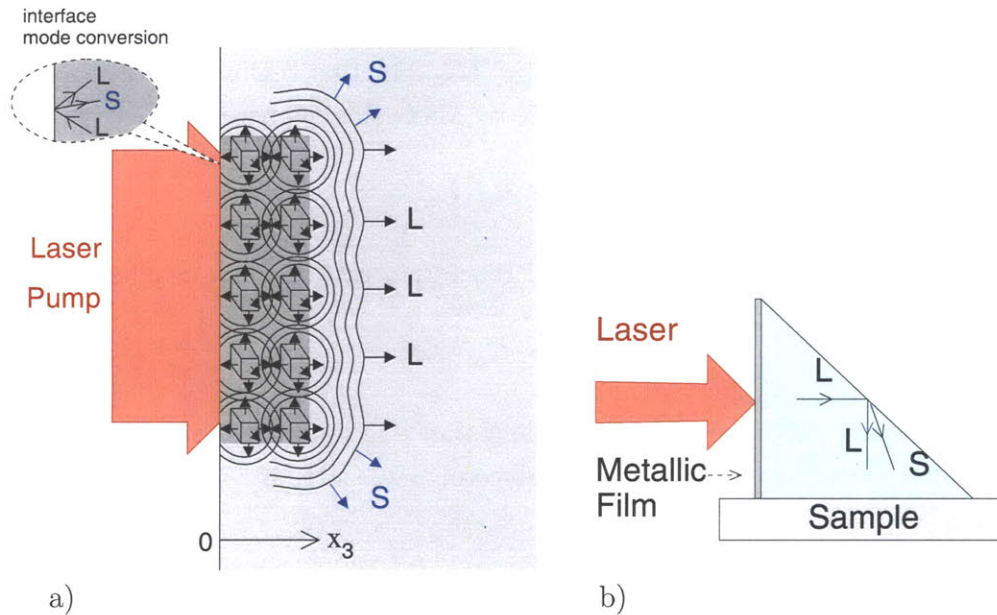


Figure 6-1: Schematic drawings of laser induced acoustic wave generation (L longitudinal and S shear acoustic waves): (a) In picosecond ultrasonics, thermoelastic acoustic wave generation in an isotropic homogeneous transducer only gives rise to longitudinal acoustic waves. Thermal expansion of each point source in the plane parallel to the transducer surface is mutually compensated by neighboring point sources and shear generation is only possible along the edges of laser heating. This is, however, insignificant due to the large ratio of the laser spot size ( $\sim 100 \mu\text{m}$ ) to the optical penetration depth ( $\sim 15 \text{ nm}$ ) into the transducer. (b) At megahertz frequencies, a photoelastic transducer-prism assembly can be employed to generate shear acoustic waves through oblique reflection of longitudinal waves at the slanted prism interface. Taken from [PRG<sup>+</sup>07].

ited to very low acoustic frequencies), in typical picosecond ultrasonic experiments the area of the homogeneously illuminated transducer surface exceeds the characteristic wavelength by many orders in size such that this effect can be neglected. In other words, the laser spot size is much larger than the optical penetration depth and the spatial extent of the resultant heating.

Various suggestions to overcome this shortcoming have been put forward, all requiring a breaking of the sample symmetry. One method is based on mode conversion of longitudinal acoustic waves obliquely incident on the hypotenuse of a prism as depicted in Figure 6-1 b). This method has been successfully demonstrated in the megahertz frequency regime where nanosecond laser pulses launch longitudinal plane acoustic waves at the face of a prism toward its hypotenuse at which the oblique reflection gives rise to shear acoustic waves through mode conversion. The implemen-



tation of this concept in gigahertz acoustic shear wave generation is, however, not straightforward. Since typical hypersound propagation distances are on the order of only a few microns at room temperature, the prism dimensions would have to be on the order of hundreds of nanometers to a few microns, making the prism extremely difficult to fabricate.

A second possibility for breaking the symmetry can be realized by attaching an isotropic material to an anisotropic material which has its crystallographic axis misaligned with respect to the interface normal. Plane longitudinal acoustic waves normally incident at the interface are partially mode-converted into shear acoustic waves upon reflection [HWM<sup>+</sup>00] and excite plane quasi-transverse waves in transmission [BP03].

Finally, a number of ideas for direct volumetric laser excitation of shear waves in the bulk of the transducer film have been proposed. As we saw above, the spherical symmetry of the thermoelastic stress tensor  $\sigma_{ij} \sim \delta_{ij}$  of an isotropic material prohibits the generation of shear modes. It has been proposed that this problem can be circumvented by deploying materials which exhibit an anisotropic (non-spherical) thermal expansion coefficient  $\alpha_{ij}$  and thereby break the symmetry at the level of the thermoelastic forces. The transducer material must have a misoriented crystal axis relative to the surface normal and must exhibit a hexagonal crystal symmetry or lower [PCR<sup>+</sup>06]. This premise originates from an analysis of the relation of the static strain tensor  $\Sigma_{ij}$  to the unrestricted expansion of the crystal,  $\Sigma_{ij} = \alpha_{ij} \Delta T$ . In the first experiment which exploited this idea [MWH<sup>+</sup>04], shear wave generation was successfully demonstrated in a Zn single crystal which was cut with a surface normal 24° off the (0001) plane.

Careful theoretical and experimental analysis of laser-induced thermoelastic generation of hypersound in anisotropic materials by Pezeril and coworkers [PRG<sup>+</sup>07] has shown that anisotropy of thermal expansion is not a necessary requirement for shear wave generation. Furthermore, they have demonstrated that the dominant mechanism of thermoelastic shear wave generation for most materials originates from the spherical part of the thermoelastic stress tensor  $\sigma_{ij}$  and is therefore effective even in materials such as cubic crystals which exhibit isotropic thermal expansion. Absorption of pump laser energy at  $t = 0$  ps by a canted crystal and subsequent thermalization results in a thermoelastic stress  $(\sigma_{kk}/3)\delta_{ij}$ . Locally, this excites only longitudinal strain even though this strain is distributed among all acoustic eigenmodes of the anisotropic material. These modes propagate normally to the interface and have quasi-longitudinal (QL) and quasi-shear (QS) character. As illustrated in Figure 6-2 a) and b), these modes also contain planar shear strain components which initially ( $t = 0$  ps) mutually compensate each other and therefore only give rise to a



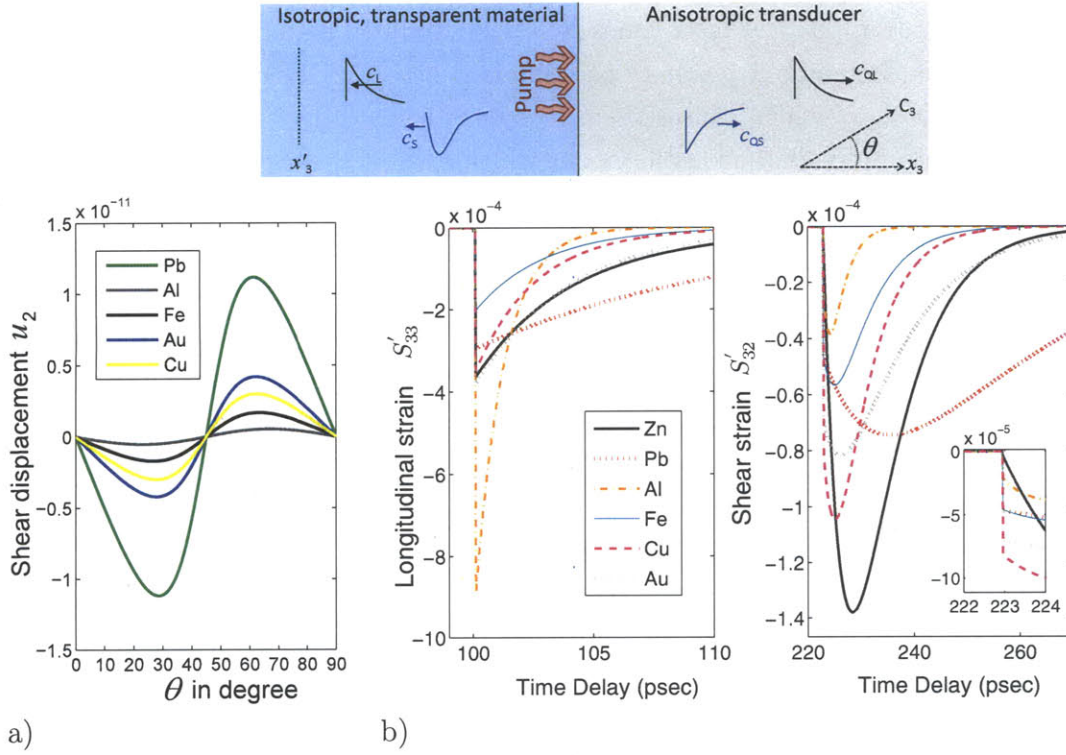


Figure 6-3: Calculation of the shear wave generation efficiency of several cubic materials. The pump laser pulse gets absorbed at the interface of a semi-infinite anisotropic transducer and a semi-infinite transparent material. The subsequent thermal expansion launches two counter-propagating plane compressional waves parallel to the interface. In case of broken crystal symmetry (tilted  $C_3$  axis with respect to the interface normal), quasi-shear components are excited that give rise to pure shear displacement  $u_2$  and strain  $S_{32}$  in the isotropic material. (a) Calculation of angle dependence of the magnitude of shear displacement  $u_2$  in a ZnO medium at infinite time. The angle  $\theta$  denotes the angle between the  $C_3$  and  $x_3$  axis in the cubic transducer materials. Maximum shear generation efficiency is predicted at  $28^\circ$  and  $62^\circ$ . Taken from [Pez05]. (b) Calculation of longitudinal strain  $S_{33}$  and shear strain  $S_{32}$  inside the ZnO medium at an arbitrarily chosen distance  $x_3 = -610$  nm from the interface. An off-axis symmetry angle of  $\theta = 28^\circ$  has been chosen and both thermal and electronic diffusion have been neglected. The longitudinal strain therefore shows an instantaneous drop while the shear strain exhibits a finite time to reach its maximum. This is a result of the asynchronous shear generation mechanism and therefore makes this technique unsuitable to reach extremely high (THz) shear frequencies. The different delay times for the start of the longitudinal signal  $\tau_{33} = 100$  ps and the shear signal  $\tau_{32} = 223$  ps are a result of the different velocities for the different acoustic modes in ZnO,  $c_l = 6096$  m/s and  $c_s = 2736$  m/s. Taken from [PRG<sup>+</sup>07]. The pump laser fluence for both calculations is  $0.1 \text{ mJ cm}^{-2}$ .

compressional plane wave (as depicted in the inset in Figure 6-2 a)). However, as a consequence of so-called asynchronous propagation of the acoustic eigenmodes, this compensation disappears at later times ( $t > 0$  ps) and real planar (quasi-)shear strain appears. This occurs as a result of the different acoustic velocities of the different modes,  $c_{QL} > c_{QS}$ , which causes them to separate spatially and temporally and to decompose into individual acoustic modes which exhibit shear components.

Calculations for a number of different semi-infinite cubic (Pb, Al, Fe, Cu, Au) and hexagonal (Zn) transducer materials attached to semi-infinite, isotropic ZnO provide insights into the mechanism of asynchronous shear generation. The sample structure is depicted at the top of Figure 6-3. An ultrashort laser pulse directed through the transparent ZnO substrate deposits energy in the metallic transducer material with a profile given by the optical penetration depth. Thermal expansion launches two counter-propagating compressional pulses, one away from and one toward the interface, both of which exhibit both quasi-longitudinal and quasi-shear character. Due to differences in the speed of sound of the different acoustic modes, the quasi-longitudinal and quasi-shear plane waves spatially and temporally separate and their transmission into the isotropic ZnO gives rise to pure longitudinal and shear waves. Figure 6-3 a) illustrates the angle dependence of shear displacement  $u_2$  in an isotropic medium. The angle  $\theta$  is defined as the angle between the  $x_3$  axis and the crystallographic  $C_3$  axis which tilts toward  $x_2$ . All cubic materials have maximum shear generation efficiency at  $28^\circ$  and  $62^\circ$ . Figure 6-3 b) shows calculations of the longitudinal  $S_{33}$  and shear  $S_{32}$  strain profiles inside the ZnO medium at an arbitrarily chosen distance from the interface of  $x_3 = -610$  nm. Because of the symmetry induced by the tilt  $\theta$  of the  $C_3$  axis, purely transverse modes  $S_{31}$  in the  $x_1$  direction cannot be excited in any of the crystals considered. In these calculations, a tilt angle  $\theta=28^\circ$  was chosen for optimal shear strain generation in all materials. The longitudinal and shear strain arrive at the chosen coordinate  $x_3$  after a delay time of  $\tau_{33} = 100$  ps and  $\tau_{32} = 223$  ps, respectively. Two aspects of the calculated strain profiles should be highlighted. First, the numerical simulations show that shear acoustic generation is not only possible in cubic misoriented crystals whose thermal dilation and static strain are both spherical, but it has an efficiency comparable to that of longitudinal acoustic generation. Secondly, the profiles provide deeper insight into the mechanism of shear generation. The difference in the shapes of the strain fields cannot be explained by classical thermoelastic generation theory as described in Section 3.2.

The shear strain field is significantly broader than the longitudinal strain field and shows different leading-edge shape. The longitudinal strain instantaneously reaches its maximum value when it arrives at  $x_3$ , indicating that longitudinal strain excitation occurs almost instantaneously upon laser irradiation. (Relaxation of the pho-

to excited hot electrons into the lattice modes on picosecond time scales is neglected in this model. In contrast, the shear strain starts from zero and only reaches its maximum after a couple of picoseconds, suggesting a generation mechanism that is non-instantaneous and that can be explained by the asynchronous mechanism of shear generation described above. As a consequence a limit on the highest possible frequencies is imposed. The rise time delay  $\delta t$  (to its maximum value) of the shear strain is solely determined by the optical penetration or heating depth  $\zeta$  of the transducer by the excitation laser pulse and the quasi-longitudinal and quasi-shear acoustic velocities in the transducer,  $c_{QL}$  and  $c_{QS}$ , respectively, [PRG<sup>+</sup>07] and can be expressed as

$$\delta t = \frac{1}{\zeta} \frac{c_s}{(c_{QS} - c_{QL})} \ln \left( \frac{c_{QS}}{c_{QL}} \right). \quad (6.12)$$

We see from this equation that high shear frequencies can be reached when  $\zeta$  is large or when the difference between the acoustic velocities in the transducer material is large. For generation of shear waves with frequencies of several hundreds of gigahertz or in the terahertz range another mechanism like magnetostriction (see future directions) must be employed.

We pursued two different approaches in the work presented in this thesis to obtain canted thin film transducers, both of which are sketched in Figure 6-2 c). The first one utilized a technique developed by Frechard *et al.* [FAC<sup>+</sup>95] which allows monocrystalline (throughout the thickness of the film) columnar layers of iron or cobalt to be obliquely grown on many substrates by molecular beam epitaxy (MBE). The deposition is performed under ultra-high vacuum ( $> 10^{-8}$  Pa) at very low rates of condensation (24 hour deposition time per film,  $\sim 50$  nm). The inclination of the initial flux of material at  $60^\circ$  to  $70^\circ$  gives rise to a tilt angle of the monocrystalline grains of about  $40^\circ$ , as a result of the so called shadowing effect. Due to this effect, the density of the films is significantly lower than that of the bulk. Surface properties of the thin films were studied by atomic force microscopy (AFM), and root-mean-square surface roughnesses of  $3.0 \pm 1.0$  nm were determined for all films on all types of substrates. The second approach takes advantage of the lattice matched growth of metallic strontium ruthenate (SrRuO<sub>3</sub> or SRO) thin films on off-axis cut strontium titanate (SrTiO<sub>3</sub> or STO) substrates by pulsed laser deposition [RBCE04]. The STO substrates are polished at an off-axis angle of  $27^\circ$  to  $28^\circ$  with respect to the basal plane (see Figure 6-3 a)). SRO (and also STO) growth is possible at thicknesses ranging from 0.4 nm up to several hundred nm. However, film roughnesses becomes significant at thicknesses over 300 nm.

## 6.1.2 Shear Strain Detection with Laser Picosecond Acoustics

Picosecond laser shear wave detection is more involved than the longitudinal strain or displacement detection schemes outlined in Section 3.3, and special requirements with regard to light polarization and detection geometry have to be met.

The experimental geometry is similar to the one described above in which photoelastic excitation generates acoustic waves in an elastically anisotropic material at its interface with an isotropic transparent substrate. This situation is depicted in Figure 6-4. The transparent material can be for example a glass, crystalline sapphire or a liquid. The resulting quasi-longitudinal and quasi-shear waves that propagate away from the interface are not probed since the detection laser beam incident from the transparent material does not penetrate into the opaque transducer. The situation is different for the pure longitudinal and shear strain waves that propagate away from the interface in the transparent material. The propagating acoustic strains cause a spatiotemporal modulation in the permittivity tensor through the photoelastic effect. Under certain conditions, the incident probe light reflects not only from the longitudinal strain (1) but also the shear strain (2). In the following paragraphs, we examine the conditions under which such experimental observations can be made.

In an optically transparent material, the strain  $\eta_{kl}$  and the deviation of the dielectric tensor  $\Delta\epsilon_{ij}$  are connected through the photoelastic tensor  $p_{ijkl}$  through the relationship  $\Delta\epsilon_{ij} = p_{ijkl} \eta_{kl}$ . In matrix notation, using the following conventional abbreviations for the strain and dielectric tensors,

$$\begin{pmatrix} \epsilon_{xx} & \epsilon_{xy} & \epsilon_{xz} \\ \epsilon_{yx} & \epsilon_{yy} & \epsilon_{yz} \\ \epsilon_{zx} & \epsilon_{zy} & \epsilon_{zz} \end{pmatrix} \equiv \begin{pmatrix} \epsilon_1 & \epsilon_6 & \epsilon_5 \\ \epsilon_6 & \epsilon_2 & \epsilon_4 \\ \epsilon_5 & \epsilon_4 & \epsilon_3 \end{pmatrix} \equiv \tilde{\epsilon} \quad \text{and} \quad (6.13)$$

$$\begin{pmatrix} \eta_{xx} & \eta_{xy} & \eta_{xz} \\ \eta_{yx} & \eta_{yy} & \eta_{yz} \\ \eta_{zx} & \eta_{zy} & \eta_{zz} \end{pmatrix} \equiv \begin{pmatrix} \eta_1 & 2\eta_6 & 2\eta_5 \\ 2\eta_6 & \eta_2 & 2\eta_4 \\ 2\eta_5 & 2\eta_4 & \eta_3 \end{pmatrix}, \quad (6.14)$$

the relation takes the following form for an optically isotropic material [MWH<sup>+</sup>04]:

$$\begin{pmatrix} \Delta\epsilon_1 \\ \Delta\epsilon_2 \\ \Delta\epsilon_3 \\ \Delta\epsilon_4 \\ \Delta\epsilon_5 \\ \Delta\epsilon_6 \end{pmatrix} = \begin{pmatrix} p_1 & p_2 & p_2 & 0 & 0 & 0 \\ p_2 & p_1 & p_2 & 0 & 0 & 0 \\ p_2 & p_2 & p_1 & 0 & 0 & 0 \\ 0 & 0 & 0 & p_3 & 0 & 0 \\ 0 & 0 & 0 & 0 & p_3 & 0 \\ 0 & 0 & 0 & 0 & 0 & p_3 \end{pmatrix} \begin{pmatrix} \eta_1 \\ \eta_2 \\ \eta_3 \\ \eta_4 \\ \eta_5 \\ \eta_6 \end{pmatrix}, \quad (6.15)$$

$$\text{with } p_1 \equiv p_{11}, \quad p_2 \equiv p_{12}, \quad p_3 \equiv p_{44} = (p_{11} - p_{12})/2.$$

The time-dependent deviation of the dielectric tensor due to the strain in our geometry can therefore be expressed as

$$\Delta\epsilon(z, t) \equiv \begin{pmatrix} p_2\eta_3 & 0 & p_3\eta_5 \\ 0 & p_2\eta_3 & p_3\eta_4 \\ p_3\eta_5 & p_3\eta_4 & p_1\eta_3 \end{pmatrix}, \quad (6.16)$$

where the diagonal elements are induced by the longitudinal strain and the off-diagonal elements are induced by the shear strain [MW01]. This can be interpreted as shear strain-induced birefringence in an optically isotropic material. In order to calculate the strain-induced reflectivity change, we require that the electric field vector of the probe light satisfy the general wave equation derived from Maxwell's equations:

$$\left( \Delta - \text{grad div} - \frac{1}{c^2} \tilde{\epsilon}(\vec{x}) \frac{\delta^2}{\delta t^2} \right) \vec{E}(\vec{x}, t) = 0. \quad (6.17)$$

Because of the relatively low frequency of the acoustic perturbation compared to the frequency of the probe light, the system can be treated as quasi-static. By choosing the  $x$ -axis to be included in the plane of incidence for the probe light,  $\vec{E}$  becomes independent of the  $y$ -coordinate.

Similar to Brillouin scattering from longitudinal waves, the reflection can be regarded as a scattering process and the change in the optical wave vector upon scattering is equated to one of the Fourier components of the scattering potential. Since the scattering potential in our scenario depends only on the  $z$ -coordinate, the  $x$ -component of the wave vector must be conserved in such scattering processes. Therefore, the electric field takes the form  $\vec{E}(\vec{x}, t) \equiv \vec{E}(z) \exp\{i(k_x x - \omega t)\}$  and the wave

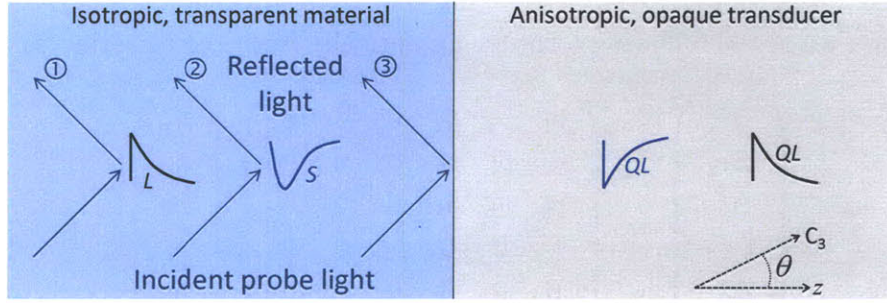


Figure 6-4: Sketch of longitudinal and shear wave interacting with probe light in an isotropic and transparent detection material.

equation 6.17 simplifies to

$$\left\{ \left( \begin{array}{ccc} \frac{\delta^2}{\delta z^2} & 0 & -ik_x \frac{\delta}{\delta z} \\ 0 & \frac{\delta^2}{\delta z^2} - k_x^2 & 0 \\ -ik_x \frac{\delta}{\delta z} & 0 & -k_x^2 \end{array} \right) - \frac{\omega^2}{c^2} \tilde{\epsilon}(z) \right\} \vec{E}(z, t) = 0. \quad (6.18)$$

Assuming an isotropic dielectric constant  $\epsilon$  in the absence of strain in the transparent medium, we can now calculate the electric field of the scattered light. The incident light from  $z < 0$  can be either  $s$  or  $p$  polarized. To simplify the problem further, we ignore longitudinal strain  $\eta_3$  ( $\equiv \eta_{zz}$ ) so that the dielectric tensor contains only off-diagonal components caused by shear strain  $\eta_4$  ( $\equiv \eta_{zy}$ ) and  $\eta_5$  ( $\equiv \eta_{zx}$ ).

For the  $s$  polarized incident light, the resulting electric field is given by

$$\begin{aligned} \vec{E}_s(\vec{x}) &= \begin{pmatrix} 0 \\ 1 \\ 0 \end{pmatrix} \exp\{i(k'z + k_x x)\} \\ &- \frac{1}{k} \begin{pmatrix} k' \\ 0 \\ k_x \end{pmatrix} \exp\{i(-k'z + k_x x)\} \frac{k_x k' k p_3 \eta_4}{(k'' + \epsilon k')(k'' + k') k''}, \end{aligned} \quad (6.19)$$

and the electric field for the  $p$  polarized incident light is given by

$$\begin{aligned} \vec{E}_p(\vec{x}) &= \frac{1}{k} \begin{pmatrix} k' \\ 0 \\ -k_x \end{pmatrix} \exp\{i(k'z + k_x x)\} \\ &+ \begin{pmatrix} 0 \\ 1 \\ 0 \end{pmatrix} \exp\{i(-k'z + k_x x)\} \frac{k_x k' k p_3 \eta_4}{(k'' + \epsilon k')(k'' + k') k''}, \end{aligned} \quad (6.20)$$



where  $k \equiv \frac{\omega}{c}$ ,  $k' \equiv \sqrt{k^2 - k_x^2}$ ,  $k'' \equiv \sqrt{\epsilon k^2 - k_x^2}$ . The first term in both cases corresponds to the incident light and the second term represents the strain-induced reflection. Note that none of the terms depends on  $\eta_5$ .

The light reflected by the propagating shear strain  $\eta_4$  ((2) in Figure 6-4) can interfere with the light reflected from the surface of the transducer (3). This will give rise to Brillouin oscillations which can be treated in a manner similar to that shown in Section 3.3.1. As we see from equations 6.19 and 6.20, certain restrictions apply in shear detection:

- i) Only  $\eta_4$  shear strain can be detected. In order to achieve maximum shear detection efficiency, the shear direction must be perpendicular to the plane of incidence of the optical probe.
- ii) The shear strain-induced term is proportional to  $k_x$ , and therefore oblique optical incidence is essential for shear strain detection.
- iii)  $\eta_4$  strain flips *s*-polarized light to *p*-polarized and vice versa.
- iv) A change in reflectivity  $\delta R \propto \eta_4$  is only possible when the incident and reflected light (with flipped polarization) interfere, which occurs when the incident light already contains both polarizations or when the reflected light gets partially depolarized by the birefringence of the anisotropic transducer.

A detailed theoretical treatment of shear strain detection in multi-layer structures can be found in [MWH<sup>+</sup>08].

### 6.1.3 Optical and Acoustic Cavity Effect

An optical and acoustic cavity is formed when a liquid layer is squeezed in between an optically reflective transducer film and a transparent detection substrate. Acoustic wavepackets generated in the transducer film traverse the thin liquid layer before they are transmitted into the detection substrate. Due to the typically very large acoustic mismatch between the liquid and the detection substrate and transducer, a significant portion of the acoustic wavepackets makes several round trips in the liquid prior essentially complete damping or to transmission into the detection substrate. Similarly, the liquid layer forms an optical cavity, analogous to a FabryPérot etalon, for the probe light. Depending on the liquid layer thickness, this cavity can result in constructive or destructive interference of the multiple transmitted acoustic wave packets or the probe light. For example, in a DC704 sample at 200 K, destructive interference of 395 nm probe light at a  $\sim 21^\circ$  incidence angle in a glass detection substrate is given at a liquid thicknesses in multiples of  $\sim 120$  nm while constructive

interference of longitudinal acoustic waves ( $\sim 42$  GHz) is observed at multiples of  $\sim 30$  nm liquid thickness. While neither the optical nor the acoustic cavity effect posed any problems for the analysis of the displacement presented in the previous chapter (neither were relevant for the data analysis), cavity effects may significantly impact the accuracy of the extracted acoustic parameters and measurement for a liquid in a shear sample configuration. Therefore, the following section will analyze the implications of the acoustic and optical cavity effect and its impact on the data analysis.

For the sake of simplicity, we consider a single, plane acoustic wave (denoted by  $\delta_{ac}$ ) launched from the acousto-optic transducer (0) at  $t = 0$  in the  $z$ -direction where it has traveled a distance  $z_{ac}$  away from the transducer-liquid interface after a time  $t > 0$ , as depicted in Figure 6-5. The polarization of the acoustic wave (be it longitudinal or shear) or the form of the acoustic wave packet (be it single or multiple pulses) do not matter in the following theoretical considerations. Moreover, as we saw above, shear wave detection requires the probe to be obliquely incident and the detection geometry to be sensitive to a flip in polarization. However, to simplify matters further we consider normally incident probe light. It will be straightforward to extend the arguments to a more complex scenario. The theory is valid for any probe polarization as long as the scattered fields and the overall reflected probe light (see Figure 6-5) have components of the same polarization.

The electric field of an incoming optical probe pulse,  $E_{in}$ , at a given position  $z$  at time  $t$ , can be written as

$$E_{in} = E_0 e^{i[\omega t + k_2 z + (k_1 - k_2)d]} , \quad (6.21)$$

where  $E_0$  denotes the initial electric field amplitude,  $d$  the liquid thickness (as shown in Figure 6-5),  $k_1$  and  $k_2$  the wave vectors of the electric field in the liquid and the substrate, respectively, and  $\omega$  the angular frequency. The phase of the electric field is arbitrarily chosen so that the electric field of the femtosecond optical probe, whose envelope we treat as a  $\delta$ -function localized in space and time, arrives at the metal surface at  $t = 0$ . The overall reflected electric field of the outgoing optical probe pulse,  $E_{out}$ , is the superposition of all the electric fields reflected at the transducer-liquid and liquid-substrate interfaces,  $E_{out}^1$ ,  $E_{out}^2$ , etc., which can be written as

$$E_{out} = R \times E_0 e^{i[\omega t - k_2 z + (k_1 + k_2)d]} . \quad (6.22)$$

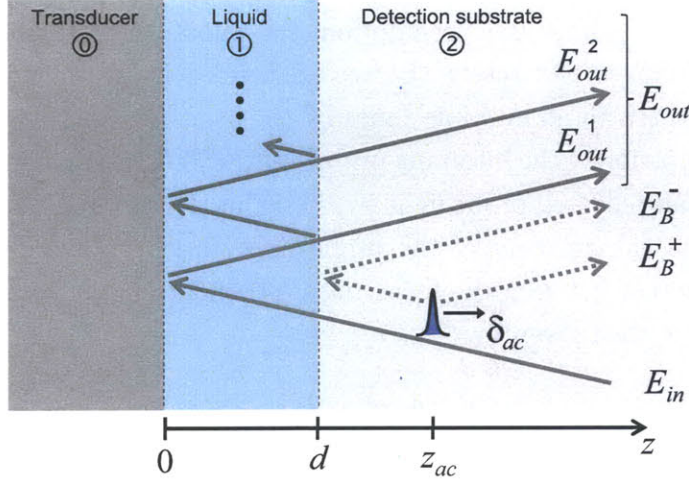


Figure 6-5: Sketch of acoustic and optical cavity. The cavity is formed by a liquid layer (1) of thickness  $d$ , squeezed in between an opaque or semi-transparent, optically reflective transducer film (0) and a transparent detection substrate (2). Longitudinal and/or shear acoustic waves, generated in the transducer film, propagate in the  $z$ -direction through the adjacent liquid layer and into the detection substrate. At time  $t$ , the acoustic wave (we only consider one acoustic wave for simplicity), denoted by  $\delta_{ac}$ , has traveled a distance  $z_{ac}$  away from the transducer-liquid interface where it induces a small change in the permittivity tensor of the substrate. Through the photoelastic effect, this perturbation backscatters a small portion of the incoming electric field,  $E_{in}$ , denoted as  $E_B^+$ , and a small portion of the electric field reflected by the transducer,  $E_{out}^1$ , denoted as  $E_B^-$ . Some portion of the incoming electric field reflected by the transducer makes one or more round-trips in the optical cavity formed by the liquid layer before it finally escapes the cavity as  $E_{out}^1$  and  $E_{out}^2$ . All these outgoing electric fields interfere with each other and produce a heterodyne photoelastic signal measured by the photodiode.

where  $R$  is the overall reflection coefficient of the Fabry-Pérot cavity,

$$\begin{aligned}
 R &= r_{21} + \frac{t_{21}t_{12} \exp[-2ik_1d]}{1 - r_{10}r_{12} \exp[-2ik_1d]} \\
 &= |R| e^{i\phi},
 \end{aligned} \tag{6.23}$$

where  $\phi$  is the optical phase shift induced by the cavity,  $r_{21}$  is the reflection coefficient from the substrate-liquid interface,  $r_{10}$  is the reflection coefficient from the liquid-transducer interface,  $t_{21}$  is the transmission coefficient from the substrate into the liquid, and  $t_{12}$  is the transmission coefficient from the liquid into the substrate.

Now, we consider the photoelastic interaction of a gigahertz acoustic plane wave, treated as a  $\delta$ -function in space at position  $z_{ac}$ , with the incoming probe electric field and its reflections from the Fabry-Pérot cavity. Since the frequency of the acoustic

wave is much lower than the frequency of the probe electric field, the system can be treated as quasistatic. Under this assumption, the photoelastic interaction depends only on the  $z_{ac}$  coordinate. Because of the weak nature of the photoelastic interaction, we will neglect light scattered multiple times by the acoustic wave. We only consider the backscattered portion of the incoming probe light,  $E_B^+$ , as well as the backscattered portion of the overall reflected probe light by the Fabry-Pérot cavity,  $E_B^-$ , as depicted in Figure 6-5. The electric field of the probe light which is backscattered by the photoelastic interaction between the incoming probe light and the acoustic wave for  $z > z_{ac}$  and time  $t$  is then given by

$$E_B^+ = \delta_{ac} \times E_0 e^{i[\omega t - k_2 z + (k_1 + k_2)d + 2ik_2(z_{ac} - d)]}, \quad (6.24)$$

where  $\delta_{ac} \times E_0$  ( $\delta_{ac} \ll 1$ ) is the amplitude of the scattered electric field.  $E_B^+$  is proportional to the amplitude of the incoming electric field  $E_0$ , the photoelastic coefficients, and the dielectric constant of the transparent substrate. The scattered electric field  $E_B^-$  originating from the interaction of the overall probe light reflected by the Fabry-Pérot cavity  $E_{out}$  with the acoustic wave at a given position  $z > z_{ac}$  and time  $t$  can be expressed as

$$E_B^- = R^2 \times (\delta_{ac} \times E_0) \times e^{i[\omega t - k_2 z + (k_1 + k_2)d - 2ik_2(z_{ac} - d)]}. \quad (6.25)$$

The scattered electric fields,  $E_B^+$  (6.24) and  $E_B^-$  (6.25), overlap with the outgoing electric field of the reflected probe light  $E_{out}$  (6.22) and interfere. The overall intensity  $I$  of the interfering scattered electric fields, as measured by the photodiode, is given by

$$\begin{aligned} I &= |E_{out} + E_B^+ + E_B^-|^2 \\ &= E_0^2 [ |R|^2 + 2|R|\delta_{ac} \cos(2k_2(z_{ac} - d) - \phi) \\ &\quad + 2|R|^3\delta_{ac} \cos(2k_2(z_{ac} - d) - \phi) \\ &\quad + \delta_{ac}^2 + \delta_{ac}^2|R|^4 + 2\delta_{ac}^2|R|^2 \cos(4k_2(z_{ac} - d) - 2\phi) ]. \end{aligned} \quad (6.26)$$

Neglecting second order terms  $\delta_{ac}^2$ , which correspond to the interference between the two scattered electric fields  $E_B^+$  and  $E_B^-$ , simplifies the overall reflected light intensity  $I$  as measured by the photodiode to be

$$\begin{aligned} I &\approx E_0^2 [ |R|^2 + 2|R|\delta_{ac} \cos(2k_2(z_{ac} - d) - \phi) \\ &\quad + 2|R|^3\delta_{ac} \cos(2k_2(z_{ac} - d) - \phi) ]. \end{aligned} \quad (6.27)$$

This equation expresses the heterodyning effect between the probe light reflected by the Fabry-Pérot cavity, usually called the reference or local oscillator field, and the two scattered light fields,  $E_B^+$  and  $E_B^-$ . Heterodyning greatly improves the detection sensitivity of the scattered field  $\delta_{ac}$ , since the signal is now proportional to  $|R| E_0^2$ , the field of the reflected probe light and the phase-sensitive superposition of the signal and reflected fields permits direct time-resolved observation of acoustic oscillation frequency as we saw earlier for longitudinal waves. In the case of shear photoelastic scattering, the scattered light has its polarization flipped and is therefore cross-polarized with respect to the reference probe. As a result in the case of incoming probe light linearly polarized parallel or perpendicular to the scattering plane, there is no heterodyning in the absence of further polarization mixing. However, without heterodyning, only the second order terms in (6.26) remain and the signal is then proportional to  $I_0 \delta_{ac}^2$  instead of  $I_0 \delta_{ac}$ . Therefore, for the specific case of shear wave detection, it is important to recombine the polarization of the reference probe and the scattered probe. Finally, the intensity of the overall scattered signal  $I_S$  detected at the photodiodes can be rewritten as

$$I_S = 2I_0 |R|(1 + |R|^2) \delta_{ac} \cos(2k_2(z_{ac} - d) - \phi), \quad (6.28)$$

such that the signal intensity is proportional to  $\cos(2k_2(z_{ac} - d) - \phi)$ . Substituting the position of the acoustic wave  $z_2$  at a given time  $t$  by  $d + c_2(t - d/c_1)$  (valid for  $t \geq d/c_1$ ), where  $c_1$  and  $c_2$  are the acoustic speeds in the liquid film and the substrate, respectively, equation 6.28 becomes

$$I_S = 2I_0 |R|(1 + |R|^2) \delta_{ac} \cos(2\pi\nu_{2,B}t - \phi_B), \quad (6.29)$$

where

$$2\pi \nu_{2,B} = 2k_2 c_2 \quad (6.30)$$

defines the frequency  $\nu_{2,B}$  of modulation of the signal intensity, called the Brillouin frequency, and

$$\phi_B = \phi_1 + \phi = 2\pi \nu_{2,B} d/c_1 + \phi \quad (6.31)$$

is the overall phase shift of the signal at frequency  $\nu_{2,B}$ . This phase shift is caused by the optical phase shift  $\phi$  expressed in equation 6.23. The acoustic phase shift is  $\phi_1 = d/c_1$ , introduced by the time delay resulting from the travel time of the acoustic wave through a liquid of thickness  $d$  at the acoustic speed  $c_1$ . The parameters of interest are the speed of sound  $c_1$  and the acoustic attenuation  $\Gamma$  of the liquid. With the sample configuration considered here, a measurement of the speed of sound  $c_1$  is

linked to measurements of both the phase shift  $\phi_B$  and the liquid thickness  $d$ . Even though the liquid thickness is unknown, it can be estimated from literature values of the speed of sound in the liquid,  $c_1$  at a similar frequency. To circumvent this problem, measurements can be performed at many different liquid thicknesses  $d$  with a sample configuration in which the liquid thickness is controlled, e.g. by a curved-flat sample design. The speed of sound can then be extracted from phase shift measurements at many different thicknesses by fitting the extracted phase shifts to the known shape of the sample topography. This strategy renders the use of any additional means or assumptions to determine the liquid sample thickness unnecessary.

A good approximation for the optical phase shift is given by

$$\phi \sim -2k_1d = -2\pi\nu_{1,B} d/c_1 , \quad (6.32)$$

which indicates that the phase shift is primarily due to the travel time of the optical probe with wave vector  $k_1$  through a liquid having a certain thickness  $d$ . This wave vector is linked to the Brillouin scattering frequency of the liquid  $\nu_{1,B}$  by equation 6.30. Equation 6.31 can then be written in the form,

$$\phi_B = \phi_1 + \phi = 2\pi(\nu_{2,B} - \nu_{1,B}) d/c_1 . \quad (6.33)$$

Thus, the overall phase shift originates from two competing contributions: the optical phase shift and the acoustic phase shift. Equation 6.33 is valid for probe light at both normal and oblique incidence. The Brillouin frequency measured in the case of oblique incidence at an angle  $\theta_{sub}$  (see Figure 6-14) is lower than that measured at normal incidence by a factor  $\cos(\theta_{sub})$ .

We have performed numerical calculations in order to test the accuracy of equation 6.33. In this approximate expression the phase shift is expressed in terms of Brillouin scattering frequencies, while the exact overall phase shift, derived from expression 6.23, can only be computed when all optical parameters at each interface of the sample structure are known (which is not always the case). We found that equation 6.33 does not deviate more than a few percent from the exact overall phase shift over a wide range of thicknesses  $d$ . However, at thicknesses of a couple of nanometers, the approximate phase shift is no longer accurate. In this case, the uncertainties become significant since the acoustic or optical wavelengths are much greater than the liquid thickness, giving rise to a phase shift that is very small. This problem of approximating phase shifts is reduced at increased Brillouin frequency of the substrate  $\nu_{2,B}$ , so that the probed acoustic wavelength of the liquid film is decreased. To our knowledge, the highest Brillouin frequencies ever recorded are  $\sim 250$  GHz at 400 nm probe light in a silicon substrate [DFA<sup>+</sup>08]. Using this as an



example, the acoustic wavelength in water at room temperature would be approximately  $1500 \text{ m s}^{-1}/250 \text{ GHz} = 6 \text{ nm}$ .

Even if the shape of the liquid's thickness topography cannot be controlled perfectly, for example in the case of ultra thin liquid layers, measurements of shear acoustic properties of such liquids are still possible when the longitudinal acoustic speed  $c_{1,L}$  is known or can be measured by other means (e.g. by Brillouin scattering in the liquid at a similar acoustic frequency). With this information regarding  $c_{1,S}$ , the shape of the liquid's topography can be reconstructed through the phase treatment of the longitudinal acoustic signal. The shear speed of sound can then be deduced from the phase analysis of the shear signal topography that has been determined. An example will be presented later in this chapter (see inset Figure 6-11 c). The uncertainties of this method are related to the uncertainties in the measurement of the longitudinal speed of sound and are typically a few percent.

The acoustic attenuation rate  $\Gamma$  is determined by measuring the photoelastic scattering amplitude  $\delta_{ac}$  in the detection substrate (equation 6.28). The photoelastic scattering amplitude  $\delta_{ac}$  is proportional to the amplitude of the acoustic wave and decreases exponentially with liquid thickness,

$$\delta_{ac} \propto \exp(-\Gamma d/c_1). \quad (6.34)$$

The intensity of the reflected reference probe light from the Fabry-Pérot cavity also depends on the liquid thickness as described by equation 6.23. This is responsible for the heterodyning at the Brillouin frequency  $\nu_{2,B}$ . Thus, the Fourier amplitude of the Fourier transformed measured signal in the detection substrate,  $I_{ac}$ , at the Brillouin frequency  $\nu_{2,B}$ , involves both contributions which follow as

$$\begin{aligned} I_{ac} &= 2I_0 |R| (1 + |R|^2) \delta_{ac} \\ &\propto 2I_0 |R| (1 + |R|^2) \exp(-\Gamma d/c_1) \end{aligned} \quad (6.35)$$

from equations 6.28 and 6.34. It is clear from equation 6.35, that the optical cavity effect, weighted by  $|R| (1 + |R|^2)$ , has an influence on the amplitude of the measured signal which if not accounted for properly can lead to an erroneous estimation of the acoustic attenuation coefficient  $\Gamma$ . The impact of the optical cavity effect can be substantially reduced by normalizing all scans recorded at different liquid thicknesses by a signal component that appears only at  $t = 0$  due to optically excited "hot" electrons in the transducer film and whose amplitude, given by  $\delta_e(t) \times E_0$  ( $\delta_e(t) \ll 1$ ), is also heterodyned with the field that is reflected from the transducer in the absence

of photoexcitation, yielding a signal intensity

$$I_e(t) = 2I_0 |R| \delta_e(t) . \quad (6.36)$$

This signal, which is over before the acoustic signal begins, provides an internal standard for the amplitude of the acoustic signal recorded at each liquid layer thickness.

Comparison of  $I_{ac}$  and  $I_e(t)$  shows that there is a systematic error related to  $|R|^2$ . However, for sample configurations used in the work presented in this chapter, the change in measured signal amplitude for different liquid thicknesses is proportional to  $|R|(1 + |R|^2)$  and the resulting changes of  $|R|^2$  are extremely weak. The top data of Figure 6-6 shows the typical change in probe reflectivity for different liquid thicknesses as a result of the optical cavity effect. The observed changes of only 5% are relatively small, and it is clear that the related systematic error, proportional to  $|R|^2$ , is negligible. However, it should be mentioned that in order to improve the detection sensitivity, it could be possible to design a sample and optical probing configuration in which the resonance of the optical cavity is enhanced only at some isolated liquid thicknesses, similar to the work of Li *et al.* [LMNM09].

The second aspect of the liquid cavity concerns its acoustic resonances at particular liquid thicknesses. These effects also modulate the amplitude of the photoelastic signal, as shown in Figure 6-6. For this example, DC704 was cooled below its glass transition temperature into a glassy state at 200 K, where the acoustic damping is low enough to substantially improve the quality factor of the acoustic cavity. The acoustic resonance disappears at higher temperatures due to much higher acoustic damping in its liquid state. Nevertheless, the acoustic cavity effect can provide additional information about film properties, since the thickness, with its corresponding acoustic resonance, resembles the acoustic wavelength of the liquid at the Brillouin frequency and hence allows the speed of sound to be determined in this manner. For our example shown in Figure 6-6, we obtain a longitudinal speed of sound of  $c_1^l = 31.2 \text{ nm} \times 42 \text{ GHz} \approx (1310 \pm 30) \text{ m s}^{-1}$ . Even in the case of a strong acoustic resonance, it is possible to measure the acoustic attenuation by fitting an exponential function to the attenuation data obtained at many different liquid thicknesses. This was done for the data of Figure 6-6 and a value of  $\Gamma/c_1^l = (2.1 \pm 0.2) \times 10^6 \text{ m}^{-1}$  for longitudinal acoustic attenuation in DC704 at 42 GHz and 200 K was obtained.

## 6.2 Experimental Methods

The following section describes the experimental implementation of shear wave generation and detection. Straightforward modifications can be made to allow to generate

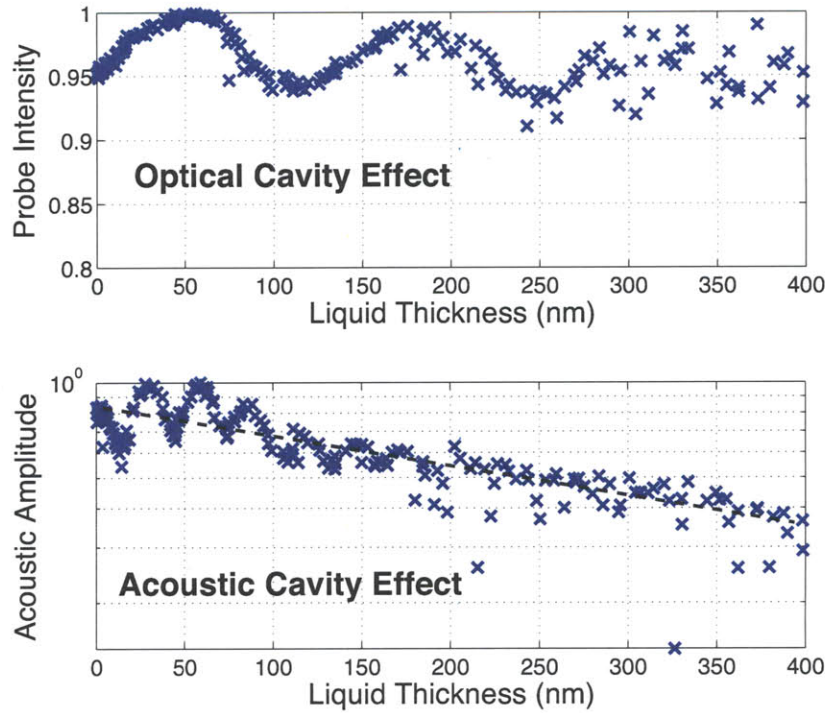


Figure 6-6: Normalized intensity of the overall reflected probe light (top) and the normalized amplitude of the Fourier transformed, longitudinal Brillouin scattering signal (bottom) for different liquid thicknesses. The sample configuration was an MBE iron transducer, DC704 at 200 K as the liquid and a glass detection substrate with a Brillouin scattering frequency of 42 GHz. The optical and acoustic cavity effects can be significant in some cases, as revealed in these plots.

shear waves. The only difference between shear wave and longitudinal transducers is the requirement of broken elastic symmetry, which we achieve either by obliquely grown MBE iron thin films or lattice matched strontium ruthenate thin films grown on off-axis cut strontium titanate, as depicted in Figure 6-2 c). The transducer must have a broken symmetry such that the  $C_3$  axis tilt is in the vertical plane so that a vertically polarized shear wave can be generated and detected. In principle, shear wave propagation could be directly monitored in a liquid using a method analogous to that used in detection of longitudinal wave propagation in sample configuration (III) shown in Figure 4-1. However, high shear acoustic attenuation rates in liquids (shear attenuation in glycerol is about an order of magnitude higher than longitudinal attenuation in the gigahertz frequency range) and low scattering efficiency of probe light by shear waves in many liquids (determined by the photoelastic tensor component  $p_3$  as defined by equation 6.15) forces us to adapt our approach as outlined below.

### 6.2.1 Shear Brillouin Scattering Detection Setup

From the theory of shear wave detection developed in the previous section, we see from equations 6.19 and 6.20 that optical sensitivity to shear waves requires a non-normal probe light incidence angle with respect to the plane of the shear wave front. A sketch of the developed shear detection scheme is shown in Figure 6-7.

The pump pulse sequence incident on the shear transducer film through the generation side substrate (GSS) launches longitudinal and shear acoustic wave packets through an adjacent thin liquid layer and into the detection substrate (DS) as depicted in configuration (II) of Figure 4-1. The incoming vertically polarized probe light is focused to a spot of about 25  $\mu\text{m}$  on the sample, interacts with both the propagating longitudinal acoustic wave and the propagating shear wave under the condition of oblique angle of incidence. This scenario is depicted in Figure 6-7 b) where only the shear acoustic wave is shown for clarity. The initially vertically polarized probe light backscatters off of the shear wave with a flip in polarization. The main part of the probe light is reflected by the birefringent transducer surface such that a small portion of it becomes depolarized. All of the reflected probe light is then collimated by a second lens, as shown in Figure 6-7 a) before the probe is separated into its vertical and horizontal polarization component by a half wave plate and a polarizing beam splitter cube.

Two different balanced detection setups were designed to record the weak oscillatory signal caused by the interference of (1) the probe light having a flipped polarization as a result of scattering off the propagating shear wave and (2) the depolarized portion of the probe light reflected by the transducer film. In detection setup (I), as sketched in Figure 6-7, the half wave plate (HWP) is used to rotate the polarization of the probe light by  $45^\circ$  such that the polarizing beam splitter (PBS) cube reflects and transmits approximately equal portions of the probe light onto each of the two photodiodes, A and B. Subtraction of the two diode signals, e.g.  $A-B$ , cancels laser noise and random intensity fluctuations such as those caused by air currents. In this detection scenario, the intensity modulation of the perpendicularly polarized light which has been scattered by the shear acoustic wave induces a slight change to the overall polarization which in turn modulates the intensity ratio between the two diodes. This very small intensity modulation, on the order of  $10^{-5}$  to  $10^{-7}$ , can only be reliably determined by phase-sensitive (lock-in) detection and therefore requires the use of an optical chopper (acousto-optic modulator) to modulate the pump beam. Detection setup (II) also deploys balanced detection. However, in this case the horizontally polarized portion of the reflected probe light is balanced against the unmodulated probe light picked off before the sample by a beamsplitter. The half wave plate before the polarizing beam splitter cube is not strictly necessary since we

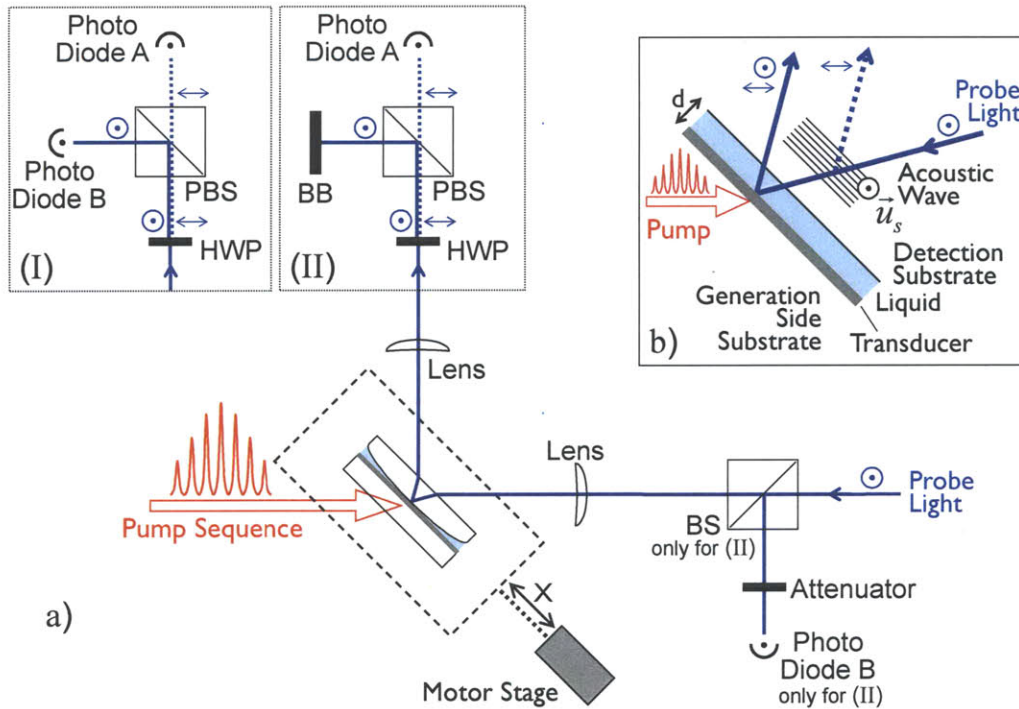


Figure 6-7: (a) Sketch of shear detection setup in front-back pump-probe geometry and (b) closeup of sample assembly: (b) An optical pump pulse sequence incident on a specialized shear transducer thin film launches longitudinal and vertically polarized shear acoustic wavepackets into an adjacent liquid layer of given thickness  $d_{\text{liquid}}$  (considered constant over the probe spot area). After propagation through the liquid, the acoustic waves are detected in a transparent solid substrate by time resolved coherent Brillouin scattering. For longitudinal waves, the theory developed in Section 3.3.1 applies and here we focus on modifications necessary for shear detection. Vertically polarized incident probe light interacts with the propagating shear wave and backscatters with  $90^\circ$  flip in polarization. Probe light reflecting off the anisotropic (birefringent) transducer gets partially depolarized and its horizontal component interferes with the polarization-flipped signal in a manner analogous to longitudinal Brillouin scattering. (a) Two different balanced photodetection schemes are capable of recording extremely weak depolarized Brillouin scattering signal. In scheme (I), the polarization of the reflected probe light from the sample is rotated by  $45^\circ$  through a half wave-plate (HWP) and subsequently separated into its horizontally and vertically polarized components by a polarizing beam splitter cube (PBS). Each component has approximately half the initial light intensity, and differential detection of diode A with diode B filters out all common noise in the signal. The polarization-flip from shear waves causes a slight rotation of the overall polarization, resulting in a tiny intensity ratio change on the diodes which can be recorded. In scheme (II), only the transmitted light through the PBS is used (the reflected portion is blocked by a beam block (BB)) and balanced with the reference probe light. In both configurations, the sample is mounted on a motorized stage and data are recorded at several lateral (X) positions, corresponding to several different liquid layer thicknesses.



are only interested in the transmitted, horizontally polarized portion of the probe light. However, the horizontally polarized portion is weaker than the sensitivity limit of the photodiode and the electronics. Therefore, we use the wave plate to increase the light intensity on photodiode A to above the sensitivity limit by a slight rotation of the polarization such that more light is leaked through. The intensity of photodiode B is then adjusted with an attenuator to match the intensity on diode A so that the diodes remain balanced.

In principle, both detection setups (I) and (II) are sensitive only to the intensity modulation of light polarized perpendicularly to the incoming probe light. Setup (I) accomplishes this through the rotation of the overall light polarization whereas setup (II) does this through modulation of the light intensity. The advantage of setup (I) is that the probe light intensity on both diodes is quite large, enabling their operation well above their sensitivity limit. The disadvantage is that this detection setup is not sensitive to signals produced by longitudinal acoustic waves, which are often necessary components in analysis of the shear acoustic signal. The advantage of setup (II) is its ability to detect both shear and longitudinal signal due to the transmission of scattered light from the longitudinal waves through the polarizing beam splitter that is allowed by slightly rotating the half wave plate to cause a small leakage beam. However, the operation of the photodiode and detection electronics just above their sensitivity limits makes this setup configuration highly noise sensitive and difficult to align.

## 6.2.2 Shear Brillouin Scattering Data

Shear Brillouin oscillations recorded by detection setup (II) in a glass substrate are shown in Figure 6-8. The excitation of the acoustic wave by a single excitation laser pulse took place at the air interface of an MBE iron thin film. After transmission into the glass substrate, the propagation of the acoustic wave was monitored by a 395 nm probe pulse having a 45° incidence angle in air ( $\sim 30^\circ$  in glass, see Figure 6-14). The Fourier transform of the oscillatory signal is shown in the inset and the shear Brillouin scattering frequency (determined by the substrate/probe angle geometry) of about 23 GHz is well resolved. No longitudinal Brillouin scattering (frequency of  $\sim 41$  GHz) is observed in the spectrum. This is a result of rotating the HWP so that only light which was perpendicularly polarized with respect to the incoming probe light by scattering from the acoustic wave was transmitted through the PBS cube and detected by the photodiode.

Shear Brillouin scattering data recorded upon transmission of the acoustic wave through two different liquid layer thicknesses into a sapphire substrate are shown in Figure 6-9. The liquid thickness was adjusted by translating the sample perpendic-

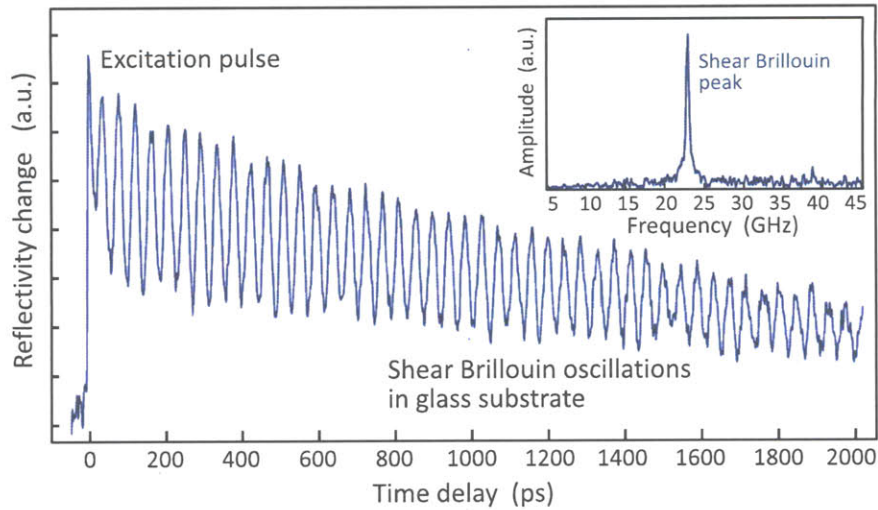


Figure 6-8: Shear Brillouin oscillations in a glass substrate. An acoustic wavepacket is generated by a single excitation pulse at the air interface of a MBE iron thin film and directly transmitted into the glass substrate where it is recorded by detection setup (II). The Fourier spectrum (inset) clearly shows a peak at the shear Brillouin scattering frequency of 23 GHz but no indication of a peak at the longitudinal scattering frequency of 41 GHz. This clearly shows the capability of the detection setup to be selective only to shear acoustic waves.

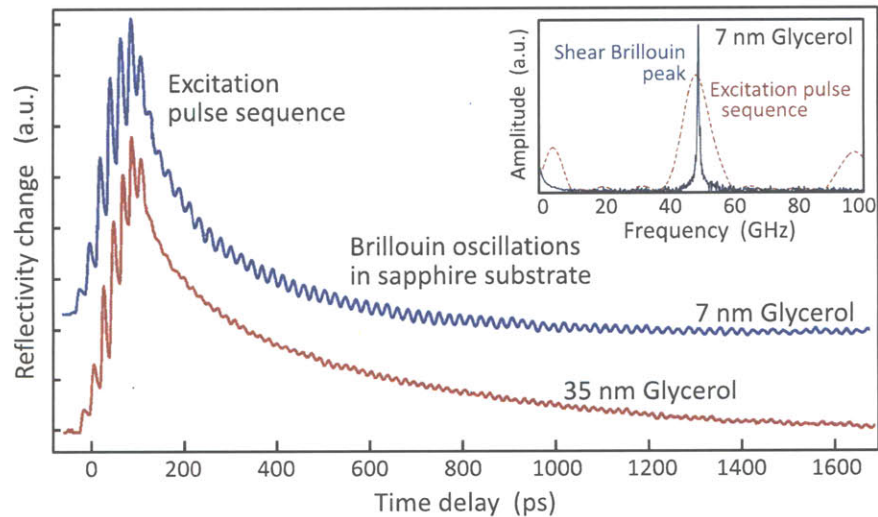


Figure 6-9: Shear Brillouin scattering oscillation in a sapphire substrate ( $\sim 47$  GHz) after transmission through two different liquid layer thicknesses, 7 nm and 35 nm of glycerol at room temperature. Weaker Brillouin scattering efficiency compared to the configuration of Figure 6-8 requires the use of an excitation pulse sequence to enhance scattering efficiency. The inset shows the Fourier transform of two selected intervals of the reflectivity data recorded for 7 nm of glycerol. The first 200 ps comprises the excitation pulse sequence, and the remaining signal comes from Brillouin scattering in the sapphire substrate.



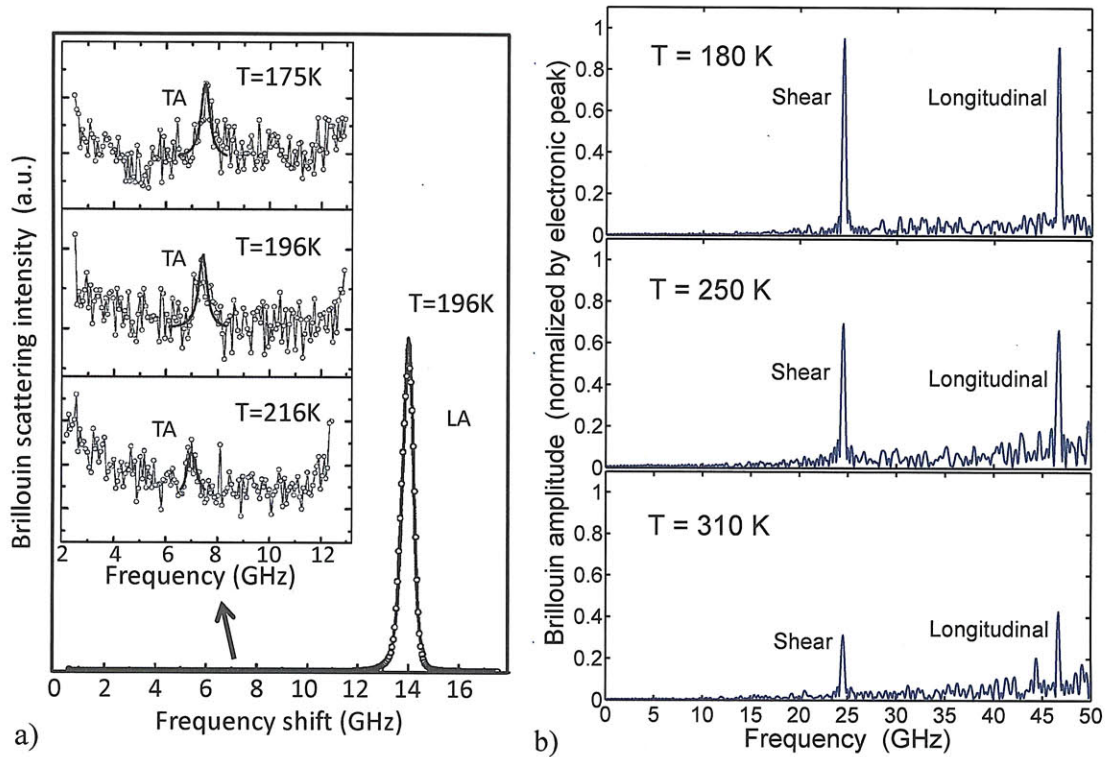


Figure 6-10: Comparison of raw data from two different measurement techniques of acoustic modes in glycerol: (a) the only available data in the literature [SCFP04] and (b) data obtained by our approach. (a) Depolarized spectra of glycerol recorded by a Sandercock-type (3+3)-pass tandem Fabry-Pérot interferometer with typical accumulation times for each spectrum of about 12 h. Despite this long data acquisition time the temperature range is limited to temperatures close to the glass transition temperature of  $T_g = 186$  K where damping is small. The large peak (LA) at 14 GHz originates from photons that were scattered by longitudinal phonons and that leaked through the crossed polarizers used to optimize detection of the shear wave signal, and the insets show expanded views of shear acoustic peaks (TA) at different temperatures. (b) Spectra obtained by Fourier transformation of time-domain Brillouin scattering recorded by our approach in a BK7 detection substrate after propagation through about 100 nm of glycerol. Time-domain data were normalized by the electronic peak and spectral brightness was enhanced by multiple pulse excitation at the shear frequency of  $\sim 24$  GHz. Longitudinal peaks at  $\sim 47$  GHz are visible due to a slight detuning of the probe light polarization by the detection half wave plate (see Figure 6-7). Typical data acquisition times per spectrum are about 20 minutes (down to 5 minutes at low temperatures). Note that spectra recorded at different liquid thicknesses are necessary to determine acoustic velocities and attenuation rates of the liquid at a particular temperature. The highest temperature (310 K) of our measurement was limited by the sample-in-vapor cryostat and can in principle exceed 400 K.

ular to the substrate surfaces using a motorized stage as sketched in Figure 6-7 a). The acoustic wave packet was generated by an optical pump pulse sequence having a frequency of 47 GHz to match the shear Brillouin scattering frequency at a probe incidence angle of  $\sim 23^\circ$  in the sapphire detection substrate ( $45^\circ$  incidence angle in air). The sample structure consisted of a glass lens as the generation side substrate which is coated with an MBE iron transducer film, and a sapphire detection substrate as shown in Figure 6-7 b). The pairing of two different substrate materials for generation side substrate and detection substrate is essential for distinguishing between Brillouin scattering originating from the acoustic wavepacket transmitted into the generation side substrate and the wavepacket that propagated through the liquid and into the detection substrate. Only Brillouin scattering detected in the detection substrate is of interest.

Figure 6-10 shows the comparison of acoustic spectra of glycerol obtained by our technique with frequency-domain Brillouin scattering by Scarponi *et al.* [SCFP04] — surprisingly the only Brillouin scattering study from transverse acoustic modes carried out on this prototypical and extremely well studied glass former. The reason for this lies in its low depolarized scattering efficiency. The intensity of the light scattered from transverse acoustic modes in frequency-domain Brillouin scattering experiments is relatively strong in liquids of highly anisotropic molecules, where the rotational dynamics provide an effective channel for depolarized scattering. The scattered intensity is much lower in systems, like glycerol, with low molecular anisotropy. Even though the typical data acquisition time per spectrum was about 12 h, the SNR of the depicted spectra is extremely poor. In frequency-domain Brillouin scattering, the characteristic frequency  $\omega_0$  and linewidth  $\Gamma$  of longitudinal and shear acoustic waves are obtained by fitting the Brillouin peaks with the damped harmonic oscillator (DHO) model function at a given wavevector  $q$ ,

$$I(q, \omega) = \frac{I_0}{\pi} \frac{\Gamma \omega_0^2}{(\omega^2 - \omega_0^2)^2 + (\Gamma \omega)^2}, \quad (6.37)$$

where  $I_0$  is the area of the peak. In case of the transverse peaks such a fit is difficult and hardly allows one to extract a reliable value for the linewidth, i.e. the shear acoustic attenuation rate. In the technique we have developed we circumvent this problem by not detecting shear waves in the liquid itself but in a detection substrate after propagation through a liquid layer of a certain thickness. This allows us to choose detection substrates with efficient depolarized scattering efficiency as described in detail above. Figure 6-10 b) shows example spectra of longitudinal and shear acoustic waves at three different temperatures after propagation through 100 nm glycerol thickness. Time-domain data were normalized by the electronic peak before

the Fourier transform was taken. Spectral brightness was enhanced by multiple pulse excitation at the shear frequency of  $\sim 24$  GHz. At  $\sim 47$  GHz, longitudinal peaks are visible due to a slight detuning of the probe light polarization incident on the polarized beam splitter by the half wave plate (see Figure 6-7).

### 6.2.3 Data Analysis

Data sets for a particular sample are recorded at a fixed temperature for multiple lateral positions  $\mathbf{X}$  corresponding to various liquid layer thicknesses. An example of such a data set for glycerol at room temperature using a curved slope sample design is shown in Figure 6-11. Even though the  $\mathbf{X}$  steps are much larger than the  $20\ \mu\text{m}$  diameter of the focused probe laser beam, the steps are sufficiently small to reliably interpolate the signal between them. A single excitation pulse rather than a pulse sequence was used for the data shown in this Figure in order to distinguish features at early times. Though excitation pulse sequences are usually used to generate a multiple cycle acoustic wave in order to enhance a particular frequency component, the use of such sequences is not necessary for studying longitudinal waves in a glass substrate, since the signal at the selected Brillouin scattering frequency is strong even when a single excitation pulse is used. The high-frequency signal oscillations at  $\nu_{sub}^l \approx 41$  GHz correspond to Brillouin scattering from longitudinal acoustic waves in the BK7 glass substrate while the low-frequency oscillations at  $\nu_{liq}^l \approx 18$  GHz correspond to Brillouin scattering from the acoustic waves in liquid glycerol. Near the center of the sample ( $\mathbf{X} \approx 0$ ) where the lens and the substrate are almost in direct contact, signal oscillations due to acoustic propagation in the substrate begin promptly. Away from the center of the sample ( $|\mathbf{X}| > 0.5\ \text{mm}$ ), the transit time through the liquid layer manifests itself as a delay in the start of substrate acoustic propagation and a phase shift in the signal oscillations relative to the phase at the center of the sample. Still further from the center ( $|\mathbf{X}| > 1\ \text{mm}$ ), the signal oscillations due to acoustic wave propagation in the substrate are further delayed and phase shifted, and these oscillations are preceded by lower-frequency oscillations arising from acoustic wave propagation in the liquid.

A second example — measurements obtained from DC704 at 200 K with a linear slope sample design — is shown in Figure 6-12. Figure 6-12 a) exhibits features similar to those discussed above for Figure 6-11 a). Since 200 K is below the glass transition temperature of DC704, there is weak acoustic attenuation in the glassy DC704 and several acoustic round trips in the liquid cavity can be monitored. At  $\mathbf{X} \approx 4\ \text{mm}$  on the sample, approximately four oscillations of Brillouin scattering in DC704 are visible before the acoustic wave reaches the liquid-detection substrate interface at about 250 ps. The acoustic pulse gets partially transmitted into the

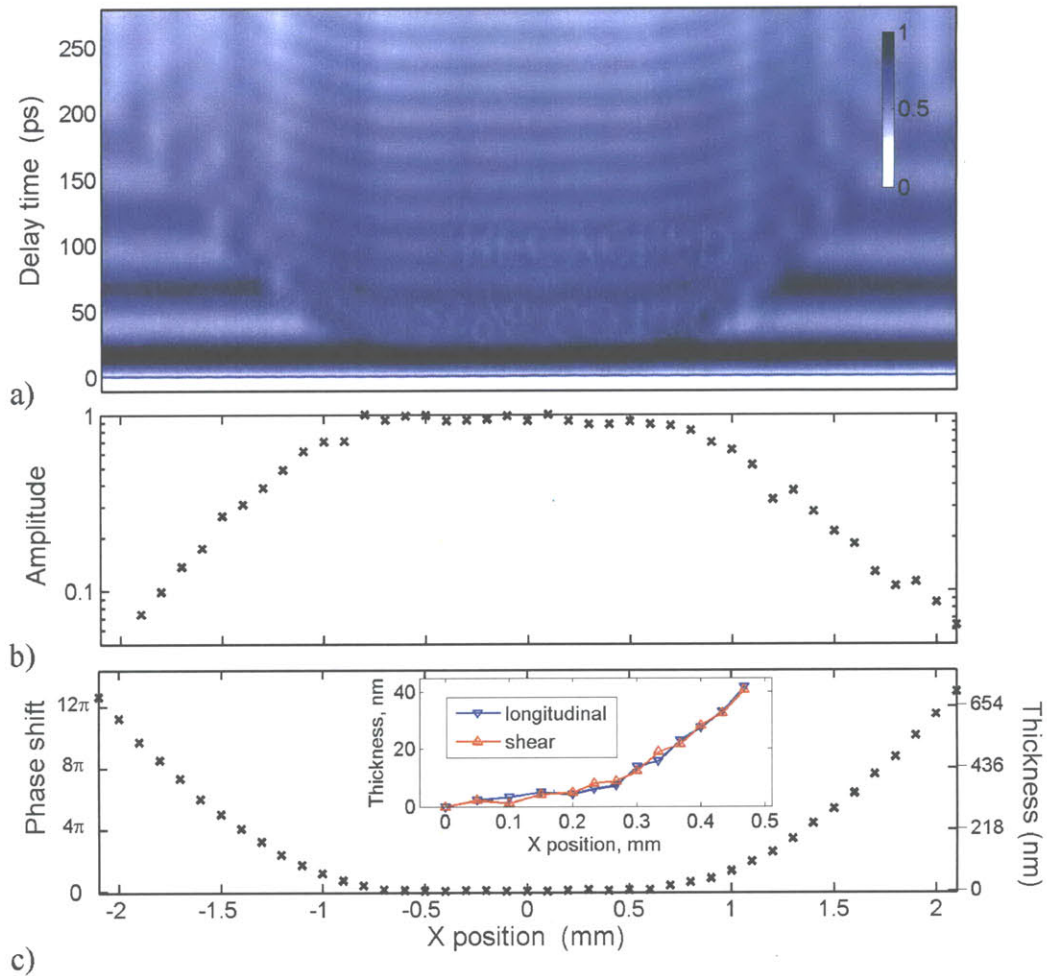


Figure 6-11: (a) Interpolated 2D plot of about 40 longitudinal wave data sets, recorded in glycerol at room temperature in a curved-flat substrate configuration, as a function of probe delay time (plotted vertically) at different lateral ( $X$ ) positions across the sample (displayed horizontally). The  $X$  steps are much larger than the  $20\ \mu\text{m}$  diameter of the focused probe laser beam, but they are sufficiently small that the signal between steps can be interpolated reliably. A single excitation pulse rather than a pulse sequence was used. The high-frequency signal oscillations at 41 GHz correspond to Brillouin scattering from longitudinal acoustic waves in the BK7 glass substrate while the low-frequency oscillations at 18 GHz correspond to Brillouin scattering from the acoustic waves in liquid glycerol. Near the center of the sample ( $X \approx 0$ ) the lens and the substrate are almost in direct contact and signal oscillations due to acoustic propagation in the substrate begin promptly. Away from the center the signal oscillations due to acoustic wave propagation in the substrate are further delayed and phase shifted, and these oscillations are preceded by lower-frequency oscillations due to acoustic wave propagation in the liquid. (b) Normalized amplitude values and (c) phase shifts of the 41 GHz high-frequency signal oscillations extracted from Brillouin scattering in the substrate. (inset) At the highest set of longitudinal (90 GHz) and shear (50 GHz) frequencies, the measurements yielded consistent values for liquid layer thickness changes across the sample, with nanometer sensitivity.



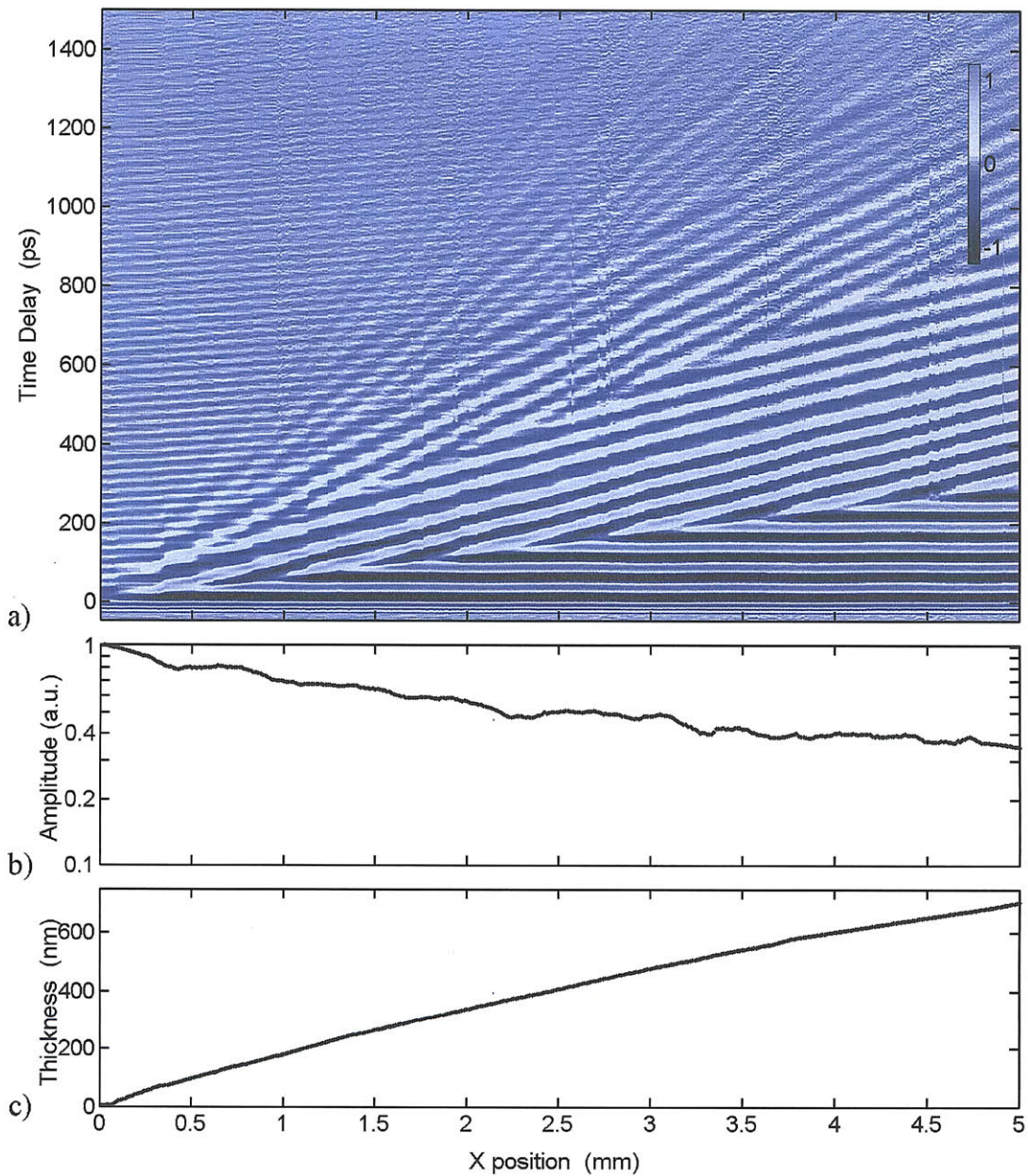


Figure 6-12: (a) Interpolated 2D plot of about 200 longitudinal wave data sets recorded in DC704 at 200 K as a function of probe delay time (plotted vertically) at different lateral ( $X$ ) positions across the sample (displayed horizontally). The liquid thickness increases almost linearly in a sample consisting of a polished and a flat substrate. The high-frequency signal oscillations at 41 GHz, clearly visible at small  $X$  positions and somewhat masked low-frequency oscillations at 21 GHz from Brillouin scattering in glassy DC704 correspond to Brillouin scattering from longitudinal acoustic waves in the BK7 glass detection substrate. Their phase changes with increasing  $X$  position. (c) Fourier analysis of this oscillation allows us to reconstruct the DC704 liquid thickness. The slope of the acoustic amplitude (b) with respect to the liquid thickness gives the acoustic attenuation.

glass detection substrate at the interface. However, the reflection and the subsequent round trip signal in the DC704 cavity remain the dominant feature in the plot. Upon the second arrival of the acoustic pulse at the liquid-detection substrate interface at 700 ps, yet another portion of it is transmitted into the detection substrate, while the remaining portion makes another round trip in the DC704, and so on. The change in the phase of the 41 GHz Brillouin oscillations in the detection substrate is clearly visible, in particular at larger time delays and small X positions. These phase shifts result from the different transit times of the acoustic pulse through different liquid thicknesses before it enters the glass substrate. The acoustic attenuation length is obtained from the differences in the acoustic amplitudes as a result of the propagation through different sample thicknesses.

From the detection theory in an acoustic/optical cavity described above we know that the detected probe light,  $I_{Sig}$  undergoes time-dependent intensity modulation at the Brillouin frequency  $\nu_{sub}$  of the substrate material,

$$I_{Sig} = I_{ac} \cos(2\pi\nu_{sub}t + \delta\phi) , \text{ where} \quad (6.38)$$

$$I_{ac} \propto \exp(-\alpha d) \text{ and} \quad (6.39)$$

$$\delta\phi \propto 2\pi(\nu_{sub} - \nu_{liq}) d/c_{liq} . \quad (6.40)$$

The Brillouin phase shift  $\delta\phi = \phi_2 - \phi_1$  is determined by the time of flight of the acoustic wave through the liquid of thickness  $d$  at the acoustic speed  $c_{liq}$ , and the Brillouin frequency  $\nu_{liq}$  of the liquid. The initial Brillouin scattering amplitude  $I_{ac}$  is given by the sample thickness and the attenuation coefficient  $\alpha$ .

Figure 6-13 a) shows the time derivative of the measured reflectivity change for two distinct positions  $X_1$  and  $X_2$  in a glycerol sample with a sapphire detection substrate. These positions correspond to two distinct liquid layer thicknesses  $d_1$  and  $d_2 > d_1$ . The excitation pulse sequence was adjusted to match the Brillouin scattering frequency in order to enhance the acoustic spectral brightness at this frequency. This excitation feature is visible in the signal until about 150 ps. Data were normalized by the electronic peak intensities of this excitation sequence before the derivatives were taken. In the following time interval between  $\sim 200$  to 900 ps, oscillations due to coherent shear waves in the sapphire detection substrate and their Fourier amplitude and phase are shown in Figure 6-13 b) and Figure 6-13 c). From these data, we determine the shear acoustic parameters of the liquid at the shear acoustic frequency of the detection substrate  $\nu_{sub}^s$ . The ratio of the Fourier amplitudes,  $A_1(\nu_{sub}^s)$  and  $A_2(\nu_{sub}^s)$ , allows us to extract the attenuation for the liquid thickness difference  $\Delta d = d_2 - d_1$



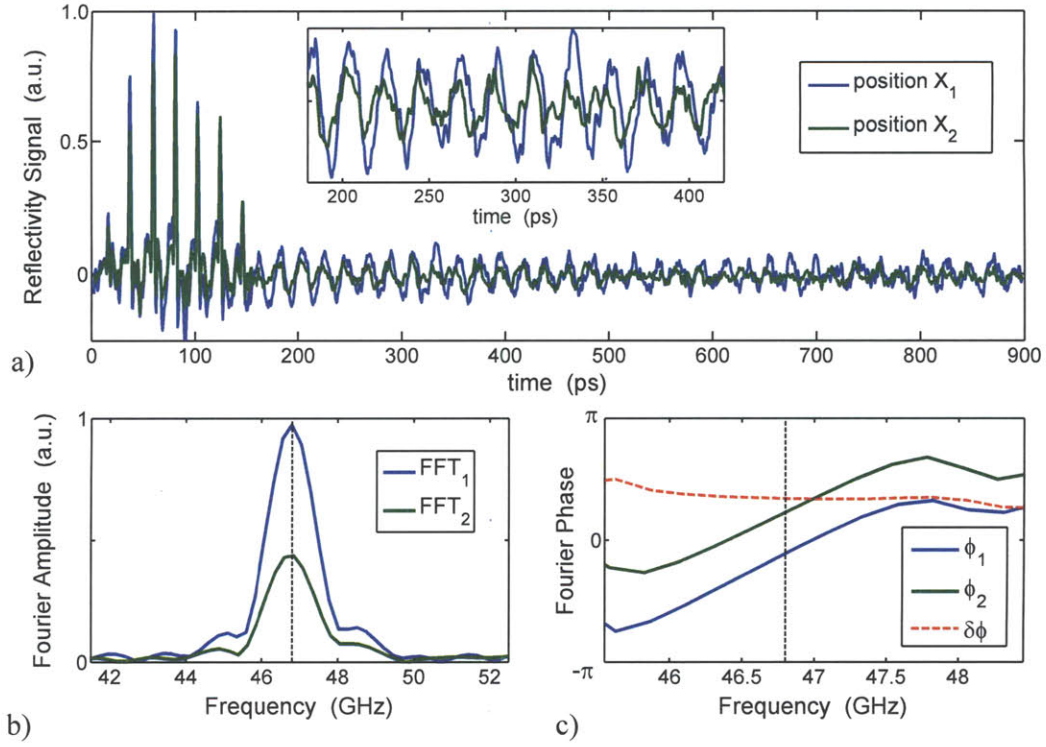


Figure 6-13: Shear waves results from a sample configuration with MBE iron acoustic transducer on a glass substrate, glycerol at room temperature, and sapphire detection substrate. (a) Time derivative of the measured polarization-flipped signal intensity for two distinct positions  $X_1$  and  $X_2$  of the sample corresponding to two distinct liquid layer thicknesses  $d_1$  and  $d_2 > d_1$ . The excitation pulse sequence is visible between 0 and 150 ps due to the electronic response that is induced in the iron film, which is detected by the probe light. This signal is followed by oscillations due to coherent shear waves in the sapphire detection substrate. (b) Acoustic amplitude spectra of both acoustic signals,  $FFT_1$  and  $FFT_2$  and (c) the corresponding phases,  $\phi_1$  and  $\phi_2$ . The phase and amplitude differences yield the acoustic speed and attenuation length respectively in the liquid at the specified Brillouin frequency. Note that only the phase in (c) at frequencies around the Brillouin peak in (b) at 46.8 GHz contains useful information.

by

$$\alpha_s = \frac{1}{\Delta d} \ln \left( \frac{A_1(\nu_{sub}^s)}{A_2(\nu_{sub}^s)} \right), \quad (6.41)$$

and the speed of sound follows from the phase difference  $\delta\phi(\nu_{sub}^s)$  by

$$c_s = \frac{2\pi(\nu_{sub}^s - \nu_{liq}^s) \Delta d}{\delta\phi(\nu_{sub}^s)}. \quad (6.42)$$

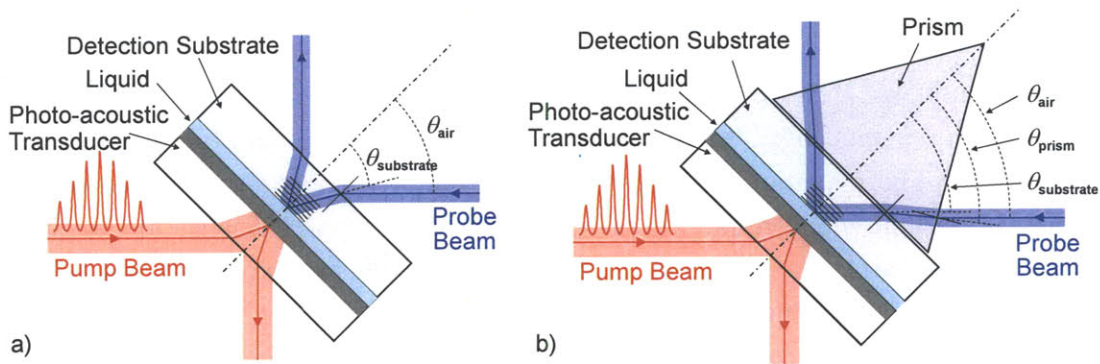


Figure 6-14: Illustration of our approach to access a range of longitudinal and shear acoustic frequencies. (a) Standard configuration for Brillouin scattering in detection substrate as introduced in Figure 4-1 by configuration (II). An oblique probe incidence angle is a requirement for optical sensitivity to shear waves as described above. Adjustment of the probe incidence angle in air  $\theta_{\text{air}}$  changes the angle in the substrate  $\theta_{\text{substrate}} < \theta_{\text{air}}$  (due to refraction) and thereby allows us to tune the Brillouin scattering frequency. However, the maximum angle in the substrate is limited by refraction and sample holder design to typically less than  $30^\circ$ , and therefore tuning of the Brillouin frequencies by 10-15% at maximum. Different detection substrates with different acoustic speeds, both longitudinal and shear, and different refractive indices further permit tuning of Brillouin frequencies. However, a new sample has to be built in order to change Brillouin frequencies in this way. The use of a prism (b) renders significantly larger probe angles in the detection substrate  $\theta_{\text{substrate}}$  possible, up to  $60^\circ$  which corresponds to a Brillouin frequency range of about 50%. In this case, the X-position on the sample must be adjusted by moving the sample perpendicular (up and down) with respect to the plane defined by the incident and emerging probe light on the sample.

where  $\nu_{\text{liq}}^s$  and  $\nu_{\text{sub}}^s$  are the Brillouin frequencies of the liquid and the substrate material, respectively. Note that it may be necessary to add multiples of  $2\pi$  to the phase difference in order to account for large differences in liquid thickness. Data sets are recorded at a number of liquid thicknesses in order to determine if the addition of  $2\pi$  phase is necessary and to decrease the uncertainty of the extracted attenuation rate and speed of sound. The entire set of phase shifts resulting from various liquid thicknesses, as shown in Figure 6-11 c), is used to determine the sound speed. Similarly, the entire set of amplitudes at multiple liquid thicknesses, as shown in Figure 6-11 b), is used to determine the attenuation rate. This procedure provides a high level of precision for the values determined. For glycerol and DC704, typical uncertainties were 30 to 50  $\text{m s}^{-1}$  for the sound speeds and 10 to 50% for the attenuation rates.

Several parameters can be adjusted to experimentally access different frequencies (see equation 3.27). For example, different frequencies can be probed by (1) changing

the scattering angle or (2) by choosing a substrate having a different refractive index  $n_{sub}$  or longitudinal or shear speeds of sound,  $c_{sub}^l$  or  $c_{sub}^s$ . Due to the high speed of sound in sapphire, either BK7 glass or sapphire was chosen as a detection substrate in our measurements to provide access to lower or higher Brillouin frequency ranges respectively. The maximum range of accessible scattering angles in each substrate,  $\theta_{substrate}$ , was limited by refraction of the probe beam toward smaller angles when entering the substrate, as depicted in Figure 6-14 a). Our approach utilized a glass prism to increase the range of accessible Brillouin scattering angles. The prism was attached to the air surface of the detection substrate, as depicted in Figure 6-14 b), in order to facilitate variable Brillouin scattering angles in the range of approximately  $\theta_{substrate} \approx 30^\circ$ - $50^\circ$  in the substrate. On the other hand, the substrate can be used without a prism in order to reach scattering angles up to the backscattering limit.

## 6.3 Results and Discussion

### 6.3.1 Glycerol

Results from shear and longitudinal wave measurements are shown in Figure 6-15 for four different sample configurations: glass substrate and sapphire substrate, each with and without a silica glass prism attached. Measurements conducted at multiple scattering angles yielded longitudinal acoustic frequencies in the 31-43 and 57-91 GHz ranges with glass and sapphire substrates respectively and corresponding shear acoustic frequencies in the 19-26 and 31-50 GHz ranges.

The shear speed of sound in glycerol at room temperature increases approximately linearly with frequency, while the longitudinal speed of sound appears to remain almost constant over the frequency range of the measurements. This suggests that the longitudinal sound speed has reached its infinite-frequency value relative to the slow, strongly frequency-dependent alpha-relaxation dynamics [SD00] that describe viscoelastic behavior of glycerol at this temperature. It also suggests that the present frequency range lies below the weakly temperature-dependent, high-frequency beta-relaxation feature in glycerol. This is consistent with dielectric measurement results [LL02] that extend to terahertz frequency ranges. The present frequency range is roughly between the one expected for the slower alpha-relaxation dynamics at room temperature and the faster beta-relaxation dynamics. For the somewhat lower frequency range of the shear acoustic measurements, the results suggest that the infinite-frequency speed has not yet been reached. This may indicate that the shear acoustic frequency range overlaps with the high-frequency edge of the alpha relaxation spectrum at room temperature. It also may indicate the high-frequency edge of an ad-

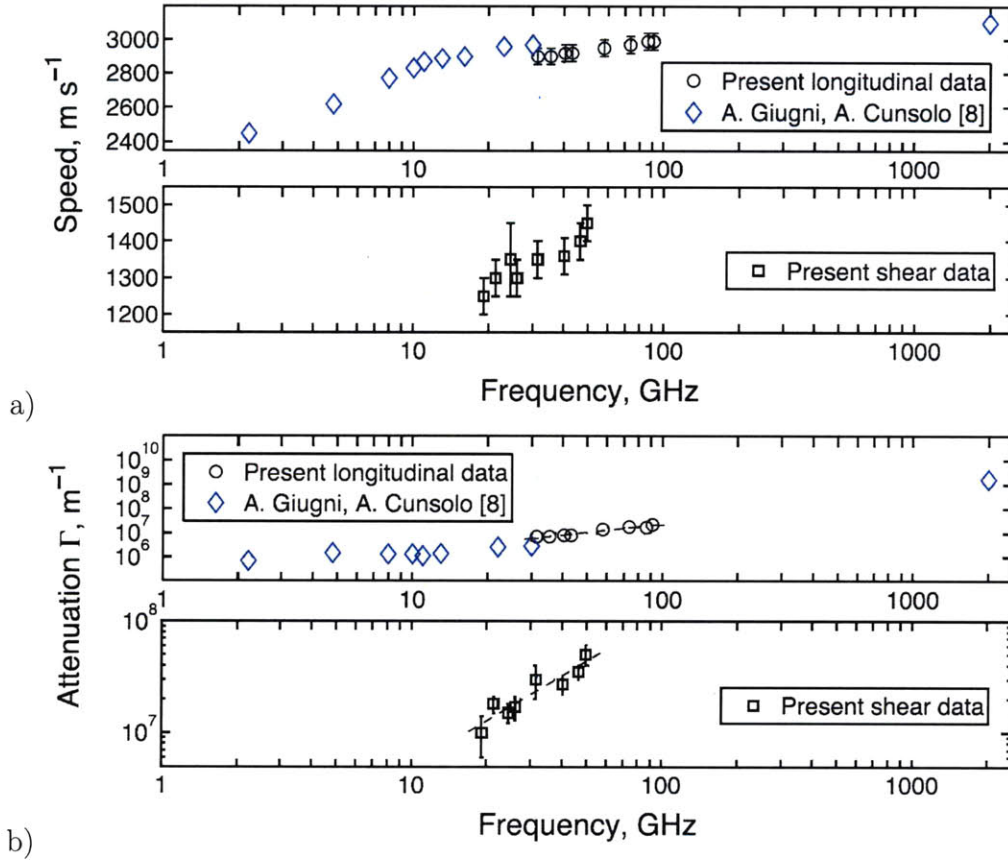


Figure 6-15: Longitudinal and shear acoustic speeds (a) and attenuation coefficients (b) in liquid glycerol at room temperature, from measurements with multiple Brillouin scattering angles using glass and sapphire substrates with and without a glass prism. Published in [PKAN09].

ditional “constant relaxation” feature that has been suggested in glycerol in the low gigahertz range [SN04, WHL<sup>+</sup>94, SCFP04, GC06, BR05].

The shear and longitudinal attenuation coefficients increase with frequency, but with a dependence that appears closer to linear than quadratic [HL59, MTZM96]. Lines of slope 1.2 in Figure 6-15 are guides for the eye. Phenomenologically, this indicates that the shear viscosity  $\eta_s$  that is linked to the shear attenuation coefficient  $\Gamma_s$  through the relation [HL59],

$$\eta_s = 3\alpha_s\rho\frac{c_s^3}{2(2\pi\nu)^2}, \quad (6.43)$$

where  $\rho$  is the density, is a decreasing function of frequency in the ranges explored here. This expression of the viscosity is valid when the acoustic wave vector  $q_s = 2\pi\nu/c_s$  exceeds the attenuation coefficient  $\alpha_s$ , i.e. when the acoustic wave is underdamped. In



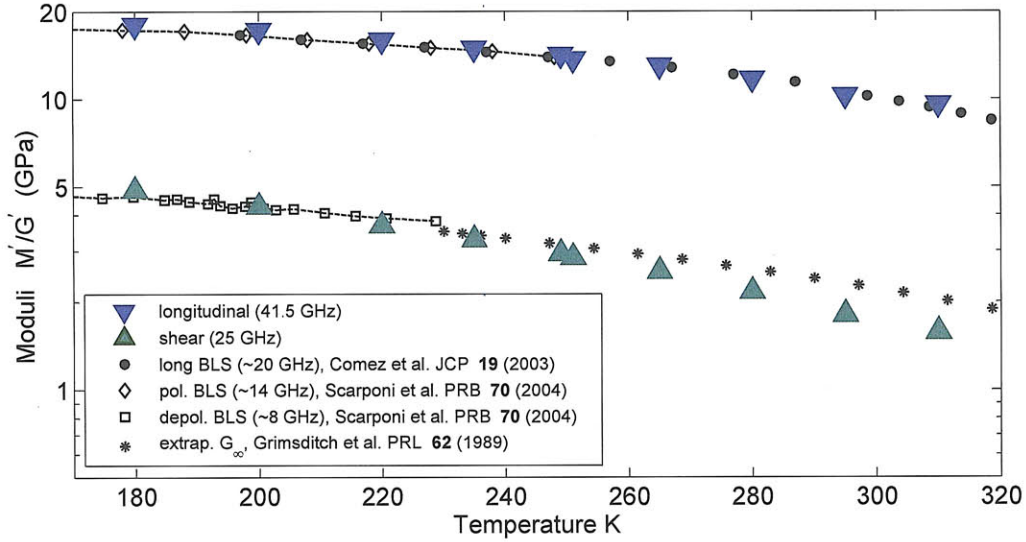


Figure 6-16: Real parts of the temperature dependent longitudinal  $M'$  and shear  $G'$  acoustic moduli of glycerol up to 310 K: triangles show the results from the present data at 41.5 GHz for longitudinal and 25 GHz for shear waves. Note that the temperature limit was only given by the sample-in-vapor cryostat used for these measurements. Reference data measured by polarized frequency-domain Brillouin scattering measurements at close frequencies are from references [CFSM03] and [SCFP04]. For shear data see reference [SCFP04] and [GB89].

the present case,  $q/\alpha_s \approx 6.5$  on average over the frequency range explored. The mean calculated value for the viscosity is  $2.9 \times 10^{-3}$  Pa s, comparable to the static viscosity of water and three orders of magnitude smaller than the static value of glycerol at room temperature [Lid98]. This further illustrates that at this temperature the present shear frequency range lies in the high-frequency wing of the alpha-feature of the shear relaxation spectrum of glycerol.

The liquid response can also be expressed in terms of the complex modulus,  $\hat{C}(\omega) = \rho \hat{c}^2(\omega)$  (for a given sample density  $\rho$ , see table A.3) which is the longitudinal modulus  $\hat{M}(\omega)$  for longitudinal waves and the shear modulus  $\hat{G}(\omega)$  for transverse waves. The complex velocity is defined by  $\hat{v}(\omega) = \omega/\hat{q}(\omega)$  through the complex wave vector  $\hat{q}(\omega) = q' + iq'' = \omega/c(\omega) + i\alpha(\omega)$ , where  $c(\omega)$  is the frequency dependent longitudinal or shear speed of sound and  $\alpha(\omega)$  is the corresponding frequency dependent acoustic attenuation rate. Results for the real parts of the acoustic moduli from temperature dependent shear and longitudinal wave measurements in glycerol conducted with a BK7 glass detection substrate are shown in Figure 6-16. Reference data from polarized frequency-domain Brillouin scattering measurements at similar frequencies ( $\sim 20$  GHz from [CFSM03] and  $\sim 14$  GHz from [SCFP04]) show good agreement

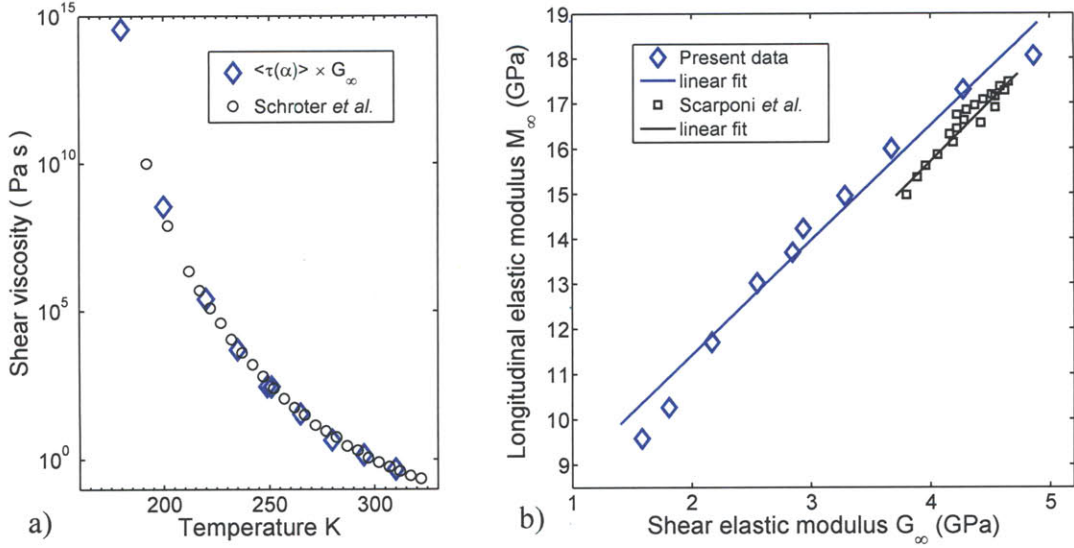


Figure 6-17: (a) Temperature dependence of the shear viscosity calculated using the relationship  $\eta_S = G_\infty \langle\tau(\alpha)\rangle$ , where the values of  $G_\infty$  are from the present work and  $\langle\tau(\alpha)\rangle$  data are from reference [LSBL00]. Circles represent measured shear viscosity from reference [SD00]. (b) Linear fit of the longitudinal elastic modulus vs. the shear elastic modulus of glycerol. Open squares are from reference [SCFP04].

with the measured longitudinal modulus, suggesting very little dispersion over this frequency and temperature range. The very small Brillouin cross section of these modes makes frequency-domain Brillouin scattering measurements from transverse acoustic modes in glycerol challenging. Therefore, measurements are limited to low temperatures where acoustic attenuation is low. The only depolarized Brillouin scattering data to our knowledge reported in literature are from Scarponi and coworkers [SCFP04] for which measurement temperatures are limited to below  $\sim 230$  K.

Extrapolation of the unrelaxed shear modulus in Figure 6-16 yields

$$G_\infty = (9.1 \pm 0.5) \times 10^9 [\text{Pa}] - (2.32 \pm 0.22) \times 10^7 [\text{Pa/K}] \times T[\text{K}]. \quad (6.44)$$

The Maxwell relationship  $\eta_S = G_\infty \langle\tau(\alpha)\rangle$  can be used to estimate the shear viscosity  $\eta_S$  from the obtained values for  $G_\infty$  and then be compared with experimental values of static shear viscosity. Figure 6-17 a) shows  $\eta_S$  values obtained through the Maxwell equation, using  $\langle\tau(\alpha)\rangle$  data measured by dielectric spectroscopy from reference [LSBL00] with static shear viscosity data taken from reference [SD00]. Data from the two different sources are in excellent agreement. We note that significant deviations from experimental values of  $\eta_S$  are usually found in systems showing secondary relaxation or strong rotational-translational coupling [DAP<sup>+</sup>98, ADM<sup>+</sup>00].



Translation-rotation coupling has not been investigated previously in glycerol, and its study through conventional means would be difficult due to its small Brillouin cross-section and polarizability anisotropy. Our results indicate that the coupling is weak in this system.

Scarponi *et al.* [SCFP04] have analyzed unrelaxed longitudinal and shear modulus data of glycerol at temperatures around the glass transition temperature in terms of Cauchy-like relations. When atoms in a material interact through a central potential, the Cauchy identity holds which, in an isotropic system, states that  $M = 3G$  [BH66]. Typically, molecular liquids don't show a central potential and therefore, Cauchy relations do not apply. Krüger *et al.* [KBB<sup>+</sup>02] found that a modified, Cauchy-like relation,

$$M_{\infty} = A + BG_{\infty} , \quad (6.45)$$

holds across a wide temperature range down to the glass transition temperatures of different liquids.  $A$  is a system dependent constant which, at ambient pressure, does not strongly depend on temperature and typical values of  $B$  are close to 3. Notably, similar values for  $A$  and  $B$  have been found in both polymerization and freezing experiments, suggesting a general behavior for the solid-like amorphous state. The validity of the modified Cauchy relation in glycerol can be tested by comparison of the temperature evolution of the unrelaxed elastic moduli,  $M_{\infty}$  and  $G_{\infty}$  from Figure 6-16 through equation 6.45. A linear fit to the data of Figure 6-16 is possible within the experimental uncertainties, giving  $A = (5.78 \pm 0.58)$  GPa and  $B = (2.73 \pm 0.12)$  as best-fit parameters. The value of  $B$  close to 3 agrees with previous evaluations on organic and inorganic glass formers [BH66].

Figure 6-18 show our results for the temperature-dependent shear speed of sound and attenuation. In Figure 6-19, the same results are presented as the real and imaginary parts of the shear modulus at 25 GHz. Data from the literature at various acoustic frequencies are also shown. Data at 30  $\mu\text{m}$  ( $\sim 25\text{-}55$  MHz) were determined through interface wave laser ultrasonics by Glorieux *et al.* [GdRG<sup>+</sup>06]. The extraction of these data was difficult and resulted in large uncertainties. Other megahertz data, between 15 MHz and 85 MHz, were investigated by Piccirelli and Litovitz [PL57] using ultrasonic pulse techniques. They reported an approximate water content in their glycerol sample of about 0.5%. Because of the extremely high attenuation, acoustic velocities and attenuation rates could not be measured directly. Instead the real and imaginary parts of the shear impedance,  $\rho c'_s$  and  $\rho c''_s$ , were measured. Results were reported in terms of  $\rho c_s'^2$  and  $G'$  in reference [PL57], from which we calculate

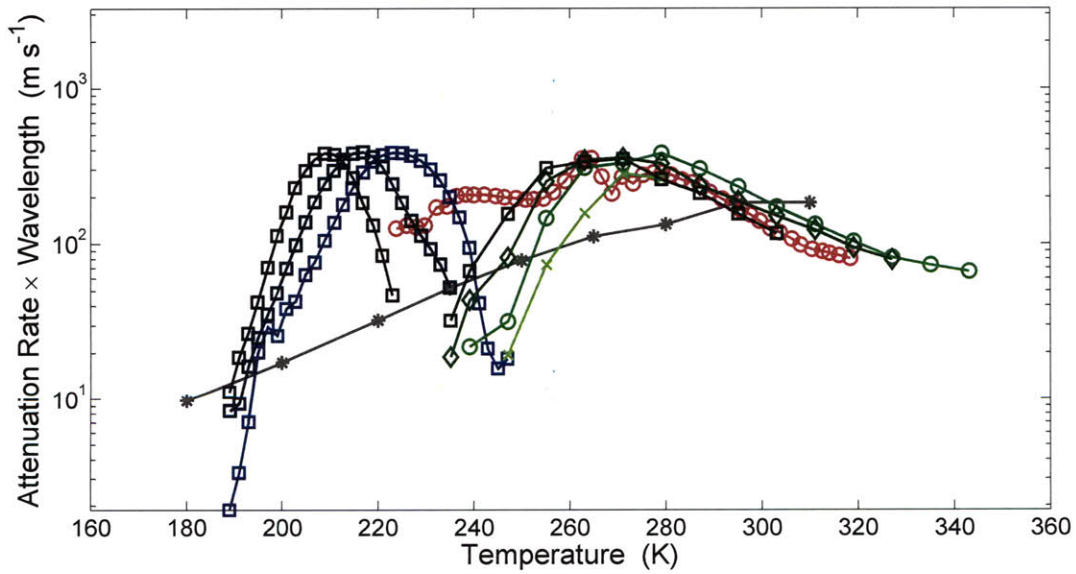
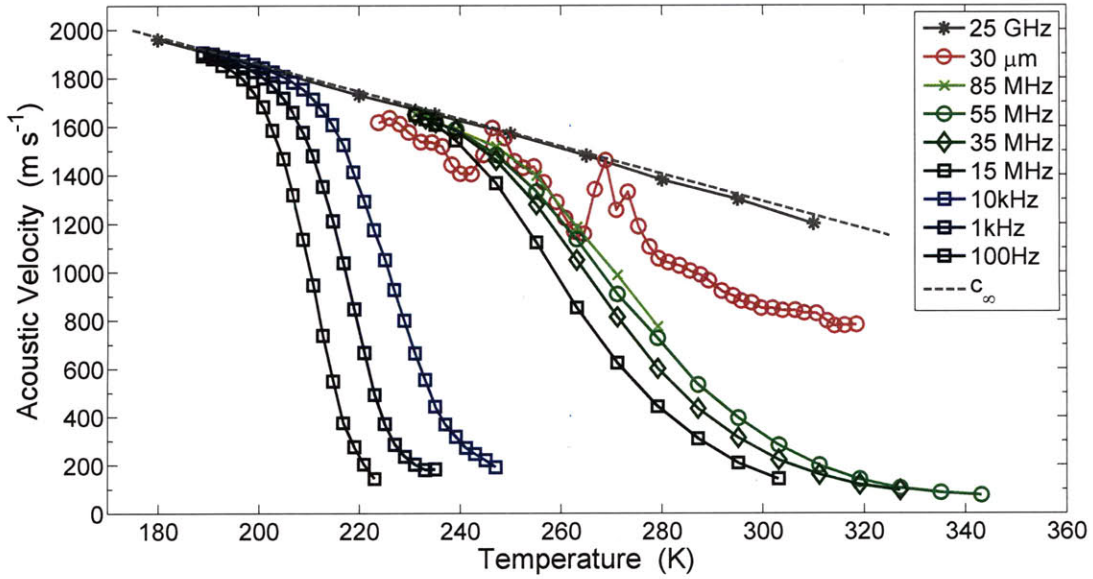


Figure 6-18: Temperature-dependent shear speed and attenuation of glycerol. Data at 25 GHz are from the present measurement, 30  $\mu\text{m}$  from Glorieux *et al.* [GdRG<sup>+</sup>06], 15 MHz to 85 MHz from Piccirelli and Litovitz [PL57], and 100 Hz, 1 kHz and 10 kHz from Jeong [Jeo87].

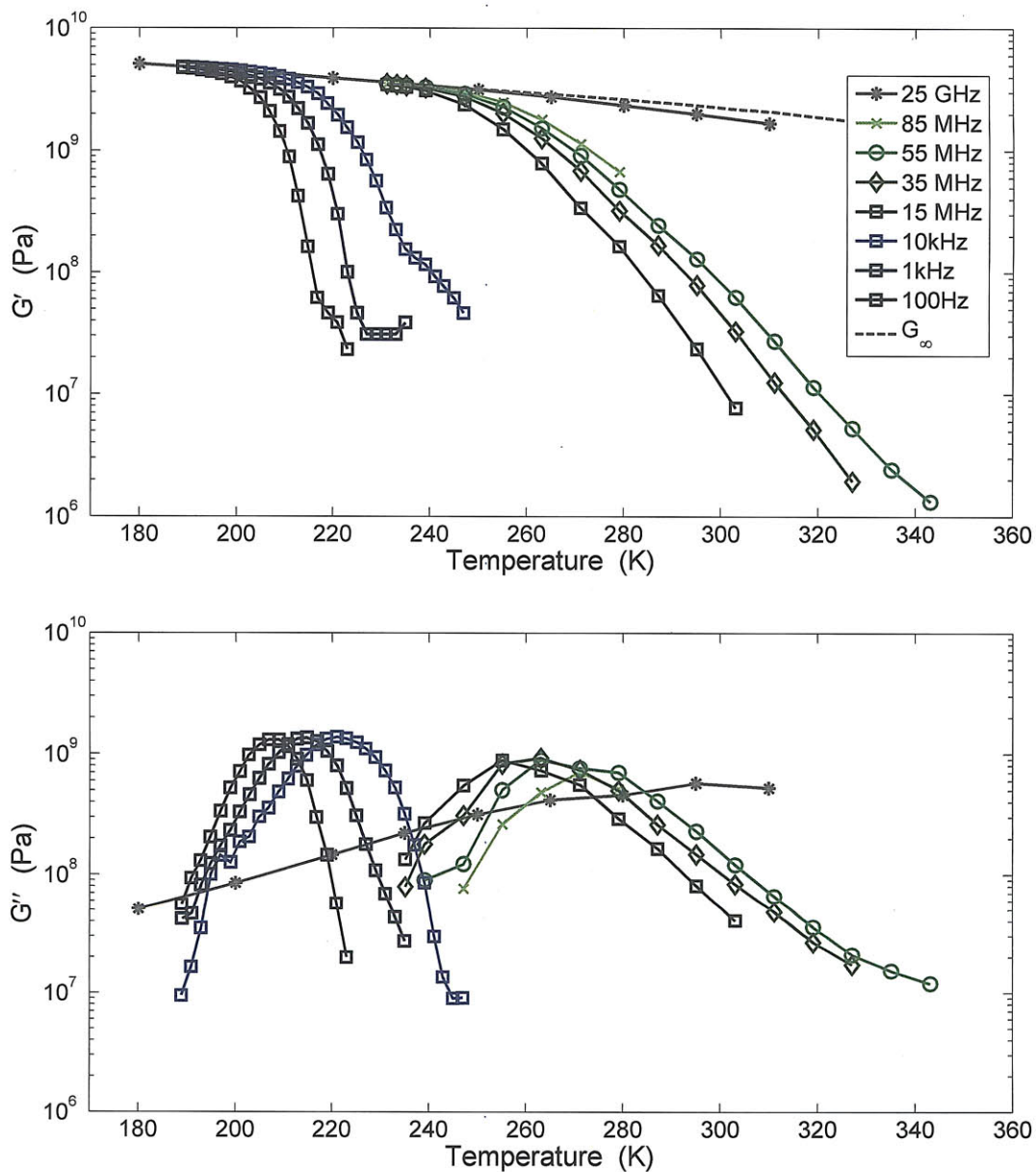


Figure 6-19: Temperature-dependent real  $G'$  and imaginary  $G''$  parts of the complex shear modulus  $\hat{G}(\omega) = G' + iG''$  of glycerol. Data sources are the same as in Figure 6-18 but in modulus representation.

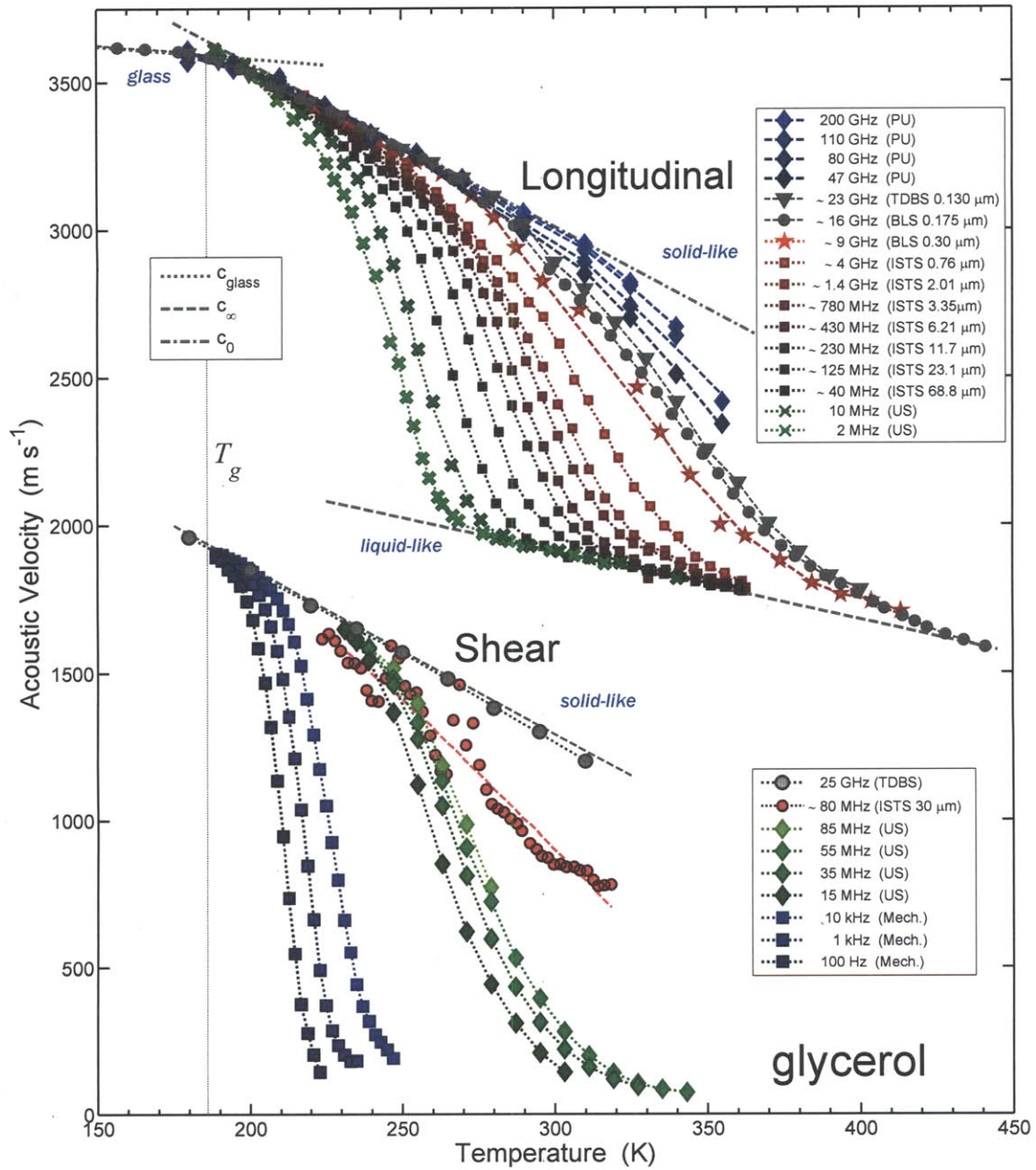


Figure 6-20: Temperature dependent longitudinal and shear speeds of sound in glycerol. Data sources are given in Figure 5-5 for longitudinal data and in Figure 6-18 for shear data.

the imaginary part of the shear modulus using

$$G'' = G' \sqrt{\left(\frac{2\rho c_s^2}{G' - 1}\right)^2 - 1} \quad (6.46)$$

from the given quantities. After obtaining the complex shear modulus, the speed of sound and attenuation rate are calculated. Low frequency shear measurements on glycerol at 100 Hz, 1 kHz and 10 kHz were made by Jeong [Jeo87]. They were obtained using a two-transducer technique in which a first quartz transducer was used to generate a sinusoidal shear strain and a second transducer was used as a detector for shear stress that has been transmitted through a certain liquid thickness. The reported data are in terms of the real and imaginary parts of the modulus and have been “normalized by the value of the real part of the shear modulus at the glass transition temperature of glycerol ( $T_g \approx 186$  K), where  $G'$  does not show any frequency dependence.” Below  $T_g$ , the structural relaxation occurs at frequencies lower than 1 Hz, and we expect no relaxation peak to be present in the entire spectrum measured by any of these techniques. Therefore, both the real and the imaginary parts of the modulus can be adjusted by multiplication with a constant factor of  $4.8 \times 10^9$  Pa to match the real part of the shear modulus, as determined at low temperature by Scarponi *et al.* [SCFP04] and our measurements.

The temperature dependent velocities of both longitudinal and shear acoustic modes are shown in Figure 6-20. For longitudinal waves, both an upper and lower boundary exists for the speed of sound. In the hydrodynamic regime, the adiabatic propagation of longitudinal acoustic waves in liquids is described by two limiting elastic moduli, the relaxed elastic modulus  $M_0$  and the unrelaxed modulus  $M_\infty$ . The first gives the adiabatic sound velocity in an equilibrated sample at low frequency  $c_0^l = (M_0/\rho)^{1/2}$ . The second gives the glass like velocity of sound in the high frequency limit when the period of the wave is smaller than the time required by the structure to equilibrate under an external perturbation (structural relaxation time  $\tau_\alpha$ ). Values for  $c_\infty^l$ ,  $c_0^l$ ,  $M_\infty$  and  $M_0$  are given in Section 5.3.2. In contrast, there is only an upper boundary in case of shear waves,  $c_\infty^s$ , since the propagation of shear acoustic waves is described by a single limiting elastic constant, the unrelaxed shear modulus  $G_\infty$  (see equation 6.44). Our acoustic velocity data, shown in Figure 6-18 or 6-20, allow the extrapolation of the unrelaxed shear sound velocity which yields

$$c_\infty^s = (2990 \pm 30) [\text{m/s}] - (5.67 \pm 0.13) [\text{m/s}] \times T[\text{K}]. \quad (6.47)$$

In the high temperature low viscosity regime shear waves do not propagate, i.e.  $G_0 = 0$ , and the classical assumption that shear waves do not exist in liquids becomes

valid. Transverse acoustic waves can eventually propagate in a liquid, provided that their frequency is comparable to, or higher than, the reciprocal of the structural relaxation time. The relaxation time — or the distribution of relaxation times — and the relaxed and unrelaxed moduli are parameters which govern the dispersion and absorption of acoustic waves in a liquid, and their experimental determination has always received a great deal of attention.

### 6.3.2 DC704

Measurements of shear acoustic properties were also carried out on DC704 at various temperatures. Results for temperatures between 210 K and 260 K are shown in Figure 6-21. In this measurement, acoustic waves were generated by a MBE iron transducer film grown on a sapphire substrate and detected in a 2.5 m BK7 glass lens. The extracted longitudinal parameters, in particular the speed of sound, match very well with the parameters determined by Brillouin scattering in the liquid itself, as shown in Figure 5-6 (a). However, the shear data quality was poor and the related error to the extracted shear attenuation exceeds 50%.

Even though the temperature range for data of DC704 is much smaller than that for glycerol, a similar analysis in terms of modified Cauchy-like relations, as stated by equation 6.45, can be carried out. In Figure 6-22 we have plotted the unrelaxed shear elastic modulus  $G_\infty$  against the unrelaxed longitudinal elastic modulus  $M_\infty$ . A linear fit to the data is possible within the experimental uncertainties, giving  $A = (2.91 \pm 0.76)$  GPa and  $B = (2.35 \pm 0.56)$  as best-fit parameters. The value of  $B$  shows a significant deviation from the expected value of 3 which we attribute to the poor quality of the data.

### 6.3.3 Water

Due to the large acoustic impedance mismatch between water and the transducer and detection substrate and to its low viscosity, the measurements on water are slightly different than for glycerol and DC704. The weakest detectable shear wave corresponds in this case to a liquid layer in the range of ten nanometers. Therefore, it was not realistic to reconstruct the topography of the liquid from the lens curvature. We overcame this problem by using the literature values for the longitudinal speed of sound in water,  $c_l = 1500 \text{ m s}^{-1}$ , from reference [SYFM05]. The liquid topography was then deduced from the analysis of the longitudinal Brillouin phase shift. Analysis of the amplitudes of the longitudinal Brillouin scattering signal enables determination of the longitudinal damping coefficient,  $\alpha_l = 35 \times 10^6 \text{ m}^{-1}$ , which is slightly higher than for glycerol. From the shear depolarized Brillouin scattering measurements,



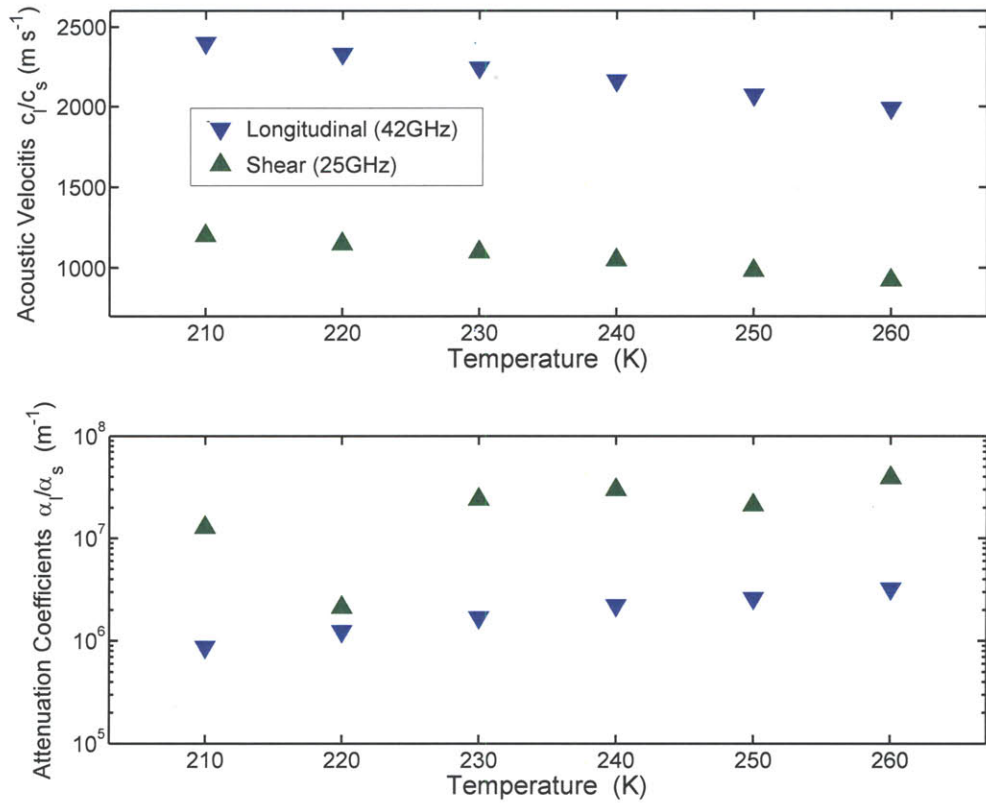


Figure 6-21: Temperature dependent longitudinal and shear speeds of sound and attenuation of DC704. The Brillouin scattering frequencies for longitudinal waves (41 GHz) and for shear waves (25 GHz) were defined by the BK7 glass detection substrate and the probe light scattering angle in the substrate of  $\sim 30^\circ$ .

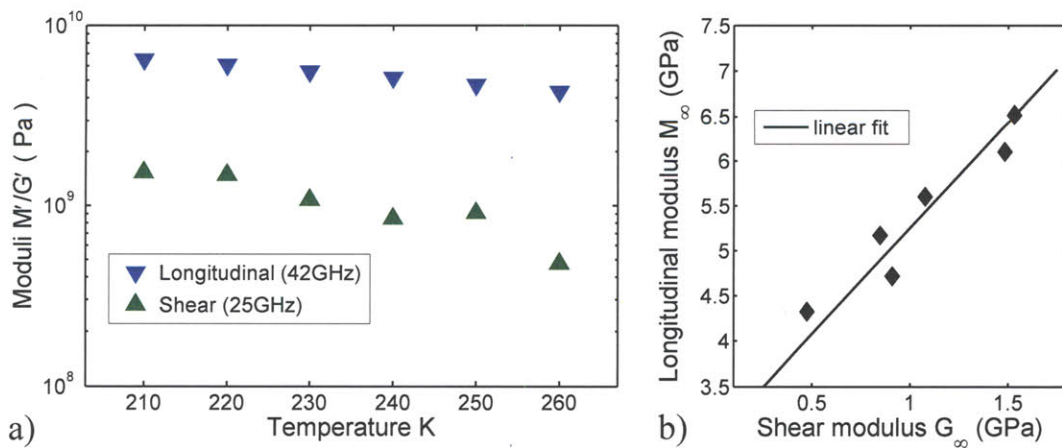


Figure 6-22: (a) Real parts of the temperature dependent longitudinal and shear moduli of DC704. (b) Linear fit of the longitudinal modulus vs. the shear modulus of DC704.

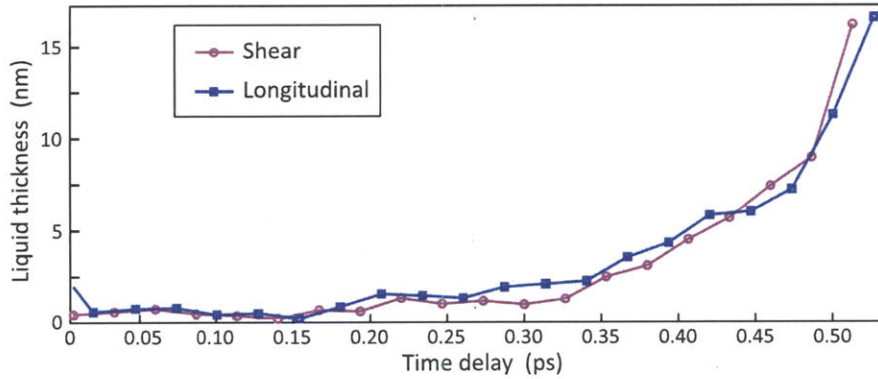


Figure 6-23: Topography of a water layer at room temperature calculated from Brillouin scattering measurements in a glass detection substrate at 42 GHz (longitudinal) and 25 GHz (shear) yields longitudinal and shear acoustic attenuation coefficients of  $\alpha_l = 35 \times 10^6 \text{ m}^{-1}$  and  $\alpha_s = 120 \times 10^6 \text{ m}^{-1}$ , respectively.

conducted at the same lateral X-positions on the sample, we were able to detect shear Brillouin frequency components at 25 GHz. By fitting the shear topography/phase shift to the longitudinal topography/phase shift (see Figure 6-23), we were able to extract a value of the shear speed of sound in water of  $c_s = 660 \text{ m s}^{-1}$ . From the analysis of the shear Brillouin amplitudes, we obtained a value for the shear attenuation,  $\alpha_s = 120 \times 10^6 \text{ m}^{-1}$ , which is about one order of magnitude higher than for glycerol at the same frequency. The shear viscosity of water in this frequency range is determined to be  $\eta_s \approx 1.4 \times 10^{-3} \text{ Pa s}$ , a value in close agreement with the static value of  $1 \times 10^{-3} \text{ Pa s}$ . This suggests that no shear relaxation is present in this frequency range. The ratio of the shear wavevector to the attenuation coefficient is  $2\pi\nu_s/c_s\alpha_s \approx 2 > 1$ , indicating that the shear wave at this frequency is purely viscoelastic rather than diffusive.

In addition to having very high attenuation rates, water also corrodes the MBE iron transducer films, posing an additional challenge to the experiment. We tried to circumvent or at least reduce the problem of corrosion by depositing thin protective layers of a few nanometer of MnO or gold on top of the iron. Otherwise, corrosion may cause the transducer film to dissolve within hours of building the sample. While this extends the lifetime of the transducer by about a factor of two, the time window is still not sufficient to conduct comprehensive studies on water. Experiments with off-axis SRO transducer films and glycerol yielded similar results as the iron transducer films and their extension to measurements with water should be straightforward. SRO is a sturdy mineral and initial measurements with water showed no signs of film degradation. However, in those measurements it was not yet possible to transmit shear acoustic waves through water.

## 6.4 Conclusions and Outlook

The work presented in this chapter demonstrates for the first time that picosecond ultrasonics can be applied not only to the measurement of longitudinal properties but also to the measurement of shear properties of liquids. Our technique of time-domain Brillouin scattering offers substantial advantages compared with conventional ultrasonic techniques or ISS for the study of acoustic waves in liquids, since frequencies (20–100 GHz) much higher than the ultrasonic ones ( $\lesssim 100$  MHz) or ISS ones ( $\lesssim 1$  GHz) and unrelaxed values of both  $M$  and  $G$  can be measured at temperatures significantly higher than  $T_g$ .

The approach developed here makes significantly higher shear acoustic frequencies than frequency-domain Brillouin scattering measurements (typically below 10 GHz) accessible, since the measured frequency is determined not by the refractive index and the shear speed of sound of the liquid (both of which are typically very low) but by the refractive index and the shear speed of sound of the detection substrate — which, through the right choice of the substrate, can exceed 100 GHz. The measured shear properties can be as high as 160 GHz, and 250 GHz for longitudinal waves in the case of a silicon detection substrate at a probe wave length of 400 nm [DFA<sup>+</sup>08]. The frequency ranges that are accessible to the current method could also be increased substantially by using 267 or 200 nm probe light, i.e. third or fourth harmonic of the  $\sim 800$  nm laser wavelength.

Another limitation of frequency-domain Brillouin scattering, which relates to the Brillouin scattering cross section from transverse acoustic modes, poses no restrictions on our approach. The scattering efficiency of Brillouin scattering is determined by the photoelastic constants,  $p_{44}$  in the case of shear waves in an isotropic medium (see equation 6.15), which has a value that is very small for symmetric molecules like glycerol. This severely restricts the applicability of frequency-domain Brillouin scattering. In contrast only the photoelastic parameter of the detection substrate is relevant in our technique. As a result, any liquid can be studied independent of its Brillouin scattering cross section.

Extensive measurements showed that the variation of liquid layer thickness across different lateral sample positions can be determined with a precision of approximately 0.5 nm (Figures 6-11 and 6-23), that optical cavity effects (evidenced by the Newton's fringes pattern in Figure 4-4) on the acoustic amplitude measurements were minimized by referencing the level of the acoustic signal to that of the electronic signal for each measurement, and that acoustic cavity effects were negligible (Figure 6-6). Thus the method provides reliable quantitative values for frequency-dependent longitudinal and shear sound speeds, attenuation rates, and complex moduli. Due to the high

acoustic frequencies investigated, the method grants access to the unrelaxed moduli (and sound speeds) up to temperatures far above  $T_g$ . A linear relation was found between the unrelaxed longitudinal and shear moduli of glycerol and DC704 with angular coefficients close to 3 as predicted by a generalized Cauchy relation. Finally, the approach used here may be applied to extremely thin liquid layers, down to a monolayer, to explore confinement and interfacial effects. [Gra91, KK95, HZS01]



# APPENDIX A

---

## Physical Properties of Various Materials

---

This appendix contains a collection of physical properties for a variety of materials that were used (or considered) for the experiments in this thesis.

### A.1 Optical Absorption and Skin Depth

The reflectance for smooth unoxidized metal films at normal incidence can be calculated from the real and imaginary parts of the refractive index [Pal98] using the Fresnel relation

$$R(\lambda) = \frac{[n(\lambda) - 1]^2 + k^2(\lambda)}{[n(\lambda) + 1]^2 + k^2(\lambda)}. \quad (\text{A.1})$$

And the optical penetration depth is obtained from the same parameters by

$$\theta(\lambda) = \frac{\lambda}{4\pi k}. \quad (\text{A.2})$$

Table A.1 lists the absorption coefficient  $A(\lambda) = 1 - R(\lambda)$  and the penetration depth for a selection of interesting materials at two wave lengths. The laser fundamental of about 800 nm and its first harmonic of about 400 nm.



	$n_{800}$	$k_{800}$	$A_{800}$	$\zeta_{800}$	$n_{400}$	$k_{400}$	$A_{400}$	$\zeta_{400}$
Metals								
Aluminum [Pal98]	2.80	8.45	13 %	7.5 nm	0.490	4.86	7 %	6.5 nm
Cobalt (Hex) [Pal98]	2.56	4.85	28 %	13 nm	1.85	3.35	40 %	9.6 nm
Copper [Pal98]	0.26	5.18	4 %	12 nm	1.32	2.12	54 %	15 nm
Gold [Pal98]	0.16	5.08	2.4 %	13 nm	1.47	1.95	41 %	16 nm
Silver [Pal98]	0.04	5.73	47 %	11 nm	0.05	2.07	4 %	15 nm
Iron [JC74]	3.02	3.87	39 %	17 nm	2.26	2.59	52 %	12 nm
Nickel [SMW03]	2.14	3.75	36 %	18 nm	1.50	2.07	57 %	16 nm
Chromium [JC74]	3.16	3.46	43 %	18 nm	2.014	2.85	47 %	11 nm
Tungsten [DPP+95]	2.96	2.23	57 %	29 nm	2.25	1.81	65 %	18 nm
Semiconductors/Semimetals								
Silicon [Pal98]	3.70	0.007	67 %	9100 nm	5.57	0.387	51 %	82 nm
a-Silicon [Pal98]	3.9	0.14	65 %	455 nm	4.30	2.10	53 %	15 nm
SrRuO <sub>3</sub> [Pal98]			%	nm			%	nm
GaAs [Pal98]	3.69	0.087	67 %	730 nm	4.37	2.15	52 %	15 nm
Ge [Pal98]	4.70	0.33	58 %	193 nm	4.14	2.22	53 %	14 nm
Substrates/Oxides								
Sapphire [MMR58]	1.760				1.7781			
Diamond [EO81]	2.408				2.471			
SrTiO <sub>3</sub> [Bon65]	2.745				2.340			
BaF <sub>2</sub> [Tro95]	1.4704				1.490			
MgF <sub>2</sub> [Dod84]	1.3751				1.3839			
CaF <sub>2</sub> [Mal63]	1.4305				1.4419			
LiNbO <sub>3</sub> [HW66]	2.2572				2.4393			
BK7 [CVI]	1.515				1.5302			
SiO <sub>2</sub> (FS) [Mal65]	1.4533				1.4696			
SiO <sub>2</sub> (Quarz) [Gho99]	1.5383				1.5577			
SF11 [CVI]	1.7648				1.8450			
LaSFN9 [CVI]	1.82				1.8984			
Liquids								
Glycerol	1.40-1.55				1.38-1.53			
DC704	1.55-1.65				1.45-1.55			
Water	1.34-1.36				1.33-1.35			

Table A.1: Optical properties of various materials calculated by equations A.2 and A.1.

	$\rho$ [ $\frac{g}{cm^3}$ ]	$v_l$ [ $\frac{nm}{ps}$ ]	$Z_l$ [MRayls]	$v_s$ [ $\frac{nm}{ps}$ ]	$Z_s$ [MRayls]
--	-----------------------------	---------------------------	----------------	---------------------------	----------------

Metals

Aluminum []	2.70	6.42	17	3.07	8.3
Cobalt []	8.8	5.80	51		
Copper []	8.93	4.76	42	2.34	20.9
Gold []	19.7	3.25	64	1.19	23.4
Silver []	10.4	3.65	38	1.61	16.7
Iron []	7.85	3.51 - 5.96	27 - 47	2.21 - 3.20	17 - 25
Nickel []	8.84	5.64	50	2.97	26.3
Chromium []	7.19	5.94	43		
Tungsten []	19.4	5.20	101		

Semiconductors/Semimetals

Silicon* [GSWB78]	2.34	8.43, 9.31, 9.36	18 - 22	5.84, 5.84, 5.10	12 - 14
a-Silicon [GSWB78]	2.21	7.5 - 8.5	16 - 19		
SrRuO <sub>3</sub> []	6.49	6.31	41		
GaAs* []	5.32	4.73, 5.24, 5.40	25 - 29	3.35, 2.48, 2.80	13 - 18
Ge* []	5.327	4.87, 5.36, 5.51	26	3.57, 2.77, 3.06	

Substrates/Oxides

Sapphire []					
Diamond* []	3.515	17.52, 18.32, 18.58		12.82, 11.66, 12.06	
SrTiO <sub>3</sub> [BR63]	5.13	7.88, 8.10, 8.14	40 - 42	4.91, 4.59, 4.70	24 - 25
BaF <sub>2</sub> []					
MgF <sub>2</sub> []					
CaF <sub>2</sub> []					
LiNbO <sub>3</sub> []					
BK7 []					
SiO <sub>2</sub> (FS) []					
SiO <sub>2</sub> (Quarz) []					
ZnO []	5.68	6.40			
SF11 []					
LaSFN9 []					

Liquids

Glycerol []					
DC704 []					
Water []	1	1.48			

\* [001], [110], [111], <http://www.ioffe.ru/SVA/NSM/Semicond/>

Table A.2: Acoustic Properties of Various Material.

	$\rho$ [ $g/cm^3$ ]	$C_V$ [ $J/kg \cdot K$ ]	$C_V$ [ $J/cm^{-3} \cdot K$ ]	$\kappa$ [ $W/m \cdot K$ ]
Glycerol (300°K) []	1.260	2430		0.29
DC704 (200°K)[Orc73, PN79]	1.170			
DC704 (300°K)[Orc73, PN79]	1.065			
Water (25°C) []			4.186	0.6
BK7 []	2.53	937	0.858	1.4
Fused Silica [TSM+02]	2.201	670-740		1.38-1.46
Quarz []	2.203	733		9.5
Ice (-10°C) []			1.938	2
SrTiO <sub>3</sub> [Sue65]				22
Sapphire [TSM+02]	3.980	750		42-46
Iron []			3.537	80
Aluminum (200°K) []	2.720			236
Aluminum (300°K) []	2.700		2.422	209
Gold []			2.492	310
Copper []			3.45	360-400
Silver []			2.44	410-430
Diamond []			1.782	1000-2300

Table A.3: Thermal properties of various materials.

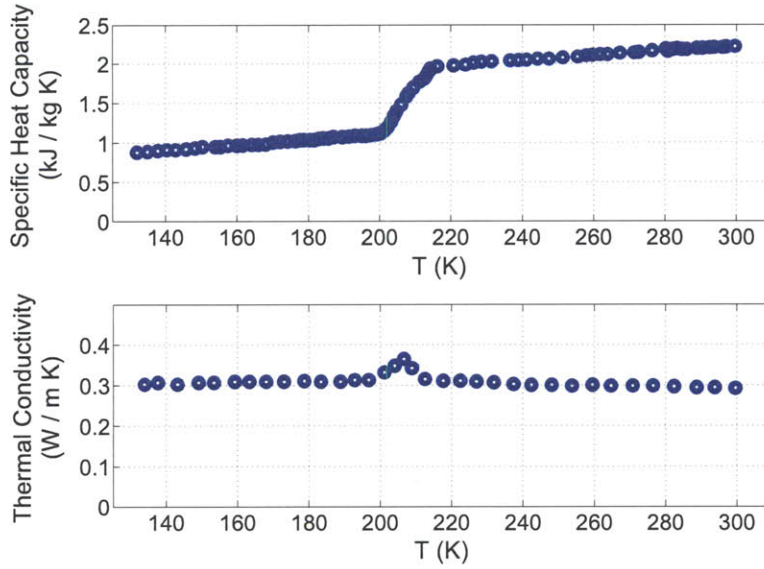


Figure A-1: Temperature dependent specific heat capacity and thermal conductivity of Glycerol. Taken from Sandberg et al. [SAB77].

## A.2 Temperature Dependent Parameters of Glycerol and DC704

### A.2.1 Glycerol

#### A.2.1.1 Density

Temperature dependent density for glycerol is given by [CFMS03]:

$$\rho(T > T_g) = 1272 \text{ [kg/m}^3\text{]} - 0.655 \text{ [kg/m}^3 \text{ K]} \times (T \text{ [K]} - 273 \text{ K}) \quad (\text{A.3})$$

$$\rho(T < T_g) = 1332 \text{ [kg/m}^3\text{]} - 0.320 \text{ [kg/m}^3 \text{ K]} \times (T \text{ [K]} - 187 \text{ K}) . \quad (\text{A.4})$$

#### A.2.1.2 Refractive Index

The dispersion formula for Glycerol at 25°C is given by  $n = C_1 + C_2\lambda^{-2} + C_3\lambda^{-4}$  with coefficients  $C_1 = 1.45797$ ,  $C_2 = 0.00598$ , and  $C_3 = -0.00036$  [RKW97].

wave length	400	450	500	550	600	650	700	750	800
ref. index	1.481	1.479	1.476	1.474	1.472	1.470	1.469	1.468	1.466

Table A.4: Refractive index of Glycerol at 25°C selected wave lengths.

The temperature dependence of the refractive index  $n$  can be evaluated from that of the temperature dependent mass density  $\rho$  using the ClausiusMossotti relation and is determined to be

$$n_{395}(T > T_g) = 1.675 - 6.5 \cdot 10^{-4} \text{ K}^{-1} \times T [\text{K}] , \text{ and} \quad (\text{A.5})$$

$$n_{395}(T < T_g) = 1.583 - 1.6 \cdot 10^{-4} \text{ K}^{-1} \times T [\text{K}] . \quad (\text{A.6})$$

## A.2.2 DC704

### A.2.2.1 Density

Temperature dependent density for DC704 is given by [Orc73, PN79]:

$$\rho(T > T_g) = 1067.9 [\text{kg/m}^3] - 0.72 [\text{kg/m}^3 \text{ K}] \times (T [\text{K}] - 298 \text{ K}) . \quad (\text{A.7})$$

### A.2.2.2 Refractive Index

The temperature dependent refractive index for DC704 at both optical detection wave lengths, 395 nm and 790 nm, was determined by means of a Michelson type interferometer. Outgassed DC704 was filled in a  $l = 10$  mm Starna cell with PTFE stopper\* and placed in the beam path of one interferometer arm inside the ST-100 (500 K) cold finger cryostat. The end mirror of this interferometer arm was placed on a motorized stage and hereby allowed to compensate for the temperature dependent optical delay experience by the femtosecond light pulses at either probe wavelength. The interferometer was initially aligned with an empty cell to give overlap of the beams from both arms of the Michelson type interferometer. In order to reestablish overlap of both beams after the liquid was filled into the cell, the motorized stage had to be moved by a distance  $d$ . The refractive index  $n$  was then given by  $n = 2d/l + 1$ . The measurement was repeated at various temperatures between 200 K and 400 K and yielded the following temperature dependent refractive indices at both probe wave lengths,

$$n_{395}(T_g \leq T \lesssim 400 \text{ K}) = 1.60 - 4.9 \cdot 10^{-4} \text{ K}^{-1} \times (T[\text{K}] - 293 \text{ K}) , \text{ and} \quad (\text{A.8})$$

$$n_{790}(T_g \leq T \lesssim 400 \text{ K}) = 1.49 - 4.1 \cdot 10^{-4} \text{ K}^{-1} \times (T[\text{K}] - 293 \text{ K}) . \quad (\text{A.9})$$

The measured slope is in excellent agreement with the temperature coefficient of  $4.2 \cdot 10^{-4} \text{ K}^{-1}$ , reported by Poulter and Nash [PN79] for 633 nm around room temperature.

---

\*[http://www.starnacells.com/d\\_cells\\_s/rect/T021.html](http://www.starnacells.com/d_cells_s/rect/T021.html)

---

# Bibliography

---

- [ADM<sup>+</sup>00] A. Aouadi, C. Dreyfus, M. Massot, R. M. Pick, T. Berger, W. Steffen, A. Patkowski, and C. Alba-Simionesco. Light scattering study of the liquidglass transition of meta-toluidine. *Journal of Chemical Physics*, 112(22):9860(14), 2000. ADM+00.
- [AG65] G. Adam and J. H. Gibbs. On the temperature dependence of cooperative relaxation properties in Glass-Forming liquids. *The Journal of Chemical Physics*, 43(1):139, 1965.
- [AHcMV72] P. W. Anderson, B. I. Halperin, and c. M. Varma. Anomalous low-temperature thermal properties of glasses and spin glasses. *Philosophical Magazine*, 25(1):1–9, 1972.
- [And95] P. W. Anderson. Through the glass lightly. *Science*, 267(5204):1615–1616, 1995.
- [Ang95] C. A. Angell. Formation of glasses from liquids and biopolymers. *Science*, 267(5206):1924–1935, 1995.
- [ANM<sup>+</sup>00] C. A. Angell, K. L. Ngai, G. B. McKenna, P. F. McMillan, and S. W. Martin. Relaxation in glassforming liquids and amorphous solids. *Journal of Applied Physics*, 88(6):3113(45), 2000.
- [BCE<sup>+</sup>04] Paola Benassi, Alessandro Cunsolo, Roberto Eramo, Andrea Giugni, Michele Nardone, and Marco Sampoli. Ultraviolet brillouin spectroscopy of glass-forming glycerol. *Philosophical Magazine*, 84(13-16):1413–1422, 2004.
- [BDHR01] R. Böhmer, G. Diezemann, G. Hinzee, and E. A. Rössler. Dynamics of supercooled liquids and glassy solids. *Progress in Nuclear Magnetic Resonance Spectroscopy*, 39(3):191–267, 2001.



- [BECW02] T. Barnes, T. Eiju, D. C. L. Cheung, and C. Y. Wu. Phase measurement accuracy of feedback interferometers. *Optics and Lasers in Engineering*, 38(6):387–404, 2002.
- [BGS84] U. Bengtzelius, W. Götze, and A. Sjolander. Dynamics of supercooled liquids and the glass transition. *Journal of Physics C: Solid State Physics*, 17(33):5915–5934, 1984.
- [BH66] M. Born and K. Huang. *Dynamical Theory of Crystal Lattices*. University Press, Oxford, 1966.
- [BK05] K. Binder and W. Kob. *Glassy materials and disordered solids : an introduction to their statistical mechanics*. World Scientific Pub. Co., [Hackensack N.J.], 2005.
- [Bon65] W. L. Bond. Measurement of the refractive indices of several crystals. *Journal of Applied Physics*, 36(5):1674, 1965.
- [BP03] T. Bienville and B. Perrin. Generation and detection of quasi transverse waves in an anisotropic crystal by picosecond ultrasonics. *Proceedings of the WCU, Paris*, September 2003.
- [BR63] R. Bell and G. Rupprecht. Elastic constants of strontium titanate. *Physical Review Letters*, 129(1):90–94, 1963.
- [BR05] A. Brodin and E. A. Rössler. Depolarized light scattering study of glycerol. *The European Physical Journal B*, 44(1):3–14, 2005.
- [Bra85] S. Brawer. *Relaxation in viscous liquids and glasses : review of phenomenology, molecular dynamics simulations, and theoretical treatment*. American Ceramic Society, Columbus Ohio, 1985.
- [CC41] K. S. Cole and R. H. Cole. Dispersion and absorption in dielectrics i. alternating current characteristics. *The Journal of Chemical Physics*, 9(4):341, 1941.
- [CCC98] J. H. Crowe, J. F. Carpenter, and L. M. Crowe. The role of vitrification in anhydrobiosis. *Annual Review of Physiology*, 60(1):73–103, 1998.
- [CFMR02] L. Comez, D. Fioretto, G. Monaco, and G. Ruocco. Brillouin scattering investigations of fast dynamics in glass forming systems. *Journal of Non-Crystalline Solids*, 307310:148(6), 2002. CFMR02.
- [CFSM03] L. Comez, D. Fioretto, F. Scarponi, and G. Monaco. Density fluctuations in the intermediate glass-former glycerol: A brillouin light scattering study. *Journal of Chemical Physics*, 119(12):6032(12), 2003.
- [CFY+05] J. D. Choi, T. Feurer, M. Yamaguchi, B. Paxton, and K. A. Nelson. Generation of ultrahigh-frequency tunable acoustic waves. *Applied Physics Letters*, 87(8):081907(3), 2005.

- [CLS04] G.-W. Chern, K.-H. Lin, and C.-K. Sun. Transmission of light through quantum heterostructures modulated by coherent acoustic phonons. *Journal of Applied Physics*, 95(3):1114, 2004.
- [CO94] T. Christensen and N. Olsen. Determination of the frequency-dependent bulk modulus of glycerol using a piezoelectric spherical shell. *Physical Review B*, 49(21):15396–15399, 1994.
- [CO95] T. Christensen and N. B. Olsen. A rheometer for the measurement of a high shear modulus covering more than seven decades of frequency below 50 kHz. *Review of Scientific Instruments*, 66(10):5019, 1995.
- [CT59] Morrel H. Cohen and David Turnbull. Molecular transport in liquids and glasses. *The Journal of Chemical Physics*, 31(5):1164(6), 1959.
- [DAP<sup>+</sup>98] C. Dreyfus, A. Aouadi, R. M. Pick, T. Berger, A. Patkowski, and W. Steffen. Light scattering measurement of shear viscosity in a fragile glass-forming liquid, metatoluidine. *Europhysics Letters (EPL)*, 42(1):55–60, 1998.
- [DC50] D. W. Davidson and R. H. Cole. Dielectric relaxation in glycerine. *The Journal of Chemical Physics*, 18:1417, 1950.
- [DC7] [http://www.lesker.com/newweb/Fluids/msds/DC\\_704\\_Oil.pdf](http://www.lesker.com/newweb/Fluids/msds/DC_704_Oil.pdf), Material data sheet of DC.
- [DFA<sup>+</sup>08] A. Devos, M. Foret, S. Ayrihac, P. Emery, and B. Ruffe. Hypersound damping in vitreous silica measured by picosecond acoustics. *Physical Review B*, 77(10):100201(R)(4), 2008.
- [DM86] S. Das and G. Mazenko. Fluctuating nonlinear hydrodynamics and the liquid-glass transition. *Physical Review A*, 34(3):2265–2282, 1986.
- [Dod84] M. J. Dodge. Refractive properties of magnesium fluoride. *Appl. Opt.*, 23(12):1980–1985, 1984.
- [DPP<sup>+</sup>95] D. Davazoglou, G. Pallis, V. Psycharis, M. Gioti, and S. Logothetidis. Structure and optical properties of tungsten thin films deposited by pyrolysis of W(CO)<sub>6</sub> at various temperatures. *Journal of Applied Physics*, 77(11):6070–6072, 1995.
- [DS01] P. G. Debenedetti and F. H. Stillinger. Supercooled liquids and the glass transition. *Nature*, 410:259–267, 2001.
- [Dyr06] J. C. Dyre. Colloquium: The glass transition and elastic models of glass-forming liquids. *Reviews of Modern Physics*, 78(3):953–972, 2006.
- [EAN96] M. D. Ediger, C. A. Angell, and S. R. Nagel. Supercooled liquids and glasses. *The Journal of Physical Chemistry*, 100(31):13200–13212, 1996.

- [Edi00] M. D. Ediger. Spatially heterogeneous dynamics in supercooled liquids. *Annual Review of Physical Chemistry*, 51(1):99–128, 2000.
- [EGR<sup>+</sup>07] Y. Ezzahri, S. Grauby, J. Rampnoux, H. Michel, G. Pernot, W. Claeys, S. Dilhaire, C. Rossignol, G. Zeng, and A. Shakouri. Coherent phonons in Si/SiGe superlattices. *Physical Review B*, 75(19), 2007.
- [EO81] D. F. Edwards and E. Ochoa. Infrared refractive index of diamond. *Journal of the Optical Society of America*, 71(5):607–608, 1981.
- [FAC<sup>+</sup>95] P. Frechard, S. Andrieu, D. Chateigner, M. Hallouis, P. Germi, and M. Pernet. Oblique growth of iron thin films on glass: a cross-sectional transmission electron microscopy study. *Thin Solid Films*, 263:42–46, 1995.
- [FFR90] B. Frick, B. Farago, and D. Richter. Temperature dependence of the nonergodicity parameter in polybutadiene in the neighborhood of the glass transition. *Physical Review Letters*, 64(24):2921–2924, 1990.
- [FGMS97] T. Franosch, W. Götze, M. R. Mayr, and A. P. Singh. Evolution of structural relaxation spectra of glycerol within the gigahertz band. *Physical Review E*, 55(3):3183–3190, 1997.
- [FKMN97] J. Fourkas, D. Kivelson, U. Mohanty, and K. A. Nelson. The Mode-Coupling theory of the glass transition. In *Supercooled liquids : advances and novel applications*, number 676 in ACS Symposium Series, page 2844. American Chemical Society, Washington DC, 1997.
- [Ful25] G. S. Fulcher. Analysis of recent measurements of the viscosity of glasses. *Journal of the American Ceramic Society*, 8(6):339–355, 1925.
- [GB89] M. Grimsditch and R. Bhadra. Shear waves through the Glass-Liquid transformation. *Physical Review Letters*, 62(22):2616, 1989.
- [GBB<sup>+</sup>04] C. Glorieux, J. D. Beers, E. H. Bentefour, K. Van de Rostyne, and K. A. Nelson. Phase mask based interferometer: Operation principle, performance, and application to thermoelastic phenomena. *Review of Scientific Instruments*, 75(9):2906(15), 2004.
- [GC06] A. Giugni and A. Cunsolo. Structural relaxation in the dynamics of glycerol: a joint visible, UV and x-ray inelastic scattering study. *Journal of Physics: Condensed Matter*, 18(3):889–902, 2006.
- [GD58] J. H. Gibbs and E. A. DiMarzio. Nature of the glass transition and the glassy state. *The Journal of Chemical Physics*, 28(3):373, 1958.
- [GdRG<sup>+</sup>06] C. Glorieux, K. Van de Rostyne, J. Goossens, G. Shkerdin, W. Lauriks, and K. A. Nelson. Shear properties of glycerol by interface wave laser ultrasonics. *Journal of Applied Physics*, 99(1):013511, 2006.

- [Gho99] G. Ghosh. Dispersion-equation coefficients for the refractive index and birefringence of calcite and quartz crystals. *Optics Communications*, 193(1):95–102, 1999.
- [Göt99] W. Götze. Recent tests of the mode-coupling theory for glassy dynamics. *Journal of Physics: Condensed Matter*, 11:A1–A45, 1999.
- [Gra91] S. Granick. Motions and relaxations of confined liquids. *Science*, 253(5026):1374–1379, 1991.
- [GS88] W. Götze and L. Sjogren. Scaling properties in supercooled liquids near the glass transition. *Journal of Physics C: Solid State Physics*, 21:3407–3421, 1988. GS88.
- [GSWB78] M. Grimsditch, W. Senn, G. Winterling, and M. H. Brodsky. Brillouin scattering from hydrogenated amorphous silicon. *Solid State Communications*, 26(4):229–233, 1978.
- [GT67] R. J. Greet and D. Turnbull. Glass transition in o-Terphenyl. *The Journal of Chemical Physics*, 46(4):1243, 1967.
- [Hec] Tina Hecksher. DNRFC Centre Glass and Time, IMFUFA, Roskilde University, Roskilde, Denmark.
- [Hec06] T. Hecksher. *Mechanical Spectrum of a Viscous Liquid*. Master thesis, IMFUFA, RUC, 2006.
- [HL59] G. Herzfeld and T. Litovitz. *Absorption and Dispersion of Ultrasonic Waves*. Academic Press, New York and London, 1959.
- [HN67] S. Havriliak and S. Negami. A complex plane representation of dielectric and mechanical relaxation processes in some polymers. *Journal of Polymer Science*, 8(4):161, 1967.
- [HO10] Tina Hecksher and Niels Boye Olson. Private communication, 2010.
- [HW66] M. V. Hobden and J. Warner. The temperature dependence of the refractive indices of pure lithium niobate. *Physical Review Letters*, 22(3):243–244, 1966.
- [HW99] D. H. Hurley and O. B. Wright. Detection of ultrafast phenomena by use of a modified sagnac interferometer. *Optics Letters*, 24(18):1305(3), 1999.
- [HWM+00] D. H. Hurley, O. B. Wright, O. Matsuda, V. E. Gusev, and O. V. Kolosov. Laser picosecond acoustics in isotropic and anisotropic materials. *Ultrasonics*, 38(1-8):470(5), 2000.

- [HZS01] M. Heuberger, M. Zäch, and N. D. Spencer. Density fluctuations under confinement: When is a fluid not a fluid? *Science*, 292(5518):905–908, 2001.
- [JB94] P. Jenniskens and D. F. Blake. Structural transitions in amorphous water ice and astrophysical implications. *Science*, 265:753756, 1994.
- [JC74] P. B. Johnson and R. W. Christy. Optical constants of transition metals: Ti, V, Cr, Mn, Fe, Co, Ni, and Pd. *Physical Review B*, 9(12):5056–5070, 1974.
- [Jeo87] Y. H. Jeong. Frequency-dependent shear modulus of glycerol near the glass transition. *Physical Review A*, 36(2):766–773, 1987.
- [JG70] G. P. Johari and M. Goldstein. Viscous liquids and the glass transition. II. secondary relaxations in glasses of rigid molecules. *The Journal of Chemical Physics*, 53(6):2372, 1970.
- [JNB86] Y. Jeong, S. Nagel, and S. Bhattacharya. Ultrasonic investigation of the glass transition in glycerol. *Physical Review A*, 34(1):602–608, 1986.
- [JNO05] B. Jakobsen, K. Niss, and N. B. Olsen. Dielectric and shear mechanical alpha and beta relaxations in seven glass-forming liquids. *The Journal of Chemical Physics*, 123(23):234511, 2005.
- [Joh10] J. A. Johnson. Private communication, 2010.
- [Kau48] Walter Kauzmann. The nature of the glassy state and the behavior of liquids at low temperatures. *Chemical Reviews*, 43(2):219–256, 1948.
- [Kaw66] K. Kawasaki. Correlation-Function approach to the transport coefficients near the critical point. i. *Physical Review*, 150(1):291–306, 1966.
- [KBB<sup>+</sup>02] J. Krüger, J. Baller, T. Britz, A. le Coutre, R. Peter, R. Bactavatchalou, and J. Schreiber. Cauchy-like relation between elastic constants in amorphous materials. *Physical Review B*, 66(1), 2002.
- [KBL01] U. Kaatz, R. Behrends, and K. Lautscham. Acoustic relaxation spectrometers for liquids. *Ultrasonics*, 39(6):393–406, 2001.
- [KK95] J. Klein and E. Kumacheva. Confinement-Induced phase transitions in simple liquids. *Science*, 269(5225):816–819, 1995.
- [Kli06] Christoph Klieber. *Ultrahigh Frequency Acoustic Waves Study of Vitreous Silica*. Diplomarbeit, Ludwig-Maximilians-Universitaet, Munich, 2006.
- [Koh54] R. Kohlrausch. Theorie des elektrischen rückstandes in der leidner flasche. *Annalen der Physik und Chemie*, 91(5682):179213, 1854.

- [Kov63] A. J. Kovacs. Transition vitreuse dans les polymres amorphes. etude phénoménologique. In *Fortschr. Hochpolym.-Forsch.*, volume 3, page 394507. Springer-Verlag, Berlin/Heidelberg, 1963.
- [Leu84] E. Leutheusser. Dynamical model of the liquid-glass transition. *Physical Review A*, 29(5):2765–2773, 1984.
- [Lid98] D. Lide. *CRC handbook of chemistry and physics, 1998-1999*. CRC Press, Boca Raton, 79th ed. edition, 1998.
- [LL01] P. Lunkenheimer and A. Loidl. Dynamic processes at the glass transition. In *Advances in Solid State Physics*, pages 405–417. Springer, Berlin / Heidelberg, 2001.
- [LL02] P. Lunkenheimer and A. Loidl. Dielectric spectroscopy of glass-forming materials: a-relaxation and excess wing. *Chemical Physics*, 284:205–219, 2002.
- [LMNM09] Y. Li, Q. Miao, A. V. Nurmikko, and H. J. Maris. Picosecond ultrasonic measurements using an optical cavity. *Journal of Applied Physics*, 105(8):083516, 2009.
- [LN97] R. L. Leheny and S. R. Nagel. High-frequency asymptotic shape of the primary relaxation in supercooled liquids. *Europhysics Letters (EPL)*, 39(4):447–452, 1997.
- [LPD+96] P. Lunkenheimer, A. Pimenov, M. Dressel, Y. G. Goncharov, R. Böhmer, and A. Loidl. Fast dynamics of Glass-Forming glycerol studied by dielectric spectroscopy. *Physical Review Letters*, 77(2):318(4), 1996.
- [LPS+96] P. Lunkenheimer, A. Pimenov, B. Schiener, R. Böhmer, and A. Loidl. High-frequency dielectric spectroscopy on glycerol. *Europhysics Letters*, 33(8):611(6), 1996.
- [LSBL00] P. Lunkenheimer, U. Schneider, R. Bran, and A. Loid. Glassy dynamics. *Contemporary Physics*, 41(1):15–36, 2000.
- [LSMT91] H. -N. Lin, R. J. Stoner, H. J. Maris, and J. Tauc. Phonon attenuation and velocity measurements in transparent materials by picosecond acoustic interferometry. *Journal of Applied Physics*, 69(7):3816, 1991.
- [Lun99] P. Lunkenheimer. *Dielectric spectroscopy of glassy dynamics*. Shaker, Aachen, 1999.
- [LWSL05] P. Lunkenheimer, R. Wehn, U. Schneider, and A. Loidl. Glassy aging dynamics. *Physical Review Letters*, 95(5), 2005.
- [MABM10] G. Meng, N. Arkus, M. P. Brenner, and V. N. Manoharan. The Free-Energy landscape of clusters of attractive hard spheres. *Science*, 327(5965):560–563, 2010.



- [Mal63] I. H. Malitson. A redetermination of some optical properties of calcium fluoride. *App. Opt.*, 2(11):1103–1107, 1963.
- [Mal65] I. H. Malitson. Interspecimen comparison of the refractive index of fused silica. *Journal of the Optical Society of America*, 55(10):1205–1209, 1965.
- [Mal92] D. Malacara. *Optical shop testing*. Wiley, New York, 2nd ed. edition, 1992.
- [Mar98] H. J. Maris. Picosecond ultrasonics. *Scientific American*, 278(1):86–89, 1998.
- [Mat07] Dmitry Matyushov. Model energy landscapes of low-temperature fluids: Dipolar hard spheres. *Physical Review E*, 76(1), 2007.
- [MBN+05] A. Moreno, S. Buldyrev, E. La Nave, I. Saika-Voivod, F. Sciortino, P. Tartaglia, and E. Zaccarelli. Energy landscape of a simple model for strong liquids. *Physical Review Letters*, 95(15), 2005.
- [MMR58] I. H. Malitson, F. V. Murphy, and W. S. Rodney. Refractive index of synthetic sapphire. *Journal of the Optical Society of America*, 48:72–73, 1958.
- [MMR06] P. Mayer, K. Miyazaki, and D. Reichman. Cooperativity beyond caging: Generalized Mode-Coupling theory. *Physical Review Letters*, 97(9):095702(4), 2006.
- [MMS+60] R. Meister, C. J. Marhoeffler, R. Sciamanda, L. Cotter, and T. Litovitz. Ultrasonic viscoelastic properties of associated liquids. *Journal of Applied Physics*, 31(5):854, 1960.
- [MTZM96] C. Morath, G. Tas, T. C. -D. Zhu, and H. J. Maris. Phonon attenuation in glasses studied by picosecond ultrasonics. *Physica B: Condensed Matter*, 219-220:296–298, 1996.
- [MW01] O. Matsuda and O. B. Wright. Theory of detection of shear strain pulses with laser picosecond acoustics. *Analytical Sciences*, 17:s216–218, 2001.
- [MWH+04] O. Matsuda, O. Wright, D. Hurley, V. Gusev, and K. Shimizu. Coherent shear phonon generation and detection with ultrashort optical pulses. *Physical Review Letters*, 93(9):095501(4), 2004.
- [MWH+08] O. Matsuda, O. Wright, D. Hurley, V. Gusev, and K. Shimizu. Coherent shear phonon generation and detection with picosecond laser acoustics. *Physical Review B*, 77(22):224110(16), 2008.
- [MWM07] M E Msall, O B Wright, and O Matsuda. Seeking shear waves in liquids with picosecond ultrasonics. *Journal of Physics: Conference Series*, 92(1):012026(4), 2007.

- [NJO05] K. Niss, B. Jakobsen, and N. B. Olsen. Dielectric and shear mechanical relaxations in glass-forming liquids: A test of the Gemant-DiMarzio-Bishop model. *The Journal of Chemical Physics*, 123(23):234510, 2005.
- [NLW00] M. Nikoonahad, S. Lee, and H. Wang. Picosecond photoacoustics using common-path interferometry. *Applied Physics Letters*, 76(4):514, 2000.
- [Orc73] R. H. Orcutt. Interlot density variation of a siloxane manometer fluid. *Journal of Vacuum Science and Technology*, 10(4):506, 1973.
- [Pal98] Edward D. Palik, editor. *Handbook of Optical Constants of Solids*. Elsevier, 1998.
- [PCR<sup>+</sup>06] T. Pezeril, N. Chigarev, P. Ruello, S. Gougeon, D. Mounier, J.-M. Breteau, P. Picart, and V. Gusev. Laser acoustics with picosecond collimated shear strain beams in single crystals and polycrystalline materials. *Physical Review B*, 73(13), 2006.
- [Pez05] T. Pezeril. *Génération et Détection d'Ondes Acoustiques Transverses Picosecondes: Théories et Expériences*. PhD thesis, Académie de Nantes, Ecole Doctorale de L'Université du Maine, Le Mans, France, 2005.
- [PKAN09] T. Pezeril, C. Klieber, S. Andrieu, and K. A. Nelson. Optical generation of Gigahertz-Frequency shear acoustic waves in liquid glycerol. *Physical Review Letters*, 102(10), 2009.
- [PL57] R. Piccirelli and T. A. Litovitz. Ultrasonic shear and compressional relaxation in liquid glycerol. *The Journal of the Acoustical Society of America*, 29(9):1009, 1957.
- [PN79] K. F. Poulter and P. J. Nash. An interferometric oil micromanometer. *J. Phys. E: Sci Instrum.*, 12:931–936, 1979.
- [PN00] Dora M. Paolucci and Keith A. Nelson. Impulsive stimulated thermal scattering study of structural relaxation in supercooled glycerol. *The Journal of Chemical Physics*, 112(15):6725, 2000.
- [Pos67] E. J. Post. Sagnac effect. *Review of Modern Physics*, 39(2):475–493, 1967.
- [PRBJ99] B. Perrin, C. Rossignol, B. Bonello, and J.-C. Jeannet. Interferometric detection in picosecond ultrasonics. *Physica B: Condensed Matter*, 263-264(1-4):571–573, 1999.
- [PRG<sup>+</sup>07] T. Pezeril, P. Ruello, S. Gougeon, N. Chigarev, D. Mounier, J.-M. Breteau, P. Picart, and V. Gusev. Generation and detection of plane coherent shear picosecond acoustic pulses by lasers: Experiment and theory. *Physical Review B*, 75(17):174307(19), 2007.

- [RBCE04] G. Rijnders, D. H. A. Blank, J. Choi, and C.-B. Eom. Enhanced surface diffusion through termination conversion during epitaxial SrRuO<sub>3</sub> growth. *Applied Physics Letters*, 84(4):505, 2004.
- [RC05] D. R. Reichman and P. Charbonneau. Mode-coupling theory. *Journal of Statistical Mechanics: Theory and Experiment*, 2005(05):P05013, 2005.
- [RFM<sup>+</sup>05] E. Rat, M. Foret, G. Massiera, R. Vialla, M. Arai, R. Vacher, and E. Courtens. Anharmonic versus relaxational sound damping in glasses. i. brillouin scattering from densified silica. *Physical Review B*, 72(21), 2005.
- [RKW97] J. Rheims, J. Koeser, and T. Wriedt. Refractive-index measurements in the near-IR using an abbe refractometer. *Meas. Sci. Technol.*, 8:601–605, 1997.
- [RMBN00] J. A. Rogers, A. A. Maznev, M. J. Banet, and K. A. Nelson. Optical generation and characterization of acoustic waves in thin films: Fundamentals and applications. *Annual Review of Materials Science*, 30(1):117–157, 2000.
- [RNS97] E. A. Rössler, V. N. Novikov, and A. P. Sokolov. Toward a general description of the dynamics of glass formers. *Phase Transitions*, 63(1):201–233, 1997.
- [Rös90] E. A. Rössler. Indications for a change of diffusion mechanism in supercooled liquids. *Physical Review Letters*, 65(13):1595–1598, 1990.
- [RRP<sup>+</sup>05] C. Rossignol, J. Rampnoux, M. Perton, B. Audoin, and S. Dilhaire. Generation and detection of shear acoustic waves in metal submicrometric films with ultrashort laser pulses. *Physical Review Letters*, 94(16), 2005.
- [RSKQ94] E. A. Rössler, A. Sokolov, A. Kisliuk, and D. Quitmann. Low-frequency raman scattering on different types of glass formers used to test predictions of mode-coupling theory. *Physical Review B*, 49(21):14967–14978, 1994.
- [SAB77] O. Sandberg, P. Andersson, and G. Backstrom. Heat capacity and thermal conductivity from pulsed wire probe measurements under pressure. *J. Phys. E: Sci. Instrum.*, 10:474–477, 1977.
- [Sag13] G. Sagnac. L'éther lumineux démontré par l'effet du vent relatif d'éther dans un interféromètre en rotation uniforme. *Comptes Rendus*, 157:708710, 1913.
- [SCC08] Aaron J. Schmidt, Xiaoyuan Chen, and Gang Chen. Pulse accumulation, radial heat conduction, and anisotropic thermal conductivity in pump-probe transient thermorefectance. *Review of Scientific Instruments*, 79(11):114902, 2008.

- [SCFP04] F. Scarponi, L. Comez, D. Fioretto, and L. Palmieri. Brillouin light scattering from transverse and longitudinal acoustic waves in glycerol. *Physical Review B*, 70(5):054203, 2004.
- [SD00] K. Schröter and E. Donth. Viscosity and shear response at the dynamic glass transition of glycerol. *The Journal of Chemical Physics*, 113(20):9101, 2000.
- [SD04] M. Shell and P. Debenedetti. Thermodynamics and the glass transition in model energy landscapes. *Physical Review E*, 69(5), 2004.
- [SDJM03] B. J. Siwick, J. R. Dwyer, R. E. Jordan, and R. J. D. Miller. An Atomic-Level view of melting using femtosecond electron diffraction. *Science*, 302(5649):1382–1385, 2003.
- [SFR95] F. Stickel, E. W. Fischer, and R. Richert. Dynamics of glass-forming liquids. i. temperature-derivative analysis of dielectric relaxation data. *The Journal of Chemical Physics*, 102(15):6251, 1995.
- [SKH<sup>+</sup>93] A. Schönhal, F. Kremer, A. Hofmann, E. Fischer, and E. Schlosser. Anomalies in the scaling of the dielectric  $\alpha$ -relaxation. *Physical Review Letters*, 70(22):3459–3462, 1993.
- [Sla02] Rebecca Slayton. *Developing a transient grating technique to probe fast acoustic dynamics in liquids*. PhD thesis, Harvard University, 2002.
- [SMW03] T. Saito, O. Matsuda, and O. B. Wright. Picosecond acoustic phonon pulse generation in nickel and chromium. *Physical Review B*, 67(20):205421, 2003.
- [SN04] R. M. Slayton and K. A. Nelson. Picosecond acoustic transmission measurements. II. probing high frequency structural relaxation in supercooled glycerol. *The Journal of Chemical Physics*, 120(8):3919, 2004.
- [SNM01] R. Slayton, K. A. Nelson, and A. A. Maznev. Transient grating measurements of film thickness in multilayer metal films. *Journal of Applied Physics*, 90(9):4392(11), 2001.
- [Sti95] F. H. Stillinger. A topographic view of supercooled liquids and glass formation. *Science*, 267(5206):1935–1939, 1995.
- [Sue65] Yasutaka Suemune. Thermal conductivity of BaTiO<sub>3</sub> and SrTiO<sub>3</sub> from 4.5 to 300K. *J. Phys. Soc. Jpn.*, 20:174–175, 1965.
- [SYFM05] L. J. Shelton, F. Yang, W. K. Ford, and H. J. Maris. Picosecond ultrasonic measurement of the velocity of phonons in water. *physica status solidi (b)*, 242(7):1379–1382, 2005.

- [TE97] S. N. Taraskin and S. R. Elliott. Phonons in vitreous silica: Dispersion and localization. *Europhysics Letters (EPL)*, 39(1):37–42, 1997.
- [TGMT86] C. Thomsen, H. Grahn, H. Maris, and J. Tauc. Surface generation and detection of phonons by picosecond light pulses. *Physical Review B*, 34(6):4129–4138, 1986.
- [TM94] G. Tas and H. J. Maris. Electron diffusion in metals studied by picosecond ultrasonics. *Physical Review B*, 49(21):15046–1554, 1994.
- [Tor] D. Torchinsky. Department of Physics, Massachusetts Institute of Technology.
- [Tor08] Darius H. Torchinsky. *Optical Study of Shear and Longitudinal Acoustic Waves and Complex Relaxation Dynamics of Glass Forming Liquids*. PhD thesis, Massachusetts Institute of Technology, Cambridge, MA, 2008.
- [Tor10] Darius H. Torchinsky. Private communication, 2010.
- [Tou10] Vincent Tournat. *Private Communication*. Laboratoire d’Acoustique de l’Université du Maine, UMR-CNRS, Université du Maine, 2010.
- [Tro95] W. J. Tropf. Temperature-dependent refractive index models for BaF<sub>2</sub>, CaF<sub>2</sub>, MgF<sub>2</sub>, SrF<sub>2</sub>, LiF, NaF, KCl, ZnS, and ZnSe. *Optical Engineering*, 34(5):1369–1373, 1995.
- [TSM<sup>+</sup>02] T. Tomaru, T. Suzuki, S. Miyoki, T. Uchiyama, C. T. Taylor, A. Yamamoto, T. Shintomi, M. Ohashi, and K. Kuroda. Thermal lensing in cryogenic sapphire substrates. *Classical and Quantum Gravity*, 19:2045–2049, 2002.
- [UY96] T. Uchino and T. Yoko. Low-Frequency raman scattering and the fast relaxation process in glycerol. *Science*, 273:480–483, 1996.
- [vCD06] P. J. S. van Capela and J. I. Dijkhuis. Optical generation and detection of shock waves in sapphire at room temperature. *Appl. Phys. Lett.*, 88:151910, 2006.
- [VCF05] R. Vacher, E. Courtens, and M. Foret. Anharmonic versus relaxational sound damping in glasses. II. vitreous silica. *Physical Review B*, 72(21), 2005.
- [WCK<sup>+</sup>08] P. Walker, R. Champion, A. Kent, D. Lehmann, and Cz. Jasiukiewicz. Excitation and detection of high-frequency coherent acoustic phonons in low-symmetry superlattices. *Physical Review B*, 78(23), 2008.
- [WG95] O. B. Wright and V. E. Gusev. Ultrafast generation of acoustic waves in copper. *IEEE Transactions on Ultrasonics, Ferroelectrics and Frequency Control*, 42(3):331–338, 1995.

- [WHL<sup>+</sup>94] J. Wuttke, J. Hernandez, G. Li, G. Coddens, H. Cummins, F. Fujara, W. Petry, and H. Sillescu. Neutron and light scattering study of supercooled glycerol. *Physical Review Letters*, 72(19):3052(5), 1994.
- [WW70] Graham Williams and David C. Watts. Non-symmetrical dielectric relaxation behaviour arising from a simple empirical decay function. *Transactions of the Faraday Society*, 66:80, 1970.
- [YAD<sup>+</sup>07] F Yang, T Atay, C H Dang, T J Grimsley, S Che, J Ma, Q Zhang, A V Nurmikko, and H J Maris. Study of phonon propagation in water using picosecond ultrasonics. *Journal of Physics: Conference Series*, 92:012024, 2007.
- [YCN88] Y.-X. Yan, L.-T. Cheng, and K. A. Nelson. The temperature-dependent distribution of relaxation times in glycerol: Time-domain light scattering study of acoustic and mountain-mode behavior in the 20 MHz-3 GHz frequency range. *Journal of Chemical Physics*, 88(10):6477–6486, 1988.
- [YN87] Y.-X. Yan and K. A. Nelson. Impulsive stimulated light scattering. II. comparison to frequency-domain light-scattering spectroscopy. *Journal of Chemical Physics*, 87(11):6257–5265, 1987. YN87.
- [YN95] Y. Yang and K. A. Nelson. Tc of the mode coupling theory evaluated from impulsive stimulated light scattering on salol. *Physical Review Letters*, 74(24):4883–4886, 1995.





---

# Curriculum Vitae

---

## Christoph Klieber

Rm. 2-084, MIT  
77 Mass Ave.  
Cambridge, MA 02139

christoph@klieber.net  
+1-617-642-1515 (US)  
+49-9221-97946 (Intl.)

22 Magazine St.  
Apt # 8  
Cambridge, MA 02139

---

### EDUCATION

#### Massachusetts Institute of Technology (2006-2010)

Cambridge, MA, USA

Ph.D. degree in Physical Chemistry, June 2010

Advisor: Professor Keith A. Nelson

- High frequency photo-acoustic spectroscopy of visco-elastic and amorphous materials.
- Study of high frequency relaxation dynamics in glass-forming liquids.
- Research toward a comprehensive understanding of phonon mediated heat transport in order to optimize conversion efficiency of thermo-electric devices.
- Development of a compact optical pulse shaper for frequencies between 1GHz and several THz.

#### Ludwig-Maximilian-University, University of Munich (2002-2006)

Munich, Germany

Diplom Physik, February 2006

Advisor: Professor Roland Kersting, Co-Advisor: Professor Keith A. Nelson

- Diploma thesis: "Ultrahigh frequency acoustic waves study of vitreous silica."

#### Jesuit College of Philosophy Munich (2002-2004)

Munich, Germany

Bakalaureal (B.A.) in Philosophy, February 2004

Advisor: Professor Godehard Brüntrup

- Focus: Ontology – Philosophy of organism and process philosophy of Alfred North Whitehead.

#### University of Bayreuth (1999-2001)

Bayreuth, Germany

Vordiplom Physik, October 2001

---

### EXPERIENCE

#### CNRS-Université Pierre et Marie Curie (Summer 2006)

Paris, France

- Simulation project with Prof. Bernhard Perrin of photo-acoustic spectroscopy in multi layer systems.

#### d-fine (risk consulting, Summer 2004)

Frankfurt, Germany

- Project in stock trading for Deutsche Bank AG.

#### Alcatel SEL AG (telecommunications system company, Summer 2001)

Stuttgart, Germany

- Development of highly stable power control units for telecommunication exchange servers.





